LEABHARLANN CHOLÁISTE NA TRÍONÓIDE, BAILE ÁTHA CLIATH | TRINITY COLLEGE LIBRARY DUBLIN
Ollscoil Átha Cliath | The University of Dublin

Terms and Conditions of Use of Digitised Theses from Trinity College Library Dublin

Copyright statement

All material supplied by Trinity College Library is protected by copyright (under the Copyright and Related Rights Act, 2000 as amended) and other relevant Intellectual Property Rights. By accessing and using a Digitised Thesis from Trinity College Library you acknowledge that all Intellectual Property Rights in any Works supplied are the sole and exclusive property of the copyright and/or other IPR holder. Specific copyright holders may not be explicitly identified. Use of materials from other sources within a thesis should not be construed as a claim over them.

A non-exclusive, non-transferable licence is hereby granted to those using or reproducing, in whole or in part, the material for valid purposes, providing the copyright owners are acknowledged using the normal conventions. Where specific permission to use material is required, this is identified and such permission must be sought from the copyright holder or agency cited.

Liability statement

By using a Digitised Thesis, I accept that Trinity College Dublin bears no legal responsibility for the accuracy, legality or comprehensiveness of materials contained within the thesis, and that Trinity College Dublin accepts no liability for indirect, consequential, or incidental, damages or losses arising from use of the thesis for whatever reason. Information located in a thesis may be subject to specific use constraints, details of which may not be explicitly described. It is the responsibility of potential and actual users to be aware of such constraints and to abide by them. By making use of material from a digitised thesis, you accept these copyright and disclaimer provisions. Where it is brought to the attention of Trinity College Library that there may be a breach of copyright or other restraint, it is the policy to withdraw or take down access to a thesis while the issue is being resolved.

Access Agreement

By using a Digitised Thesis from Trinity College Library you are bound by the following Terms & Conditions. Please read them carefully.

I have read and I understand the following statement: All material supplied via a Digitised Thesis from Trinity College Library is protected by copyright and other intellectual property rights, and duplication or sale of all or part of any of a thesis is not permitted, except that material may be duplicated by you for your research use or for educational purposes in electronic or print form providing the copyright owners are acknowledged using the normal conventions. You must obtain permission for any other use. Electronic or print copies may not be offered, whether for sale or otherwise to anyone. This copy has been supplied on the understanding that it is copyright material and that no quotation from the thesis may be published without proper acknowledgement.

Structures and Optical Properties of Reconstructed Si and Ge Surfaces



Soumya Banerjee

School of Physics

Trinity College Dublin

A thesis submitted for the degree of

Philosophiæ Doctor (PhD)

October 2015

TRINITY LIBRARY
27 JUL 2016
DUBLIN

Thesis 10963

Declaration

This thesis has been submitted to the University of Dublin for examination for the degree of Doctor in Philosophy by the undersigned.

This thesis has not been submitted as an exercise for a degree to any other university.

I declare that With the exception of the assistance noted in the acknowledgements, this thesis is entirely my own work.

I agree to deposit this thesis in the University's open access institutional repository or allow the library to do so on my behalf, subject to Irish Copyright Legislation and Trinity College Library conditions of use and acknowledgement.

Trinity College,
Dublin

Acknowledgments

First and foremost I would like to thank my supervisors Prof. John F. McGilp and Dr. Charles H. Patterson. They worked closely with me throughout the four years of my research, giving advice and guidance when needed. They always encouraged discussion and debate within the group, which lead to a great working environment.

The whole group who I have worked with over the last five years all has had an input into this work. I would like to thank Lina for showing me the basics of UHV and RAS systems, and sample mounting and cleaning, Martin for helping me always when I have any problem, Chris for his help with all kind of technical support and Pankaj and Eric for their help in computation. As with any thesis, there are countless others who have had an input so I hope I don't forget anybody; Karsten, Cormac, Iggy, Rugerro and the summer and the 4th year student that have come through the group in the last five years.

I am very grateful of all the support I have received from the electronics and mechanical workshops in the school of physics. Joe, Dave, Mick, and Ken have also provided valuable help and advice during this research. I am thankful to TCHPC, IITAC and ICHEC for the high end computing facility and Paddy, Jimmy and Allen for helping me out with any problem.

I would also like to thank all my friends who have been with me in all ups and downs in these five years. No thesis would be possible with out all the help and encouragement received from my parents, Saraswati and Debi Prosad Banerjee, and my wife, Tanya.

Abstract

An approach combining reflection anisotropy spectroscopy (RAS) measurement and hybrid density functional theory (DFT) was taken to test and model various reconstructed surfaces of group-IV semiconductors (Si and Ge) in this project. The results obtained demonstrate that hybrid DFT offers a computationally efficient approach to calculating the optical response of surface structures. Using hybrid DFT functionals, structural, electronic and optical properties were calculated for Si(111)-(2×1) superstructures with modified Pandey (MP) chains. The (2×1) surface with asymmetric π chains has two variants, which are $\pm$MP chain structures. The +MP chain structure was found to be more stable than the -MP chain structure by a very small total energy difference (2 meV). Bond lengths between atoms in surface and the next layer are reported and compared with previous experimental data and calculated values. Electronic structures for both the MP structures were calculated which revealed two surface states (occupied and unoccupied). The occupied and unoccupied surface states were found to be mainly localised on the outermost and innermost Si atoms of the asymmetric π chain, respectively. Direct band gaps are reported here to be 0.29 and 0.40 eV, with optical gaps of 0.29 and 0.40 eV for + and -MP structures, respectively. The calculated imaginary parts of dielectric functions for $\pm$MP structures show large peaks below 1 eV with the electric field aligned in the π chain direction. The large positive peaks in RA spectra of + and -MP surfaces are found to be at 0.43 and 0.57 eV, respectively, with the experimental value at 0.46 eV. Transitions responsible for those peaks are identified as surface state transitions.

Si(111)-(5×2) surfaces, with 0.6 and 0.7 monolayer (ML) Au atom coverages, and with and without Si adatoms, were calculated. The Si honeycomb chain (HC) along with the $SiAu_4$ butterfly wing configuration are found to be very stable structural units of this surface. The Au-Au rungs in $SiAu_4$ butterfly wing motif are found to be rotated as a result of adatom decoration. Without adatoms all Si(111)-(5×2) surfaces show metallic behaviour in their calculated electronic structures. Adatom decorated surface with 0.7 ML coverage produced a gap

opening with a value of ~0.45 eV. RA spectra calculated for the different surfaces produced positive peaks under 1 eV and a good number of structures over 1 eV. Transitions responsible for the peaks in the RA spectra are identified and reported here.

Clean Si(110) forms a very large 16×2 unit cell, which presents a challenge to both theory and experiment. Both short and long heating processes were used to obtain double and single domain surfaces of Si(110)-(16×2). Low energy electron diffraction (LEED) images show that the angle between two domains in double domain surface is 110^o, which explains the surface contribution in the RA spectrum of the double domain surface. LEED spots were found to be formed almost perpendicular to the direct current (DC) direction used for sample heating, which is different from previous experiments. Directions of the bulk and surface optic axes were determined and found to be in the same direction. Hybrid DFT calculations were carried out to calculate the optical properties of the partially optimised adatom-tetramer-interstitial (ATI) model of Si(110)-(16×2) surface. The calculated RA spectra of Si(110)-(16×2) has low energy structures which are absent in the experiment. The RA spectra of Si(110)-(1×1) was also calculated and compared to the experimental RA spectra of native-oxide-covered Si(110).

Vicinal Ge(001) surfaces offcut towards <111> and <110> produced double and single domain surfaces, respectively, when Ar^+-ion etched and annealed. LEED images of clean and Sb deposited Ge(001) surfaces showed that Ge-Ge and Sb-Sb dimers are aligned in the same direction. Experimental RA spectra of clean single and double domain Ge(001)-(2×1) surfaces were compared, which revealed differences below 2.0 eV. The RA spectrum was also recorded for Sb deposited Ge(001) surface. Using hybrid DFT methods, surface structures of clean Ge(001) and Ge(001)-(2×1)-Sb were optimised to get their electronic structures and optical responses. Surface states in the electronic structures were found to be mainly localised on dimer atoms (Ge or Sb dimers) and on Ge atoms just beneath the surface layers. The calculated RA spectra of all the surfaces have negative minima below 1.5 eV, which arise from the transitions between the sur-

face states. RA spectra of clean Ge(001) were found to be very different from that of the Sb deposited Ge(001) surface. Good agreement between theory and experiment was obtained, even though the step structure was not included in the theoretical calculations.

Contents

1 Introduction **1**

1.1 Opening remarks 1

1.2 Si(111)-(2 × 1) 4

1.2.1 Modified Pandey (MP) chain 4

1.2.2 Electronic structure 5

1.2.3 Optical properties 7

1.3 Si(111)-(5 × 2)-Au 8

1.3.1 Proposed models 9

1.3.2 Band structure 11

1.3.3 Optical properties 13

1.4 Si(110)-(16 × 2) 14

1.4.1 Preparation of Si(110)-(16 × 2) 15

1.4.2 Structural models for Si(110)-(16 × 2) 16

1.4.3 Electronic structure and optical properties 17

1.5 Ge(001) 19

1.5.1 Clean Ge(001) surfaces 19

1.5.2 Ge(001)-(2 × 1)Sb 22

1.5.3 Electronic and optical properties of Ge(001) and Ge(001)-(2 × 1) 23

1.6 Purpose of this thesis 24

2 Theoretical Background and Computational Detail **26**

2.1 Hartree-Fock and Density Functional Theories 26

2.1.1 Hartree-Fock Theory 27

2.1.2 Density Functional Theory 30
2.2 Generalized Gradient Approximations (GGA) 32
2.3 Hybrid DFT 34
2.4 The CRYSTAL code 35
2.4.1 Localised orbital vs. plane-wave basis sets 37
2.5 Electronic vs. optical bandgap 39
2.6 Dielectric Function 40
2.7 The EXCITON code 42
2.8 Reflectance Anisotropy Spectroscopy 42

3 Experimental Detail **46**
3.1 Sample preparation 46
3.1.1 Si(110) 48
3.1.2 Ge(001) 49
3.2 Sample characterisation 51
3.2.1 Low energy electron diffraction and Auger electron spectroscopy 51
3.3 Reflection anisotropy spectroscopy 54
3.3.1 Photoelastic modulator RAS 56

4 Si(111)-(2×1) and (5×2)-Au surfaces **62**
4.1 Si(111)-(2×1) 62
4.1.1 Surface structure of Si(111)-(2×1) 62
4.1.2 Electronic Structure 65
4.1.3 Optical Properties 69
4.2 Si(111)-(5×2)-Au 73
4.2.1 Surface structure of Si(111)-(5×2)-Au 73
4.2.2 Electronic structure 78
4.2.3 Optical Properties 85
4.3 Discussion and conclusion 93

5 Si(110) **95**
5.1 Native-oxide-covered Si(110) 95

5.2 Experiment 97
5.3 Clean double domain (16 × 2) surface 98
5.4 Clean single domain (16 × 2) surface 100
5.4.1 Investigating the optic axes of the (16 × 2) surface 101
5.5 *Ab initio* calculation of Si(110)-(16 × 2) 105
5.6 Discussion and conclusion 108

6 Ge(001) 109
6.1 Experiment 109
6.2 *Ab initio* calculations 113
6.2.1 Equilibrium structures of clean Ge(001) 113
6.2.2 Ge(001)-(2 × 1)-Sb 116
6.3 Band Structure 118
6.3.1 Clean Ge(001) 118
6.3.2 Ge(001)-(2 × 1)-Sb 122
6.4 Optical Properties 123
6.4.1 Bulk Ge 123
6.4.2 Clean Ge 124
6.4.3 Ge(001)-(2 × 1)-Sb 129
6.5 Comparison with clean Si(001) surfaces 130
6.6 Discussion and conclusion 132

7 Conclusion and future work 134
7.1 Conclusion 134
7.2 Future work 138

A Detail of Calculations 139

B Basis Sets 141

C Jones Matrices 146

D FlexRAS Labview Program 148

References 151

Publications

C. H. Patterson, S. Banerjee, and J. F. McGilp, "Optical and phonon excitations of modified Pandey chains at the Si(111)-(2 × 1) surface", *Phys. Rev. B*,84, 155314 (2011).

S. Banerjee, J. F. McGilp, and C. H. Patterson, "Reflectance anisotropy spectroscopy of clean and Sb covered Ge(001) surfaces and comparison with clean Si(001) surfaces", *physica status solidi (b)*, 252, 78 (2015).

C. H. Patterson, S. Banerjee and J. F. McGilp, "Structure relations and optical spectra of the (5×2), $\sqrt{3}$ and (6×6) phases of Au on Si(111)", submitted to *physica status solidi*, August 2015.

List of Figures

1.1 (a) Top and (b) side views of positive (left) and negative-tilt (right) MP structures 4
1.2 Brillouin zone and band structure of +MP structure 6
1.3 Brillouin zone and band structure of -MP structure 6
1.4 RA spectrum of a single domain Si(111)-(2 × 1) surface 8
1.5 The EBH model 10
1.6 ARPES data from single domain Si(111)-(5 × 2)-Au 12
1.7 Calculated band structure of Si(111)-Au in four different scenarios 13
1.8 RAS signal from Si(111)-(5 × 2)-Au 14
1.9 STM image of a typical Si(110)-(16 × 2) reconstructed surface . . 15
1.10 Pentamers model of Si(110)-(16 × 2) 17
1.11 ARPES of Si(110)-(16 × 2) surface 18
1.12 ARPES of Si(110)-(16 × 2) surface 18
1.13 (a) Side and (b) top views of Ge(001) surface 20

2.1 Three Phase Model to describe RA spectroscopy 43

3.1 The sample mount used for UHV experiments 47
3.2 The emissivity of Si 47
3.3 Short heating temperature profile 48
3.4 Schematic diagram of ISIS3000 ion source. 49
3.5 Schematic diagram of the NTEZ 40-2-16-KS-2006178 from MBE-Komponenten 50
3.6 Variation in vapour pressure with increasing temperature 51
3.7 Variation in mean escape depth with increasing electron energy . 52

3.8 LEED image, taken from the clean single domain Si(110)-(16×2) surface. 53
3.9 Schematic of the LEED-Auger system 53
3.10 RAS signal from native-oxide-covered Si(110). 55
3.11 A schematic of a PEM RAS system 58
3.12 The broad-band RAS system 59
3.13 The emission from a high pressure Xenon bulb 60

4.1 Atomic structures of the modified Pandey chain model 63
4.2 (a)Top view of the (2×1) superlattice of the MP chain model . . 66
4.3 Electronic structure of +MP chain model 66
4.4 Electronic structure of -MP chain model 67
4.5 Calculated imaginary part of the dielectric function for +MP structure 70
4.6 Calculated imaginary part of the dielectric function for -MP structure 71
4.7 The calculated RA spectra of ±MP structures 72
4.8 (a) Modulus squared of the transition matrix element, $p^i_{nn'k}$ 73
4.9 Top and side views of fully relaxed EBH model 74
4.10 Top and side view of EBH structure of Si(111)-(5×4)-Au 75
4.11 Si(111)-(5×2)-Au superstructure proposed by Abukawa *et al* . . 76
4.12 Comparison between proposed (a) EBH and (b) KK model 76
4.13 Top and side views of relaxed KK model of Si(111)-(5×2)-Au unit cell 77
4.14 Top and side views of relaxed KK model with one Si adatom per (5×4) unit cell 78
4.15 SBZ of $5 \times 1, \times 2$and $\times 4$ unit cells 79
4.16 Hybrid DFT calculations of the electronic structure for the EBH model of Si(111)-(5×2)-Au 80
4.17 Hybrid DFT calculations of the electronic structure for the KK model of Si(111)-(5×2)-Au 81
4.18 Hybrid DFT calculations of the electronic structure for the EBH model of Si(111)-(5×4)-Au 83

4.19 Hybrid DFT calculations of the electronic structure for the KK model of Si(111)-(5 × 4)-Au 84
4.20 Comparison between the imaginary part of calculated dielectric functions of EBH structure 86
4.21 Comparison between experimental and theoretical RA spectra of EBH Si(111)-(5 × 2)-Au 87
4.22 Calculated imaginary part of the dielectric functions of EBH structure (one Si adatom per (5 × 4) unit cell) 87
4.23 Experimental and theoretical RA spectra of EBH structure (one adatom per Si(111)-(5 × 4)-Au unit cell) 88
4.24 Calculated imaginary part of the dielectric function of the KK structure 88
4.25 Experimental and theoretical RA spectra for the KK structure . . 89
4.26 Comparison between the imaginary part of calculated dielectric functions of the KK structure (one Si adatom per (5 × 4) unit cell) 89
4.27 Comparison between the imaginary part of calculated dielectric functions of the KK structure (one Si adatom per (5 × 4) unit cell) 90
4.28 Comparison between calculated and experimental RA spectra of the KK structure (one Si adatom per (5 × 4) unit cell) 91

5.1 Various positions of the sample and direction of LEED pattern of clean single domain (16 × 2) surface 96
5.2 A typical window strain signal 96
5.3 Comparison between the positive, negative and inverted negative maximum RA spectra of native oxide covered Si(110) 97
5.4 LEED pattern of the clean double domain (16 × 2) surface taken at 72.1 eV. 99
5.5 Comparison between RA spectra of native oxide covered Si(110) (red) and clean double domain (16 × 2) structure (green). 99
5.6 LEED image of the single domain surface taken at 78.9 eV after overnight heating. 100

5.7 Comparison between the RA spectra of native oxide covered Si(110) sample and after heating the sample over night 101
5.8 RA spectra of single domain Si(110)-(16 × 2), as a function of azimuthal angle. 102
5.9 RAS values at 1.36 eV are plotted with varying angle and fitted with cosine curve. 103
5.10 RAS values at 1.78 eV are plotted with varying angle and fitted with cosine curve. 103
5.11 RAS values at 3.28 eV are plotted with varying angle and fitted with cosine curve. 104
5.12 RAS values at 4.22 eV are plotted with varying angle and fitted with cosine curve. 104
5.13 (a) Top and (b) side views of ATI model 106
5.14 The calculated imaginary part of Si(110)-(16 × 2) and bulk Si . . 106
5.15 Comparison between experimental and calculated RA spectra for Si(110)-(16 × 2) surface 107
5.16 Comparison between measured RA spectrum of native oxide layered Si(110) and calculated RA spectrum for for H terminated Si(110)-(1 × 1) slab 107

6.1 Double domain (2 × 1) LEED image of the clean Ge(001) 110
6.2 Predominantly single domain (2 × 1) LEED image of clean Ge(001) 110
6.3 Predominantly single domain (2 × 1) LEED image of Sb deposited on Ge(001) 111
6.4 Sample positions 111
6.5 Comparison between RA spectra measured from clean Ge(001) samples 112
6.6 Difference between RA spectra of single and double domain clean Ge(001) surfaces. 112
6.7 Atomic structure of the Ge(001)-(2 × 1) surface along with its underlying bulk 114

6.8 Atomic structure of Ge(001)-p(2 × 2) surface along with its underlying bulk . . . 115
6.9 Atomic structure of the Ge(001)-c(4 × 2) surface along with its underlying bulk . . . 115
6.10 Atomic structure of the Ge(001)-(2 × 1)-Sb surface along with its underlying bulk . . . 116
6.11 Electronic structure of the clean Ge(001)-(2 × 1) . . . 119
6.12 Electronic structure of the asymmetric p(2 × 2) clean surface . . . 120
6.13 Electronic structure of the clean Ge(001)-c(4 × 2) . . . 121
6.14 Electronic structure of the symmetric (2 × 1)-Sb . . . 123
6.15 (a) Real and (b) imaginary part of the dielectric function of bulk Ge 124
6.16 Calculated imaginary part of the dielectric function of Ge(001)-(2×1) 125
6.17 RA spectrum of Ge(001)-(2 × 1) . . . 125
6.18 Calculated imaginary part of dielectric function of Ge(001)-p(2 × 2) 126
6.19 Calculated RA spectrum of Ge(001)-p(2 × 2). . . . 126
6.20 Calculated imaginary part of dielectric function of Ge(001)-c(4 × 2) 127
6.21 RA spectra of Ge(001)-c(4 × 2) . . . 128
6.22 Calculated imaginary part of the dielectric function of Ge(001)-(2 × 1)-Sb . . . 129
6.23 RA spectra of Ge(001)-(2 × 1)-Sb . . . 130
6.24 RA spectra of clean Si(001) surfaces . . . 131

D.1 The front panel of the RAS LabView program . . . 149
D.2 The Adjustment mode, this mode is used for alignment . . . 150
D.3 Main Spectral mode . . . 150
D.4 Transient mode . . . 151

List of Tables

1.1 Energy differences for various reconstructions of Ge(001). 22

4.1 Surface bond lengths in Å in MP structures 64

4.2 Positions of surface states in eV relative to the E_F in the ±MP structure. 68

5.1 Values of ϕ_0 with its error at different energies. 105

6.1 Dimer and back bond lengths at the Ge(001)-(2 × 1) surface in Å. 114

6.2 Dimer and back bond lengths at the Ge(001)-c(4 × 2) surface in Å. 114

6.3 Dimer and back bond lengths at the Ge(001)-(2 × 1)-Sb surface in Å. 117

6.4 Band gaps of clean Ge(001) surfaces from hybrid DFT calculations in eV. 120

A.1 Lattice parameters for different slabs. 140

List of Acronyms

0D	0-Dimensional
1D	1-Dimensional
2D	2-Dimensional
3D	3-Dimensional
AES	Auger Electron Spectroscopy
AFM	Atomic Force Microscopy
ARPES	Angle Resolved Photoemssion Spectroscopy
ATI	Adatom-Tetramer-Interstitial
Au D	Gold double chain
Au S	Gold single chain
B3LYP	Becke-3-Lee-Yang-Par
BSSE	Basis Set Superposition Error
CBM	Conduction Band Minimum
CMOS	Complementary Metal-Oxide Semiconductor
DFT	Density Functional Theory
DOS	Density of States
E_F	Fermi Energy
EM	Electromigration
GEA	Gradient Expansion Approximation
GGA	Generalised Gradient Approximation
HOMO	Highest Occupied Molecular Orbital
IPES	Inverse Photoemission Spectroscopy
LDA	Local Density Approximation
LEED	Low Energy Electron Diffraction
LUMO	Lowest Unoccupied Molecular Orbital
MBE	Molecular Beam Epitaxy
MD	Molecular Dynamics
ML	Monolayer
MOKE	Magneto Optical Kerr Effect
MP	Modified Pandey

PBN	Poly-Boron Nitride
PEM	Photo-Elastic Modulator
PW	Perdew-Wang
RAS	Reflection Anisotropy Spectroscopy
RDS	Reflectance Difference Spectroscopy
RHEED	Reflection High Energy Electron Diffraction
SBZ	Surface Brillouin Zone
SDR	Surface Differential Reflectivity
SEX-AFS	Surface Extended X-ray Absorption Fine Structure
Si HC	Silicon Honeycomb
STM	Scanning Tunnelling Microscopy
STS	Scanning Tunnelling Spectroscopy
SXD	Surface X-ray Diffraction
UHV	Ultra High Vacuum
VASP	Vienna Ab-initio Simulation Package
VBM	Valence Band Maximum
VWN	Vosko-Wilks-Nussair
XMCD	X-ray magnetic circular dichroism
XSW	X-ray Standing Wave

List of Element Abbreviations

Ag	Silver
Al	Aluminium
Ar	Argon
As	Arsenide
Au	Gold
Ba	Barium
C	Carbon
Ca	Calcium
Cd	Cadmium
Cu	Copper
F	Florine
Ga	Gallium
Ge	Germanium
H	Hydrogen
Hg	Mercury
In	Indium
K	Potassium
Mg	Magnesium
N	Nitrogen
Na	Sodium
O	Oxygen
Pb	Lead
Pr	Praseodymium
Sb	Antimony
Si	Silicon
Te	Tellurium
Xe	Xenon
Zn	Zinc

Chapter 1

Introduction

1.1 Opening remarks

When a crystal is cut in a specific direction the forces on the surface differ from those on the bulk atoms, which may result in surface reconstruction. When these systems are energetically relaxed, sometimes they form special ordered structures like one dimensional atomic chains or rows of dimers due to surface reconstruction. Systems with reconstructed surfaces can exhibit completely different electronic and optical properties than the bulk. This has become increasingly important with the development of nanoscience and nanotechnology. As material systems become smaller, the surface to volume ratio increases, and surfaces and interfaces become increasingly important in determining the properties of the nanostructures.

The change in optical properties can be used to help characterise structural and electronic properties. This special area of optics is called *epioptics* [1] to distinguish it from conventional optical spectroscopies. These optical techniques, reviewed recently [2], have advantages over conventional surface techniques as they can be used, in a wide range of ambients, to probe gas-soild interface, as well as any interfaces combining liquids and solids, due to the large penetration depth of the optical radiation. Sensitivity and ability to discriminate surface from the bulk are the two challenging things for the techniques to probe surface

and interface structures. Sensitivity of these techniques can be improved by improving the instruments. On the other hand, conventional optical techniques can be used to identify the heterogeneous structures on a substrate, with very good resolution. Scanning near-field optics can be used to get nanoscale lateral resolution. By exploiting the symmetry difference between bulk and the surface or interface, a class of separate techniques (both linear and nonlinear) can suppress the bulk contribution.

Some of the surfaces are optically anisotropic in the surface plane, while the bulk is optically isotropic in cubic materials like semiconductors. A combination of optical experimental measurements and computer simulations may then be used to identify those special structures on the surfaces by exploiting the optical anisotropy. RAS is a linear optical technique that provides optical information about ordered surfaces and interfaces that are anisotropic in the surface plane. RAS is a technique where the difference in the reflectance of a surface for normal incidence light is measured for two orthogonal polarisations of the light over the visible and near-visible range of photon energies. The potential of RAS as a non-destructive optical probe was first reported in the 1980s [3–10]. In 1985, Aspnes and co-workers published the first RAS study of native-oxide-covered Si(110) and Ge(110) surfaces [3], while Berkovits and co-workers published the first results from a well-charactered III-V semiconductor surface [11]. The early work was aimed at the study of III-V semiconductor surfaces, and the impetus for the development of RAS, primarily by Aspnes and co-workers [3–10], was the need for a real time optical probe for use in semiconductor growth systems. The original papers referred to the technique as reflectance difference spectroscopy (RDS). The term RAS was applied to the technique [12] to distinguish it from surface differential reflection (SDR), which compares the difference in reflection of linearly polarised light, aligned along orthogonal directions of a single crystal sample, with that of a reference sample. Since the first published work on the RDS/RAS technique [3–11], RAS is rapidly becoming an established technique for *in situ* semiconductor growth monitoring, as can be seen in a recent review [13]. RAS associated with semiconductor research has dominated the field, but RAS is finding

increasing application in fields of more immediate relevance to technological development such as clean single crystal metals [14–18] and semiconductors [4, 19], self-organisation of organics on surfaces [20, 21], surface reconstructions [22–24], aligned nanostructures on surfaces [25–30] and systems which have been strained along one axis [31–34]. It has mainly been used as a fingerprint technique, because calculating the optical response from first principles is computationally expensive.

This thesis investigates a recently developed more efficient *ab initio* approach, hybrid DFT, for calculating the optical response of different reconstructions for Si and Ge for comparison with experiment. In this work the RA spectra are calculated and measured experimentally for different Si and Ge systems. Some of the structures, like Si(111)-(5 × 2)-Au [35] or Si(110)-(16 × 2) [36], are controversial. The aim of this research is to test the hybrid DFT approach for calculating minimum energy structures and RA spectra using accepted structures (clean Si(111)-(2 × 1) [37], Ge(001) [38], Ge(001)-(2 × 1)-Sb [39]) and measuring their RA spectra. RAS measures the optical transitions between the occupied states and the empty excited states. The well known underestimation of excited state energies within the local density approximation [40] makes calculating the RA spectra a serious challenge for hybrid DFT. Having tested the approach, the controversial Si(110)-(16 × 2) and Si(111)-(5 × 2)-Au surface structures were investigated. Regarding the choice of these systems, the Si(111)-(2 × 1) structure is well understood, but some details of the electronic structure remain to be resolved. Si(110) is the least understood of the main surfaces of Si and is becoming technologically important [41, 42]. However, the (16 × 2) reconstruction is very large for *ab initio* calculations. The Si(111)-(5 × 2)-Au structure shows quasi one-dimensional (1D) electronic structure and has attracted considerable interest. Finally Ge(001) is becoming important both for electronic device and solar cell technology [43].

1.2 Si(111)-(2×1)

1.2.1 Modified Pandey (MP) chain

The cleaved Si(111) surface exhibits a (2×1) reconstructed structure whose two dimensional unit cell is only twice as large as the bulk configuration in one direction, in contrast to the lowest energy structure, Si(111)-(7×7). This simple (2×1) surface has been studied for over fifty years since 1961 [37, 44–49]. The model for the (2×1) surface reconstruction, proposed by Haneman [44], was supported by Pandey and Phillips in 1975 [50], by comparing calculated electronic structure with ARPES. The model was challenged by Chadi with the help of total energy calculations [51].

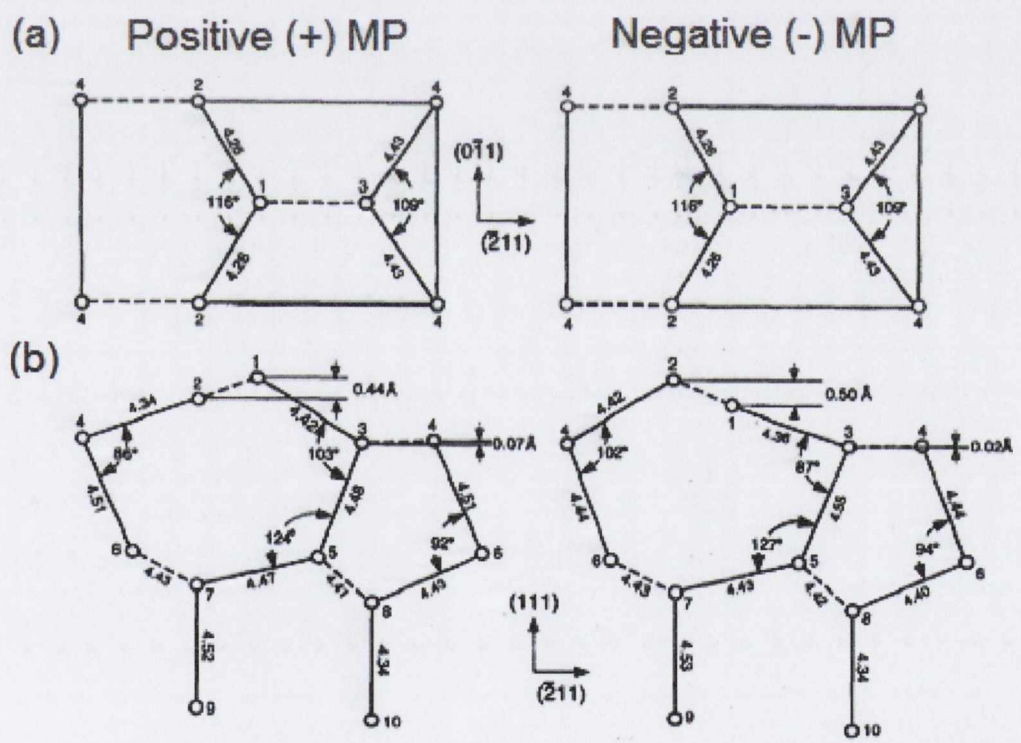


Figure 1.1: (a) Top and (b) side views of positive (left) and negative-tilt (right) MP structures after Zitzlsperger *et al.* [52].

The Pandey π-bonded chain model from 1982 for the (2×1) construction of the Si(111) surface predicts that the atoms in the π chain lie in the same horizontal plane [37]. This structure was not consistent with detailed LEED

studies [46, 53] and the possibility of an asymmetric arrangement of atoms in the π chain was reported [52]. This model was called a modified Pandey (MP) chain model. It was predicted that the MP chains are tilted in one direction throughout the surface. Some early total energy calculations of the atomic coordinates of the surface structure supported these LEED data [47, 54]. Zitzlspergerer *et al.* reported the possibility of positive (+MP) and negative (-MP) buckling [52] in different unit cells (Fig. 1.1) in detail. With the help of DFT it was shown that both the buckling structures are similar and very close in terms of total energy. The co-existence of both structures on the same surface was consistent with dynamical LEED [48] analysis. The most recent LEED analysis considered the +MP structure and mixtures of ±MP structures, but did not consider the -MP structure separately.

One more dimension was added to the complexity of the problem in the form of the total energy of the structure. The energy difference between +MP and -MP structures is very small, making the determination of the lowest energy structure challenging. Based on the SLAB-MINDO molecular orbital method, the negative buckled structure (Fig. 1.1) was reported to have slightly lower energy,with an energy difference of 6 meV/surface atom [55]. This prediction was supported by Zitzlsperger*et al.* [52], Stekolnikov *et al.* [56] and Garleff *et al.* [57] with LDA-DFT studies, with energy differences of 2.7, 10 and 12 meV per unit cell, respectively. A recent DFT-GW study of these surfaces [58] found both ±MP structures to have a very small total energy difference and that, for n-doped Si(111), the dopant electrons stabilise the -MP structure.

1.2.2 Electronic structure

In the 1970s the number of surface states in the electronic structure for the clean Si(111)-(2 × 1) surface was uncertain [50, 59, 60]. In the 1980s some calculations predicted two surface states, one occupied and one empty [61]. Later, ARPES [62] and IPES [63] studies mapped the dispersion of filled and vacant surface-state bands in the bulk band gap for the (2 × 1) surface. ARPES gave the position of

the occupied surface state as 0.5 eV below the Fermi energy and IPES reported the unoccupied surface state at 0.25 eV above E_F. These results gave a band gap, which was 0.3 eV higher than the optical gap (see section 1.2.3) [64, 65]. In the early 1990s many-body calculations obtained better agreement with experiment for the occupied states [54].

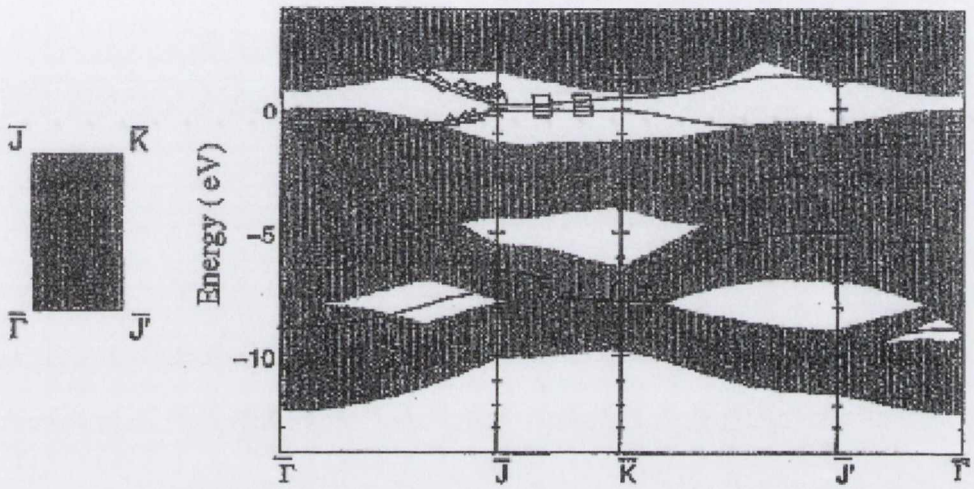


Figure 1.2: Brillouin zone and band structure of +MP structure (after [52]).

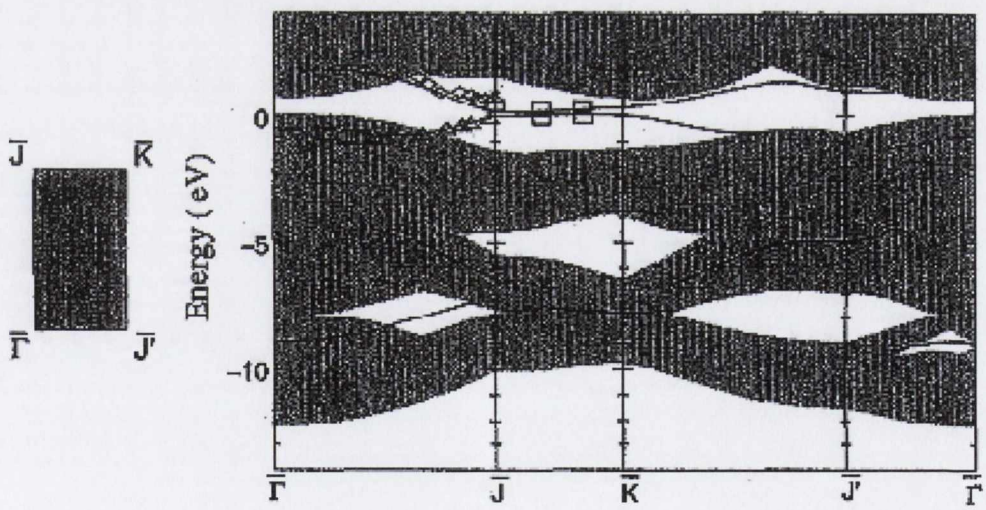


Figure 1.3: Brillouin zone and band structure of -MP structure (after [52]).

In 1997 electronic structures, for both ±MP chain models, were calculated using DFT-LDA [52](Fig. 1.2 and 1.3) and the band gaps for +MP and -MP

structures were predicted as 0.33 and 0.15 eV, which are smaller than the experimental optical gap value of 0.47 eV [66]. In the early 2000 some *ab initio* calculations were done to predict the band gap [56, 57] but all predictions failed to match experiment and triggered an argument over whether or not the surface was semiconducting. Recently, the HOMO-LUMO gap was measured to be 0.83 and 0.47 eV, for +MP and -MP models respectively, by STM and it was proposed that n-type Si(111) stabilises the -MP structure, and it is this gap that is measured by optical techniques [58].

1.2.3 Optical properties

Studies of UHV-cleaved (111) surfaces of Ge and Si in the 1970s, using multiple internal reflections and surface differential reflectivity (SDR), were the first to show that the surface optical response was detectable and could provide valuable information on surface crystallographic and electronic structure [67, 68]. A key experiment in 1984 showed the 0.47 eV transition to be strongly polarised along the Pandey chains [54]. For many years, the main peak in the optical spectrum of the Si(111)-(2 × 1) surface, at 0.47 eV (Fig. 1.4), was the subject of discussion, arising from the difference between the optical band gap, and the band gap determined from electron spectroscopies [50, 54, 58, 66, 67, 69–71]. Theoretical predictions of strongly bound (∼0.3 eV) surface-state excitons were supported by experiments in the late 1980s [54, 63], while in the early 1990s, a calculation [72], which included band gap corrections (due to electron-hole interaction) to LDA found good agreement with photoemission [54, 62] and optical measurements [66], but not with STM [73] or photoemission from highly n-doped samples [65]. These differences appear to have been resolved recently by taken into account the effect of n-doping on the stability of the -MP structure, as discussed above [58]. More recent optical experiments in the infrared region at and below 0.47 eV have confirmed a single optical transition polarised along the Pandey chains [23, 74, 75].

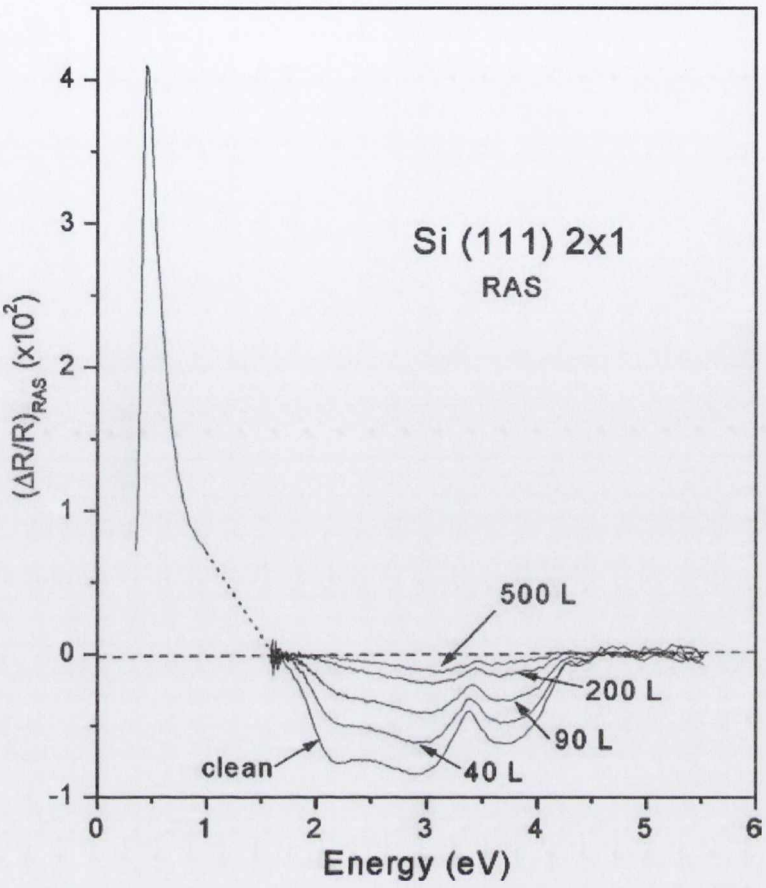


Figure 1.4: RA spectrum of a single domain Si(111)-(2×1) surface after [75]. It also shows the change of spectrum with oxygen exposure in L.

1.3 Si(111)-(5×2)-Au

When metals are deposited on semiconductor surfaces, they can form atomic chains by self assembly in some cases, particularly where there are well-ordered step structures. The chains can sometimes exhibit quasi 1D behaviour in the band structure. There are some unique properties of metals in 1D, e.g. transport behaviour changes as electrons can not avoid each other. For a three dimensional (3D) free electron metal, the density of states varies as $\sqrt{E}$, but in 1D the density of states drastically changes and produces a series of spikes called van Hove singularities [76,77]. If an electron is promoted from one van Hove singularity to the next, strong absorption peaks are obtained, and so such singularities are very

important in optical spectroscopy.

Another property, shown by 1D metallic chains is the Peierls instability [78]. If metal atoms are arranged in a linear chain in a periodic manner, with lattice constant a, the electrons form a parabolic metallic band. If the periodicity is slightly altered and doubled in the chain direction with lattice constant $2a$, then the bands back-fold at the Brillouin zone (BZ) boundary and a gap is opened, which results in a lower energy structure. This instability means that an unsupported 1D chain of metallic atoms will always have a semiconducting ground state. The energy saving is small, however, so the instability would be expected to be seen at low temperature. In real systems the metallic chain is supported on a substrate, such as Si, and the transition can be suppressed due to the interaction between the chain and the substrate lattice. Atomic chains grown on semiconductor surfaces by self-assembly are promising for investigating quasi-1D behaviour. The transition between the room temperature Si(111)-(4×1)-In structure and the low temperature Si(111)-(8×2)-In structure appears to be an example of a Peierls transitions in surface chain structures [79–81].

Since the original work over 40 years ago [82] the Si(111)-Au surfaces have been intensively studied. More recently, Si(111)-(5×2)-Au has attracted great interest as a representative of a self-organised quasi-1D metal chain system [83–86], and has showed 1D phenomena such as atomic-scale Schottky barriers [87], 1D domain-wall hopping [88], and confined doping on a metallic chain [89]. The highly anisotropic (5×2) structure exhibits metallic behaviour in one direction only [35,85,90]. However, the Si(111)-(5×2)-Au structure remains controversial, partly because an early coverage study [91] turned out to be incorreect [92], leading to models with too few Au atoms per unit cell. In addition, the structure is very sensitive to the adatom coverage [35].

1.3.1 Proposed models

It is generally agreed that linear metallic chains, which may be up to $\sim$1 μm long, are formed on the surface by self-assembly [82,93,94]. As mentioned above,

earlier work was based on the wrong Au coverage [95–98]. Careful studies now place the Au coverage at between 0.6 ML [35, 92] and 0.7 ML [99]. The incorrect coverage of 0.4 ML allowed only 2 Au chains to be formed, but the higher coverages favour a 3 Au chain model [35].

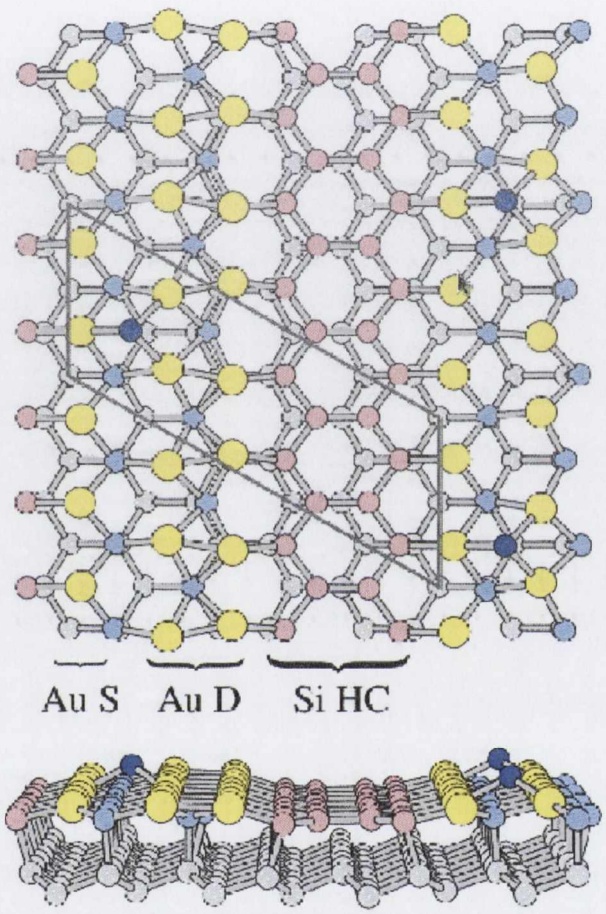


Figure 1.5: The EBH model consists of a double Au chain (AuD) and a single Au chain (Au S), and one Si honeycomb chain (Si HC) (after [35]).

One of the most important building blocks of the (5×2) structure is a Si HC, which is a graphitic chain of Si atoms. The proposed structures for many adsorbates on Si(111), such as Si(111)-(3×1)-Ag, -Na, -Ca, -K [100,101], Si(111)-(5×2)-Au [35], and -$(\sqrt{3} \times \sqrt{3})$-Au [102] have Si HC structures, which are energetically very stable [35, 100–102]. The metal atoms act as a re-bonding row between HCs. In 2009 Erwin *et al.* (thereafter, EBH) [35] proposed three Au

chains between two HCs (Fig. 1.5). They minimised the surface energy after adding Si adatoms with (5×4) periodicity. In the presence of adatoms the periodicity of the underlying substrate spontaneously doubled from (5×1) to (5×2) because of the dimerisation within the Au double row (Fig. 1.5).

Another stability factor of this model is Si adatoms [35]. The bright protrusions in STM images were recognised as Si adatoms rather than Au by both experiment [103] and theory [94]. A Si adatom sits between two Au rows to form a (5×4) superlattice [35, 85, 94, 104, 105]. According to Erwin *et al.*, adatoms donate electrons to the chains, causing them to change from metallic to semiconducting [35]. One adatom per (5×4) unit cell, which means 0.5 ML coverage of Si adatoms, was confirmed by Kwon *et al.* [99]. It was reported that the optical properties of the surface change quite significantly with the adatom coverage [106].

1.3.2 Band structure

The electronic structure of Si(111)$-(5 \times 2)-$Au has attracted considerable interest, as mentioned above [93, 107–109]. Collins *et al.* reported that Si(111) $-$ $(5 \times 2)-$Au showed a 1D band in photoemission spectroscopy at room temperature, which was metallic [83]. Hill *et al.* proposed that the metallic surface states arise from the Si adatoms, not the Au at the surface [84]. Losio *et al.* reported that the Au-induced surface state band loses its one-dimensional character below the Fermi level and shows a gradually increasing dispersion perpendicular to the Au chains [107]. Matsuda *et al.* [110] reinvestigated the band structure of the Si(111)(5×2)-Au surface with a p-type crystal and an intentional miscut of 2^{o} towards $[\bar{1}12]$ to ensure a single domain structure via growth from aligned steps. The single domain structure allowed the full symmetry of the surface to be explored. The ARPES results in Fig. 1.6 show surface bands denoted, S_1, S_2, S_3, S'_3 and S_4. The shaded region is the bulk band structure projected onto the (1×1) surface Brillouin zone (SBZ).

The S_1 band has almost perfect 1D dispersion along the direction of the 1D chain structure of the Si(111)-(5×2)-Au surface. The S_1 band is an intrinsic

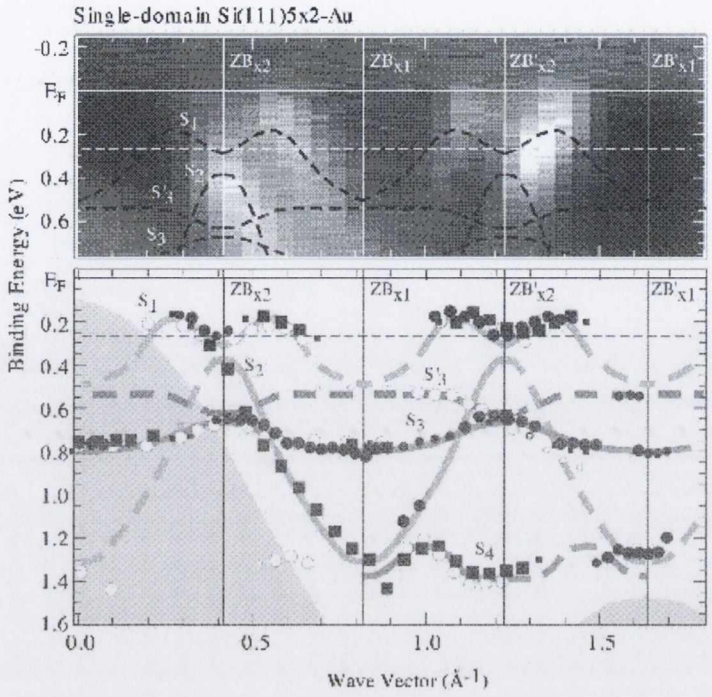


Figure 1.6: ARPES data from single domain Si(111)-(5 × 2)-Au (after [110]).

feature of the Si(111)(5 × 2)-Au surface. The gap between S_1 and S_2 bands (about 0.3 eV) can be explained by a simple band picture of splitting between S_1 and S_2 (an anti-crossing behaviour). Some earlier work at low temperature had attributed the gap to a Peierls distortion of the quasi-1D electronic state, but Matsuda *et al.* argued that the observed S_1 band gap to be ∼0.2 eV and excluded this possibility, as the surface appears to be semiconducting. There was further progress when a higher coverage of Au was confirmed [92]. In 2009 Erwin *et al.* proposed a three chain model [35], which agrees quite well with the existing experimental results. The population of Si adatoms plays a crucial role (Fig. 1.7), and there was good experimental evidence that the equilibrated structure comprises of areas with no Si adatoms, and areas with one adatom per (5 × 4) unit cell, giving an average coverage of 0.5 ML [103]. They found that the Si(111)-(5 × 2)-Au surface structure is most energetically favourable with one adatom per (5 × 4) unit cell, where every Si adatom dopes the surface with 2 electrons [94].

The calculated band structure of Si(111)-Au in four different scenarios is shown

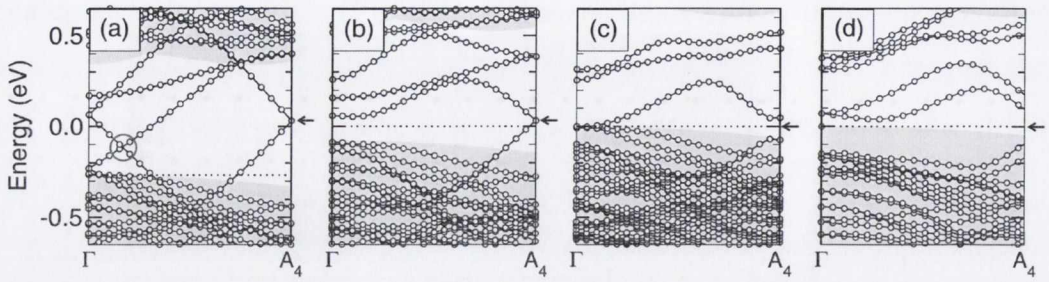


Figure 1.7: Calculated band structure of Si(111)-Au in four different scenarios. (a) (5×1) undecorated, undoped. (b) (5×2) doped with 2 electrons per (5×4) cell. (c) (5×4) one adatom per (5×4) unit cell; (d) as (c), including spin-orbit coupling (after [35]).

in Fig. 1.7. The energy bands of the undoped (5×1) surface, in which there are zone-boundary degeneracy and band crossing, is shown Fig. 1.7(a). The band structure of the (5×2) surface, doped by 2 electrons, is shown in Fig. 1.7(b) with the zone-boundary degeneracy intact but a large hybridisation gap at the band crossing of the undoped surface and the Fermi level is pushed into this gap. Fig. 1.7(c) and (d) are showing the band structure of the surface with 1/4 silicon adatoms coverage per (5×1) unit cell, without and with spin-orbit coupling lifting the zone-boundary degeneracy. Fig. 1.7(d) shows that electron doping opens a gap in the band structure. The observed surface is phase separated into undecorated (5×2) regions and adatom doped (5×4) regions in equal proportion. The band gap opening and transition from metallic to semiconducting system, due to the Si adatoms, was supported recently [99].

1.3.3 Optical properties

There have been a number of RAS studies of Si(111)-(5×2)-Au and related structures [28, 30, 106, 111], which have shown that the optical response is very sensitive to the detail of the surface structure, including the local step structure. The RA response also is very sensitive to the Si adatom coverage. Fig. 1.8 shows the effect of depositing additional Si adatoms on the RA spectral signature, which is still unexplained [112]. The equilibrium (5×2) structure corresponds to 50% adatom site occupancy per (5×4) unit cell. The RA response for 100% occupancy

is dramatically different. It is clear that this system offers a significant challenge for *ab initio* RA response calculation, both because of the large unit cell and the sensitivity to the adatom coverage, and no calculation had been published at the beginning of this project.

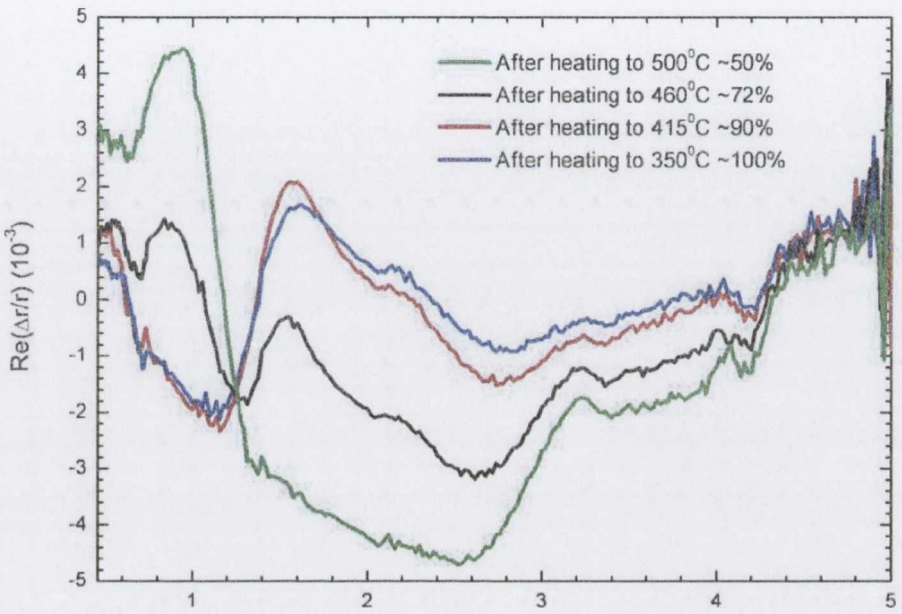


Figure 1.8: RAS signal from Si(111)-(5×2)-Au with additional adatom occupancy (after [112]).

1.4 Si(110)-(16 × 2)

The Si(110) surface has become important for fabricating complementary metal-oxide semiconductor (CMOS) circuits with high hole mobility. CMOS transistors based on the Si(110) surface have higher hole mobilities than those based on a Si(001) interfaces [113]. Further, the Si(110) surface has strongly anisotropic properties. A surface with an anisotropic structure is a good template for nanowire growth and in fact Si(110) has been used to grow nanowires of different materials [41, 42]. The clean Si(110) reconstructs to form a (16 × 2) superstructure that is still not well understood because of the difficulty in surface preparation, the depth of the reconstruction, the large size of the unit cell, and the lack of technological importance until recently.

1.4.1 Preparation of Si(110)-(16 × 2)

Preparation of clean single domain Si(110)-(16 × 2) surface is very difficult. Two recipes have been used successfully. One is a relatively short, high temperature procedure [114], where the Si(110) sample is flashed at high temperature, annealed at lower temperature and then cooled down slowly. This sometimes produces double domain Si(110)-(16 × 2) structures where real space stripes (observed by STM) run along $[1\bar{1}2]$ and $[\bar{1}12]$ directions. The LEED spots of 16× rows in this case are in the $[\bar{1}1\bar{1}]$ and $[1\bar{1}\bar{1}]$ directions (Fig.1.9).

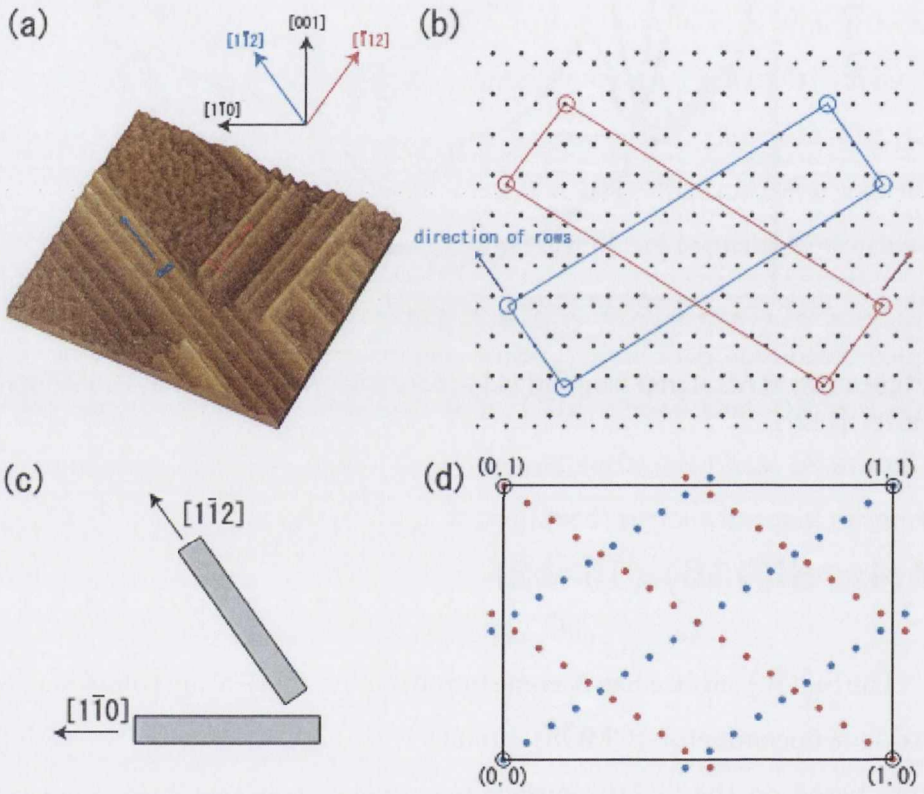


Figure 1.9: (a) STM image of a typical Si(110)-(16 × 2) reconstructed surface (after Ref. [115]). The reconstruction rows running along $[1\bar{1}2]$ and $[\bar{1}12]$ directions are indicated by blue and red arrows. The unit cell of (16 × 2) is schematically shown by red and blue rectangles. A coexisting disordered area can be seen at the top corner. (b) Two equivalent unit cells for (16 × 2) reconstruction (red and blue). Black dots represent atoms of unreconstructed Si(110) surface. (c) Schematic drawing of two specimens used in this study. (d) Reciprocal lattice scheme for (16 × 2) (blue and red dots). Black open circles represent (1 × 1) spots.

Another process, which takes longer and uses lower temperatures, is reported to

produce single domain (16 × 2) surfaces reliably [115, 116]. It involves direction-controlled DC heating. A great deal of interest was given to the direction of heating i.e. the direction of DC [115]. It was reported that a well-defined single domain Si(110)-(16 × 2) surface structure was achieved by heating the sample along the $[1\bar{1}2]$ direction, while heating along the $[1\bar{1}0]$ direction disorders the surface. It was thought that DC heating can induce electromigration (EM) of surface Si atoms in order to line up the reconstruction rows when the DC direction matches the orientation of the row, in this case $[1\bar{1}2]$ [115].

1.4.2 Structural models for Si(110)-(16 × 2)

There is no generally accepted model of the (16 × 2) reconstruction. STM studies have reported various structural features, such as dimers, trimers, pentamers and zig-zag chains, and models have been developed based on such features [117–122]. Some STM experiments appear to show the presence of dimers and trimers on the up and down steps running along the [110] direction [117, 118]. This alternatively raised and lowered structure may be the most stable form of clean (110) surfaces of the diamond structure, as this kind of structure was reported previously on Ge(110) [123] and SiGe/Si(110) [124] surfaces. Later STM studies [117–120] suggested that the (16 × 2) surface consists of zigzag chains along the $[\bar{1}11]$ direction, accompanied by bond rotation and bond contraction-relaxation. They also suggested the presence of equally spaced and alternatively raised (up-stripes) and lowered (down-stripes) stripes parallel to the $[\bar{1}12]$ direction, where the steps are separated by atomic steps with height $a_0/2\sqrt{2}$ (a_0 is the bulk lattice constant).

STM images of the stripes are not very clear, which has led to a number of other structures being proposed, involving features such as adatoms, dimers, missing rows, tetramers with interstitial atoms and pentamers [117, 119–122]. Those different predictions make the surface very interesting and controversial. High resolution ARPES and STM studies by Nakamoto *et al.* in 2009 [114] showed that the adatom-tetramer-interstitial (ATI) model of An *et al.* [119], which had

been regarded as promising, could not account for the images observed. Buckling of Si atoms, in every second row of the first Si layer between pentamers, was proposed. Fig. 1.10 shows the complexity of the model that was required to account for the data. In 2011 a model with tetramers and adatoms was proposed based on experimental and theoretical STM images [125]. There appear to be no total energy calculations on the structures proposed in Ref. [114] and [125], probably due to the size of the unit cell and the depth of the reconstruction.

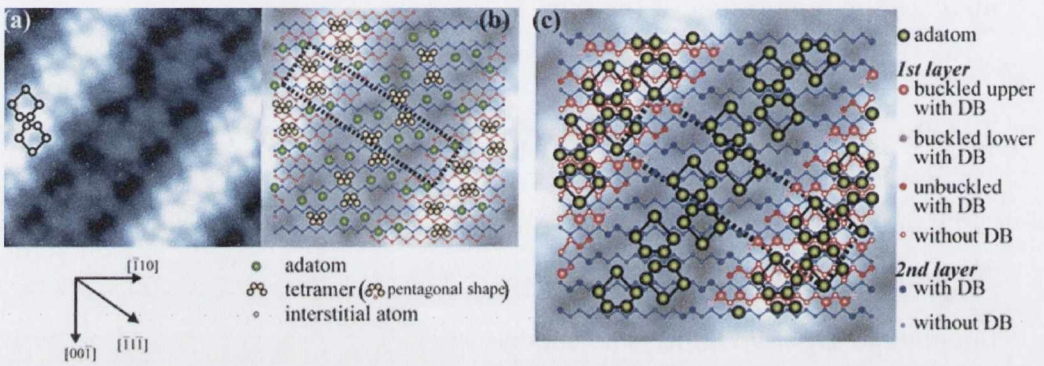


Figure 1.10: Pentamers model of Si(110)-(16 × 2) (after Ref. [114]). DB refers to dangling bonds.

1.4.3 Electronic structure and optical properties

Compared to a large number of studies on the atomic structure, only a few studies have been performed on the valence electronic structure of this surface [114, 121, 126], which can provide insight about the physical properties of the system. The early studies [121, 126] found that the surface was semiconducting and that there were four surface states below 5 eV binding energy (E_{B}), and the surface state with lowest E_{B} had 0.6 eV dispersion width. However, Kim *et al.* in 2007 found only two surface states at 0.4 and 0.9 eV, with dispersions below 0.2 eV, when they studied ARPES in three high symmetry directions, $[\bar{1}10]$, $[\bar{1}1\bar{1}]$, and $[00\bar{1}]$ in the (1×1) surface Brillouin zone [36]. Nakamoto *et al.* in 2009 again found four surface states [114] (shown in Figs. 1.11 and 1.12) in the bulk band gap. The state with lowest binding energy (S_1) is localised on the pentamers (see above), and other surface states ($S_2 - S_4$) are associated with the steps. An attempt to identify the atoms in the superstructure on which the surface states

are localised, was made in 2011 [125]. Just one surface state was reported localised on the tetramer structures and adatoms. A recent calculation found that pentamers appear in the band structure 0.45 eV below E_F, while states closer to the Fermi level derive from steps [127]. The source of the surface states observed in ARPES remains unclear.

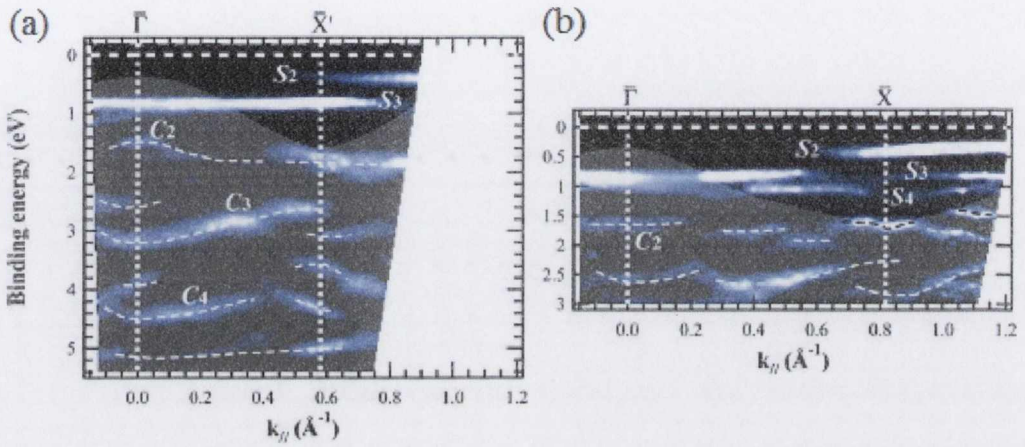


Figure 1.11: ARPES of Si(110)-(16 × 2) surface, measured along (a) [00$\bar{1}$] ($\bar{\Gamma}$-$\bar{X}'$) and (b) [$\bar{1}$10] ($\bar{\Gamma}$-$\bar{X}$) directions. The shaded areas are bulk band projections (after [114]).

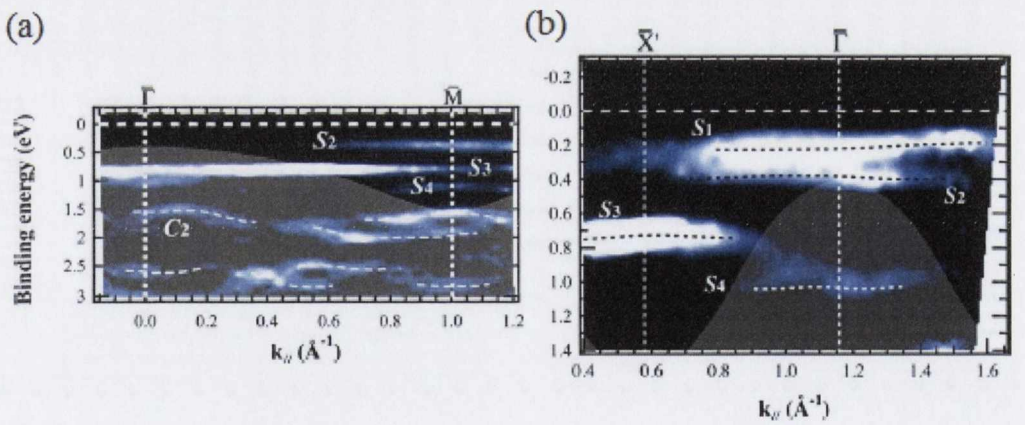


Figure 1.12: ARPES of Si(110)-(16 × 2) surface, measured along (a) [$\bar{1}\bar{1}$] ($\bar{\Gamma}$-$\bar{M}$) and (b) [00$\bar{1}$] ($\bar{X}'$-$\bar{\Gamma}$) directions. The shaded areas are bulk band projections (after [114]).

There appears to have been only one study of optical transitions at the Si(110)-(16 × 2) surface. SDR was measured by Cricenti *et al.* in 1995 [121, 128] and found 3 positive maxima around 1.8, 2.45 and 3.4 eV energies. An attempt to

calculate the SDR response was made recently [127], but it failed to produce good agreement with experiment.

1.5 Ge(001)

1.5.1 Clean Ge(001) surfaces

There have been a number of studies of the clean Ge(001) surface [38, 129–134]. The atoms on the unreconstructed Ge(001) surface have two broken bonds (Fig.1.13(a)). It is energetically favourable for neighbouring atoms to move together to form new bonds. When Schlier and Farnsworth proposed the dimer models for both Si and Ge (001) surfaces to explain the (2×1) LEED pattern which they observed [134], they assumed that the dimers were symmetric. In the late 1970s Chadi [135] proposed that the surface dimers of Si and Ge(001) could buckle (see Fig. 1.13). The buckling opens a gap between occupied and unoccupied surface states lowering the energy of the dimer. Chadi [135] used a tight-binding scheme to optimise the total energy of the dimerised surface without imposing any symmetry constraints. He found that the surface dimers spontaneously buckle, and that the symmetric dimer configuration is unstable. Buckling of the dimers lowers the energy of the occupied states and increases the energy of the unoccupied states. In 1987 Kubby *et al.* [38] reported (2×1), $p(2 \times 2)$ and $c(4 \times 2)$ reconstructions (see Fig.1.13), with asymmetric dimers, after investigating Ge(001) by tunnelling microscopy, which was supported by Lay *et al.* [136] and Mitome *et al.* [132]. Later on, the formation of asymmetric dimers was also confirmed theoretically [137–139]. Symmetric dimers were observed near step edges by room temperature STM [137, 140, 141], from which it was inferred that symmetric appearing dimers are a result of flipflop motion of the buckled asymmetric dimers [142]. It was predicted that, on both the Si(001) and Ge(001) surfaces at room temperature, the dimer orientation is disordered, but at low temperature, a well ordered superstructure is possible [143].

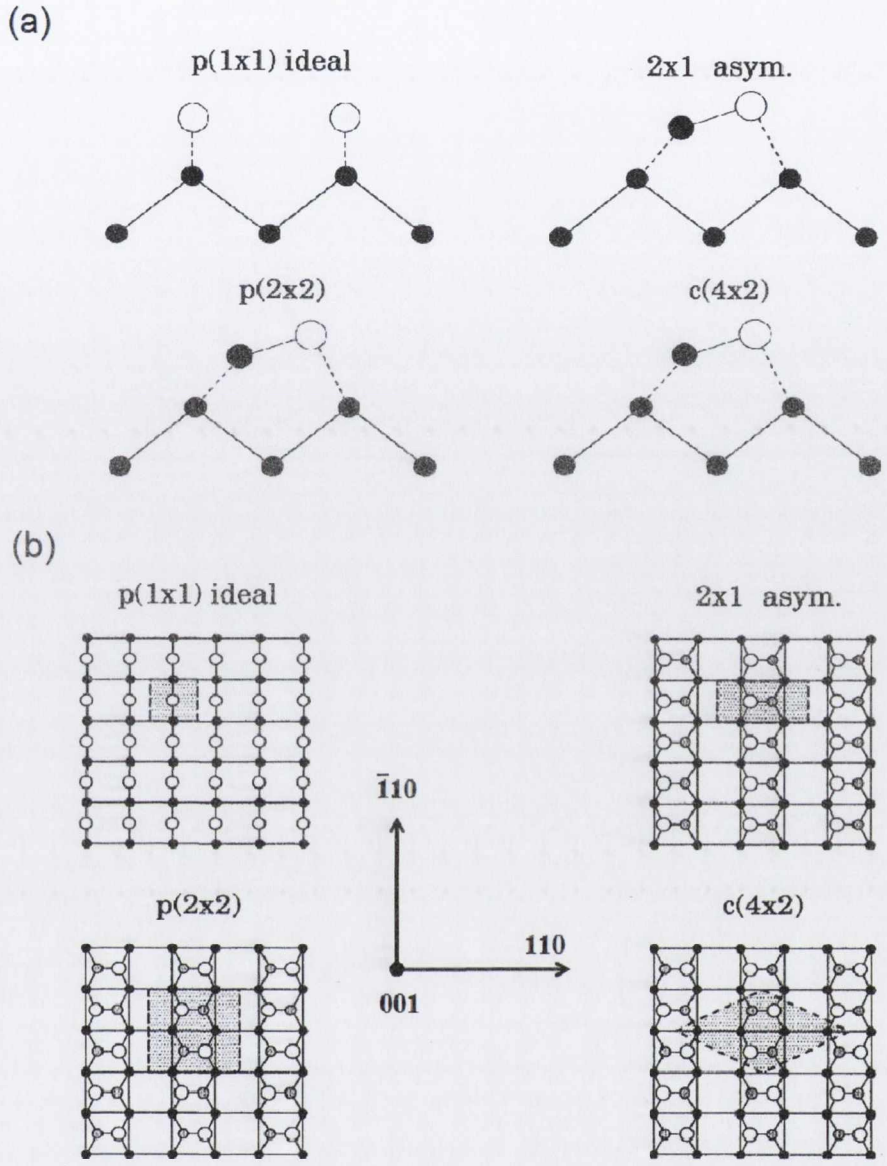


Figure 1.13: (a) Side and (b) top views of Ge(001) surface: p(1×1) unreconstructed; p(2×1) asymmetric; $p(2 \times 2)$ and $c(4 \times 2)$ reconstructions (after [144]). Dimer rows and bonds lie in ($\bar{1}10$) and (110) directions respectively. In (b) smaller and darker circles represent deeper atoms. The small black circles are second layer atoms and the larger grey and white circles are surface atoms. In the buckled dimer reconstructions the large white circles protrude further out of the surface than the grey circles. The dashed lines and shaded areas show the surface unit cells.

Allowing the surface dimers to buckle with respect to the surface plane enables the formation of various higher order reconstructions. Within a single substrate

dimer row the neighbouring dimers buckle always in opposite directions [145]. In-phase buckling of adjacent dimer rows leads to a (2×1) reconstruction, whereas out-of-phase buckling results in $p(2\times2)$, $c(4\times2)$ reconstructions (see Fig. 1.13(b)). Possible ground-state configurations were predicted to be $p(2 \times 2)$ and $c(4 \times 2)$. To verify the prediction Kevan [130], using ARPES and LEED, reported a $c(4 \times 2)\leftrightarrow(2 \times 1)$ transition at 200 K, while Johnson *et al.* [146] showed, using surface x-ray diffraction, that the Ge(001) surface undergoes a further reversible $(2 \times 1)\leftrightarrow(1 \times 1)$ transition at 955 K. Further, Culberston *et al.* [147] reported a sharp $c(4 \times 2)$ LEED diffraction pattern from Ge(001) at 100 K and a (2×1) diffraction pattern with smeared $c(4 \times 2)$ at 300 K. Superstructure formation depends on the weaker forces associated with long range ordering and is expected to depend sensitively on minor differences in surface preparation, which may explain why different studies have observed slightly different results [135, 148–150].

The driving force behind dimer formation is the reduction in the density of dangling bonds from two to one per surface atom. Along with dimerisation comes the development of anisotropic surface stress; the surface is under compressive stress along substrate dimer rows direction and under tensile stress along the direction perpendicular to the substrate dimer rows. RAS is expected to be a powerful probe of single domain anisotropic reconstructed Ge(001) surfaces.

Ab initio calculations of total energy show that, among the reconstructed surfaces, $p(2 \times 2)$ and $c(4 \times 2)$ reconstructions are the lowest energy reconstructions, being nearly degenerate in energy [138, 139, 151] (see Table 1.1). In 1987 Needles *et al.* calculated the total energy of Ge(001) systems using an *ab initio* approach [138]. They relaxed the three superstructures (non-buckled and buckled (2×1), and c(4×2)), which resulted in less than 2% of stretching of bond lengths (with respect to bulk bond), 14^o dimer tilting (with respect to non-buckled (2×1)), and an energy reduction of -0.29 eV/dimer (with respect to non-buckled (2×1)) for $c(4 \times 2)$. The energy difference between this reconstruction and $p(2 \times 2)$ is very small, and between $c(4 \times 2)$ and buckled (2×1) is 0.05 eV/dimer, which was consistent with the previous results [152, 153], allowing for the second layer relaxation of the structure. The charge transfer between up and

down dimer atoms causes dipole interactions between dimers, and this interaction favours the $p(2 \times 2)$ reconstruction. However, elastic interaction between dimers prefers $c(4 \times 2)$ [153]. There is generally good agreement between theory [154,155] and experiment [149,150] for the most stable structures, but there is considerable scatter in experimentally determined bond lengths from different techniques (Tables 6.1 and 6.2).

Table 1.1: Energy differences for various reconstructions of Ge(001).

Reconstruction	eV/dimer Ref. [138]	eV/dimer Ref. [139]	eV/dimer Ref. [151]
(2×1)	0.000	0.000	0.000
$c(4 \times 2)$	-0.05	-0.066	-0.088
$p(2 \times 2)$		-0.069	-0.087

1.5.2 Ge(001)-(2×1)Sb

The adsorption of group V elements on both Si(001) and Ge(001) has attracted much attention [156–163], mainly driven by the large technological importance in III/V epitaxy on group IV elements [162]. Both As and Sb are reported to form symmetrical dimer type reconstruction on Si(001), as seen by ARPES [158], STM [159,161,163] and surface extended X-ray absorption fine structure (SEXAFS) [157]. For the As/Ge(001) system, ARPES also finds symmetric As-As dimers [160], suggesting that this type of reconstruction is a general rule for the adsorption of group V elements on group IV semiconductors.

In 1990 synchrotron photoemission studies determined the coverage of Sb to be just less than 1 ML in forming Ge(001)-(2×1)-Sb [162]. It was suggested that the Sb atoms replace the Ge atoms in the top most layer to form a (2×1) surface reconstruction and there was no dimerisation between Sb atoms. Two years later this surface was studied by surface X-ray diffraction (SXD) [164]. The authors proposed an asymmetric dimer model in which the midpoint of the dimer is shifted laterally by 0.16 Å. The Sb-Sb dimer bond length from SXD was reported to be 2.90 Å (Table 6.3). However, in 1995, Lessmann *et al.* reported in an X-ray standing wave (XSW) study that Sb atoms form symmetric dimer

bonds on the Ge(001) surface [39]. The Sb-Sb dimer bond length in this case was reported to be 3.06 Å. Takeuchi *et al.* proposed symmetric dimers based on DFT total energy calculations [165]. Their calculated dimer distance was almost the same as that of the SXD study [164]. Another DFT study in 2004 reported a similar Sb-Sb dimer bond length [166].

Another important feature for the surface is the back bond distance between the Sb atom and the Ge atom in the next layer. This distance was reported as 2.49 Å by the SXD study [164]. DFT studies [165, 166] produced very similar results.

1.5.3 Electronic and optical properties of Ge(001) and Ge(001)-(2×1)

The valence band electronic structure of the Ge(001) clean surface has been studied by ARPES for more than two decades [130, 131, 152, 167, 168]. Interestingly, Ge(001) undergoes a metal-semiconductor transition at 200 K [130, 152]. The metallic properties of Ge(001) have been observed using ARPES and inverse photoemission spectroscopy (IPES) in other studies [167, 168]. Kevan *et al.* suggested that this metallic state near the Fermi level (E_F) is due to a (2×1) domain associated to the symmetric dimers, though they did not exclude the possibility of defects [130, 152]. In 2004 using STM/scanning tunnelling spectroscopy (STS), Gurlu *et al.* observed the presence of a metallic state for (2×1) domains, at room temperature, which was absent for $c(4 \times 2)$. This metallic state was attributed to flip-flopping dimers of the (2×1) structure [169]. More, recently Schwingenschlögl *et al.* [170] showed from their density of states (DOS) calculations that the atomic orbitals of the upper atom of the buckled dimers dominate below E_F, whereas states from the lower atom contribute above E_F.

As the clean reconstructed Ge(001) surfaces are mostly anisotropic, RAS has the potential to probe these surfaces. Wentink *et al.* [171], in an early study of Ge(001)-(2×1), probed the optical anisotropies using spectroscopic ellipsometry. At the start of this project there was only one RAS study of clean Ge(001)-

(2×1), in 1995, by Yasuda *et al* [22]. In the same year Shkrebtii *et al.* used *ab initio* molecular dynamics (MD) to calculate the optical response of the various reconstructions [172]. This early work was not successful, comparison with experiment revealing sign reversal for key features. Very recently, RAS from vicuna Ge(001)-(2×1) has been published [173,174]. There are no RAS studies of Ge(001)-(2×1)-Sb.

1.6 Purpose of this thesis

As there is a good amount of data related to the systems investigated during this research, it is very important to summarise this chapter. It will help people to easily get an insight about how this thesis contributes to this field of research. The main purpose of this thesis is to test the approach with hybrid DFT (with 5 % Fock exchange weight) to develop a clear understanding of the electronic and optical properties of different reconstructed surfaces of Si and Ge. At the start of this project, a small surface, Si(111)-(2×1), is used for this purpose. The minimum energy surface between + and -MP structure is still controversial and the difference between HOMO-LUMO gap and optical gap of this surface is not explained satisfactorily. These two long standing problems for this system are addressed in Chapter 4

Another controversial surface, Si(111)-(5×2)-Au is used here to test our approach. The correct structure of this reconstructed surface is still not obtained as accurate coverage of Au atoms is not determined. The latest Si adatom decorated structure with 0.6 ML Au atom coverage fails to explain some experimental data and answer whether the surface is metallic or semiconducting. Previously, it is seen that the RA spectrum changes dramatically with the change of the adatom coverage, which is still unexplained. These two problems are investigated in Chapter 4 to get the correct structure of both clean and Si adatom decorated Si(111)-(5×2).

One of the least investigated low index Si surfaces is Si(110) as it reconstructs

into a huge and complex (16×2) unit cell. The process to prepare this surface is hard and there is no reliable procedure which can produce Si(110)-(16×2) surface every time. Also, little is known whether the electromigration plays a vital role in preparation of this surface and the surface reconstruction depends on the bulk registry of Si(110). Those problems are addressed in Chapter 5.

Lastly, different reconstructed surfaces of Ge(001) are taken to check whether the approach also works for Ge. The electronic properties of Ge(001)-(2×1) was a matter of controversy for sometime as it was not confirmed whether the surface is semiconducting or metallic. Previously calculated RA spectra for different reconstructed Ge(001) surfaces fail to match the experiments and all the RA spectra in literature were measured above 1.5 eV which were insufficient to detect the surface response. These problems are addressed in Chapter 6. Antimony deposited Ge(001) surface is investigated in the same chapter. The controversy regarding the orientation of Sb dimers in Si(001)-(2×1)-Sb is addressed and RA spectra of this surface is calculated and measured for the first time in this course of work.

Chapter 2

Theoretical Background and Computational Detail

2.1 Hartree-Fock and Density Functional Theories

The Thomas-Fermi model [175, 176] paved the way of DFT by density functional method. In 1964 Hohenberg and Kohn [177] proposed DFT for simulating the quantum mechanical problem using computers. This theory describes the electronic structure of a system in terms of the electronic density, $n(\mathbf{r})$, as a function of position vector $\mathbf{r}$. In this method the many-body problem of interacting electrons in a static potential is reduced to a problem of non-interacting particles moving in an effective potential. This potential is calculated as a functional of the charge density. For the last half century, the basic concept of DFT has remained the same, but the accuracy of computations has significantly increased as new algorithms and functionals have become available. Nowadays the speed of computers, and computational techniques such as parallel computing, opened up the scope for extensive and more realistic simulations. Modern day simulation does not only calculate charge density and total energy but can also reproduce the results of a wide range of experiments, such as STM [99], atomic force microscopy

(AFM) [178] or X-ray magnetic circular dichroism (XMCD) [179].

If a system of N non-interacting particles has 3N degrees of freedom then DFT reduces the number of degrees of freedom to 3 since it requires only the total density functional n(**r**), which minimises a total energy functional. This is achieved by solving a self-consistent field matrix eigenvalue problem. Since there are many assumptions involved and the calculations are not exact in most many-body simulations, results often deviate from experimentally obtained results. Thus the assumptions, which need to be carefully considered, depend on the electronic structure of the material. New calculation algorithms and correction schemes are being devised in order to keep up with the experimental data produced. The calculation scheme adopted in this work is described in the following sections. Comparison with experimental results has been made and computational parameters have been chosen on the basis of experience and a number of literature reviews [?, 180, 181].

2.1.1 Hartree-Fock Theory

The many-body non-relativistic and time-independent Schrödinger equation for an isolated N-electron atomic or molecular system is given by

$$\hat{H}\Psi = E\Psi. \tag{2.1.1}$$

E is the electronic energy, $\Psi = \Psi(\mathbf{x_1}, \mathbf{x_2}, \ldots, \mathbf{x_n})$ is the wave function, and $\hat{H}$ is the Hamiltonian operator,

$$\hat{H} = -\frac{1}{2}\nabla^2 + v(\mathbf{r}) + \frac{n(\mathbf{r})}{|\mathbf{r} - \mathbf{r}'|}. \tag{2.1.2}$$

in which

$$v(\mathbf{r}) = -\sum_{\alpha} \frac{Z_\alpha}{\mathbf{r}_\alpha}. \tag{2.1.3}$$

is the "external" potential due to nuclei of charges Z_α acting on electron and $n(\mathbf{r}) = |\Psi(\mathbf{r})|^2$. The coordinates of an electron contains a space coordinate, $\mathbf{r}$,

and a spin coordinate σ. Atomic units were used throughout this work as this unit is used by the codes used here.

We may write Eq. 2.1.2 more compactly as,

$$\hat{H} = \hat{T} + \hat{V}_{ne} + \hat{V}_{ee}, \tag{2.1.4}$$

where

$$\hat{T} = \frac{1}{2}\nabla^2, \tag{2.1.5}$$

is the kinetic energy operator,

$$\hat{V}_{ne} = v(\mathbf{r}), \tag{2.1.6}$$

is the electron-nuclear energy operator and

$$\hat{V}_{ee} = \frac{n(\mathbf{r})}{|\mathbf{r} - \mathbf{r}'|}, \tag{2.1.7}$$

is the electron-electron coulomb energy operator. Within the Born-Oppenheimer approximation the total energy, W, can be written as the electronic energy, E, plus the nuclear repulsion energy,

$$V_{nn} = \sum_{\alpha<\beta} \frac{Z_\alpha Z_\beta}{R_{\alpha\beta}}. \tag{2.1.8}$$

That is,

$$W = E + V_{nn}. \tag{2.1.9}$$

It is immaterial whether one solves Eq. 2.1.1 for E and adds V_{nn} afterwards or includes V_{nn} in the definition of $\hat{H}$ and works with the Schrödinger equation in the form, $\hat{H}\Psi = W\Psi$.

Eq. 2.1.1 must be solved subject to appropriate boundary conditions and Pauli's exclusion principle. $E[\Psi]$ in Eq. 2.1.1 must be minimised, using a variational principal, to get the ground-state energy and true ground-state wave function. After taking an initial guess for Ψ, the charge density matrix is cal-

culated using the wavefunction, which is then fed into Schrödinger's equation, diagonalise the Hamiltonian, minimise the energy, get wave-functions and again feed those wave-functions in Schrödinger equation. The process is continued until self-consistency is achieved.

Although the Schrödinger equation is exact in the non-relativistic regime, it is not possible to solve it exactly, except for trivially simple problems. There are two reasons for that: one mole of solid contains $N \sim 10^{23}$ electrons and the many-electron wave-function contains $3N$ degrees of freedom. Furthermore, the Coulomb interaction between electrons makes electronic motions correlated. Therefore, the many-body wave-function which incorporates electron correlation is a very complicated mathematical object as correlation-effects prevent the separation of electronic degrees of freedom into N single particle equations of motion. Thus we must search for approximations that render the Schrödinger equation tractable to numerical solution, whilst retaining as much of the key physics as possible.

The simplest approximation is the Hartree-Fock approximation. In this approximation interactions between electrons are Coulomb and exchange interactions, but correlation effects are completely neglected. The electron-electron repulsion energy term of Eq. 2.1.2 produces two terms according to the Hartree-Fock approximation: one is the Coulomb repulsion term E_{C} and another is the exchange term, E_{X},

$$E_{\mathrm{C}}[\psi] = \frac{1}{2}\sum_{\sigma}\sum_{i,j}\int d^3r \int d^3r' \frac{\psi^*_{i\sigma}(\mathbf{r})\psi^*_{j\sigma}(\mathbf{r}')\psi_{i\sigma}(\mathbf{r})\psi_{j\sigma}(\mathbf{r}')}{|\mathbf{r}-\mathbf{r}'|}, \tag{2.1.10}$$

$$E_{\mathrm{X}}[\psi] = -\frac{1}{2}\sum_{\sigma}\sum_{i,j}\int d^3r \int d^3r' \frac{\psi^*_{i\sigma}(\mathbf{r})\psi^*_{j\sigma}(\mathbf{r}')\psi_{i\sigma}(\mathbf{r})\psi_{j\sigma}(\mathbf{r}')}{|\mathbf{r}-\mathbf{r}'|}, \tag{2.1.11}$$

where each of the functions ψ_i satisfies a one-electron Schrödinger equation. Sum over σ is restricted to parallel spins in Eq. 2.1.1. The many-body wave-function is written as a Slater Determinant to satisfy Pauli's exclusion principle which means that the many-body wave function should be antisymmetric, if the particle

coordinates are interchanged,

$$\Psi_{\mathrm{HF}} = \frac{1}{\sqrt{N!}}\det[\psi_1\psi_2\ldots\psi_N]. \tag{2.1.12}$$

In the Hartree-Fock approximation the orthonormal ψ_i are obtained which minimise the energy for this determinantal form of Ψ. The Hartree-Fock method is a non-linear "self-consistent-field" method. The Hartree-Fock approximation does not take correlation effects into account. Thus it overestimates the energy gap in strongly correlated systems. The requirement for a computationally practicable scheme that successfully incorporates the effects of both exchange and correlation leads us to consider the conceptually simple and elegant DFT.

2.1.2 Density Functional Theory

DFT is based on the following theorems:

Theorem 1. The external potential ($V_{ext}(\mathbf{r})$) is a unique functional of the electron charge density ($n(\mathbf{r})$) only. Thus the Hamiltonian, and hence all ground-state properties, are determined solely by the electron charge density.

Theorem 2. The ground-state energy may be obtained variationally: the density that minimises the total energy is the exact ground-state density.

The key variable in DFT is charge density ($n(\mathbf{r})$) which for a normalised Ψ is given by,

$$n(\mathbf{r}) = N\sum_{\sigma}\int_0^{N-1} d\mathbf{x}_1\ldots\int d\mathbf{x}_N|\Psi(\sigma,\mathbf{x}_1,\ldots\mathbf{x}_N)|^2. \tag{2.1.13}$$

The total energy functional can be written in terms of Ψ as

$$E[n(\mathbf{r})] =< \Psi|H|\Psi > . \tag{2.1.14}$$

Minimisation of the total energy functional in Eq. 2.1.14 with respect to the charge density, subject to the constraint of a fixed particle number, *i.e.* $\int n(\mathbf{r})d\mathbf{r} =$

N, yields

$$\delta[F[n(\mathbf{r})] + \int v_{ext}(\mathbf{r})n(\mathbf{r})d\mathbf{r} - \mu(\int n(\mathbf{r})d\mathbf{r} - N)] = 0, \tag{2.1.15}$$

where μ is a Lagrange multiplier associated with the constraint condition. The Euler-Lagrange equation associated with minimisation of this functional is then

$$\mu = \frac{\delta F[n(\mathbf{r})]}{\delta n} + v_{ext}(\mathbf{r}). \tag{2.1.16}$$

The Kohn-Sham formulation allows us to write the universal functional $F[n(\mathbf{r})]$ as

$$F[n(\mathbf{r})] = T_s[n(\mathbf{r})] + E_H[n(\mathbf{r})] + E_{XC}[n(\mathbf{r})], \tag{2.1.17}$$

where the last term is the exchange-correlation energy. $T_s[n(\mathbf{r})]$ is the kinetic energy, written in terms of single, non-interacting particle orbitals as

$$T_s[n(\mathbf{r})] = -\frac{1}{2}\sum_{i=1}^{N}\int \psi_i^*(\mathbf{r})\nabla^2\psi_i(\mathbf{r}). \tag{2.1.18}$$

$E_H[n(\mathbf{r})]$ is the Hartree term (Coulomb repulsion energy)

$$E_H[n(\mathbf{r})] = \frac{1}{2}\int\int \frac{n(\mathbf{r})n(\mathbf{r}')}{|\mathbf{r}-\mathbf{r}'|}d\mathbf{r}d\mathbf{r}', \tag{2.1.19}$$

which includes a self-interaction term. Thus the Euler-Lagrange equation (Eq. 2.1.15) becomes

$$\mu = \frac{\delta T_s[n(\mathbf{r})]}{\delta n} + v_{KS}(\mathbf{r}), \tag{2.1.20}$$

where v_{KS} is the effective Kohn-Sham potential.

$$v_{KS} = v_{ext}(\mathbf{r}) + v_H(\mathbf{r}) + v_{XC}(\mathbf{r}). \tag{2.1.21}$$

The Hartree potential is given by

$$v_H(\mathbf{r}) = \frac{\delta E_H[n(\mathbf{r})]}{\delta n} = \frac{1}{2}\int \frac{n(\mathbf{r}')}{|\mathbf{r}-\mathbf{r}'|}d\mathbf{r}' \tag{2.1.22}$$

and the exchange-correlation potential is given by

$$v_{XC}(\mathbf{r}) = \frac{\delta E_{XC}[n(\mathbf{r})]}{\delta n}. \tag{2.1.23}$$

Therefore, we need to solve a single-particle Schrödinger type equation with a Kohn-Sham potential (v_{KS})

$$(-\frac{1}{2}\nabla^2 + v_{KS}(\mathbf{r}))\psi_i(\mathbf{r}) = \epsilon_i\psi_i(\mathbf{r}) \tag{2.1.24}$$

The exchange-correlation term is not known exactly. So this term is approximated by, e.g. a Local Density Approximation (LDA) [182]. This approximation is made in case of a slowly varying electron density and the exchange-correlation energy is given by

$$E_{XC}^{LDA}[n(\mathbf{r})] = \int d\mathbf{r}\epsilon_{XC}[n(\mathbf{r})] \tag{2.1.25}$$

where ϵ_{XC} is the exchange-correlation energy per particle of a homogeneous electron gas with density $n(\mathbf{r})$. With the following condition,

$$n^{KS}(\mathbf{r}) = \sum_{i}^{occupied} |\psi_i(\mathbf{r})|^2 \tag{2.1.26}$$

to obtain the Kohn-Sham density [182], LDA becomes a self-consistent procedure. For any system where the charge density varies slowly, LDA seems to perform well. LDA calculates band structures and other measurable quantities such as dielectric parameters for narrow gap semiconductor systems that are in good agreement with experiment [183].

2.2 Generalized Gradient Approximations (GGA)

$E_{XC}^{LDA}(\rho)$ is by definition the exact functional for a homogeneous electron gas and has been also shown to give a qualitatively good description of the ground state properties of a variety of highly inhomogeneous systems [184]. However, LDA does not always provide sufficiently accurate results. For example, it almost

always overestimates the binding energy and underestimates the bond-length of weakly bound molecules and solids [184]. The calculation of properties of solids using DFT can further be improved by introducing derivatives of the electronic density into the functional. A simple and systematic extension of LDA is the gradient expansion approximation (GEA) [185]

$$E_{XC}^{GEA} = \int \rho(\mathbf{r})\epsilon_{XC}^{LDA}(\rho(\mathbf{r}))d\mathbf{r} + \int B_{XC}(\rho(\mathbf{r}))|\Delta\rho(\mathbf{r})|^2 d\mathbf{r} + \ldots, \tag{2.2.1}$$

which is asymptotically valid for densities that vary slowly over space. By using a constant B_{XC}, determined variationally for each atom, Herman *et al.* showed that the gradient expansion up to second order improves total energies of atoms [186]. An improvement in the exchange energies is also obtained when the exact expansion coefficient for exchange, B_X, is used in an exchange-only calculation [187]. However, inclusion of correlation in the second order expansion gives energies that are less accurate than LDA [188].

The analysis of this failure led some authors [189, 190] to introduce a generalization of the gradient expansion, which takes the gradient of the density into account at the same coordinates as LDA. It can be written as:

$$E_{XC}^{GGA} = \int \epsilon_{XC}(n_\uparrow, n_\downarrow, \nabla n_\uparrow, \nabla n\downarrow)n(\mathbf{r})d\mathbf{r} \tag{2.2.2}$$

Many different GGA's have been proposed since then [189, 191–198]. The Becke exchange [191] combined with Perdew correlation functional [192] (BP), the Perdew-Wang exchange-correlation [192, 193] (PW86) and more recent version of the same functional [195] (PW91) are among the most commonly used functionals and have been tested by using different computational schemes. These approximate functionals seem to give a good description of several finite systems: they improve the values of the total energies of atoms [199], the cohesive energy, equilibrium distances and vibration frequencies of weakly bound molecules (IIA-IIB dimers) [200], the cohesive energies of most first-row and second-row molecules [201] and atomic clusters [202]. They also give a better estimate of the

cohesive energy of simple metals [199], third-row elements [203] and hydrogen bonded systems [204, 205]. For iron, the ferromagnetic *bcc* ground state [203] and high pressure phase transition [206] were predicted correctly. While there is a general agreement about the improvement yielded by GGA over LDA in the description of the structural properties of $3d$ transition metals [203, 207–211], contradictory results have been found for $4d$ and $5d$ metals [209–212]. For these systems, different theoretical schemes have been used to solve the Kohn-Sham equations and the approximations introduced in these methods make it difficult to establish the accuracy of the functionals. A similar problem is encountered in the literature regarding semiconductor systems. Si, Ge and GaAs have been studied within the pseudopotential approach in combination with different generalised gradient approximation functionals. The pseudopotentials have been constructed either in density functional LDA scheme and screened within the generalised gradient approximation [209, 213] or generated including gradient corrections [200] and applied to bulk systems with and without non linear core correction [180, 181, 214]

2.3 Hybrid DFT

Due to poor agreement with experiment in some cases as mentioned above hybrid HF/DFT methods were proposed [215]. The main concept of this functional is that it incorporates a combination of HF exchange and conventional density functional approximations to exchange with weights that sum to unity. Becke's three-parameter exchange functional [216] and the nonlocal correlation functional of Lee, Yang, and Parr [217] were combined to form one of such hybrid functionals [215]. It has the form

$$E_{XC} = (1 - a_0)E_X^{LDA} + a_0 E_X^{HF} + a_X \Delta E_X^{B88} + E_C^{LDA} + a_C \Delta E_C^{PW91}. \qquad (2.3.1)$$

Where ΔE_X^{B88} is Becke's gradient correction to the exchange functional and ΔE_C^{PW91} is the Perdew-Wang gradient correction to the correlation functional [218]. The coefficients are weight parameters which sum to unity and are determined from linear least square fits to thermochemistry results [216,219]. Since LYP does not have an easily separable local component, the Vosko-Wilks-Nussair (VWN) local correlation expression has been used to provide the different coefficients of local and gradient corrected correlation functionals:

$$E_{XC}^{B3LYP} = (1 - a_0)E_X^{LDA} + a_0 E_X^{HF} + a_X \Delta E_X^{B88} + a_C E_C^{LYP} + (1 - a_C)\Delta E_C^{VWN}. \tag{2.3.2}$$

B3LYP functional became quite successful in strongly correlated systems [219]. The reason behind the success is possibly the reduction of self-interaction by introduction of HF exchange along with the use of a better correlation functional that takes the dynamical correlation effects into account [220]. This results in larger exchange splitting and better prediction of magnetic moments in spin-polarized materials [219]. For Si and Ge $a_0 = 0.05$ was used throughout this work as for both the elements, with this value, excellent agreement between theory and experiment was obtained, in case of the bulk band gap and dielectric function.

2.4 The CRYSTAL code

The CRYSTAL [221] code used in this research, uses a Gaussian orbital basis set. CRYSTAL treats each crystalline orbital (CO), $\Psi_i(\mathbf{r}, \mathbf{k})$, as linear combination of Bloch functions, $\phi_\mu(\mathbf{r}, \mathbf{k})$, defined in terms of local functions, $\psi_\mu(\mathbf{r})$, (namely atomic orbitals, AOs).

$$\Psi_i(\mathbf{r}, \mathbf{k}) = \sum_\mu a_{\mu,i}(\mathbf{k})\phi_\mu(\mathbf{r}, \mathbf{k}). \tag{2.4.1}$$

$$\phi_\mu(\mathbf{r},\mathbf{k}) = \sum_T \psi_\mu(\mathbf{r} - \mathbf{A}_\mu - \mathbf{T})e^{i\mathbf{k}.\mathbf{T}}. \tag{2.4.2}$$

$\mathbf{A}_\mu$ denotes the coordinate of a nucleus in the zeroth lattice cell on which ψ_μ is centred and summed over all lattice vectors, $\mathbf{T}$. The local functions are expressed as linear combinations of a certain number, n, of individually normalised Gaussian type functions, G, characterised by the same centre, with fixed coefficients, d_j, and exponents, α_j, defined in the input

$$\psi_\mu(\mathbf{r} - \mathbf{A}_\mu - \mathbf{T}) = \sum_j^n d_j G(\alpha_j, \mathbf{r} - \mathbf{A}_\mu - \mathbf{T}). \tag{2.4.3}$$

where,

$$G(\alpha_j, \mathbf{r} - \mathbf{A}_\mu - \mathbf{T}) = e^{-\alpha_j(\mathbf{r}-\mathbf{A}_\mu-\mathbf{T})^2} \tag{2.4.4}$$

The initial density, n($\mathbf{r}$), is computed from the wavefunctions, $\Psi_i(\mathbf{r},\mathbf{k})$, using Eq. 2.1.13 as a function of position coordinate. The k-points are sampled from the Brillouin zone of the corresponding real space lattice cell. Monkhorst and Pack [222] proposed a method of choosing a set of k-points. It is a rectangular grid of evenly spaced points of dimensions $N_x \times N_y \times N_z$. The accuracy of the calculation depends on how well one can sample the k-points. The optimum grid size can be achieved from a convergence test where the total energy is plotted with respect to increasing number of k-points. Normally, the total energy decreases rapidly and then oscillates with decay as the number of k-points increases. The oscillation amplitude should reduce below a certain tolerance limit once the k-point convergence is reached.

A DFT self consistent field calculation requires diagonalisation of the eigenvalue equation (Eq.2.1.14) which gives the eigenvalues, $\epsilon_i(\mathbf{k})$, as continuous functions of $\mathbf{k}$. When the diagonalisation is numerically computed, the density of the 3D k-point grid is a deciding factor in the accuracy of the eigenvalues. On the other hand increasing the number of k-points will increase the required computer-time

as a function, $T = 3^N \times T_{diag}$, where T_{diag} is the time needed for diagonalisation of the eigenvalue matrix at a single k-point. An optimum value for the k-point density must be achieved, obtained from a k-point convergence test, for best results. CRYSTAL uses parallel computing techniques and in a computer cluster system it distributes the diagonalisation of the eigenvalue matrix to different computing processors for different k-points. This speeds up the computation by a large amount.

Another important issue regarding the computational technique is the choice of basis sets. This is discussed in detail in Appendix B. The basis sets for different atomic orbitals of different elements are generated by some of the CRYSTAL authors and others (authors from University of Cologne), which are available online [221]. All the structures shown in this work were made with the help of XCrysDen [223] code.

2.4.1 Localised orbital vs. plane-wave basis sets

It was mentioned before that CRYSTAL uses localised orbital Gaussian basis sets. Some simulation codes such as VASP (Vienna Ab-initio Simulation Package) [224] and Quantum Espresso [225] use plane wave orbital basis sets of the form

$$\phi_{n\mathbf{k}}(\mathbf{r}) = u_n(\mathbf{r})e^{i\mathbf{k}.\mathbf{r}} \tag{2.4.5}$$

where,

$$u_n(\mathbf{r}) = \sum_{\mathbf{K}} C_{n,\mathbf{K}} e^{i\mathbf{K}.\mathbf{r}} \tag{2.4.6}$$

$\mathbf{K}$ is a reciprocal lattice vector. Hence the wave-functions are given by,

$$\phi_{n\mathbf{k}}(\mathbf{r}) = \sum_{\mathbf{K}} C_{n,\mathbf{K}} e^{i(\mathbf{k}+\mathbf{K}).\mathbf{r}} \tag{2.4.7}$$

The main advantages of using a plane-wave basis sets are

1. A plane-wave basis is independent of atomic sites.

2. A plane-wave basis is parameterised only by a cutoff energy and it converges in a smooth and monotonic manner to the desired wave-function and it does not exhibit basis-set superposition error (BSSE). BSSE arises from the overlapping of neighbouring-site localised orbitals, which effectively increases the number of basis sets per atomic site and contributes to the total energy.

The main disadvantages of plane-wave basis sets are

1. In a plane-wave basis set the number of orbital wave-functions is very large and therefore calculation of exact exchange using this basis is extremely expensive in computer time. This is because the exchange matrix elements have to be computed between every set of pairs of orbital wave-functions. This is very important for the current work since a Hartree-Fock-GGA hybrid DFT method is adopted.

2. A plane-wave has to use a pseudo-potential to describe the core electrons of a small ion which tend to be concentrated very close to the atomic nuclei. This results in large wave-function and density gradients near the nuclei, which are correctly described only by a large plane-wave basis set, which implies a very high energy cutoff.

Inspite of the fact that the advantages of using a plane-wave basis clearly supersedes its disadvantages, localised-orbital basis sets are used in this work for the following reasons,

1. A localised orbital basis features a lower number of wave-functions in comparison to its plane-wave counterpart (in the order of magnitude of the number of atomic orbitals of a corresponding atom) and is most suited for the current work as the hybrid Hartree-Fock exchange functionals are involved.

2. A localised orbital basis set can describe the core potential in an exact all-electron wavefunction, which is important for small core atoms, so one does not have to worry about convergenced basis set problem for small-core systems.

The main disadvantages of localised orbital basis sets are:

1. Unlike the plane-wave basis sets, the localised orbital basis sets are not parameterised to only the energy cutoff and must be described explicitly for all different species of atoms. Transferability of these basis sets are therefore questionable and have to be tested before used in a modelling of a new material.

2. BSSE is a major drawback of localised orbital basis sets. This can be corrected by computing this error by repeating all the calculations using a mixed (overlapped) basis set, and the error is subtracted a *posteriori* from the non-corrected energy [226]. The mixed augmented local orbital basis sets are formed by introducing *ghost orbitals*, basis set functions which have no electrons or protons on interstitial sites.

2.5 Electronic vs. optical bandgap

In semiconductors, the band gap is defined as the energy difference between the valence band maximum (VBM) and the conduction band minimum (CBM). There are two types of semiconductors: 1) direct band gap semiconductors which have VBM and CBM at the same point and 2) indirect band gap semiconductors in which the VBM and CBM do not occur at the same point at k space. To measure this band gap, generally two methods are used, one is electronic spectroscopy and another is optical spectroscopy. In electronic spectroscopy, an extra electron is either injected into or taken out of the solid during the process and the band gap measured by this process is called electronic band gap (transport gap). In optical spectroscopy, electrons are excited from valence to conduction band but the total charge of the material remains same and the band cap measured by this procedure is called optical band gap. The optical band gap is the threshold for photons to be absorbed, while the transport gap is the threshold for creating an electron-hole pair that is not bound together. While measuring the band gap electronically, the Coulomb repulsion caused by all the other electrons has to be overcome to get the extra electrons in or out. In materials with a large exciton binding energy, it is possible for a photon to have just barely enough energy to create an exciton (bound electron-hole pair), but not enough energy

to separate the electron and the hole (which are electrically attracted to each other). Therefore, an electronic gap is usually larger than an optical gap and the difference is the Coulomb energy for the particular system. The contribution behind the difference between electronic and optical gaps come from exchange interactions as well as Coulomb repulsion.

In almost all inorganic bulk semiconductors, such as Si, Ge, etc., there is very little interaction between electrons and holes (very small exciton binding energy). The energy absorption edge is equal to the energy difference between an electron in the valence band and a hole in the conduction band and therefore, the optical and electronic band gap are essentially identical and the distinction between them is ignored. However, some inorganic surfaces have large exciton binding energy and for those cases, the optical gap differs significantly from the electronic gap due to the excitonic effect.

2.6 Dielectric Function

In this section, the quantum mechanical theory of direct transitions between bands and dielectric function calculation will be discussed after Ref. [227]. Let's consider an external electromagnetic field is applied to excite an electron from initial state $\psi_i = \Omega^{-1/2} e^{i\mathbf{k}'.\mathbf{r}} u_v(\mathbf{r}, \mathbf{k}')$ in the valence band to a final state $\psi_j = \Omega^{-1/2} e^{i\mathbf{k}''.\mathbf{r}} u_c(\mathbf{r}, \mathbf{k}'')$ in the conduction band, described by the Block functions. To calculate the dielectric function the transition rate of that electron from ψ_i to ψ_j has to be calculated.

Let us consider under the Coulomb gauge, $\nabla.\mathbf{A} = 0$, a transverse field producing a perturbation of the form

$$H' = -(iA/2)[e^{i(\mathbf{q}.\mathbf{r}-\omega t)} + e^{-i(\mathbf{q}.\mathbf{r}-\omega t)}](\mathbf{a_0}.\nabla). \tag{2.6.1}$$

where $A = \sqrt{(8\pi/\varepsilon_1\omega)}$ is the magnitude of the vector potential, and ε_1 and ω are the real part of dielectric constants and frequency of the incident light, respectively. To calculate the transition rate for absorption processes the spatial

part of the perturbation matrix elements can be simplified, putting the expression for ψ_i and ψ_j, as

$$H'_{ji}(\mathbf{r}) = -\frac{iA}{2\Omega}\int u_c^*[\mathbf{a_0}.\nabla u_v + iu_v\mathbf{a_0}.\mathbf{k}']e^{i(\mathbf{k}'+\mathbf{q}-\mathbf{k}'').\mathbf{r}}d\mathbf{r}. \tag{2.6.2}$$

Because of the periodicity of the functions u_c and u_v, the integral can be expressed as a sum over unit cells, i.e.

$$H'_{ji}(\mathbf{r}) = \sum_n e^{i(\mathbf{k}'+\mathbf{q}-\mathbf{k}'').\mathbf{R_n}}\int_{cell} f(\mathbf{r}', \mathbf{k}', \mathbf{k}'', \mathbf{q})d\mathbf{r}. \tag{2.6.3}$$

For direct interband transitions in the reduced zone scheme,

$$\sum_n e^{i(\mathbf{k}'+\mathbf{q}-\mathbf{k}'').\mathbf{R_n}} = N_c = \frac{\Omega}{\Delta}, \tag{2.6.4}$$

where N_c, Ω and Δ are the number of unit cells in the crystal, the volume of the crystal and the volume of a unit cell.

Under these assumptions discussed above, the perturbation matrix elements can be written as,

$$H'_{ji}(\mathbf{r}) = \frac{iA}{2\Delta}\int_{cell} u_c^*[\mathbf{a_0}.\nabla u_v + iu_v\mathbf{a_0}.\mathbf{k}']d\mathbf{r}. \tag{2.6.5}$$

As the periodic parts of Bloch functions are orthonormal, for allowed direct transitions it can be written that

$$H'_{ji} = \frac{A}{2}\mathbf{a_0}.\mathbf{p_{ij}}, \tag{2.6.6}$$

where $\mathbf{p_{ij}} = -(i/\Delta)\int_{cell} u_c^*\nabla u_v d\mathbf{r}$ are the matrix elements of momentum operator.

Now for possible transitions, the transition rate of an electron from state ψ_i to ψ_j is

$$W_{ij} = 2\pi|H'_{ij}|^2\delta(\epsilon_{ji} - \hbar\omega) = (\pi A^2/2)|\mathbf{a_0}.\mathbf{p_{ij}}|^2\delta(\epsilon_{ji} - \hbar\omega). \tag{2.6.7}$$

Thus, using the value of A^2 we obtain the total transition rate from valence band to conduction band as

$$W_{cv} = (1/\varepsilon_1 \pi\omega) \int d\mathbf{k} |\mathbf{a_0}.\mathbf{p_{ij}}|^2 \delta(\epsilon_{ji} - \hbar\omega). \tag{2.6.8}$$

Finally the complex imaginary part of the dielectric function is

$$\varepsilon_2(\omega) = (1/\pi\omega^2) \int d\mathbf{k} |\mathbf{a_0}.\mathbf{p_{ij}}|^2 \delta(\epsilon_{ji} - \hbar\omega) \tag{2.6.9}$$

which will be used in the next section to calculate the reflectance anisotropy (RA) spectra of a system.

2.7 The EXCITON code

The EXCITON code, developed by the electronic structure theory group in School of Physics, Trinity College Dublin [228], is used here to calculate the imaginary part of the dielectric function. It takes the wave-functions generated by CRYSTAL as input and produce the dielectric function. It can also produce contour maps and localisation of the wave-functions on the electronic states.

2.8 Reflectance Anisotropy Spectroscopy

The theoretical understanding of the RA spectra can be best described by a Three Phase Model which was developed from Fresnel theory by McIntyre and Aspnes [229], with extensions by Selci *et al.* [230] and Cole *et al.* [231]. According to this model (Fig. 2.1) the surface of a cubic solid is regarded as a semi-infinite bulk substrate (phase (3)) beneath a surface layer (phase(2)), which is in turn beneath a semi-infinite vacuum layer (phase (1)) with complex dielectric constants $\hat{\varepsilon}_3$, $\hat{\varepsilon}_2$ and $\hat{\varepsilon}_1$, respectively.

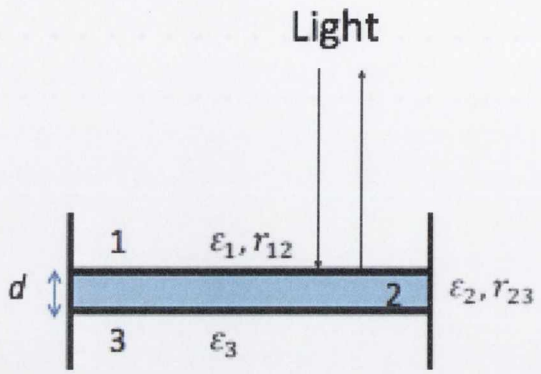


Figure 2.1: Three Phase Model to describe RA spectroscopy by McIntyre and Aspens [229]

The equivalent Fresnel coefficient of this three-phase system is

$$r_{123} = \frac{r_{12} + r_{23}e^{-2i\beta}}{1 + r_{12}r_{23}e^{-2i\beta}}, \tag{2.8.1}$$

where $\beta = \frac{2\pi\hat{n}_2 d\cos\varphi_2}{\lambda}$ is the change in phase of the beam during one traversal of the thin film of thickness d and

$$r_{\perp jk} = \frac{\mu_k\xi_j - \mu_j\xi_k}{\mu_k\xi_j + \mu_j\xi_k}, \quad r_{\parallel jk} = \frac{\hat{\varepsilon}_k\xi_j - \hat{\varepsilon}_j\xi_k}{\hat{\varepsilon}_k\xi_j + \hat{\varepsilon}_j\xi_k} \tag{2.8.2}$$

are the the Fresnel coefficients of the interface between two phases j and k for perpendicular and parallel polarised radiation with respect to the electric field, where the angle-dependent quantity in terms of real angle of incidence, φ_1, and index of refraction, n_1, and complex angle of incidence, φ_j, and index of refraction, $\hat{n}_j$, is defined as

$$\xi_j = \hat{n}_j\cos\varphi_j = (\hat{n}_j^2 - n_1^2\sin^2\varphi_1)^{1/2} \tag{2.8.3}$$

μ_j, μ_k and $\hat{\varepsilon}_j$, $\hat{\varepsilon}_k$ are, respectively, magnetic permeabilities and complex dielectric constants of the two phases. When $d \ll \lambda$, Eq. 2.8.1 can be expanded to first

order in β to give

$$r_{123} = \frac{r_{12} + r_{23}(1 - 2i\beta)}{1 + r_{12}r_{23}(1 - 2i\beta)}. \tag{2.8.4}$$

Using the identity,

$$r_{13} = \frac{r_{12} + r_{23}}{1 + r_{12}r_{23}}. \tag{2.8.5}$$

we can write

$$\frac{r_{123}}{r_{13}} = \frac{1 - 2i\beta[r_{23}/(r_{12} + r_{23})]}{1 - 2i\beta[r_{12}r_{23}/(1 + r_{12}r_{23})]}. \tag{2.8.6}$$

Expanding the denominator as a binomial series and neglecting terms higher than first order in β, we obtain

$$\frac{r_{123}}{r_{13}} = 1 + 2i\beta[\frac{r_{23}(r_{12}^2 - 1)}{(r_{12} + r_{23})(1 + r_{12}r_{23})}]. \tag{2.8.7}$$

Since phase (1) is transparent, $\hat{\varepsilon}_1$ is real. Thus the normalised reflectivity change can be defined as

$$\frac{\Delta R}{R} = \frac{R(d) - R(0)}{R(0)}, \tag{2.8.8}$$

where $R(d) = |r_{123}|^2$ and $R(0) = |r_{23}|^2$. It can further be simplified to

$$\frac{\Delta R}{R} = \frac{8\pi d n_1}{\lambda} \mathrm{Im}(\frac{\hat{\varepsilon}_2 - \hat{\varepsilon}_3}{\varepsilon_1 - \hat{\varepsilon}_3}) \tag{2.8.9}$$

under the assumption that $\mu_1 = \mu_2 = \mu_3 = 1$ in the optical frequency range. If ε_1 and n_1 are considered as 1 (dielectric function and the refractive index of the vacuum) the real and imaginary parts of the dielectric functions are separated along with their components in the two perpendicular directions then the final equation can be written in terms of atomic units as

$$\frac{\Delta R}{R} = \frac{8\pi d}{\lambda} \frac{(\varepsilon_{2x}^i - \varepsilon_{2y}^i)\varepsilon_3^r + (\varepsilon_{2y}^r - \varepsilon_{2x}^r)\varepsilon_3^i}{\varepsilon_3^{r\,2} + \varepsilon_3^{i\,2}} \tag{2.8.10}$$

where ε_{2x}^r and ε_{2x}^i are the real and imaginary parts of the surface (phase 2) dielectric functions, respectively, with electric field aligned in x direction, ε_{2y}^r and ε_{2y}^i are the real and imaginary parts of the surface dielectric functions, respectively, with electric field aligned in y direction, and ε_3^r and ε_3^i are the real and imaginary parts of the bulk (phase 3) dielectric function. The EXCITON code produces file

with real and imaginary parts of the bulk and surface dielectric functions in two perpendicular directions. Then they are used to calculate the final values of Eq. 2.8.10.

Chapter 3

Experimental Detail

3.1 Sample preparation

In this course of research clean Si(110)-(16 × 2), Ge(001)-(2 × 1), and Ge(001)-(2 × 1)-Sb surfaces were prepared in the laboratory. Clean and well-ordered Si samples were prepared by sample heating, and Ge surfaces were prepared by Ar^+ ion bombardment followed by annealing. Antimony was deposited on clean Ge(001) surface by molecular beam epitaxy (MBE) which will be discussed later. Sample heating in ultra-high vacuum (UHV, 10^{-10} mbar and below) can be achieved by a number of different methods. A filament can be used behind the sample to radiatively heat the sample. A similar method is electron bombardment heating which uses thermionic electrons emitted from a filament and by an electric field accelerated to high energies to heat a sample by transfer of kinetic energy on collision. A third method, used in this work, involves passing a high current through the sample, called resistive heating. In the case of Si the resistive heating method is the most convenient because Si, like all semiconductors, has a negative thermal coefficient of resistance. This means that as Si gets hotter its conductance goes up due to an increase in thermal charge carriers. The first stage of resistive heating is to apply a high voltage across the sample to breakdown the native oxide layer and to create enough thermal carriers for current to begin flowing. When a current is established the sample can be uniformly heated

from around 150° C to its melting point. Each sample can go through several cleaning cycles but eventually the sample degrades due to microscopic roughness called blooming.

Samples are mounted in UHV using a simple clamp (Figure 3.1). Current can then be passed through the sample by applying a voltage between the terminals marked positive and negative.

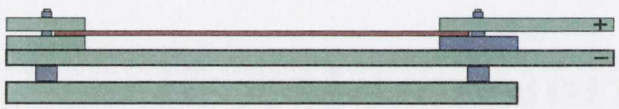


Figure 3.1: The sample mount used for UHV experiments. The green pieces are tantalum, the grey pieces are Al_2O_3 and the orange piece is the Si or Ge sample.

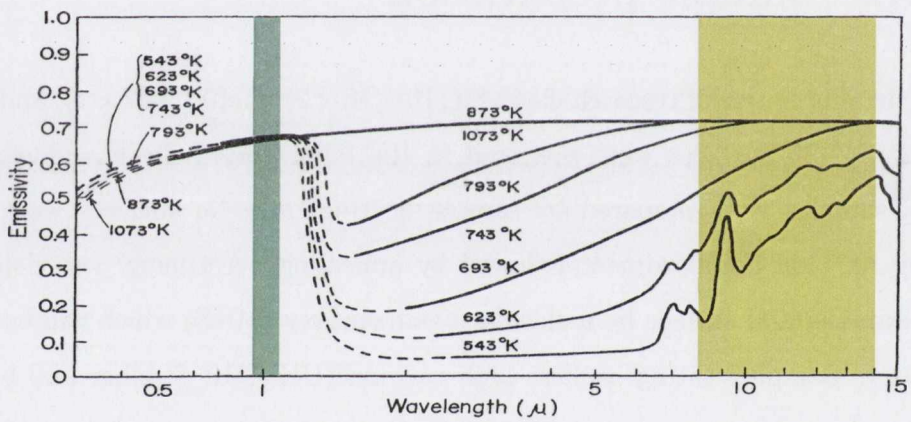


Figure 3.2: The emissivity of Si. In the green region the wavelengths are detected by the high temperature pyrometer and in the yellow region the wavelengths are detected by the low temperature pyrometer (after [232]).

The sample temperature was measured using optical pyrometry. Pyrometry calculates the temperature of a sample based on the colour of light it emits (the peak of its blackbody radiation spectrum). It was used for centuries by blacksmiths and glass blowers to tell if their furnaces were at the correct temperature. An important property of the material that needs to be known before pyrometry can be used is its emissivity. This is a measure of how similar to a true blackbody the material is. A value of 1 indicates a perfect blackbody. The pyrometers, used during the course of this work, operated in the range of 570°C to 3000°C

and detected wavelengths in the range from 9000 Åto 35000 Å. Figure 3.2 shows the emissivity of Si as a function of wavelength of emitted radiation. For the high temperature pyrometer the emissivity of Si is stable over a broad range of temperatures and has a value of 0.66.

3.1.1 Si(110)

All of the samples were cut from commercially available flat n-type, Ph doped Si(110) ($\pm 0.5^o$), 1-20 Ω-cm wafers as the substrate. Samples are cleaned in UHV by firstly degassing at 600°C for several hours until the pressure is below 10^{-10} mbar and then following a temperature profile [114] or prolonged heating [115]. The prolonged heating causes electromigration in the direction of applied current to form a clean single domain Si(001)-(16 × 2) surface.

At first annealing of the native oxide covered Si(110) surface followed the temperature profile shown in Fig. 3.3 [114]. This was found to be unreliable to produce a single domain surface, and an alternative approach involving annealing the sample overnight which is discussed in Ref. [115], was found to be more reliable.

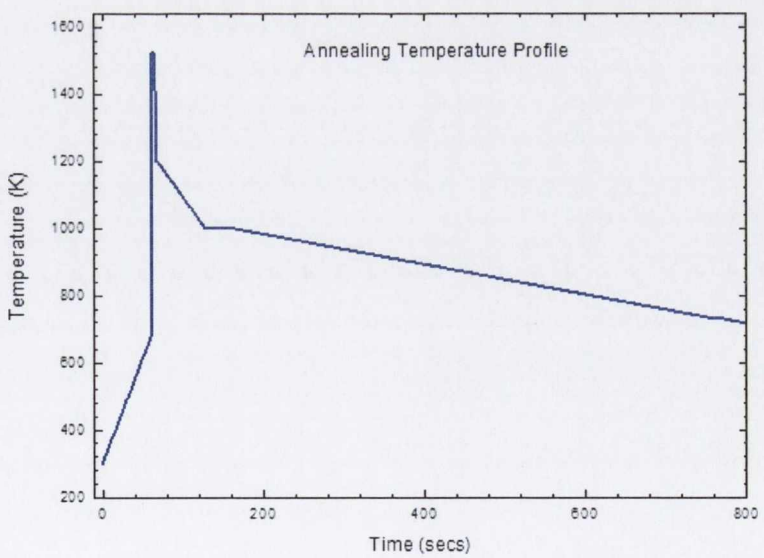


Figure 3.3: Short heating temperature profile [114].

3.1.2 Ge(001)

All the samples were cut from commercially available p/n-type, 0.008-0.05/0.005-0.25 Ω-cm, Ga/As-doped, Ge (001) wafers, offcut towards either <111> or <110>. The samples were cleaned by firstly degassing at 580°C for one hour until the pressure is below 10^{-10} mbar, followed by Ar^+ ion etching and annealing as discussed below.

3.1.2.1 Argon ion etching

Argon ion etching was used to clean the Ge(001) samples. An ISIS3000 version 2 ion gun from PSP vacuum technology was used, which has dual tungsten filaments and is designed for clean UHV operation. The other pins of the feedthrough are connected with anode, filament common and focus. Argon gas is leaked into the chamber by a gas line attached to the ion gun. This ion gun operates from 5×10^{-6} to 2×10^{-5} mbar.

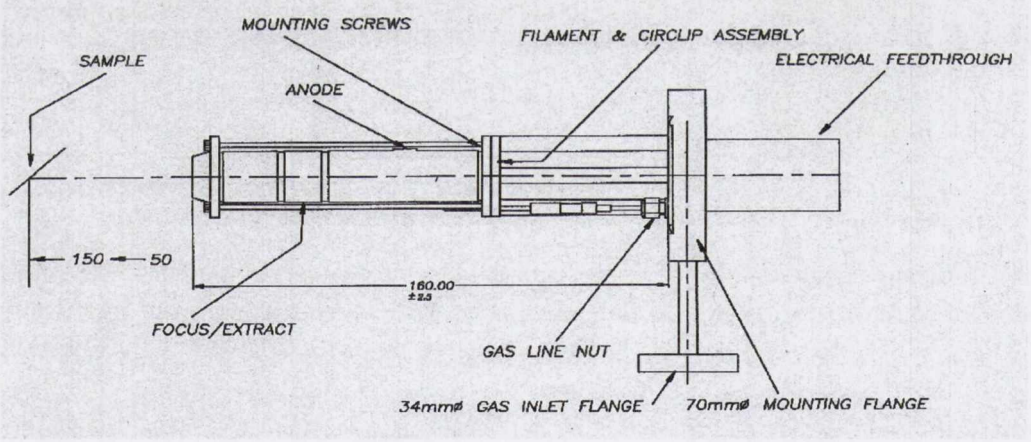


Figure 3.4: Schematic diagram of ISIS3000 ion source.

An emission current of 30-40 mA delivered a drain current at the sample of 13 μA for the 500 eV kinetic energy Ar^+ ion used. The ions bombard the surface of the sample and remove the native oxide layer and surface contaminants. The samples are bombarded for 20-30 mins, followed by annealing for 30 mins, the cycle being repeated typically 10 times until a clean and well-ordered surface was

obtained, as confirmed by LEED and Auger electron spectroscopy (AES).

3.1.2.2 Molecular beam epitaxy

Antimony was deposited on clean Ge(001) surface using a MBE Knudsen cell. A Low Temperature Effusion cell (NTEZ 40-2-16-KS-2006178) from MBE-Komponenten (Fig. 3.5) designed for clean UHV operation up to 1000°C was used for the evaporation of Sb. Insulating pyrolytic boron nitride (PBN) ceramic plates are shielded by tantalum plates to prevent out-gassing during operation. The NTEZ provided very clean evaporation (background pressure of 5×10^{-10} mbar) and precise flux control. The crucible material used for the evaporation was PBN. The power supply and temperature was controlled by a proportional-integral-derivative (PID) controller. The temperature of the Knudsen cell was measured by a K-type thermocouple.

These cells heat the materials to a temperature where they have significant vapour pressure. The vapour pressure as a function of temperature is shown in Fig. 3.6. The Knudsen cell was heated to 430°C to achieve 10^{-4} mbar vapour pressure of Sb. Adsorption occurs when the sample is placed in the flux and deposition rate is ~10 Å in 60 sec, or 2 nm/hr, allowing for accurate coverages in the submonolayer regime. Deposition rate is measured using a quartz crystal oscillator. The resonant oscillation frequency of the quartz crystal decreases as the mass of the crystal increases due to deposition. For example 10 Å of Sb would reduce the crystal frequency by about 54 Hz when the resonant frequency is 6 MHz. The approximate deposition rate of Sb was 0.06 ML s^{-1} at 430° C.

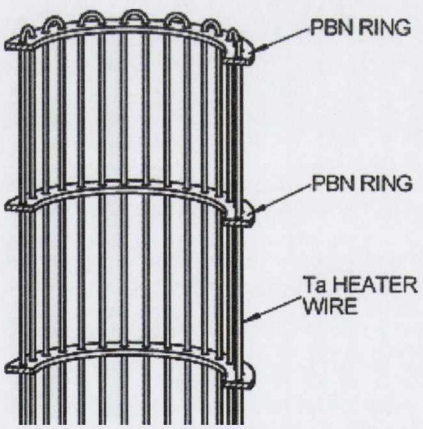


Figure 3.5: Schematic diagram of the NTEZ 40-2-16-KS-2006178 from MBE-Komponenten

After etching, the Ge(001) samples were annealed at 580°C for 30 minutes [146, 149, 233]. The temperatures of the sample were measured using the optical pyrometer. The emissivity of the pyrometry was determined to be 0.75 for Ge by placing a Ge(001) substrate with a K-type thermocouple attached in a furnace at 600° C. After depositing ~4 ML of Sb, the sample was annealed at 400° for 5-10 minutes. The current required to attain 400° C was determined by attaching a K-type thermocouple to a Ge substrate in a separate experiment as this was below the operating range of the pyrometer. After heating the sample, it was cooled down to room temperature at a rate of ~1° C/sec [146, 149, 233].

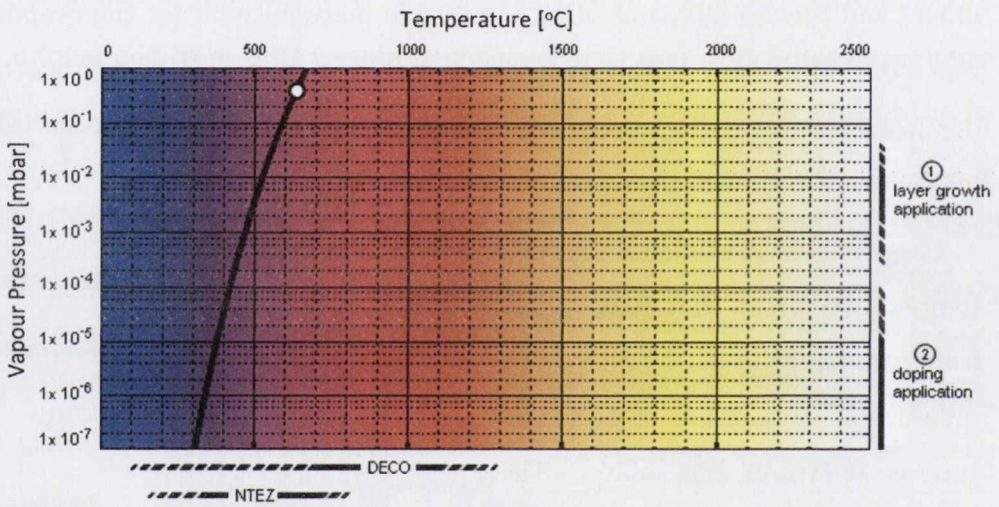


Figure 3.6: Variation in vapour pressure with increasing temperature after [234].

3.2 Sample characterisation

3.2.1 Low energy electron diffraction and Auger electron spectroscopy

Low energy electron diffraction (LEED) is an electron based technique to determine the surface structure of crystalline materials [235]. It has surface sensitivity due to the low penetration depth of electrons in the region from 10 eV to 200 eV (figure 3.7). LEED can provide detailed surface atomic structure information

by monitoring the spot intensity as the beam energy is scanned [235]. However, LEED was used in this project purely to confirm well ordered surfaces. A LEED image is an image of the reciprocal lattice of the surface. Figure 3.8 is an example of a LEED image from a clean Si(110)-(16 × 2) reconstructed surface. The 6° offset vicinal Ge(001) surfaces showed the spot splitting associated with surfaces possessing ordered steps.

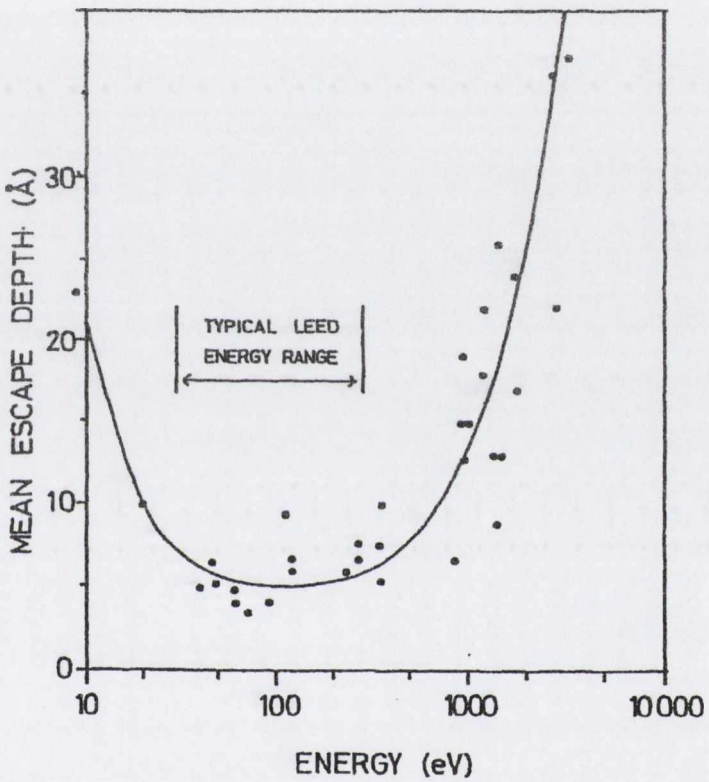


Figure 3.7: Variation in mean escape depth with increasing electron energy after [236].

LEED spots are formed from electrons that are back-scattered and diffracted from the surface onto a fluorescent screen. Low energy electrons (<200eV) are used because they will have a de Broglie wavelength similar to that of the surface atom spacing and they have a very small inelastic scattering mean free path, giving surface sensitivity. A schematic of the LEED/AES system is shown in Fig. 3.9.

Auger electron spectroscopy is a complementary technique to LEED, which can be used to study surface composition and monitor the cleanliness of a surface.

Auger electrons are emitted from an atom as it relaxes after a core electron has been ejected. They have a unique energy spectrum for each atom and are used to determine the chemical composition of the surface.

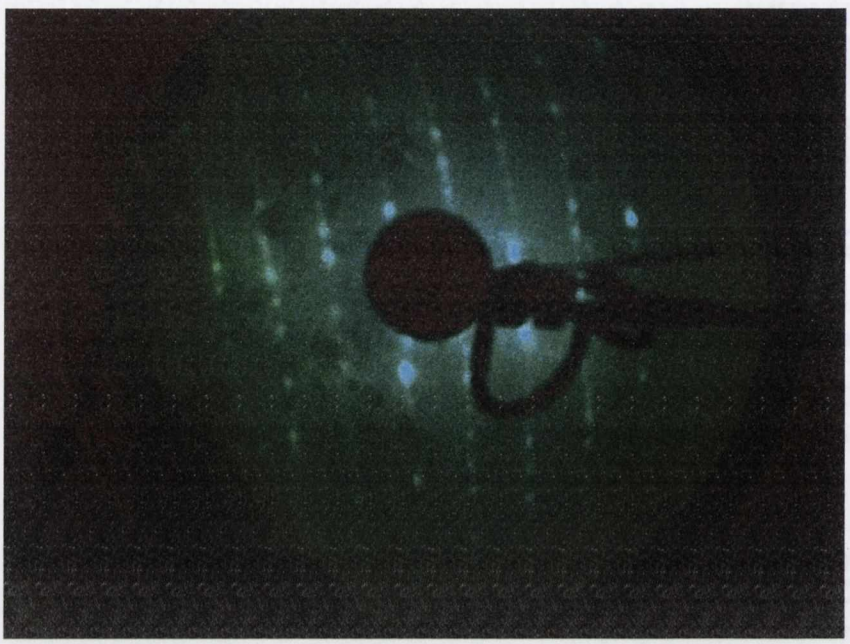


Figure 3.8: LEED image, taken from the clean single domain Si(110)-(16×2) surface.

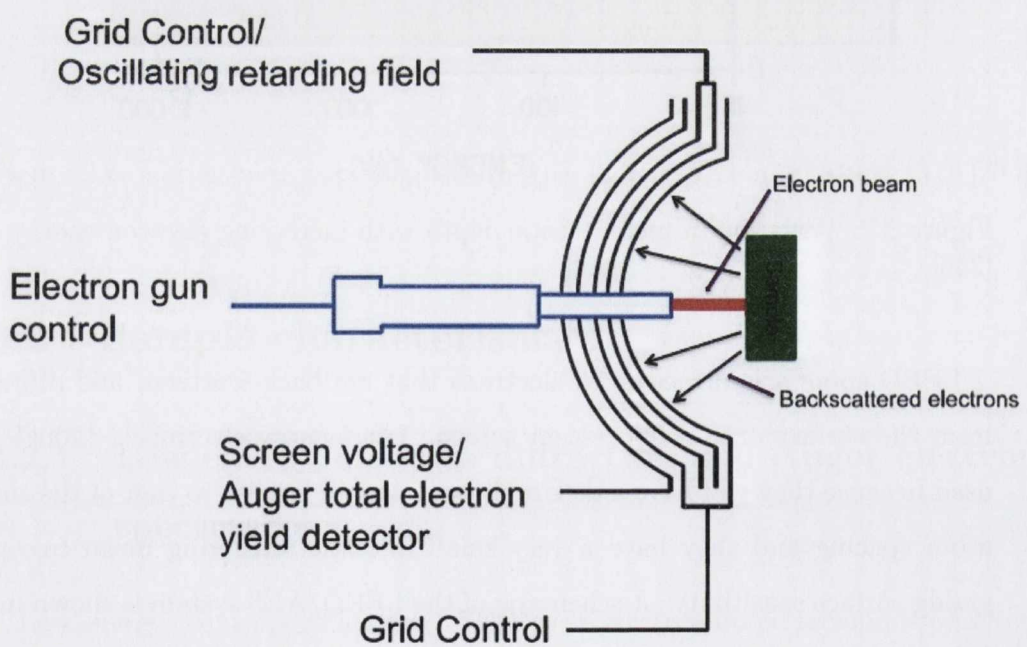


Figure 3.9: Schematic of the LEED-Auger system. To change from LEED to AES the inner grids are switched to an oscillating retarding field and the drain current from the screen is measured with a lock-in amplifier.

Both LEED and AES were carried out using the same apparatus, an Omicron SpectraLEED rear view LEED/AES system (Fig. 3.9). It consists of a front mounted electron gun, four high transparency grids, and a phosphor screen. For AES experiments the drain current on the screen was measured.

3.3 Reflection anisotropy spectroscopy

Since the first surface optics experiment by Chiarotti *et al* in 1968 [237], various types of experimental techniques have been developed [238]. In particular, exploitation of the differences in symmetry between the bulk and the interface is used in optical techniques to characterise the interface. The interaction of an electromagnetic (EM) field of optical frequency ω with condensed matter can be written in terms of the polarisation amplitude.

$$P(0,\omega,2\omega,\ldots) = \epsilon_0[\chi^{(1)}(\omega).E(\omega) + \chi^{(2)}(0,\omega,2\omega) : E(\omega)E(\omega) + \ldots]. \qquad (3.3.1)$$

where $\chi^{(i)}$ is the ith-order dielectric susceptibility tensor which describes the material response. The first term on the right hand side of Eq. 3.3.1 describes the linear optical response, which can be measured, for example, by spectroscopic ellipsometry. The dielectric tensor is related to the linear susceptibility by $\epsilon(\omega) = 1 + \chi^{(1)}(\omega)$. Within the dielectric approximation, an nth rank tensor process can exhibit up to n-fold rotational anisotropies. There are specific experimental techniques based on different rank tensors, which provide surface and interface information very efficiently [238]. RAS, a form of spectroscopic ellipsometry performed at near normal incidence, can detect two-fold in-plane rotational anisotropy. Anisotropic shaped entities on an isotropic material that are aligned in a common direction on an isotropic substrate may generate a RAS signal. RAS is capable of operating in a wide range of environments.

Reflection anisotropy spectroscopy measures the difference in reflectance between light polarised in orthogonal directions in the surface plane (Δr) at near normal incidence, normalised by the mean reflectance r. The RAS signal can be

simply described by:

$$\frac{\Delta r}{r} = \frac{2(r_x - r_y)}{r_x + r_y} \tag{3.3.2}$$

where r_x and r_y are the complex Fresnel reflectance coefficients for light polarised in the x and y direction respectively. RAS can achieve surface and interface sensitivity in systems where the bulk is isotropic and the surface or interface is optically anisotropic. For cubic and amorphous materials it is clear that there is no bulk anisotropy so any RAS signal must come from the surface. Unreconstructed (111) and (100) surfaces of cubic materials are isotropic and show no RAS signal, however the (110) surface is anisotropic and will have a RAS signal (figure 3.10). Reconstructed (111) or (100) surfaces from cubic materials can give a RAS signal but normally they will be in a number of equivalent domains, and domain averaging will mean no RAS signal is recorded. This is because RAS will sample over a macroscopic area due to the size of the beam spot and domain averaging will mean no RAS signal is seen. however, in some cases vicinal surfaces lead to the formation of a dominant domain [28, 239].

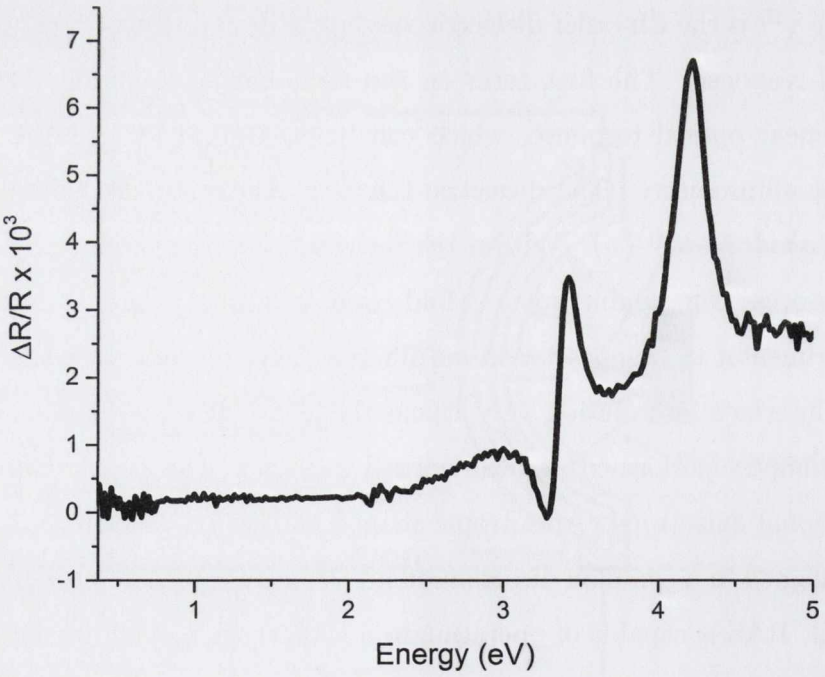


Figure 3.10: RAS signal from native-oxide-covered Si(110).

At present there are no standard methods for interpreting RA spectra. With

the advent of more powerful supercomputers, RA spectra can be calculated from first principles. When RA spectra are analysed from first principles they can provide quite strict limits on the surface structure. Small differences in surface structure can lead to significant changes in the band structure near the Fermi level. As any direct optical measurement probes both the ground and excited state additional computational power is required to calculate optical spectra compared to techniques which only probe the ground state. It is well known, for example, that the widely used density functional theory (DFT) approach significantly underestimates the band gap of semiconductors. However, if these problems can be overcome, RAS can be used to confirm one structural model ahead of others, as has been shown recently for the Si(111)-4 $\times$ 1-In surface [240].

There are several methods of recording RA spectra. They differ in the mechanism by which they switch the polarisation of the light. There are two main methods, mechanical rotation of the sample or polarisation, and photoelastic modulator (PEM) switching of the polarisation. Problems such as beam wobble favour the PEM over a mechanically rotating system.

3.3.1 Photoelastic modulator RAS

A PEM is a device that modulates the phase of the light in one optical axis (hence changing the polarisation state of the light). It is essentially a dynamic waveplate. It works by applying an electric field to a piezoelectric crystal, which is coupled to a suitable transparent material, such as quartz or CaF_2. The piezoelectric response induces a stress in the material, which changes its birefringent properties. Light polarised along the modulation axis of PEM will undergo a phase modulation of Γ, while light polarised perpendicular to the modulation axis will be unchanged.

$$\Gamma = \Gamma_0 \sin \omega t \tag{3.3.3}$$

where Γ_0 is the modulation amplitude and ω is the modulation frequency. Half-wave modulation will rotate the plane of polarisation and it can be shown that a value of $\Gamma_0 = 2.405$ rad produces this. The crystal must be driven at its

resonance frequency, which is $\sim 10^5$ Hz for most materials. Another advantage of PEM phase modulation is that both the real and imaginary parts of $\Delta r/r$ can be measured.

In the Jones matrix formulation (discussed in Appendix C) change in the amplitude of the electric field by a PEM can be described by:

$$\begin{pmatrix} \cos\frac{\Gamma}{2} & i\sin\frac{\Gamma}{2} \\ i\sin\frac{\Gamma}{2} & \cos\frac{\Gamma}{2} \end{pmatrix}. \tag{3.3.4}$$

If an experiment is constructed such that the PEM axis and input polarisation are at 45° to the anisotropic axis of the sample, the amplitude of the electric field output (A) is proportional to:

$$A \propto \begin{pmatrix} \cos\frac{\Gamma}{2} & i\sin\frac{\Gamma}{2} \\ i\sin\frac{\Gamma}{2} & \cos\frac{\Gamma}{2} \end{pmatrix} \begin{pmatrix} r_x & 0 \\ 0 & r_y \end{pmatrix} \begin{pmatrix} 1 \\ 1 \end{pmatrix} \propto \begin{pmatrix} r_x\cos\frac{\Gamma}{2} + ir_y\sin\frac{\Gamma}{2} \\ r_y\cos\frac{\Gamma}{2} + ir_x\sin\frac{\Gamma}{2} \end{pmatrix} \tag{3.3.5}$$

This produces a phase modulation at the detector. In order to turn the phase modulation into an intensity modulation, an analyser polariser is used at 45° to the PEM axis (parallel to the sample axis). This means the amplitude at the detector is:

$$A \propto \begin{pmatrix} 1 & 0 \\ 0 & 0 \end{pmatrix} \begin{pmatrix} r_x\cos\frac{\Gamma}{2} + ir_y\sin\frac{\Gamma}{2} \\ r_y\cos\frac{\Gamma}{2} + ir_x\sin\frac{\Gamma}{2} \end{pmatrix} \propto \begin{pmatrix} r_x\cos\frac{\Gamma}{2} + ir_y\sin\frac{\Gamma}{2} \\ 0 \end{pmatrix} \tag{3.3.6}$$

The voltage on the detector is proportional to $|A|^2$, and is a harmonic series of V_0, V_ω, $V_{2\omega}$ etc. By performing a Fourier transform it is found that each term depends on a Bessel function J_n, where n is the order of the Bessel function. Odd harmonics are found to depend solely on the imaginary part of $\Delta r/r$ while even harmonics depend solely on the real part of $\Delta r/r$:

$$\frac{V_\omega}{V_0} \propto J_1(\Gamma_0) Im(\tfrac{\Delta r}{r}) \sin(\omega t) \tag{3.3.7}$$

$$\frac{V_{2\omega}}{V_0} \propto J_2(\Gamma_0) Re(\tfrac{\Delta r}{r}) \cos(2\omega t) \tag{3.3.8}$$

$$\frac{V_{3\omega}}{V_0} \propto \quad J_3(\Gamma_0) Im(\tfrac{\Delta r}{r}) \sin(3\omega t) \tag{3.3.9}$$

The PEM RAS system, as well as giving excellent signal-to-noise and access to both real and imaginary parts of the RA spectroscopy signal, allows us to perform some very simple calibration measurements. For example, if the input polariser is misaligned with respect to the PEM axis there will be a constant offset in the signal. This can be used to check for nonlinearities in the PEM or other components.

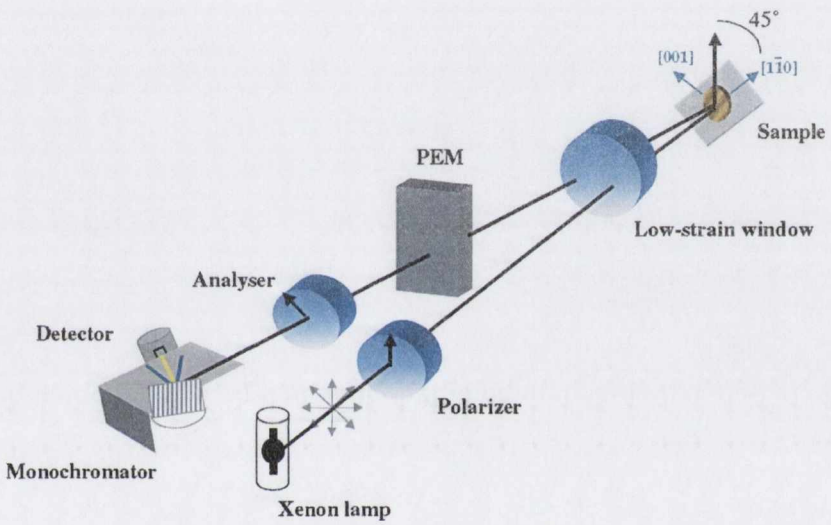


Figure 3.11: A schematic of a PEM RAS system after [13].

The broad band PEM RAS system used had an extended infra-red (IR) response. The design of the system is shown in Fig.3.11. The broad band system consists of a high pressure Xe lamp, MgF_2 coated Al mirrors, a filter wheel, MgF_2 Rochon polarisers, CaF_2 PEM (Hinds instruments, II/CF57), a three grating monochromator (Bentham Instruments, TMc300-USB), a Si-InGaAs detector (Elektronik-Manufaktur Mahisdorf) and a Peltier cooled InAs detector (Elektronik-Manufature). Detectors were changed using a stepper motor (Fig. 3.12). The DC signal was read using a sensitive analogue to digital converter and the AC signal was read with a lock-in with a reference frequency of twice the PEM frequency. A flexible LabView program was used to allow interchangeability between several different components. The program also allowed several types of measurement. These include spectral RAS, time dependent RAS (to monitor

growth), magnetic field dependent RAS (essentially measuring the magneto optical Kerr effect, MOKE), PEM voltage dependent RAS (to calibrate the PEM) and alignment mode where the DC and AC signals are plotted for alignment of samples and other components. Further details can be found in Ref. [112].

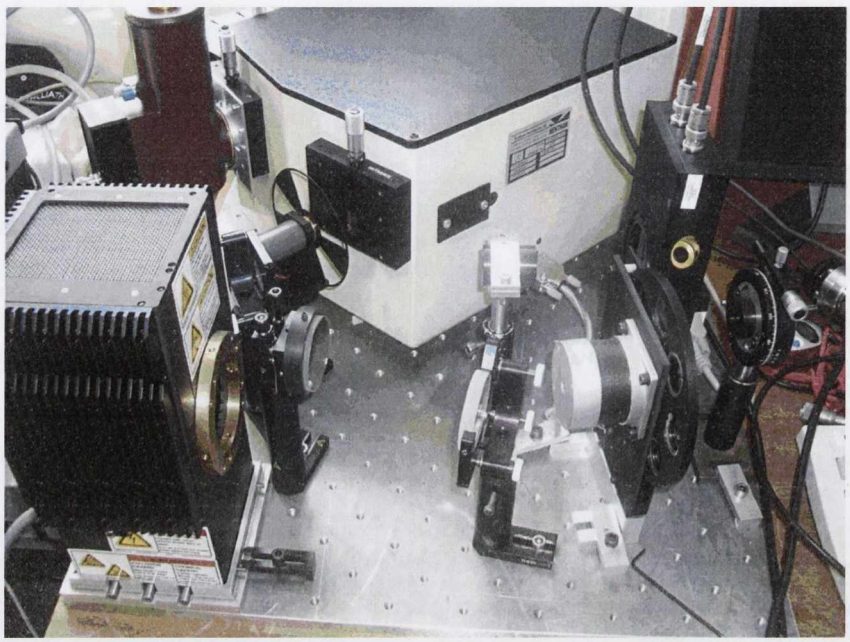


Figure 3.12: The broad-band RAS system

The high pressure Xe lamp uses a high voltage to ignite a plasma and then only requires a modest power (75W) to maintain the light output. They produce light over a very broad range from 0.25 eV to 5.5 eV. In a Xe lamp the majority of the light is produced in a tiny ($\leq$ 1 mm^2) area around the electrodes, which means the focal size can also be small. Even though the Xe is at high pressure the lamp still produces strong emission lines, especially around 1.2 eV (figure 3.13). Intensity is limited in the IR and UV mainly because of light being absorbed in the bulb material.

Focusing and beam alignment in the RAS systems was performed using MgF_2 coated Al mirrors. These mirrors have a good reflectance over a large spectral range and are resistant to corrosion. They offer $\geq$ 90% reflectance from 3 eV to 0.12 eV, and a $\geq$ 85% reflectance from 5 eV to 3 eV. The main focusing mirror had a focal length of 1 m, which allows the beam to be directed through a low

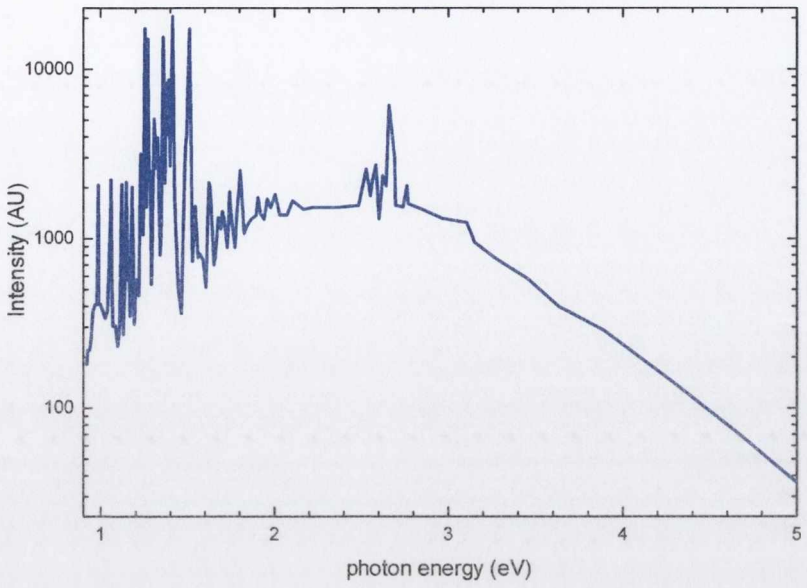


Figure 3.13: The emission from a high pressure Xenon bulb

strain quartz window into the vacuum chamber. A secondary focusing mirror was used to focus into the monochromator.

MgF_2 Rochon polarisers were used in the broadband system. They separate the light into two beams with an angular separation of about 3°, varying slightly with wavelength. They have an extinction ratio of at least 10^{-5} and work in the region from 9 eV to 0.2 eV.

The PEM, which modulates the light at 57 kHz is an IR optimised CaF_2 PEM. It is designed to work in the region from 0.65 eV to 0.22 eV but by extending the LabView calibration file it is possible to use it up to 5 eV.

The monochromator and filter wheel select the energy of the light. The monochromator for the broad band system has 3 gratings, one for $\geq$2.1 eV, one for 2.1 eV to 0.8 eV, and the 3rd for $\leq$0.8 eV. Under normal conditions the slit width on the monochromator is 1 mm, giving resolutions of 1.35 nm, 5.4 nm and 10.8 nm respectively, for the different energy ranges. The filter wheel is used to remove 2nd order effects in the monochromator. There are 4 filters for different energy ranges. A neutral density filter was also incorporated to help prevent detectors overloading in the region of the strong lamp lines.

Three detectors were used to cover the spectral range. For the region above 1.4 eV a Si detector was used, which had a $\times 30$ DC amplifier for the region above 4 eV. An InGaAs detector covered the range 0.75 eV to 1.4 eV, using the same electronics as the Si detector. The electronics for these detectors consisted of a filter to split the DC and AC signals, which were then connected to the analogue to digital converter and lock-in, respectively. To switch between these two detectors a stepper-motor was used. The signal cables into the lock-in amplifier were switched using solid state relays. The third detector was an InAs Peltier cooled detector. It was designed to work in the region from 0.75 eV to 0.37 eV with significantly more noise than the Si and InGaAs detectors. This problem was resolved by recording a much higher density of points in the region of this detector and using a long time constant.

Chapter 4

Si(111)-(2×1) and (5×2)-Au surfaces

4.1 Si(111)-(2×1)

4.1.1 Surface structure of Si(111)-(2×1)

The Pandey π-bonded chain model [37] of Si(111)-(2×1) reconstruction is a very well known semiconductor surface, so it is a good model system to test the hybrid DFT approach. The atomic structure of this system was well tested by both experiment (LEED [46,48,53]) and DFT total energy methods [47,52,54,55]. Earlier, Pandey predicted that atoms in the π chain lie in the same horizontal plane [37]. This structure was not consistent with LEED data [53] and a buckled π chain model was proposed. The two silicon atoms in each unit cell of the π chains are inequivalent, even in the Pandey model. As a result, there are two inequivalent buckling geometries in which one of the π-chain atoms is outermost. In either case, one filled, localised on the outermost atom of the π chain and one vacant surface state, localised on the inner atom of the π chain are found. The half-filled nature of the surface states, which break the symmetry and forms a gap, may be causing the buckling of the π chains.

This inequivalent Pandey chain was referred to as a MP chain and the energy

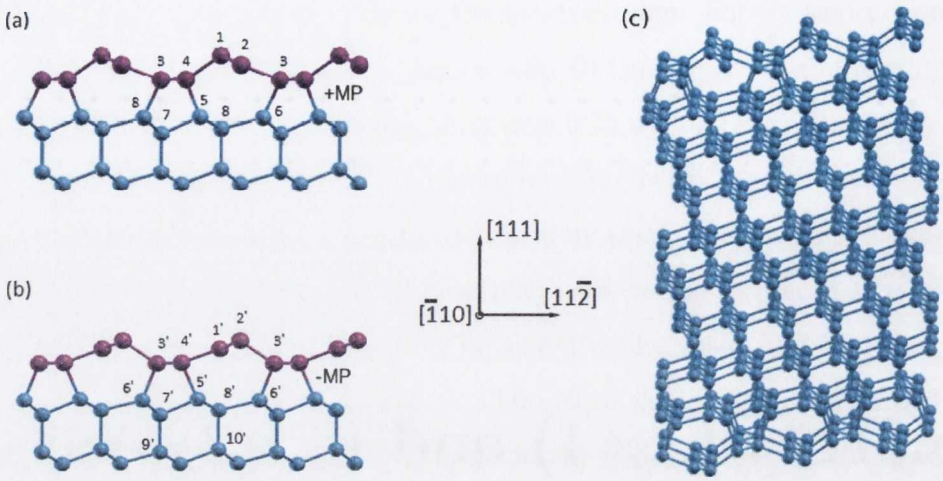


Figure 4.1: Atomic structures of the modified Pandey chain model with (a) positive (+MP) and (b) negative (-MP) tilts, viewed along the [$\bar{1}$10] (chain) direction. (c) Fully optimised slab with 8 Si bilayers.

difference between negative-tilt (-) and positive-tilt (+) MP chains is very small, as mentioned before. The same nomenclature is used here; the buckled structures are shown in Fig. 4.1. Fig. 4.1 (a) and 4.1 (b) show the +MP and -MP chain structures, respectively. The MP chain in a (2×1) unit cell runs along the [$\bar{1}$10] direction as shown in Fig. 4.1. Without relaxation, i.e. in the (1×1) bulk unit cell, each Si atom on the surface has one dangling bond. Upon relaxation they form buckled π chains with each other [37]. Here, each (2×1) slab (for both $\pm$MP chains), which has 40 Si atoms, with 8 Si bilayers sandwiched between two surfaces, were used for geometry optimisation (Detail of calculation is discussed in Appendix A). The structure was reproduced after Ref. [52]. Then the structure was relaxed using the B3LYP hybrid DFT computational technique, discussed in Chapter 2.

Using hybrid DFT, it is found that the +MP structure is more stable than the -MP structure which is inconsistent with previous total energy minimisation calculations, which found -MP is more stable [52,55,241]. The total energy difference between these two systems is 2 meV, which is very small. The whole energy minimization calculation was done using CRYSTAL [221]. All electron calculation was used with Gaussian basis sets described in Appendix B. Relaxed lattice parameters, obtained by hybrid DFT, for the (2×1) slab are 7.719 and 3.878 Å,

which are larger than the bulk lattice (1×1) distance (3.839 Å) by 0.53 and 1%, respectively. Bond lengths from the relaxed ±MP structures are given in Table 4.1, where they are compared to bond lengths derived from the most recent LEED analysis for this surface [48] and a previous LDA-DFT calculation [52].

Table 4.1: Surface bond lengths in Å in MP structures from LDA DFT, hybrid DFT, and LEED. Atoms' numbers are shown in Fig.4.1. For -MP structure the numbers are primed.

Atom Pair	$-$MP[1]	$+$MP[1]	$-$MP[2]	$+$MP[2]	LEED $+$MP[3]	$-$MP[4]	$+$MP[4]
1-2	2.314	2.310	2.25	2.25	2.271	2.27	2.27
1-4	2.409	2.353	2.34	2.30	2.313		
2-3	2.358	2.412	2.30	2.34	2.347		
3-4	2.401	2.400	2.34	2.34	2.384		
4-5	2.398	2.443	2.35	2.39	2.371		
3-6	2.469	2.428	2.41	2.37	2.423		
5-7	2.350	2.362	2.33	2.34	2.359		
5-8	2.379	2.382	2.34	2.34	2.277		
6-7	2.370	2.368	2.34	2.33	2.393		
6-8	2.417	2.406	2.34	2.36	2.386		
7-9	2.332	2.330	2.40	2.39			
8-10	2.444	2.445	2.30	2.30			
Bulk		2.371[5]			2.352		

[1]Hybrid DFT (this work).

[2]DFT LDA Ref. [52].

[3]Reference [48].

[4]Reference [241].

[5]Hybrid DFT calculation on bulk cell using same basis set (this work).

From Table 4.1 it can be seen that the most bond lengths from LEED are larger than the LDA-DFT and smaller than hybrid DFT values. This is to be expected since hybrid DFT and DFT, respectively, generally overestimates or underestimates experimentally determined bond lengths. The exceptions happen for three bond lengths (1-4, 5-8, and 6-7) derived from LEED data in Table 4.1 as 1-4 and 5-8 bond lengths are smaller than either calculation, whereas 6-7 bond length is larger. Bond 1-4 is the back bond between the outermost atom in the π chain and the atom in the next layer. Xu *et al.* [48] reported it to be 2.313 Å, but average of bond lengths from total energy calculations produces a bond length of

2.35 Å (Table 4.1). Bond 5-8 is a bulklike bond in the layer below the π chain. Xu *et al.* found it to be 2.277 Å while a bond length of 2.38 Å is predicted by this work. Xu *et al.* predicted the adjacent bulklike bond 6-7 to be 2.39 Å, while a bond length of 2.37 Å is resulted from this hybrid DFT calculation. The relative vertical displacement of atoms 1 and 2 is considered as the extent of buckling, which is termed as the b_1 parameter, in the previous study. Xu *et al.* found b_1 to be 0.51 Å for the +MP structure, while this work produced $b_1 = 0.502$ Å for +MP and 0.556 Å for the -MP structure. Zitzlsperger *et al.* predicted $b_1 = 0.4$ Å for the +MP and 0.50 Å for the -MP structure [55], while Bussetti *et al.* reported $b_1 = 0.53$ Å for the +MP and 0.59 Å for the -MP structure [58]. These values are in reasonable agreement with LEED data for the +MP structure, and LDA-DFT and hybrid DFT calculations agree that buckling in the -MP structure is larger.

4.1.2 Electronic Structure

At first, the electronic structure of bulk Si was calculated using hybrid DFT with 5 % Fock exchange, which produced the band gap, 1.3 eV very close to the experimental value, 1.1 eV at room temperature [263].

Each Si in the π chains has a dangling Si 3p state oriented roughly perpendicular to the chain. Two orbitals from these dangling p states of two Si atoms, per unit cell, combine to form two surface states (Figs. 4.3 and 4.4); close to the $\overline{\text{J}}$ and $\overline{\text{K}}$ points of the SBZ. The occupied state is strongly localised on the top atom in the π chain of both MP structures while the vacant state is strongly localised on the inner atom of the π chain. The states (pink circles) localised on atoms numbered as 3 and 4 for +MP and 3' and 4' for -MP structures are well buried into the bulk band region.

ARPES and IPES studied the filled [62] and vacant [63] surface-state bands in the Si(111)-(2 × 1) surface. ARPES found an additional peak in heavily doped n-type samples at the $\overline{\text{J}}$ point of the SBZ [58,242]. They argued that this peak is produced by the filling of the vacant surface state at its minimum energy point

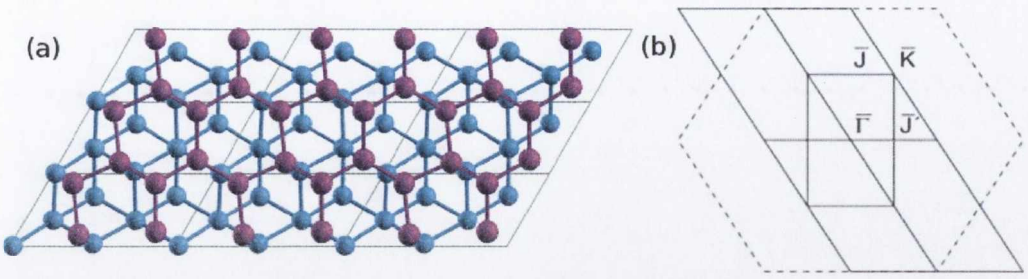


Figure 4.2: (a) Top view of the (2×1) superlattice of the MP chain model real-space unit cell. (b) Four reciprocal space unit cells and SBZ for the (2×1) superlattice of the MP chain model (solid lines) with (1×1) surface reciprocal lattice (dotted lines).

by extra n-type carriers introduced by doping.

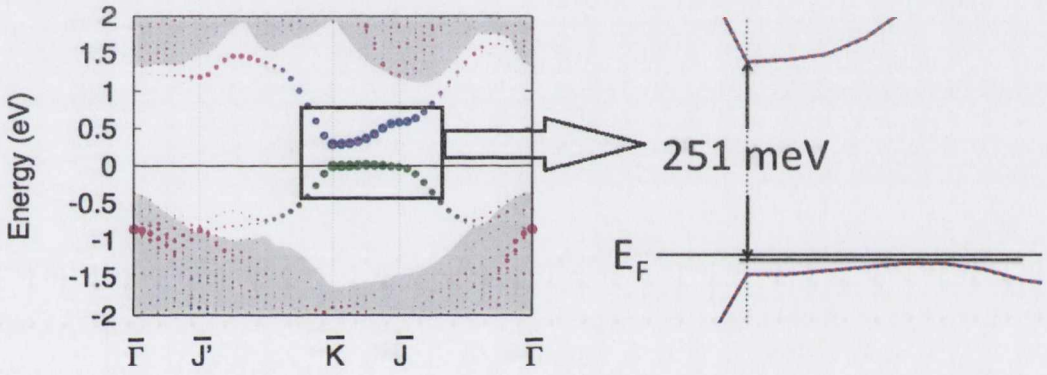


Figure 4.3: Electronic structure of +MP chain model (left) and magnified surface band gap region (right). Surface band structure is projected onto the Si atoms in the π chain. The states with green (blue) circles are strongly localised on the top (bottom) Si atoms of the dimers. The pink circles represent the states mainly localised on the atoms numbered 3 and 4 in Fig. 4.1(a). The projected bulk band structure is shown by grey region. The indirect band gap ($\overline{\text{K}}$-$\overline{\text{J}}$) is 251 meV (right).

The electronic structure from hybrid DFT calculations for the +MP and -MP structures are shown in Fig. 4.3 and Fig. 4.4. With respect to the E_F, the relative positions of calculated occupied surface-state energies at $\overline{\text{K}}$ and $\overline{\text{J}}$ points for +MP structure, are -16 and -31 meV, respectively. For -MP, the energies of occupied surface-state at those points with respect to its E_F are -31 and -63 meV. The indirect band gap ($\overline{\text{K}}$-$\overline{\text{J}}$) for the +MP structure is 251 meV, while the minimum direct gap at $\overline{\text{K}}$ is 297 meV. In the -MP structure the minimum direct gap at $\overline{\text{K}}$ is 399 meV.

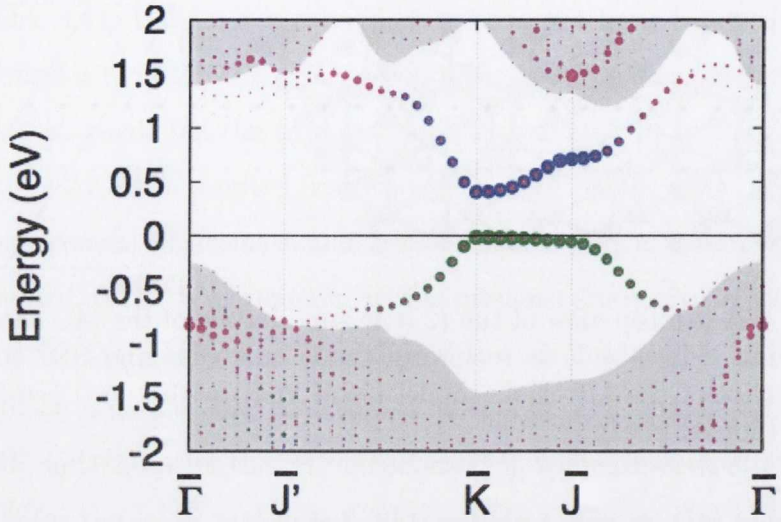


Figure 4.4: Electronic structure of -MP chain model. Surface band structure is projected onto the Si atoms in the π chain. The states with green (blue) circles are strongly localised on the top (bottom) Si atoms of the dimers. The HOMO-LUMO gap which is the band gap at the $\overline{\mathrm{K}}$ point is 0.45 eV. The pink circles represent the states mainly localised on the atoms numbered 3' and 4' in Fig. 4.1(b). The projected bulk band structure is shown by grey region.

The presence of strong electron-electron effects in this surface was noted in Sec. 1.2.1. Surface-state energies and optical band gaps were predicted previously by GW [54, 58] and BSE calculations [70, 72], respectively, where excitonic electron-hole effects were taken into account. Highest occupied molecular orbital (HOMO)-lowest unoccupied molecular orbital (LUMO) gaps from STM and ARPES experiments and GW calculations are given in the first two columns of Table 4.2. The HOMO-LUMO gap ranges from 0.35 to 0.79 eV for +MP and 0.19 to 0.46 eV for -MP surface, whereas the optical gap (third column of Table 4.2) ranges from 0.23 to 0.47 eV for +MP and 0.31 to 0.48 in for -MP surface in the previous calculations. The GW calculations in Ref. [58] (Table 4.2) are in agreement with experimental value of the HOMO-LUMO gap for the +MP structure, 0.83 eV, estimated from STM [58].

If electron-hole interactions in the excited state are not taken into account, the optical transition energy is overestimated by the excitonic binding energy, even with accurate particle or hole energies. To solve the problem, a 5% Fock exchange weight is used here. With that weight the calculated $\epsilon_2(\omega)$ spectrum

of bulk Si agrees well with experiment even when no electron-hole effects are included directly in the optical spectrum calculation. This is achieved by varying the relative amount of Fock exchange in the functional as the predicted band gap increases approximately linearly with the relative amount of Fock exchange. When DFT calculations are used to compute optical spectra without inclusion of many-body effects, a very common approach is adopted, in which the conduction bands are simply shifted upward rigidly until optimal agreement with experiment is achieved [243]. In the present work the shift occurs because Fock exchange has been included in the exchange correlation functional and wave functions and energy eigenvalues are obtained self-consistently.

Table 4.2: Positions of surface states in eV relative to the E_F in the ±MP structure.

	HL Gap +MP	HL Gap -MP	Optical Gap +MP	Optical Gap -MP
STM[1]	0.83	0.47		
ARPES[2]		0.45		
HybridDFT[3]	0.29	0.40	0.29	0.40
GW[4]	0.75		0.45	
GW[5]	0.62		0.47	
GW[6]	0.69		0.43	
GW[7]	0.79			
DFT – LDA[8]	0.35	0.19		
GW[8]	0.77	0.46		

[1]STM data, Ref. [58].

[2]ARPES data n-type surface with both surface states occupied at $\bar{\mathrm{J}}$ point, Ref. [58].

[3]This work.

[4]Calculation in tight-binding basis using fitted HL gap, Ref. [72].

[5]Plasmon pole approximation applied to diagonal elements of inverse dielectric matrix, Ref. [54].

[6]Generalized plasmon pole approximation, Ref. [70].

[7]DFT calculation with conduction bands shifted upward by 0.5 eV based on self-energy estimates at 4 k points, Ref. [58].

[8]LDA-DFT and GW calculation, Ref. [241]

DFT in the local density approximation (LDA) or generalised gradient approximation (GGA) using plane-wave basis sets, is widely used to calculate the optical properties of semiconductors from first-principles. DFT predicts optical spectra of semiconductors incorrectly as it underestimates band gaps of semiconductors. it can be corrected either by performing a perturbative GW calculation before the optical response calculation or simply by shifting conduction bands upward by a constant amount. I some cases Bethe-Salpeter equation (BSE) is solved in order to include electron-hole attraction in the excited state Hamiltonian and this may reduce the energy required for an optical excitation [70]. In a perturbative GW calculation the LDA or GGA exchange-correlation potential from the DFT self-consistent field calculation is replaced by a Fock exchange term screened by the dielectric function. In a narrow-gap semiconductor such as Si, the extent of screening of Fock exchange in a GW calculation is large at small wave vectors, so the wave vector and energy-dependent weight of Fock exchange is small. The predicted band gap of a material depends strongly on Fock exchange; (unscreened) Hartree-Fock theory overestimates the band gap of Si by more than 5 eV [244].

The hybrid DFT HOMO-LUMO gap for the +MP structure is 0.30 eV, smaller than the gap from GW calculations and STM, cited in Table 4.2. However, the HOMO-LUMO gap for -MP (0.40 eV) obtained here is in reasonable agreement with calculations and experiments (Table 4.2). The onset of optical absorption in the Si(111)-(2×1) surface occurs between 0.3 and 0.4 eV, according to differential reflectivity [64] and RAS experiments [75]. The optical gaps predicted by this hybrid DFT and previous calculations, range from 0.29 to 0.47 eV for +MP and 0.31 eV to 0.48 eV for -MP surfaces (Table 4.2).

4.1.3 Optical Properties

Fig. 4.5 and 4.6 show the imaginary part of dielectric function for + and -MP structures, respectively. ϵ_2, for both the MP structures, has strong peaks under 1 eV when the electric field is in the $[\bar{1}10]$ direction (y direction, shown by green

dashed line) and very small peaks when the electric field is in the $[11\bar{2}]$ direction (x direction, shown by red line). This reflects in the RA spectra (Fig. 4.7) as we simply take the difference of reflectivities in two perpendicular directions for sub-bulk band gap frequencies. Those figures also show the imaginary part of the bulk dielectric function for Si (blue dashed line). We can see that transitions begin at 2.4 eV for bulk. Whereas the (2×1) surfaces ($\pm$MP) have peak below 0.6 eV. So those peaks can be considered as surface contributions. For both the cases ($\pm$MP), ϵ_2 is featureless (red line) with electric field aligned with dimer bonds. When electric field is aligned with dimer rows, ϵ_2 has large peaks (green dashed lines).

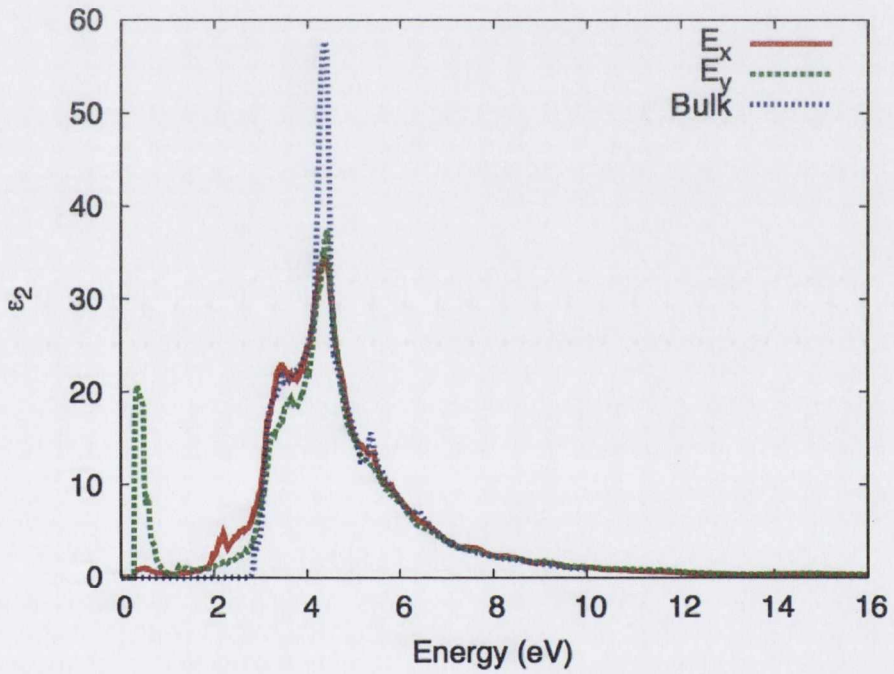


Figure 4.5: Calculated imaginary part of the dielectric function for +MP structure. Red and green dashed lines depict ϵ_2 for Si(111)-(2×1) with an electric field aligned in the direction (x direction) and perpendicular (y direction) to the dimer bond. The blue dashed line shows the imaginary part of bulk dielectric function.

As mentioned above, the occurrence of filled and vacant surface states localised on adjacent Si atoms in π chains of the $\pm$MP structures results in large charge transfers between filled and vacant 3p dangling bond states and large optical absorption cross sections. The thickness of the slab, in this case, is just over 30 Å. Surface and bulk susceptibilities were calculated using the EXCITON

code [228] using a 16×32 grid of k points in the surface Brillouin zone and a $24 \times 24 \times 24$ grid in the bulk Brillouin zone. Integration over the Brillouin zone was performed using an interpolation method [245].

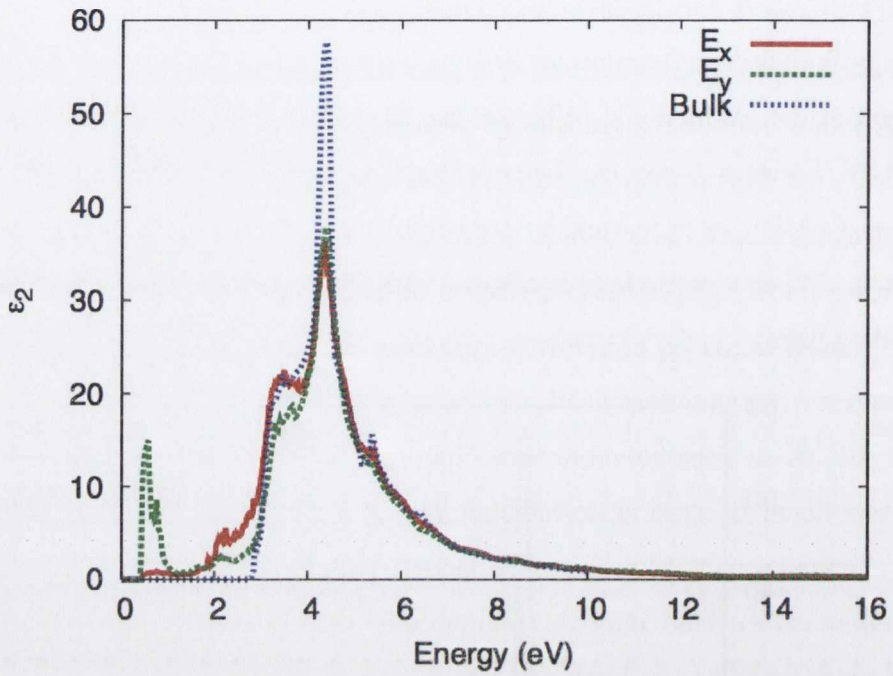


Figure 4.6: Calculated imaginary part of the dielectric function for -MP structure. Red and green dashed lines depict ϵ_2 for Si(111)-(2×1) with electric field aligned in dimer bond (x direction) and dimer row (y direction) directions, respectively. The blue dashed line shows the imaginary part of bulk dielectric function.

The RA spectra calculated for $\pm$MP structures are compared to a RA spectrum from experiment [75] in Fig. 4.7. No scaling has been applied to the spectra from hybrid DFT calculations. The RA spectrum below 1 eV is a single, asymmetric peak with a sharp leading edge. The experimental peak position is 0.46 eV while the hybrid DFT predicts peak positions, for +MP and -MP structures are 0.43 and 0.57 eV, respectively. The linewidth for either MP structure is greater than the experimental linewidth.

The optical response of this surface is highly anisotropic, being very large parallel to the π chains and very small perpendicular to the chains in the infrared. In the visible region (between 2 and 4 eV) the imaginary part of the surface dielectric function perpendicular to the π chains is greater than that parallel to the chains. Fig. 4.8(a) shows a surface wave vector dependent grayscale plot of

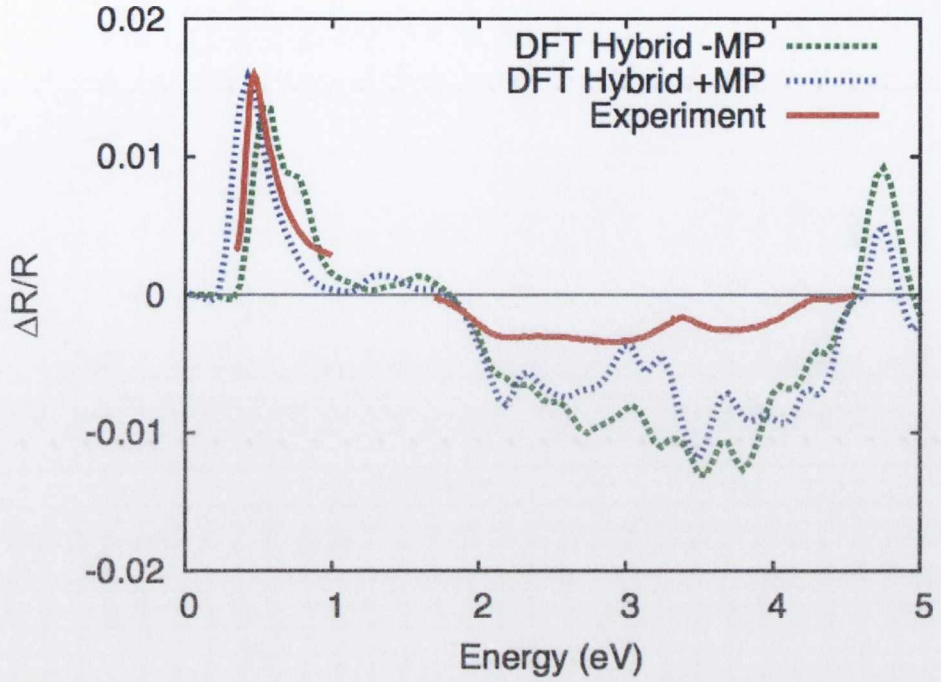


Figure 4.7: The calculated RA spectra of ±MP structures compared to experimental data. Experimental data are redrawn from Ref. [75] and were collected in two spectral regions.

the modulus squared of the momentum matrix element for transitions between the occupied and vacant surface states for the +MP structure when the electric vector of the incident radiation is parallel or perpendicular to the π chains. Transitions between states other than the two surface states were excluded when generating Fig. 4.8(a). When the electric vector is parallel to the chains, this matrix element is maximum at the $\overline{\mathrm{J}}$ point and has large amplitude only along the $\overline{\mathrm{K}}$-$\overline{\mathrm{J}}$-$\overline{\mathrm{K}}$ line in the Brillouin zone. When the electric vector is perpendicular to the chains, the matrix element vanishes in this region of reciprocal space and instead is large close to the $\overline{\mathrm{J}'}$ points.

The surface susceptibility depends on both the momentum matrix element and, at resonance, the inverse square of the transition energy. Transition energies for the occupied and vacant surface states in the MP structure, as a function of position in the surface Brillouin zone, are shown in Fig. 4.8(b). Figures 4.8(a) and 4.8(b) show that predominance of the response along the π chains in the infrared depends on both optical matrix elements and transition energies. When

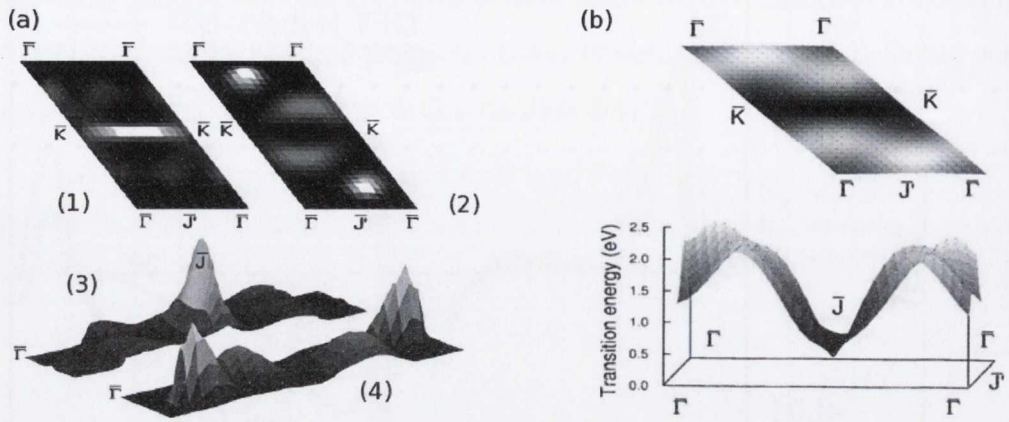


Figure 4.8: (a) Modulus squared of the transition matrix element, $p^i_{nn'k}$, between occupied and vacant surface states over one unit cell in reciprocal space for the +MP structure (after [49]). (1), (2) Field parallel to $[\bar{1}10]$, (3), (4) Field parallel to $[11\bar{2}]$. (b) Optical transition energy between occupied and vacant surface states over one unit cell in reciprocal space for the +MP structure (after [49]). Darker areas in the upper panel correspond to lower transition energies.

the electric vector is parallel to the π chains, the matrix element at $\bar{\mathrm{J}}$ is large and the corresponding transition energy is small (around 0.3 eV); on the other hand, when the electric vector is perpendicular to the π chains, the matrix element is large close to $\bar{\mathrm{J}}$ but the transition energy is large (over 2.0 eV), leading to a large difference (~300) in the optical response magnitude, parallel or perpendicular to the π chains.

4.2 Si(111)-(5 × 2)-Au

4.2.1 Surface structure of Si(111)-(5 × 2)-Au

The various surface structures that have been proposed for Si(111)-(5 × 2)-Au have been discussed in Chapter 1.6. With the help of hybrid DFT, the EBH model [35], were relaxed, both with and without Si adatoms (Fig. 4.9 and 4.10). As discussed previously this structure has 3 Au chains and a Si HC structure along the ×2 direction. One special feature of this surface is the $SiAu_4$ butterfly wing configuration, which consists of four Au atoms at four corners and Si atom at

the centre (Fig. 4.9). In this special type of structure a Si atom on the surface is coordinated with five atoms (four neighbouring Au atoms on the surface and one Si atom in the next layer) which exceeds the normal coordination number of Si. As the $SiAu_4$ motif with butterfly shape can be found other Si(111) surfaces like the (6×6) [246], it can be said that it plays a very important role in stabilisation of these surfaces. Also, on the relaxation, it was found that the HC becomes quite flat on addition of adatoms, as found by Erwin [35].

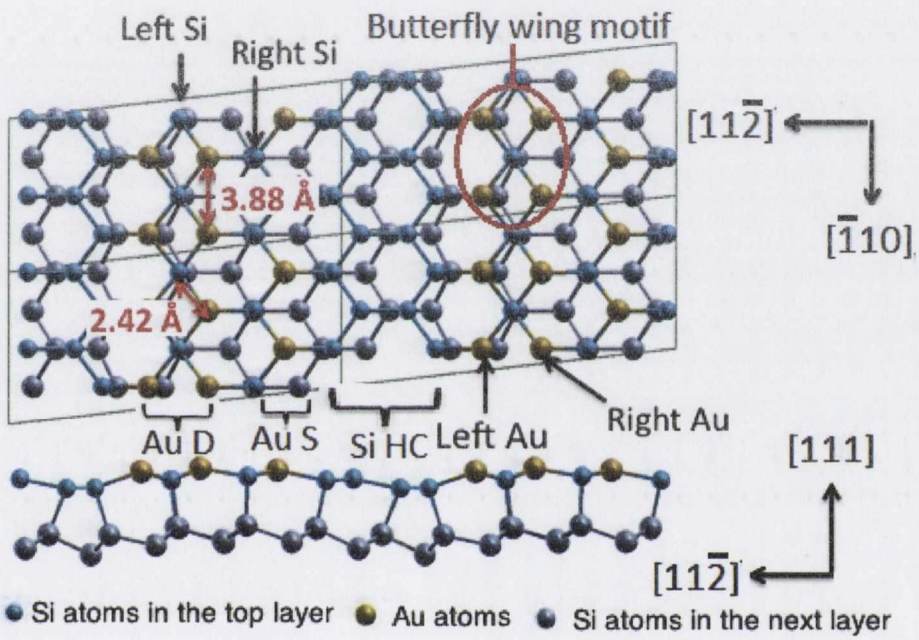


Figure 4.9: Top and side views of fully relaxed EBH model reproduced after Ref. [35] of Si(111)-(5×2)-Au surface without adatoms. It also shows the parallel and perpendicular directions to Au chains.

Along the Au chain direction, the two Au atoms on either side of Si in $SiAu_4$ form Au-Au rungs (Fig. 4.10), which were reported to be parallel and separated by the Si surface lattice constant [35]. With the addition of one adatom per (5×4) unit cell, the Au-Au rungs rotate from their parallel alignment, according to Erwin *et al* [35]. Similar separation between Au-Au rungs in the Si(111)-(5×2) surface, and the same kind of rotation with one adatom per (5×4) cell, were found by the hybrid DFT calculations. In the adatom decorated Si(111)-(5×4)-Au surface, the Au-Au dimer distance in the rungs was found to be 2.94Å by Erwin *et al.*, which is close to the bulk bond length (2.88 Å) in Au metal. Hybrid

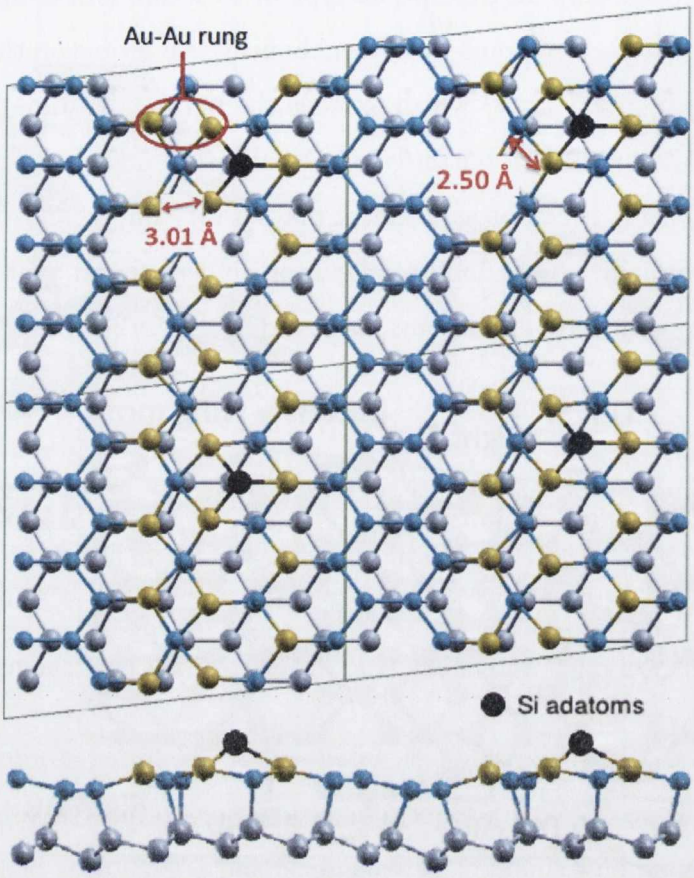


Figure 4.10: Top and side view of EBH structure of Si(111)-(5 × 4)-Au with one Si adatom per (5 × 4) unit cell. Same colour scheme is used as previous figure, for different atoms.

DFT predicts this Au-Au distance larger than Ref. [35] by ∼2.3 % (3.01 Å in Fig. 4.10), which exceeds the Au bulk bond length by 4.5 %. The length of Au-Si bonds in the $SiAu_4$ motif adjacent to the adatom changes from 2.42 to 2.50 Å (Fig. 4.9 and 4.10). The change of Si-Si bond lengths in the HC is insignificant after adding adatoms and it seems to be very stable.

In 2013 another structural model was proposed by Abukawa and Nishigaya (thereafter, AN) in a reflection high energy electron diffraction (RHEED) study [90]. This structure, which has same Au coverage as EBH model, is shown in Fig. 4.11. The AN model consists of four Au chains and does not have a Si HC. The model was predicted to match the Y-shaped features in STM images [35,247,248]. Lately Seino *et al.* [249], Shirasawa *et al.* [250], and Hogan *et al.* [251] excluded

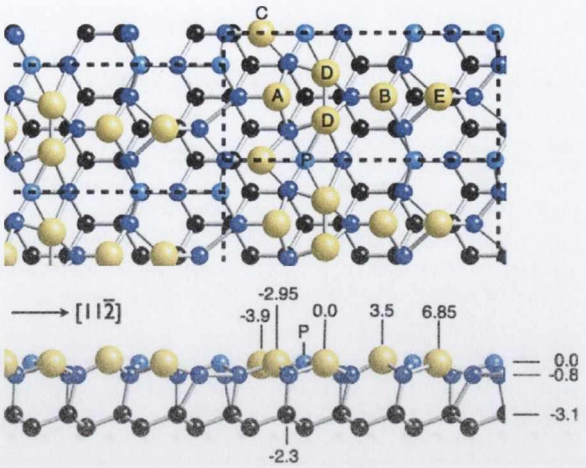


Figure 4.11: Si(111)-(5 × 2)-Au superstructure proposed by Abukawa *et al* [90]. It does not have a Si HC, unlike the EBH model.

the model as a possible structure. Hogan *et al.* supported the presence of Si HCs. Unlike all other structures, the AN structure has seven membered ring, which is made of three Au atoms and four Si atoms. When the AN model was relaxed, it was found to be unstable, both here and in Ref. [251].

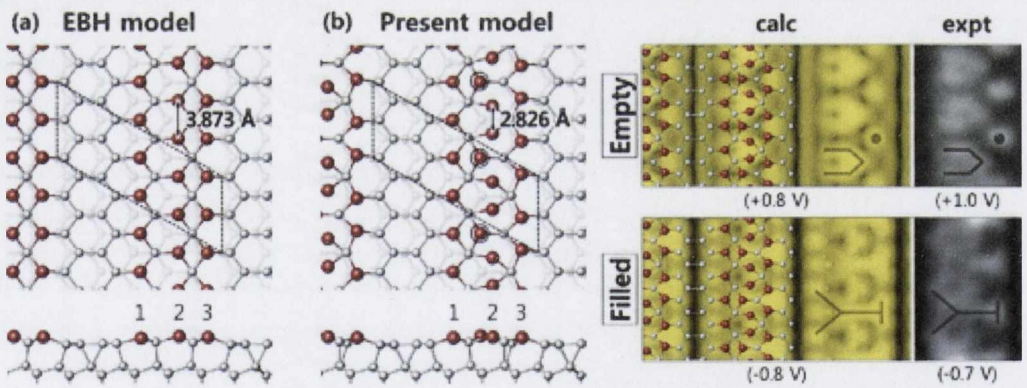


Figure 4.12: Comparison between proposed (a) EBH [35] and (b) KK [99] model of Si(111)-(5 × 2)-Au with Si adatoms (after [99]). Simulated STM images of the KK model agree quite well with experiment.

The latest structure, proposed by Kwon and Kang (hereafter, KK), has a Si HC and 7 Au atoms per (5 × 2) unit cell (Fig. 4.12) [99]. The V-shaped (empty) and Y-shaped (filled) features of their calculated STM images agree quite well with experiment [35, 247, 248]. This structure has been preferred over EBH recently,

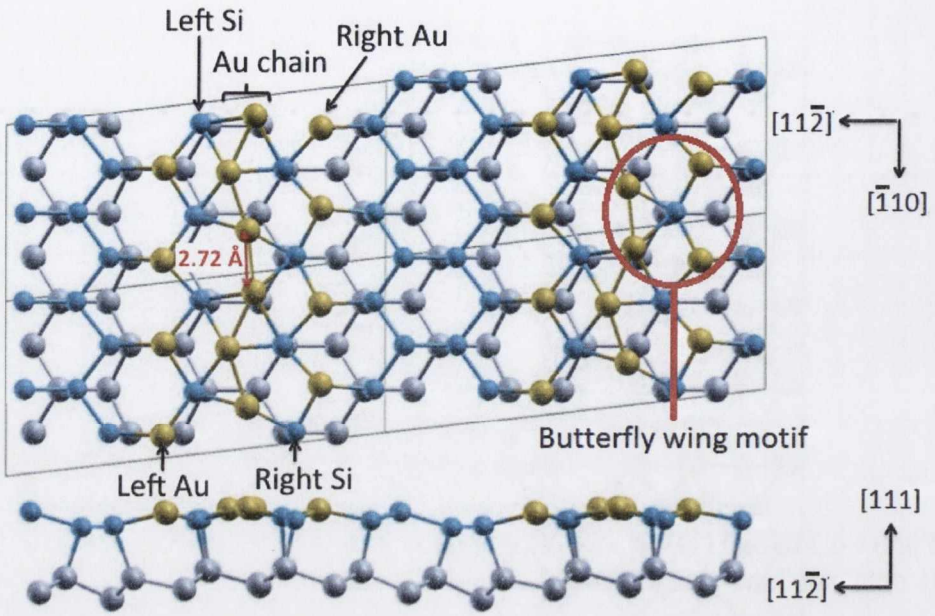


Figure 4.13: Top and side views of relaxed KK model of Si(111)-(5 × 2)-Au unit cell, reproduced after Kwon *et al* [99]. It has 7 Au atoms per (5×2) unit cell. The same colour scheme is used as in Fig 4.9 for the different atoms.The Au dimer separation is 2.72 Å.

both theoretically and experimentally, by Shirasawa *et al.* [250] and Hötzel *et al.* [252], with some evidence for the higher Au coverage. The KK structure has a Si HC and two rows of the $SiAu_4$ butterfly wing motif (Fig. 4.13), while EBH has only one row of that particular type of structure (Fig. 4.12). When an extra Au atom was added to the EBH (5 × 2) unit cell, one row in the double Au chain is modified along the chain direction. The Au atoms shift toward each other and form Au-Au dimers as shown in the Fig. 4.13. Without adsorption of an adatom, the Au-Au distance in the EBH structure is found to be 3.88 Å by hybrid DFT calculations (Fig. 4.9), in contrast to 3.87 Å in Ref. [35]. In the KK model this Au-Au distance is reduced to 2.72 Å in hybrid DFT calculation, as shown in Fig. 4.13 (2.83 Å in Ref. [99]). This type of short Au dimer was strongly suggested by Abukawa and Nishigaya in their RHEED study [90]. After adding one adatom per (5 × 4) KK cell, the bond length of the Au-Au dimer adjacent to the adatom increases to 2.83 Å (2.91 Å in Ref. [99]) as shown in Fig. 4.14, whereas the distant dimer distance remains unchanged. The Si adatom site in this case is H_3 (over an Si atom in the second bulk bilayer). These results are consistent with Kwon

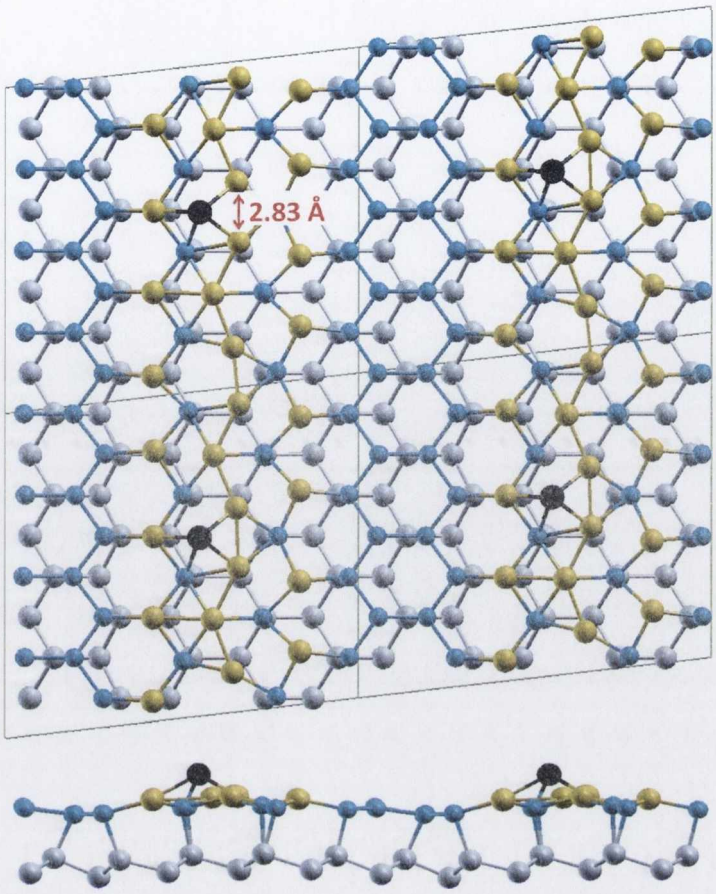


Figure 4.14: Top and side views of relaxed KK model with one Si adatom per (5×4) unit cell. The same colour scheme is used as in Fig 4.9 for the different atoms. The Au dimer separation is 2.83 Å, adjacent to the Si adatom.

and Kang [99].

4.2.2 Electronic structure

Photoemission studies [83,85,86,107,239] have addressed whether this surface is conducting or semiconducting. However, experiments have been inconsistent in detecting surface conducting states. To resolve the problem, DFT calculations were done [35,99,251] and compared with ARPES. Here in this work electronic structures were calculated for two different structures (EBH and KK) to see whether the calculated results are reproducible and which is in better agreement with ARPES. Fig. 4.15 shows the SBZ schemes of (5×1), (5×2) and (5×4) unit cells along with the (1×1) unit cell. Most ARPES experiments and calculations

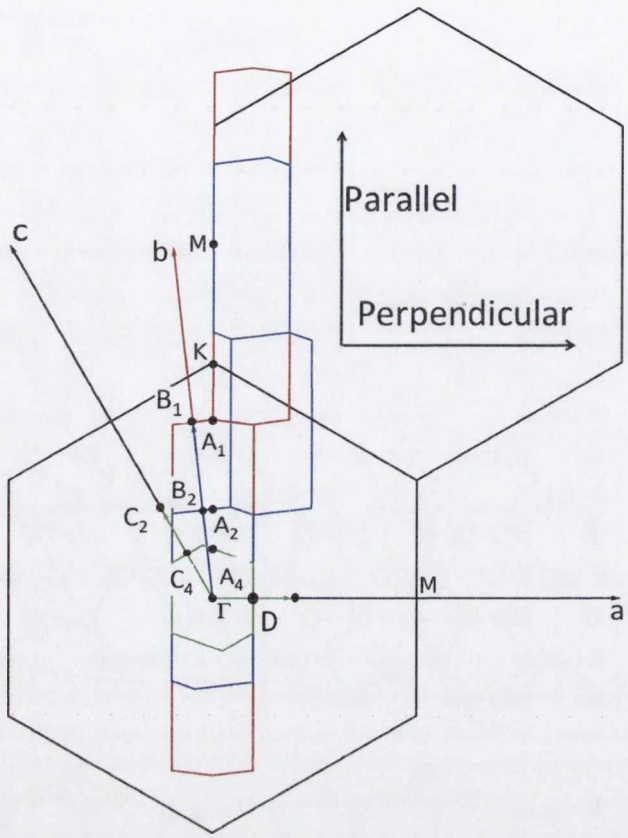


Figure 4.15: SBZ of 5×1, $\times 2$ and $\times 4$ unit cells with the underlying (1×1) cell. The direction, linking the A_2 and A_1 points, is parallel to the Au chain direction. The reciprocal vectors are **a**, **b** and **c**. B_2 and B_1 are points at the SBZ boundaries along **b** and C_4 and C_2 are points at the SBZ boundaries along **c**.

were done in the directions parallel to the Au chain ($\Gamma A_4 A_2 A_1$ direction). Here the electronic structures were calculated along the $\Gamma B_2 B_1$ direction for (5×2) unit cell, which is close to parallel to the Au chain direction (Fig. 4.15). For the (5×4) unit cell, the direction used in this work is $\Gamma C_4 C_2$. It was assumed that there is little band dispersion perpendicular to the Au chains, which can be seen later. The high symmetry points B_2 and B_1 for the (5×2) unit cell are considered equivalent to A_2 and A_1, respectively. C_4 and C_2 for (5×4) unit cell are considered equivalent to A_4 and A_2, respectively. The electronic structures were also calculated along the perpendicular to the Au chains (ΓD).

Figures 4.16 and 4.17 show the electronic structures of the Si(111)-(5×2)-Au surfaces for the EBH and KK models, along with the ARPES result [85]. Calculated band structures are similar, but with some subtle differences. The

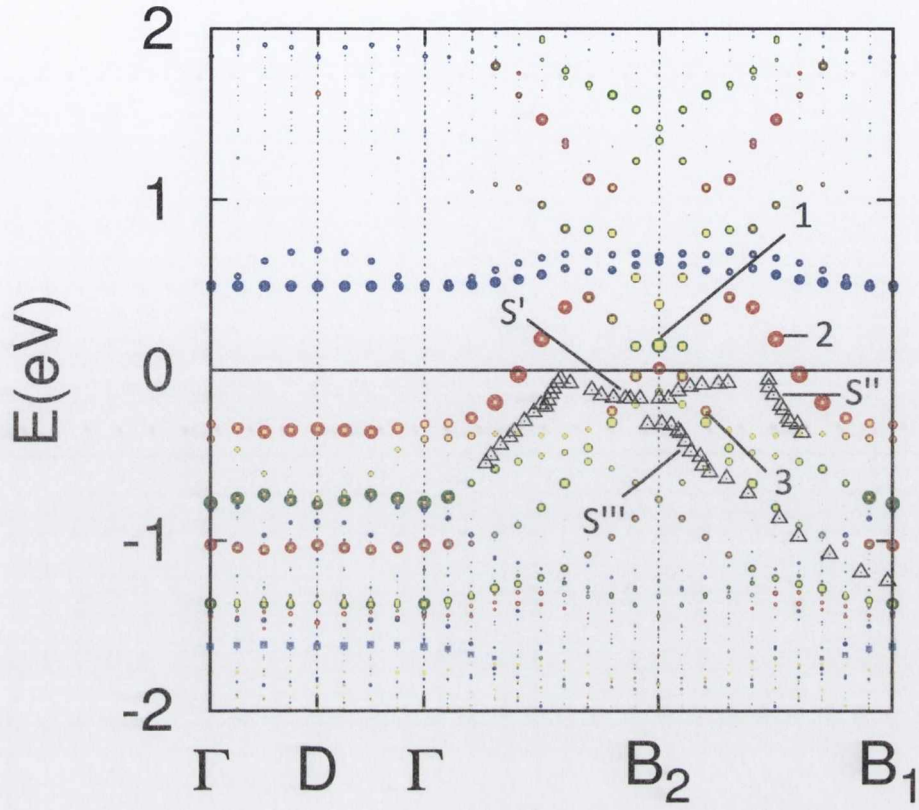


Figure 4.16: Hybrid DFT calculations of the electronic structure for the EBH model of Si(111)-(5 × 2)-Au compared, with the ARPES data [85] (triangles). The surface band structure is projected onto the various atoms in the surface. Blue, red and green circles represent the states localised on Si atoms in the Si HC, and left and right Si atoms (Fig. 4.9), respectively. Turquoise, pink and yellow squares represent the states manly localised on left and right Au atoms and Au atoms in Au S (Fig. 4.9), respectively.

blue unoccupied band, which is mainly localised on the Si atoms in Si HC, has a very similar dispersion for both models. The band is quite flat, which indicates the stability of the Si HC, also reported earlier [35, 100–102]. This band occurs at higher energy in previously calculated electronic structures [99, 249, 252]. Two surface states for EBH model 1 and 2 (Fig. 4.16) are mainly localised on the right and left Si atoms (Fig. 4.9). Another surface state numbered 3 is mainly localised on the left Si atoms. The hybrid DFT results are compared with the ARPES data from Ref. [85] in Fig. 4.16 and subsequent figures. The photoemission bands are labeled as S', S", S"' (1", 1', 2, respectively in Ref. [85]). The agreement is not very good, but the the band dispersion in this electronic structure looks quite

similar to the calculated band structure of Erwin *et al.* [35]. If the calculated bands are pushed down by half an eV in Fig. 4.16 then the agreement would be much better with experiment, which indicates to the fact that the EBH structure is electron deficient. The experimentally prepared surface is more electron rich than the EBH model which is achieved later by adding one Au atom per (5×2) unit cell and one Si adatom per (5×4) unit cell. It pushes down the conduction bands labelled as 1 and 2 into the valence band region, hence those bands become occupied. There is a surface state just below the Si HC band, which is mainly localised on the Au atoms in the Au S chain. Along the perpendicular direction of Au chain, a well localised occupied state, 0.3 eV below E_F, comes from the left Si atoms.

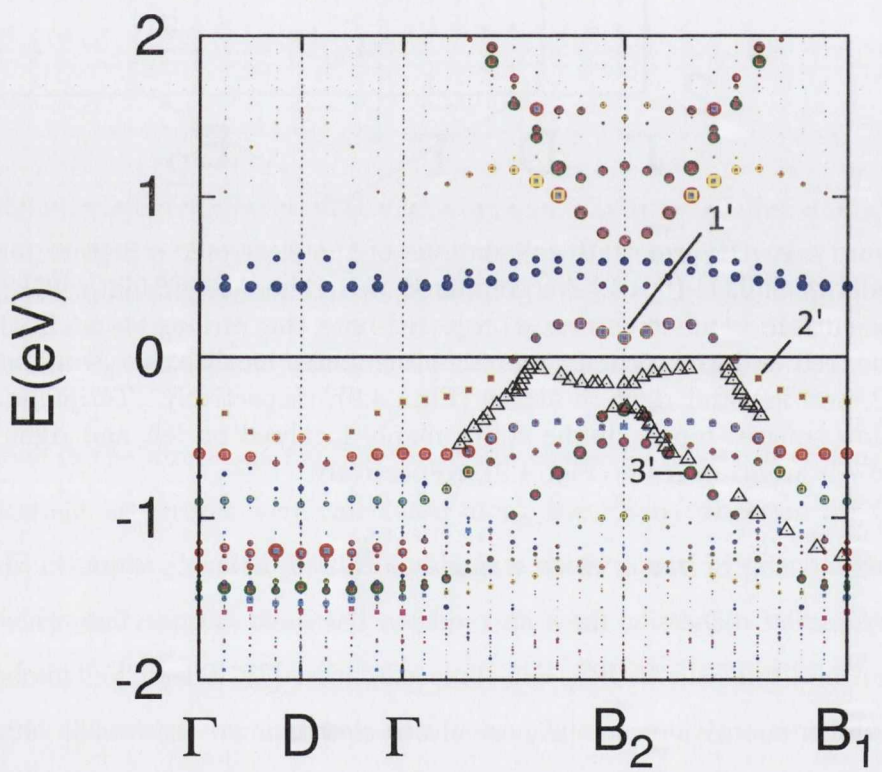


Figure 4.17: Hybrid DFT calculations of the electronic structure for the KK model of Si(111)-(5×2)-Au, compared with the ARPES data [85] (triangles). The surface band structure is projected onto the various atoms in the surface. Red and green circles represent the states localised on Si atoms left and right to the Au chain, respectively (Fig. 4.13). Blue circles correspond to Si atoms in Si HC. Yellow squares represent states localised on Au chain atoms. Turquoise and pink squares represent states localised on left and right Au atoms to the Au chain, respectively.

For the KK model along the Au chain direction, a surface state, similar to 1 (thereafter, 1') in case of the EBH model, is localised mainly on Si (red circles) and Au (turquoise squares) atoms in the left side of the Au chain. The band similar to 2 (thereafter, 2') is mainly localised on the Au chains and Au atoms on the right of the Au chain. The surface state similar to 3 (thereafter, 3') agrees well with a part of ARPES. This state is mainly localised on Si and Au atoms on the right of the Au chain (Fig. 4.13). The overall agreement with ARPES is not very good. Only band 3' is in a good agreement with S"' in the experiment. The calculated band structure in Ref. [99] has similar bands to 1', 2' and 3', but the 2' band is less dispersive than the S_2 in Ref. [99]. The metallic band, S_h, reported in Ref. [252] has similar dispersion to 1' and 2'. Two unoccupied surface bands, above the Si HC bands, agree very well with Ref. [99] and are localised on the Si and Au atoms in either side of the Au chain (Fig. 4.13). According to KK [99], the surface states are localised on the Si and Au atoms on either side of the Au chain, which agrees reasonably with what is found here. All the calculations indicate that without Si adatoms, the Si(111)-(5 × 2)-Au surface is metallic and at least one band for both the models shows metallic behaviour. Along the perpendicular direction of the Au chain (ΓDΓ in Fig. 4.16 and 4.17), two unoccupied states, which have small dispersions, are localised on the Si atoms in the Si HC. Occupied states which are not well localised on the Au chain atoms and the right Au atoms, occur near the zone boundary and Γ.

Figures 4.18 and 4.19 show the band structure of the EBH and KK models for the Si(111)-(5 × 4)-Au surface, respectively, with one Si adatom per (5 × 4) unit cell. The band structures were doubled to compare with experiment. No band gap opening was found for the EBH structure with an adatom, which is inconsistent with Refs. [35] and [249]. The unoccupied bands, divided in either sides of 0.5 eV above E_F (Fig. 4.18), are mainly localised on Si atoms in Si HC. There is a band crossing at the zone boundary (C_4). The unoccupied states below the Si HC states, which cross along ΓC_4, are mainly localised on right Au atoms of the AuD chain. Along the ΓD direction, perpendicular to the chain, the states, mainly localised on the right Au atoms in the AuD chain and the Si

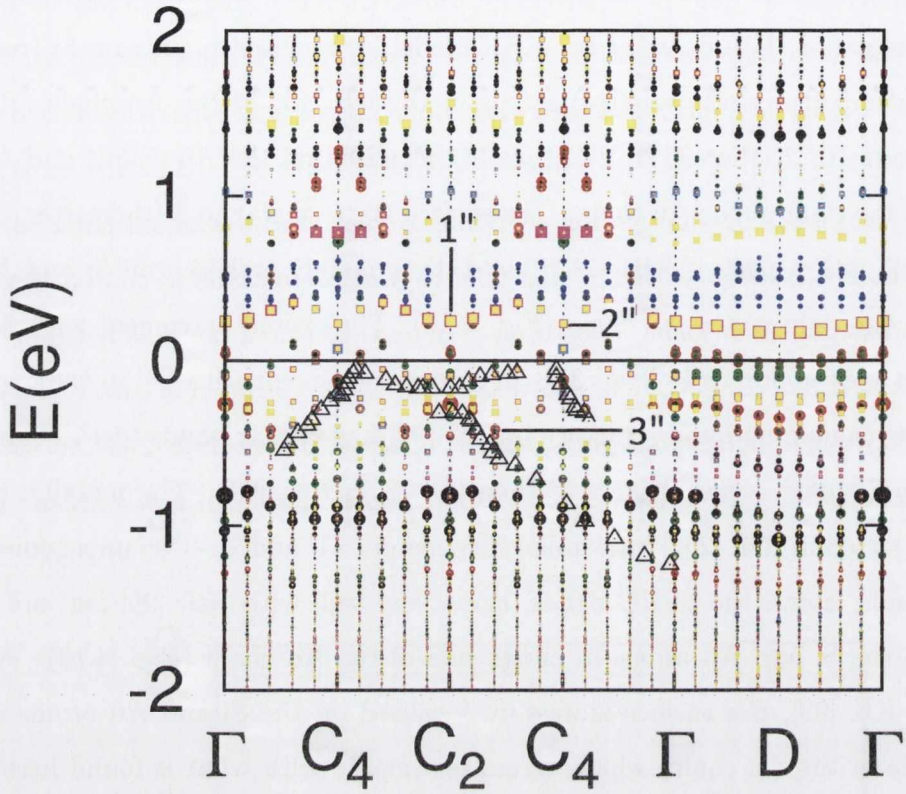


Figure 4.18: Hybrid DFT calculations of the electronic structure for the EBH model of Si(111)-(5 × 4)-Au (with 0.5 ML adatom coverage), compared with the ARPES data [85]. The surface band structure is projected onto the various atoms in the surface. The same colour scheme is used in this figure as in Fig. 4.16. Black circles represent states localised on Si adatoms.

HC atoms occur at around the same energy as the other direction. The occupied bands near C_4 at around 0.75 eV below E_F are mainly localised on the right Si atoms. An occupied state at around 0.20 eV below E_F in either direction is mainly localised on Au atoms in AuS chain. Along the perpendicular direction to the Au chains, there are two states, one is just above and another is at 0.25 eV below E_F. They are mainly localised on left Si atoms. The states mainly localised on the Si adatoms can be seen clearly between 0.75 and 1.0 eV below E_F along both directions (black) circles. There are some states along the ΓC_4 direction between 0.5 and 0.75 eV below E_F, which are localised on the right Si atoms. The agreement between the calculation and the ARPES data is not good, except for the 3" band in the calculation that can be compared with the S"' band in the ARPES. If the calculated energies were moved down by ~0.45 eV

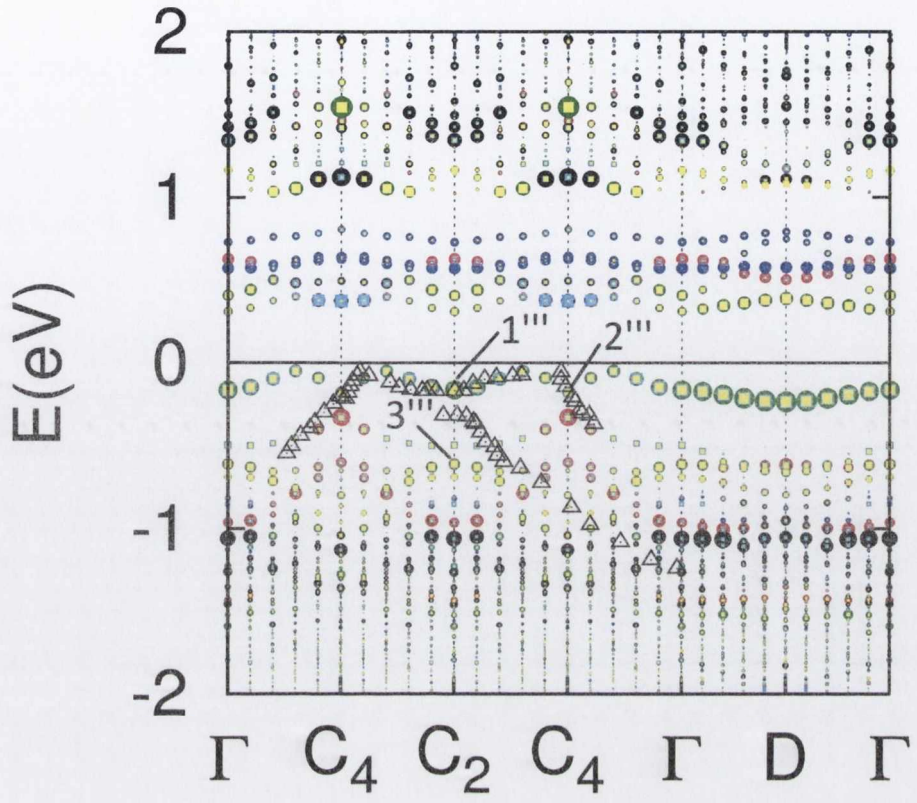


Figure 4.19: Hybrid DFT calculations of the electronic structure for the KK model of Si(111)-(5 × 4)-Au with one Si adatom per (5 × 4) unit cell, compared with the ARPES data [85] (triangles). The surface band structure is projected onto the various atoms in the surface. The same colour scheme is used in this figure as in Fig. 4.17. Black circles represent state localised on Si adatoms.

downward then the agreement would be much better. The agreement between some previous calculations [94,249] and hybrid DFT is very poor. However, Seino *et al.* [252] reproduced the band structure of EBH model very well.

The main difference between the electronic structures of adatom decorated KK and the other three surfaces, discussed above, is that the Fermi level is pushed into the gap for adatom decorated KK model. As a result the adatom decorated surface becomes semiconducting, with the CBM at 0.4 eV above and the VBM at 0.05 eV below E_F. The band gap at Γ is $\sim$ 0.47 eV, which agrees very well with Ref. [99] ($\sim$ 0.50 eV), while the indirect band gap is $\sim$ 0.35 eV along ΓC_4 direction. The band crossing appears at the same position as the adatom decorated EBH (5 × 4) cell. From the figure we can see that ARPES data [85] agrees well with

hybrid DFT calculation, except for the 3"' band. However, the calculated band structure is quite different in Ref. [99], where the highest occupied band is pushed further into the valence band region, a result that is in good agreement with another photoemission study [86]. In the hybrid DFT calculation the top most valence band is localised on the right Si atoms beside the Au chain. The Si HC signature is still present in the conduction band region, though a band, mainly localised on left and right Au and left Si atoms appears in the gap, which was absent for the (5×2)-Au phase the KK model. The unoccupied states at around Γ and along the perpendicular direction, which are marked with red circles, are localised on left Si atoms. In the perpendicular direction there are unoccupied and occupied states, which are mainly, localised on right Si atoms and Au chain atoms. The occupied and unoccupied states coming from adatoms (black circles) occur for Γ at around 1.0 eV below E_F, and for C_4 at around 1.1 eV above E_F.

4.2.3 Optical Properties

Fig. 4.20 shows the imaginary part of calculated dielectric functions, in two perpendicular directions, for the EBH (5×2) unit cell without adatoms and with Au reconstructed surfaces on both sides of the slab, along with the calculated bulk dielectric function of Si. From the figure it can be seen that transitions in the imaginary part of the bulk dielectric function start from 2.4 eV, so all the transitions below 2.4 eV can be attributed to the surface. The transitions parallel to Au chains are much stronger than those in the perpendicular direction. The RA spectrum calculated for EBH model is compared with experiment in Fig. 4.21. All the RA experimental data used here were extracted from Ref. [112]. To identify the energy states involved in the transitions, which are contributing to the dielectric function, the transitions momentum matrices are examined. If the values of transition momentum matrices are over a particular number (representing about 10% of the weight of a large transition) then the transitions are considered to be strong enough to contribute to the dielectric functions. There are two maxima at around 0.4 and 0.8 eV. The lower energy one comes from

transitions near Γ between occupied states mainly localised on Au and right Si atoms (Fig. 4.9). The other one is the result of transitions between the occupied states, mainly localised on Au, left and right Si (Fig. 4.9), and also between bulk Si atoms and unoccupied states mainly localised on Si atoms in Si HC between. The minimum at around 1.3 eV is produced by transitions between the occupied states, mainly localised on Au and right, left and bulk Si atoms and unoccupied states, mainly localised on left and right Si atoms and Si atoms in the Si HC. The small hump at around 1.9 eV results from the transitions between the occupied states, mainly localised on Au and right Si atoms and unoccupied states, mainly localised on Au, left, right and bulk Si and Si atoms in Si HC. The overall agreement between theory and experiment in Fig. 4.21 is reasonable except the calculated positive maximum shifted towards lower energy with respect to experiment because the experimental surface is more electron rich than the EBH model which shows half filled surface state.

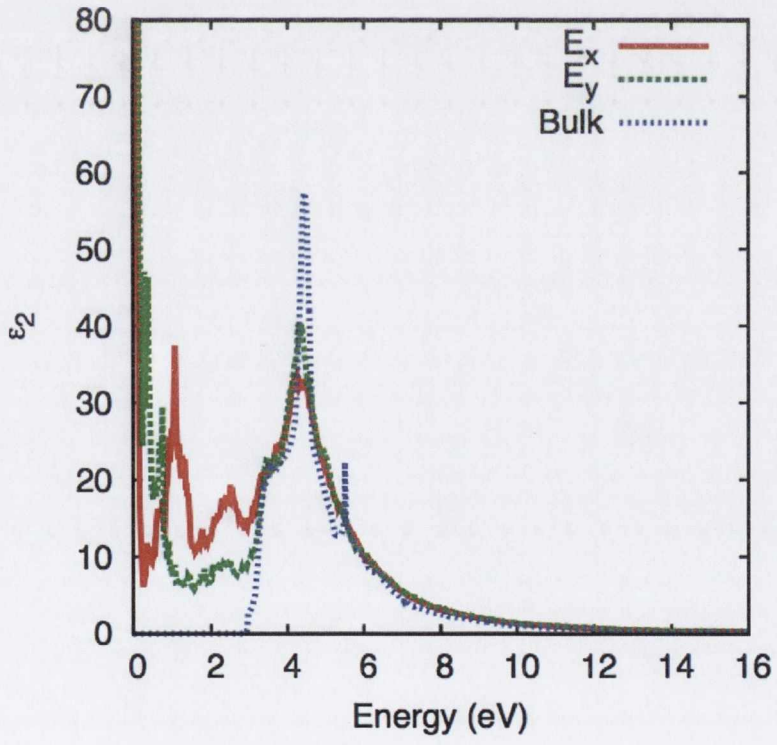


Figure 4.20: Comparison between the imaginary part of calculated dielectric functions of EBH structure without adatom ((5×2) unit cell), with electric field, aligned perpendicular (E_x) (red) and parallel (E_y) (green dashed) to Au chain direction, along with the calculated bulk dielectric function for Si (blue dashed).

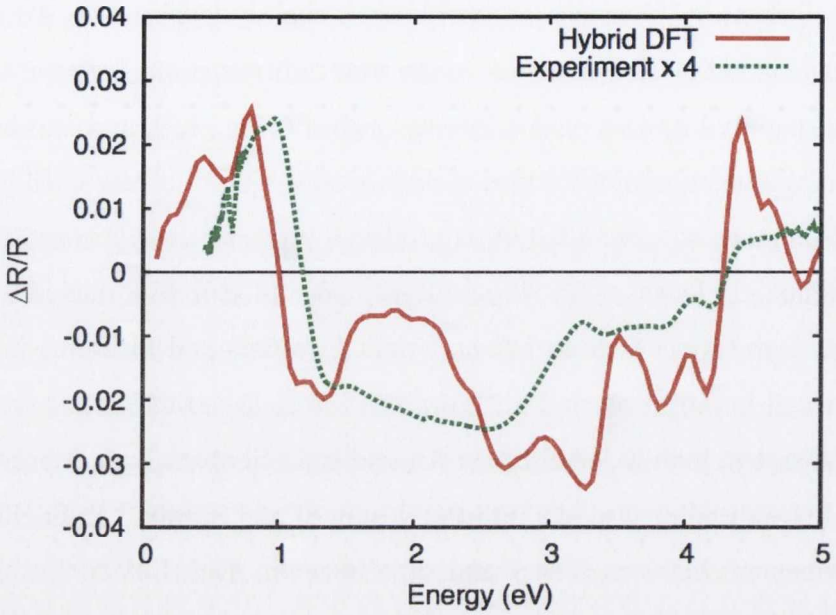


Figure 4.21: Comparison between experimental (green dashed) and theoretical (red) RA spectra of EBH Si(111)-(5 × 2)-Au without adatom. Experimental data were scaled ×4 to compare with the calculation.

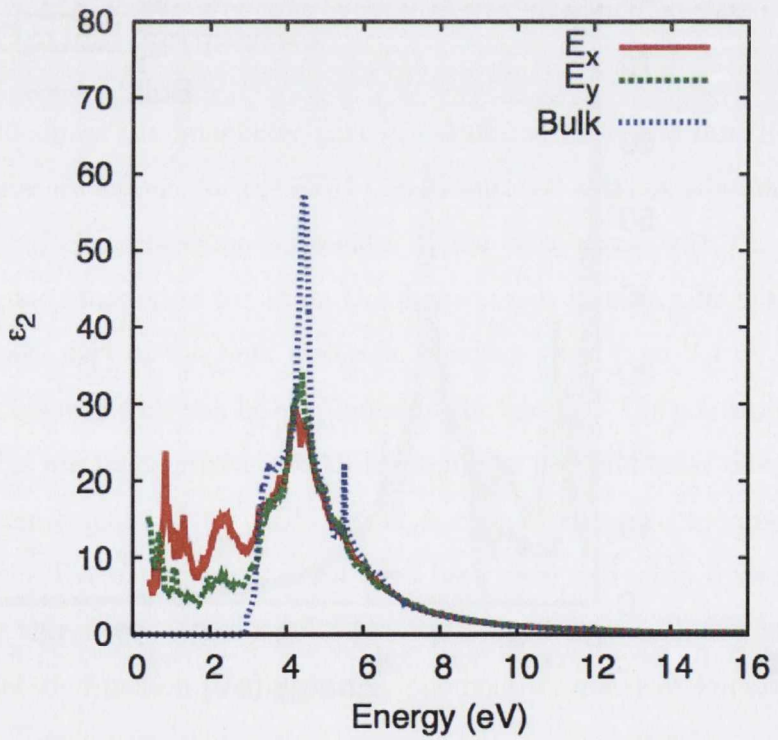


Figure 4.22: Calculated Imaginary part of the dielectric functions of EBH structure (one Si adatom per (5 × 4) unit cell) with electric field aligned in perpendicular (E_x) (red) and parallel (E_y) (green dashed) directions with respect to the Au chains. It also shows the bulk dielectric function (blue dashed).

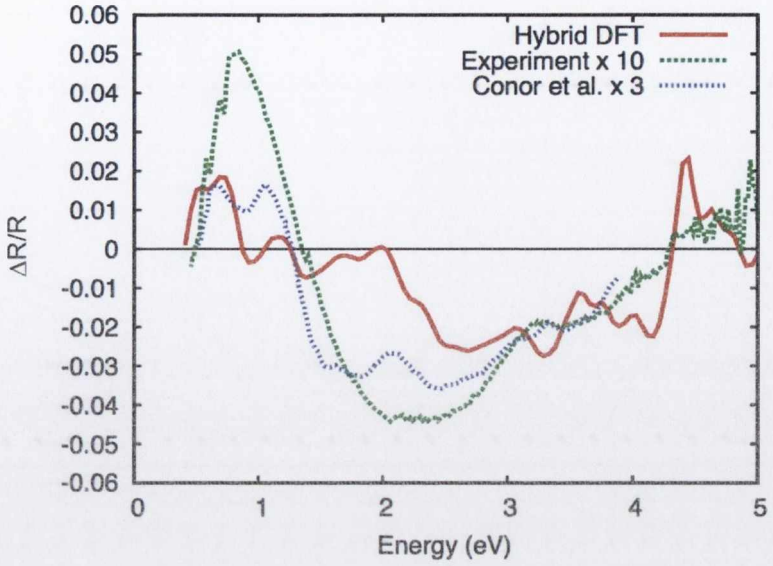


Figure 4.23: Experimental (0.5 ML adatom coverage) (green dashed) and theoretical (red) RA spectra of EBH structure (one adatom per Si(111)-(5 × 4)-Au unit cell). Experimental data were scaled ×10 for comparison. It also compares a recent DFT-LDA calculation on the EBH model by Hogan *et al.* (blue dashed) [251].

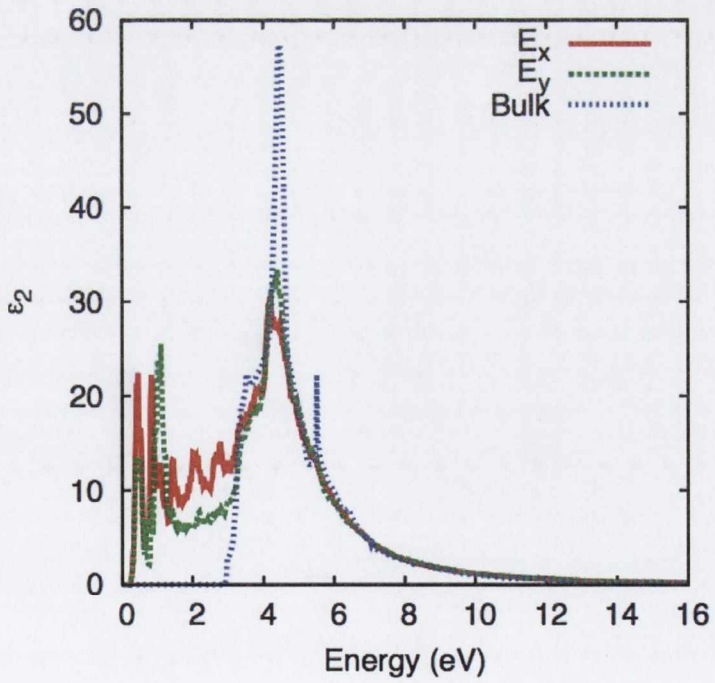


Figure 4.24: Calculated imaginary part of the dielectric function of the KK structure, without adatoms ((5 × 2) cell), and with electric fields aligned perpendicular (E_x) (red) and parallel (E_y) (green dashed) to the Au chains. It also shows the dielectric function of bulk Si (blue dashed).

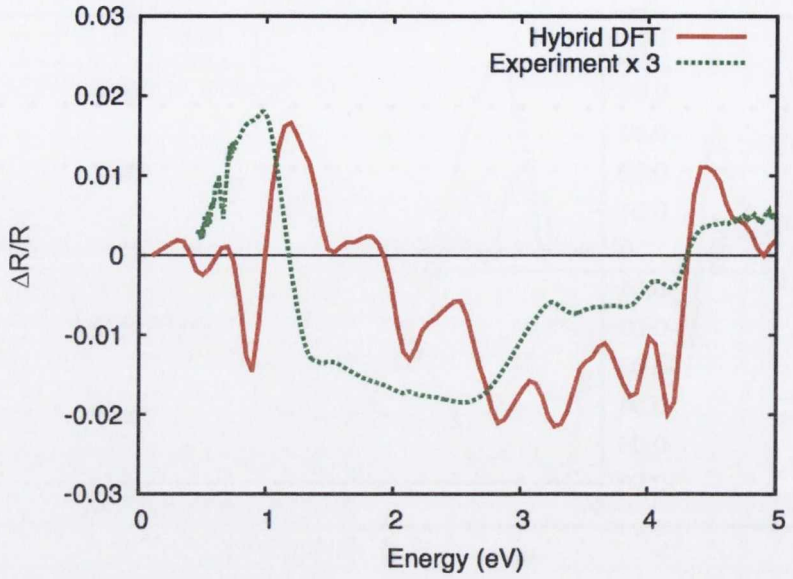


Figure 4.25: Experimental (green dashed) and theoretical (red) RA spectra for the KK structure, without adatoms ((5×2) cell). Experimental data were scaled $\times 3$ to compare with theory.

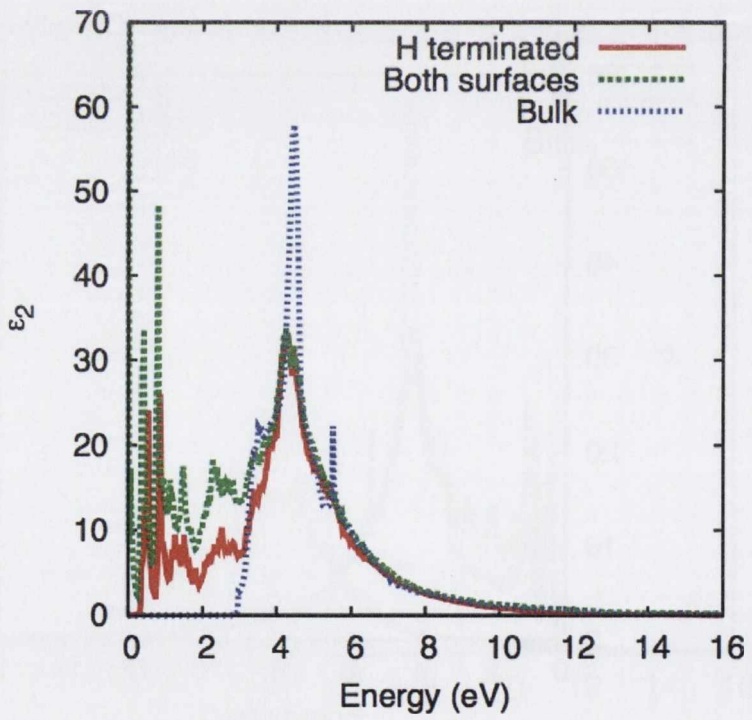


Figure 4.26: Comparison between the imaginary part of calculated dielectric functions of the KK structure (one Si adatom per (5×4) unit cell) with single (red) and double (green dashed) surfaces, and electric field aligned perpendicular to the Au chains. It also shows the bulk dielectric function (blue dashed).

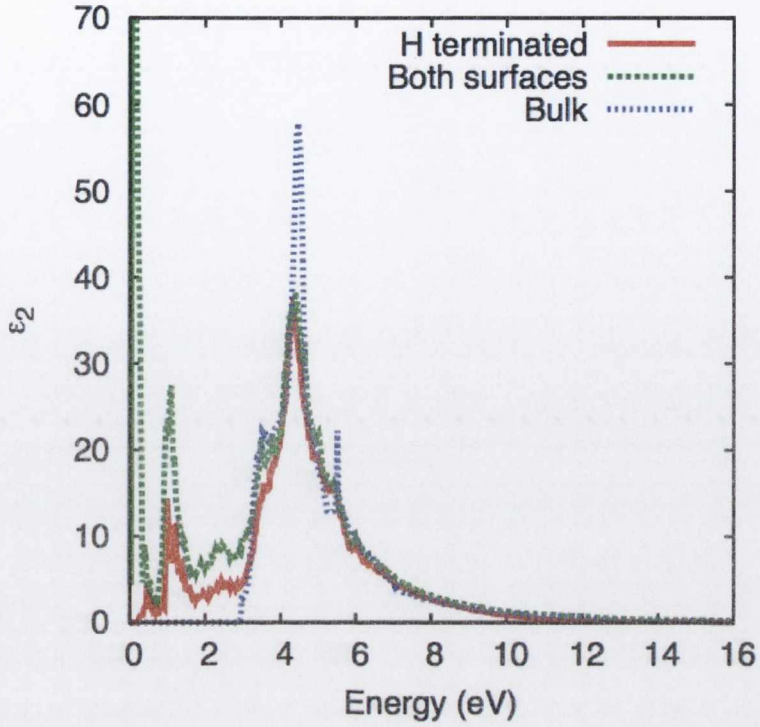


Figure 4.27: Comparison between the imaginary part of calculated dielectric functions of the KK structure (one Si adatom per (5×4) unit cell) with single (red) and double (green dashed) surfaces and electric field aligned parallel to the Au chains, along with the bulk dielectric function (blue dashed).

Figures 4.22 and 4.23 show the imaginary part of the dielectric functions, calculated in two perpendicular directions, and the RA spectra of the EBH model with one adatom per (5×4) unit cell. ϵ_2 has a peak at around 0.5 eV when the electric field is parallel to Au chains, while it is featureless over 2.0 eV. ϵ_2 calculated with the electric field perpendicular to the Au chains is full of structure which produces negative peaks in the RA spectrum. The large positive peak at around 0.7 eV in the RA spectrum can be attributed to the transitions between the occupied states, mainly localised on the left Au atoms, and occupied and unoccupied states, mainly localised on the Au atoms in AuS, right Au, and left Si atoms. The small positive peak at around 1.2 eV arises due to the transitions between occupied states, mainly localised on the Au atoms in AuS and the right Si atoms, occupied and unoccupied states, mainly localised on the left Si and right Au atoms, and unoccupied states, mainly localised on the Si atoms in Si HC. The small nega-

tive peak at around 1.4 eV comes from the transitions between occupied states, mainly localised on the Au atoms in AuS, and left Au and Si atoms, occupied and unoccupied states, mainly localised on the right Au atoms and unoccupied states, mainly localised on the Si atoms in Si HC. Another small peak around at 2.0 eV results from the transitions between occupied states, mainly localised on the left Si atoms, occupied and unoccupied states, mainly localised on the Au atoms in AuS, and unoccupied states, mainly localised on the Si atoms in Si HC. The calculated RA spectrum is compared with experiment and also a recent calculation [251] of the EBH model using DFT-LDA. The previously calculated RA spectrum is shifted by +0.5 eV in Ref. [251] to resolve the underestimated band gap problem in DFT-LDA. The overall agreement between their calculation and experiment is very good, when it is recalled that changes in reflectivity of a few percent are being measured. The large positive peak is attributed to transitions between Au dimer states and the broad negative peak is attributed to transitions between Si atoms in Si HC in that calculation. Overall agreement between the hybrid DFT calculation and experiment is less impressive.

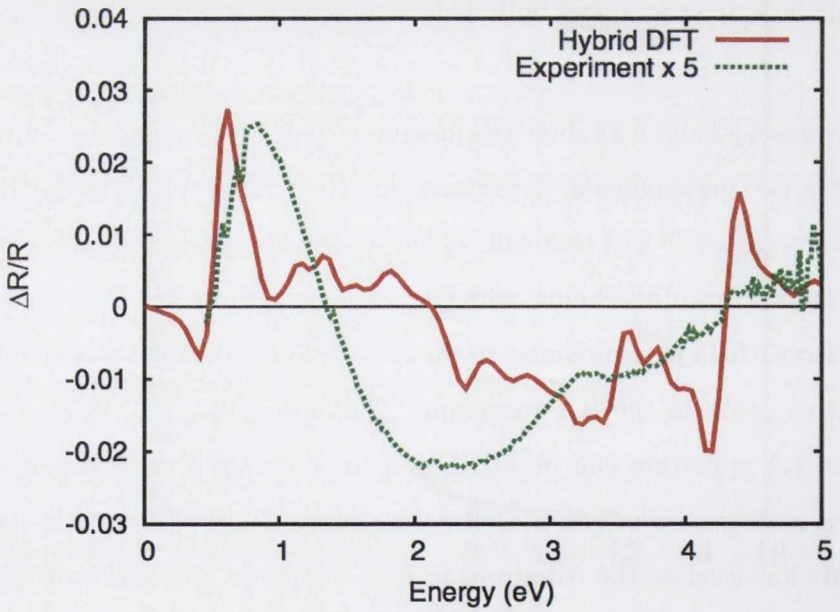


Figure 4.28: Comparison between calculated (red) and experimental (green dashed) RA spectra of the KK structure (one Si adatom per (5 × 4) unit cell). The RA spectrum of the (5 × 4) surface with 0.5 ML Si adatom coverage was scaled ×5 to compare with the calculation.

Figures 4.24 and 4.25 show the calculated imaginary part of dielectric function and the RA spectra of the KK structure of Si(5 × 2)-Au with no adatom coverage. Above 1.2 eV, ϵ_2, calculated with the electric field aligned perpendicular to the Au chains (E_x), is quite featureless in comparison to the parallel direction (E_y). The RA spectrum of this surface has two minima below 1 eV. The first one occurs at around 0.49 eV, which has contributions from transitions between occupied states mainly localised on right Au atoms and left Si atoms. The other one comes from transitions between occupied and unoccupied states, mainly localised on left and right Si atoms, and right Au atoms and occupied states localised mainly on left Si atoms and Si atoms in Si HC. The large positive peak at around 1.1 eV has contributions from transitions between occupied and unoccupied states mainly localised on the left and right Au atoms and unoccupied states localised mainly on Si atoms in Si HC. The small peak at around 1.8 eV has contributions from transitions between occupied states mainly localised on Si left atoms, and unoccupied states mainly localised on the bulk Si atoms. The negative maximum at around 2.1 eV has contributions from transitions between occupied states mainly localised on left and right Si atoms, Au atoms and Au chain, and unoccupied states localised mainly on Si atoms in Si HC. The agreement between experiment and calculation is poor.

The imaginary part of dielectric functions and RA spectra calculated for the adatom decorated KK model are shown in Figs. 4.26, 4.27, and 4.28. The slab dielectric functions were calculated with a single reconstructed surface, the other surface being hydrogen terminated, and also with double reconstructed surfaces. From the figures it can be seen the surface optical response is larger for the slab, which has double reconstructed surfaces, as both surfaces are contributing in the dielectric functions. The calculated RA spectrum is compared with experiment in Fig. 4.28. There is a weak negative minimum at ~0.4 eV which has contributions coming from the transitions between occupied and unoccupied states, mainly localised on the Au chain and right Si atoms beside the Au chain. The large positive peak at ~0.6 eV has contributions from the transitions between the occupied and unoccupied states, mainly localised on Au chain, Si atoms in Si

HC, left Au atoms, and right and left Si atoms beside the Au chain. Three little distinct positive humps between 1.1-2.0 eV energy range are resulting from same kind of transitions as the large peak, except the transitions responsible for the hump at ~1.3 eV also include some bulk states. Below 3 eV, the RA spectrum of the KK model with adatom produces slightly better agreement with experiment than the equivalent EBH model, but no definitive conclusions can be drawn from the optical spectra.

4.3 Discussion and conclusion

Hybrid DFT calculations were performed for two well studied surfaces: Si(111)-(2 × 1) and Si(111)-(5 × 2), using a Fock exchange potential with 5 % weight. This particular weighting provided good agreement with the experimental static dielectric constant of bulk Si, as discussed earlier. Using this weight, bond lengths and electronic structures for ±MP chain models were calculated and found to be in good agreement with previous calculations and experiments. However, the lowest energy structure in this work differs from the previous calculations. With very small energy difference between -MP and +MP structures, it is difficult to say which one has the lowest total energy. Two surface states were identified which are mainly localised on the Si atoms in the π chain. The HOMO-LUMO gaps and optical gaps are found to be in reasonable agreement with previous studies.

Optical calculations done on the Si(111)-(2 × 1) surface show large low energy peaks for ±MP structures, which were attributed to surface state transitions. The intense peaks were explained using transition momentum matrices. The calculated RA spectra are in excellent agreement with experiment.

Using the same Fock exchange weight the EBH, AN and KK models were optimised (details of calculations are described in Appendix A). While the EBH and KK models were fully optimised, the SCF calculations did not converge for the AN model, which results in the exclusion of this structure. The optimised

surface atomic structures are in reasonable agreement with previous data. One of the main structural units in both surfaces reported here is a $SiAu_4$ butterfly-wing motif, along with the well accepted Si HC structure. The structural change due to Si adatom decoration is clearly visible for the EBH and KK models.

The electronic structures for two different models were calculated which indicate that without Si adatoms, the Si(111)-(5×2)-Au surface is metallic, which is consistent with previous calculations. Adatom decoration did not open any gap around E_F for the EBH model. Gap opening occurred in the KK model when it was decorated with 0.5 ML adatoms coverage, which is evidence in favour of the KK model. Also, the ARPES data agree the best with the electronic structure of the adatom decorated KK model.

RA spectra were calculated for the EBH and KK models, with and without adatoms. None gave better agreement than the other. The best agreement with experiment was produced by recent DFT-LDA RA spectra calculations of the EBH model [251]. In that calculation it was argued that the experimental RA spectra is a collective optical response from the small clean and adatom decorated domains. This could not be explored here due to the complexity of the system and limited computational resource.

Considering the overall situation it can be said, in agreement with some of the latest calculations, that the KK model with 0.7 ML Au atom coverage is the most likely model at present, though the agreement with the RA spectrum is still to be achieved. However, more work is needed, as none of the models is conclusive. Though an attempt is made here to identify the transitions responsible for different peaks below 2.5 eV in RA spectra, more investigation is needed to understand the effects of different structural units on the optical transitions. A potential future project is a theoretical study on the effect of adatom coverage variation on the RA spectra, which was reported to be very dramatic by a previous experiment [112].

Chapter 5

Si(110)

5.1 Native-oxide-covered Si(110)

Careful alignment of all optical components is essential if differences in signal of <1 in 10^4 are to be detected. Native-oxide-covered Si(110) is commonly used as a test sample, as it is readily available and has a large RA signal. Measurement of the RA spectrum of an in situ sample in a UHV system is made through a strain-relieved fused silica window. However, any kind of window, whether it is glass or fused silica, adds some strain to the measurement. In order to correct for the strain signal, a measurement can be made with the sample at 45^o, where there is no sample signal. Alternatively, measurements at 0^o and 90^o give an equal and opposite sample response (Fig. 5.1), and adding these signals together leaves a residual of twice the strain response. Figure 5.1(c) corresponds to 45^o to the vertical position. Figure 5.2 shows a typical window strain signal, measured directly (45^o) and indirectly ($\frac{1}{2}[0^o + 90^o]$). It can be seen that both approaches give the same result. All the RA spectra presented are corrected for window strain.

Fig. 5.3 shows the corrected RA spectra for the native oxide covered Si(110) for its positive and negative maximum positions. It also shows the corrected and inverted RA spectra for the negative maximum position. It can be seen that positive and inverted negative maximum RA spectra agree very well. This confirms

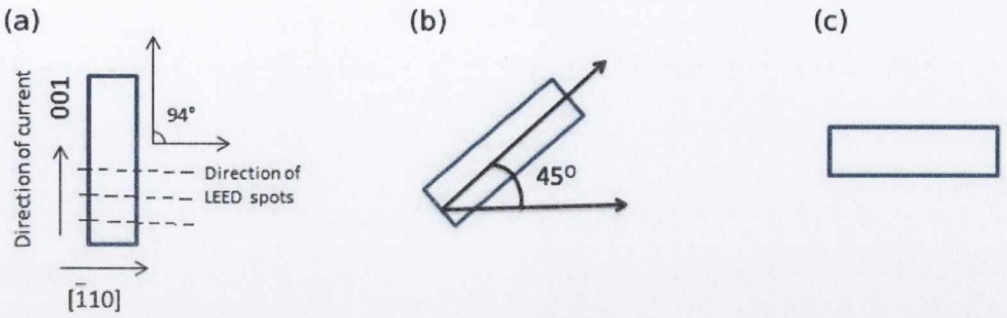


Figure 5.1: Various positions of the sample and direction of LEED pattern of clean single domain (16 × 2) surface. (a), (b) and (c) show negative maximum, zero and positive maximum positions, respectively.

that the window strain correction is effective and that the optical components are well aligned. The spectrum in Fig. 5.3 agrees well with previous work [4]. The spectrum has two positive peaks (at 3.40 and 4.22 eV) and one negative peak (at 3.22 eV), above 3 eV, all associated with the bulk optical response [3]. There is no peak under 3 eV, which is consistent with the native-oxide-covered Si(110) having no surface states in the band gap.

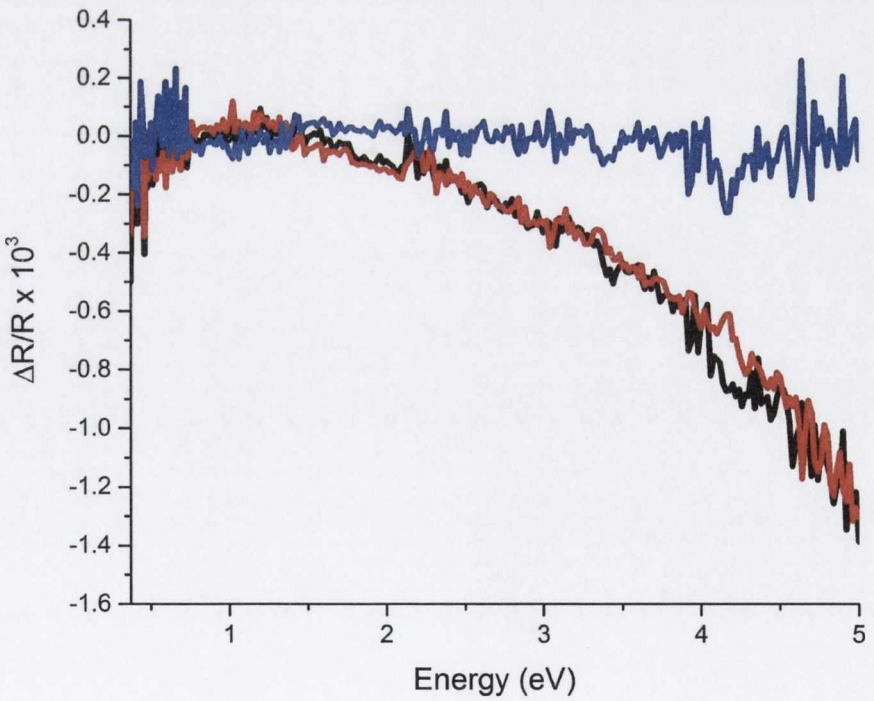


Figure 5.2: A typical window strain signal measured directly (45^o, black line), indirectly ($\frac{1}{2}[0^o + 90^o]$) (red line), and the difference (blue line).

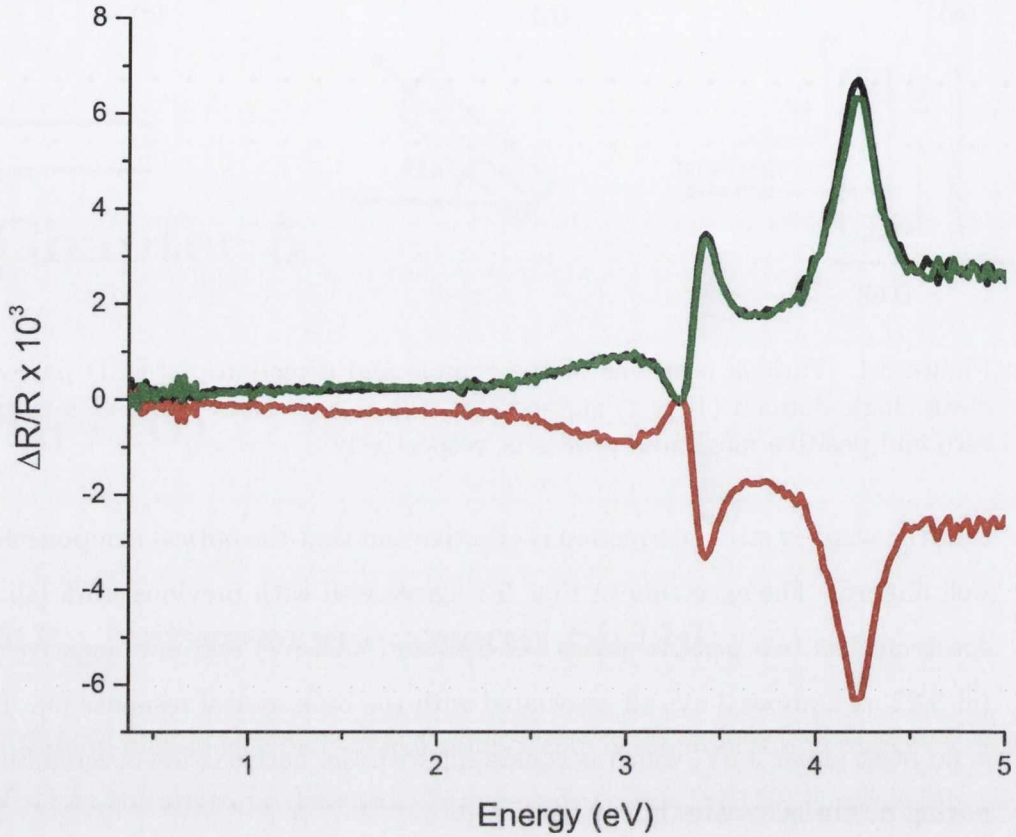


Figure 5.3: Comparison between the positive, negative and inverted negative maximum RA spectra of native oxide covered Si(110). All of them are corrected for the window strain. The black, red and green lines are positive, negative and inverted negative maximum RA spectra, respectively.

5.2 Experiment

The Si(110) sample was degassed as discussed in Chapter 3. The sample was then aligned and set at its positive maximum position. The sample was heated, manually, using the procedure of Sakamoto *et al* [114], as discussed in Chapter 3. After this short heating of the sample, the RA spectrum (Fig. 5.5), which is discussed later in Sec. 5.3, was measured without moving the sample. The LEED image was taken (Fig. 5.4) and typically showed a double domain (16×2) surface. Repeating this procedure a number of times occasionally produced a single domain surface, aligned in one of the double domain directions.

In order to obtain a single domain (16 × 2) structure more reliably the long heating procedure described by Yokoyama *et al* [253] was used (Chapter 3). A single domain structure was generally obtained, as confirmed by LEED. Both procedures desorb the native oxide layer and leave a clean, well-ordered surface, as confirmed by LEED and AES. The same LEED images were found over the whole sample surface. The sample was also rotated azimuthally from 0^o to 100^o and RA spectra were taken every 5^o to investigate the position of the surface optic axes.

The long term behaviour of the samples in UHV was observed to be strikingly different, depending on the preparation procedure. The more reliable long heating procedure produced a stable single domain structure. If the short heating procedure produced a single domain structure, this was observed to revert to a double domain structure after a few hours. This was not affected by the background pressure in the UHV system or by exposing the surface to 10^{-6} mbar of hydrogen. It is possible that the short heating process leaves more strain in the surface, which drives double domain formation, but the mobility of Si atoms in the surface region at room temperature necessary to accomplish this, is significant.

5.3 Clean double domain (16 × 2) surface

The LEED image and the RA spectrum of clean double domain (16 × 2) surface are shown in Fig. 5.4 and 5.5, respectively. Comparison of the native-oxide-covered RA spectrum with the double domain response shows new surface featured between 1.0 and 2.5 eV. This is expected, as the two domains are aligned at 110^o with each other. If they were exactly at 90^o to each other the surface response would cancel out. It can be seen that the clean surface response differs at higher energy, mainly in the form of a surface contribution.

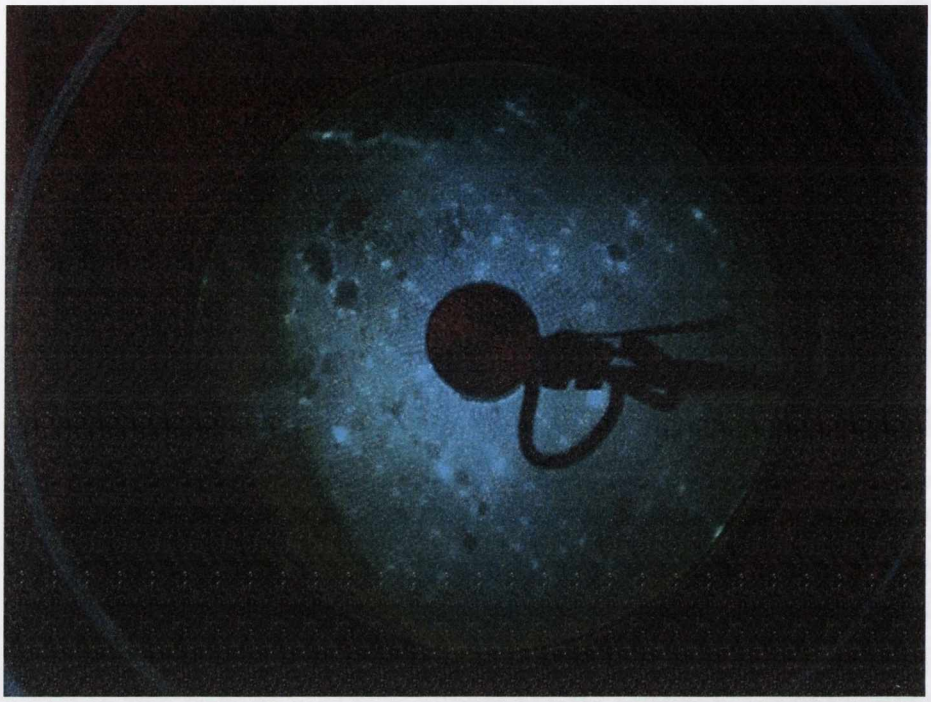


Figure 5.4: LEED pattern of the clean double domain (16 × 2) surface taken at 72.1 eV.

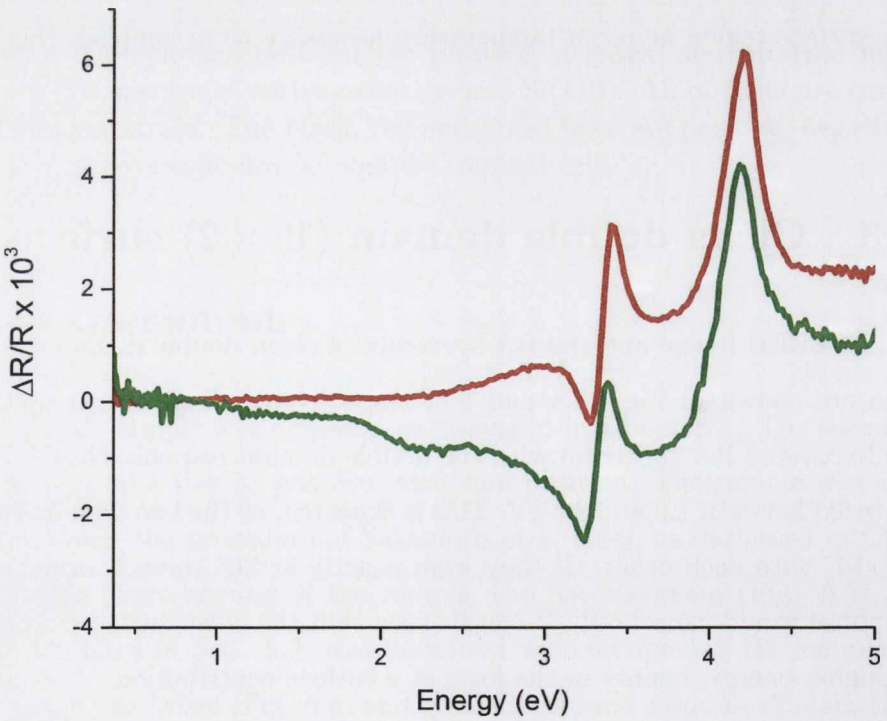


Figure 5.5: Comparison between RA spectra of native oxide covered Si(110) (red) and clean double domain (16 × 2) structure (green).

5.4 Clean single domain (16×2) surface

A single domain surface allows the full symmetry of the structure to be explored. Fig. 5.6 is the LEED image of a clean single domain (16×2) surface. The sample is at positive maximum position. The LEED spots are arranged in arrays which are at 94^o from the vertical position (Fig. 5.1(a)) of the sample. Comparison of Figs. 5.4 and 5.6 shows that the single domain does not form along either of the domain directions of Fig. 5.4, but rather with $16\times$ spots running close to the $[\bar{1}10]$ direction, almost exactly between the array of the double domain structure. The direction differs from that found by Yokohama *et al.* [253] by $\sim 30^o$. While Shakamoto *et al.* [114] produced with opposite domain, with $16\times$ spots along $[\bar{1}1\bar{1}]$, by DC heating along $[1\bar{1}2](the direction of the arrays), orthogonal to the 16\times$ spots. It was argued that EM produced this domain. The direction of the DC heating used here was along [001] and the $16\times$ spots are close to $[\bar{1}10]$, the orthogonal direction (Fig. 5.6). It appears possible that EM plays a dominant role in the direction of domain formation on this surface.

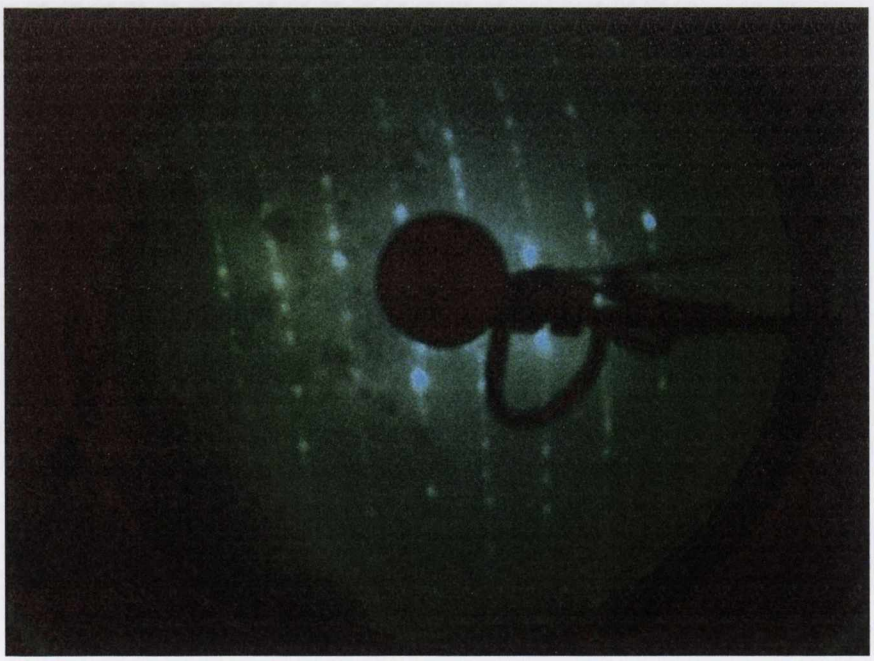


Figure 5.6: LEED image of the single domain surface taken at 78.9 eV after overnight heating.

After taking the LEED image, the RA spectrum was measured in the same

sample position. The RA spectrum is shown in Fig. ??. The features of the RA spectra below 3 eV are now much more prominent, as expected from a single domain structure, and the background change is larger. The surface features are broad, with a positive going peak at 1.8 eV, and negative going peaks at 1.4 eV and 2.3 eV.

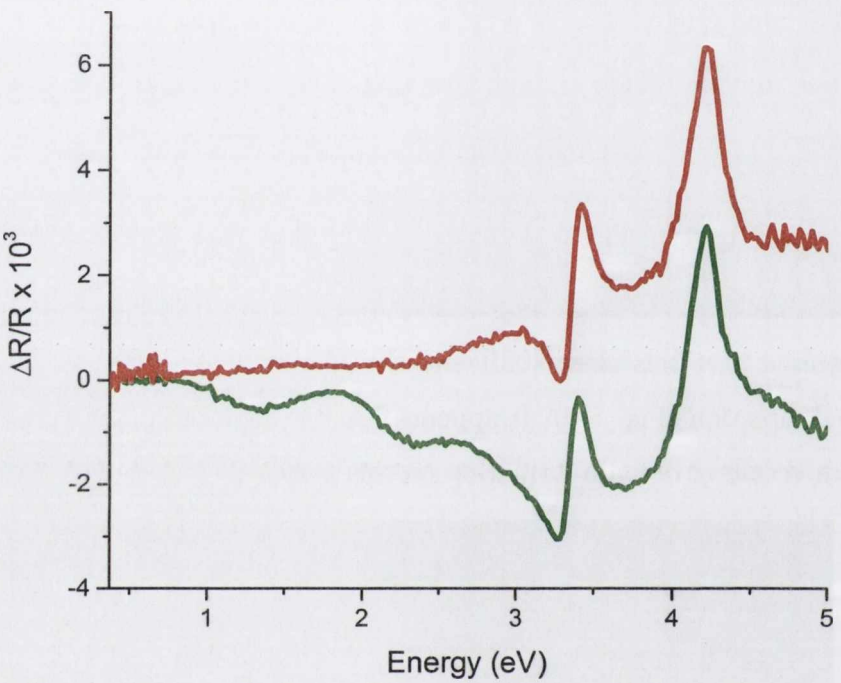


Figure 5.7: Comparison between the RA spectra of native oxide covered Si(110) sample (red) and after heating the sample over night (green).

5.4.1 Investigating the optic axes of the (16×2) surface

The sample was rotated in steps of 5^o and RA spectra were taken after every step, the LEED pattern being checked regularly to see if the surface was changing to double domain. All the RA spectra are plotted in Fig. 5.8. From the figure it can be seen that the peaks at different energies are changing with angle. The RAS values of the peaks at 1.36, 1.78, 3.28 and 4.22 eV were plotted as function of angle and fitted with a cosine curve as shown in Figs. 5.9 to 5.12. The data were fitted to $y = y_0 + Acos[2(\phi - \phi_0)]$, where ϕ is the azimuthal angle relative to

a principal crystallographic axis and ϕ_0 is the optic axis direction in the surface plane [13]. If ϕ_0=0, the optic axis is aligned with the crystallographic axis and the null occurs at 45^o, as discussed previously. In case of lower energy peaks (for 1.36 and 1.78 eV), which are a surface response, the signal is small and the points are scattered (Fig. 5.9 and 5.10), resulting in significantly larger error estimates for these features in Table 5.1. The values of ϕ_0 along with their error values, rounded up to whole numbers, are shown in Table 5.1. Table 5.1 shows that all the ϕ_0 values are clustered around zero degrees. Allowing for the error in the fit, this is good evidence that both the bulk and surface optic axes are aligned along $[1\bar{1}0]$ and [001]. This is the expected result for the bulk [3], but is a new result for surface optical transitions.

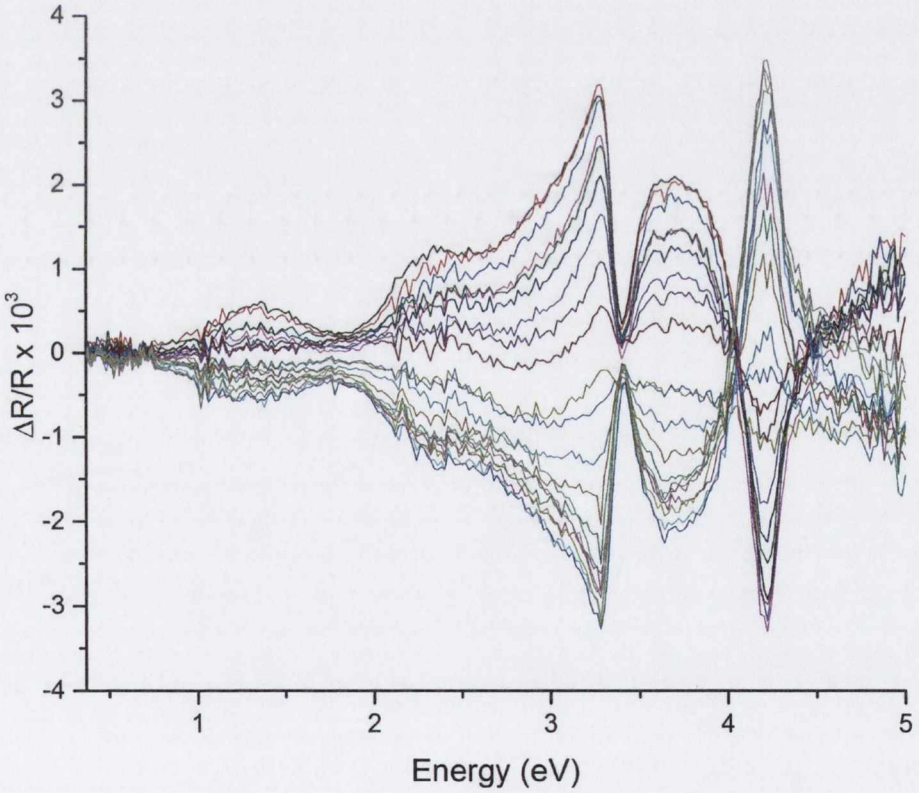


Figure 5.8: RA spectra of single domain Si(110)-(16 × 2), as a function of azimuthal angle.

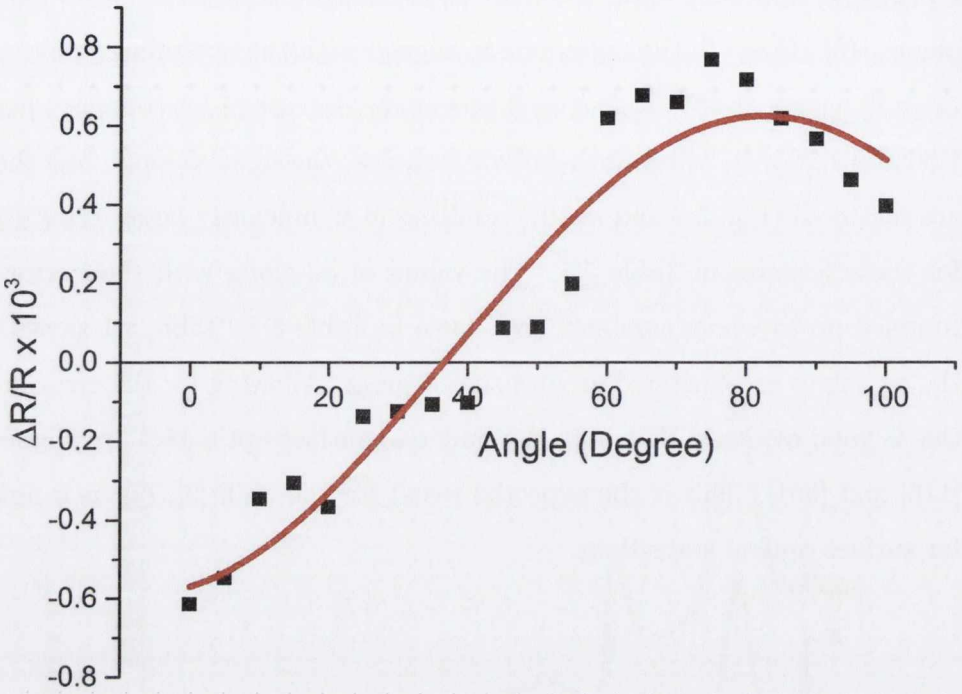


Figure 5.9: RAS values at 1.36 eV are plotted with varying angle and fitted with cosine curve.

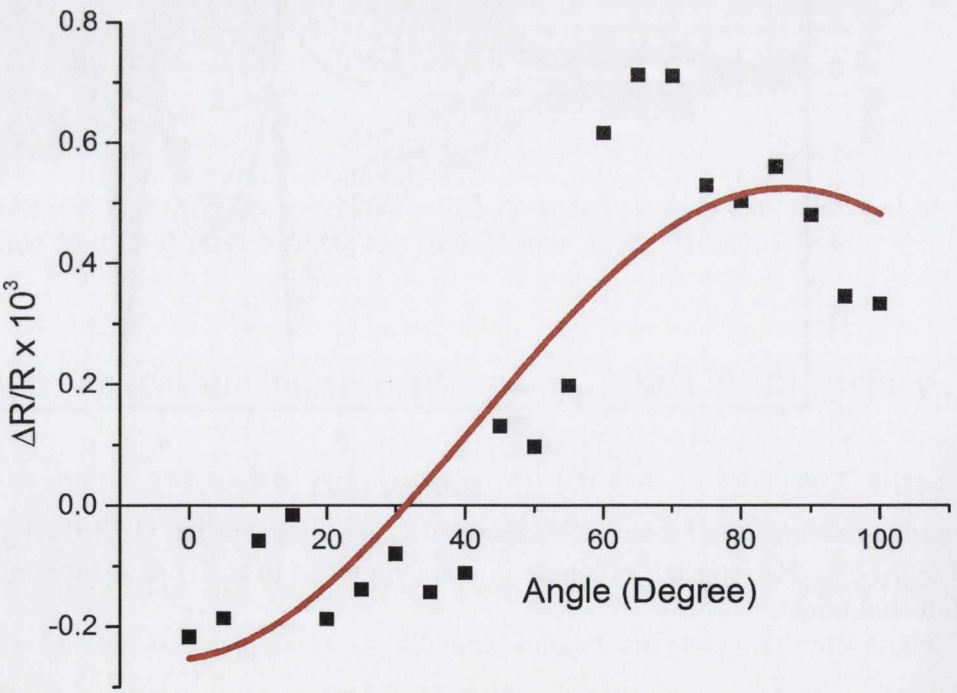


Figure 5.10: RAS values at 1.78 eV are plotted with varying angle and fitted with cosine curve.

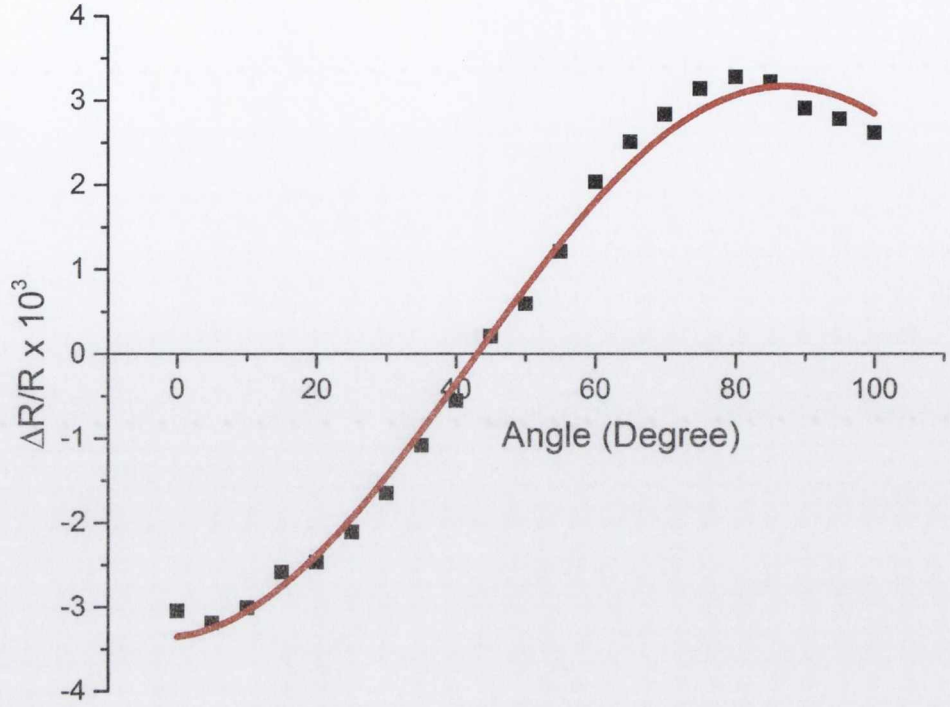


Figure 5.11: RAS values at 3.28 eV are plotted with varying angle and fitted with cosine curve.

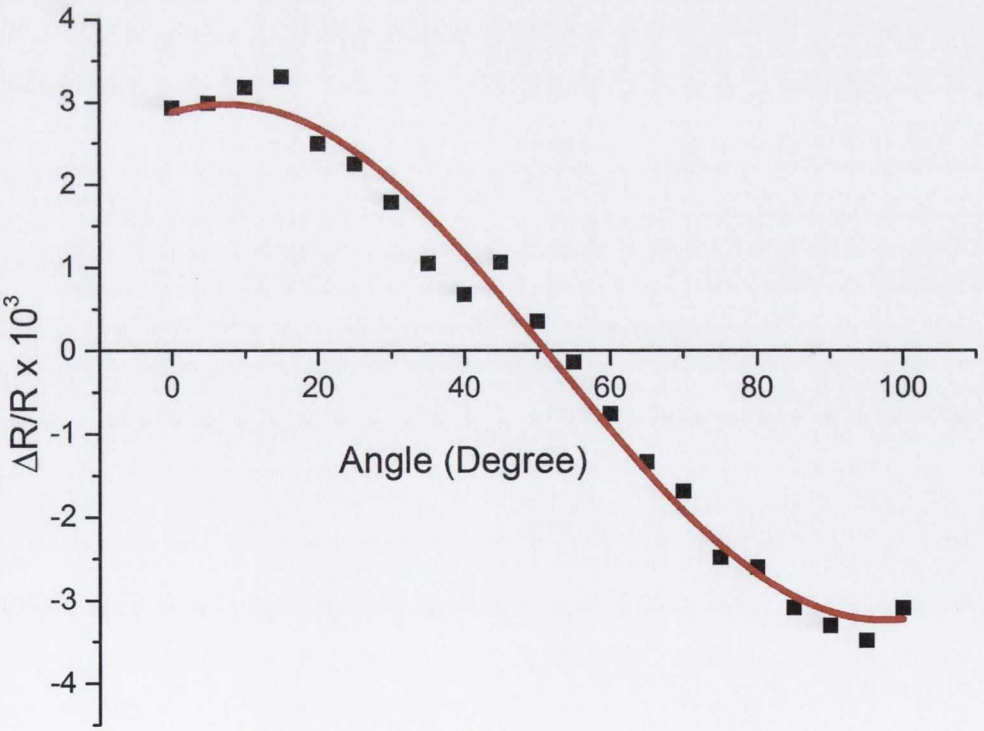


Figure 5.12: RAS values at 4.22 eV are plotted with varying angle and fitted with cosine curve.

Table 5.1: Values of ϕ_0 with its error at different energies.

Energy(eV)	ϕ_0(degree)	Error
1.36	-8	± 3
1.78	-4	± 6
3.28	-3	± 1
4.22	+7	± 2

5.5 *Ab initio* calculation of Si(110)-(16×2)

Structural coordinates were taken form the ATI model of Ref. [254]. The supercell consists of only 3 layers of Si atoms beneath the reconstructed surface, being limited by the surface size of the unit cell. The other side of the slab was terminated by H atoms (Fig. 5.13). Due to the limitation of computational power the structure could not be fully optimised in total energy calculations. The value of the lattice constant, used, is 5.431 Å. Other details of the calculation may be found in Appendix A. As the structure was not fully optimised it is not possible to compare the bond lengths of the surface atoms or step width of the substrate with previous literature. The surface has steps in $[\bar{1}10]$ direction. Four adatoms with a substrate atom make bonds to form pentamer like structures. There is a Si atom in the centre of the pentamer and is coordinated with five Si atoms in the pentamer. Two adatoms are situated close to a pentamer.

Using the partially optimised ATI structure, the dielectric function for the slab was calculated. From Fig. 5.14 it can be seen that the imaginary part of the dielectric functions have large number of low energy structures consistent with previous ARPES work, which found many states in the bulk band gap [114]. The region over 3 eV matches very poorly with the bulk dielectric function. This is because a sufficiently thick slab could not be used to get the bulk contribution. Using the dielectric functions, the RA spectrum was calculated and compared with the single domain Si(110)-(16×2) experimental result (Fig. 5.16). The bulk contribution is largely absent in the calculation, as expected, while there is much more low energy structure than is observed in the experiment. This disagreement is mainly because of the inability to obtain and fully optimise the correct

structure. This, together with calculated response a factor of 50 larger than the experimental result, indicates that this calculation was of limited value.

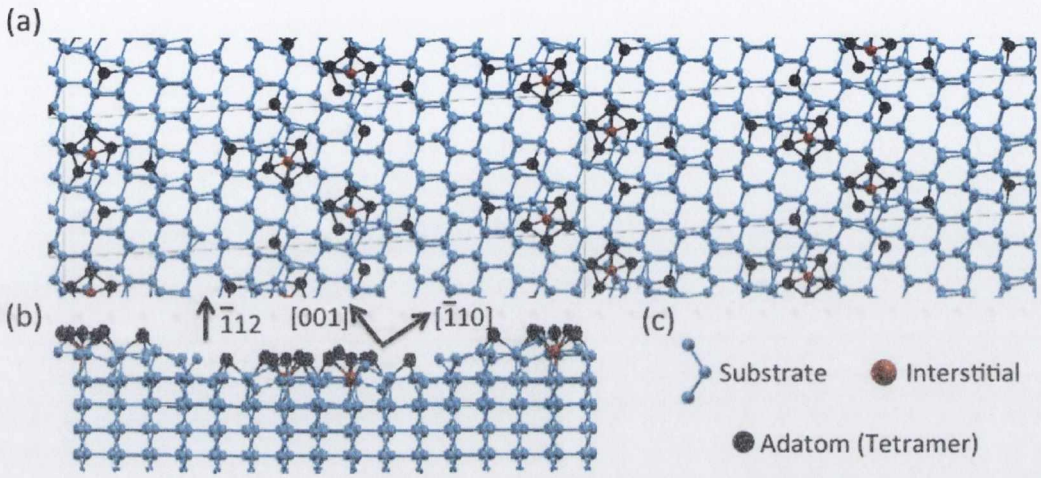


Figure 5.13: (a) Top and (b) side views of ATI model [254] along with the different directions. (c) Different Si atoms are shown in different colours. Black atoms represent adatoms in tetramers and other sites. Blue and red atoms are Si atoms from substrate and interstitial atoms, respectively.

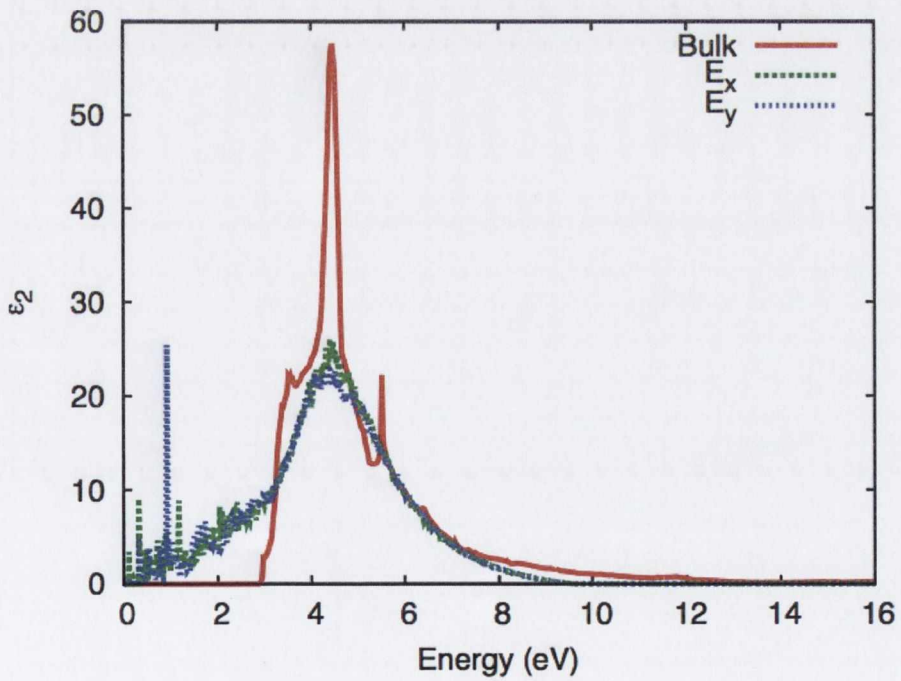


Figure 5.14: The calculated imaginary part of Si(110)-(16 × 2) and bulk Si. The red line is the bulk dielectric function of Si. Green and blue dashed lines are the Si(111)-(16 × 2) dielectric functions with electric fields in [$\bar{1}\bar{1}$] (E_x) and [$\bar{1}$12] (E_y) directions, respectively.

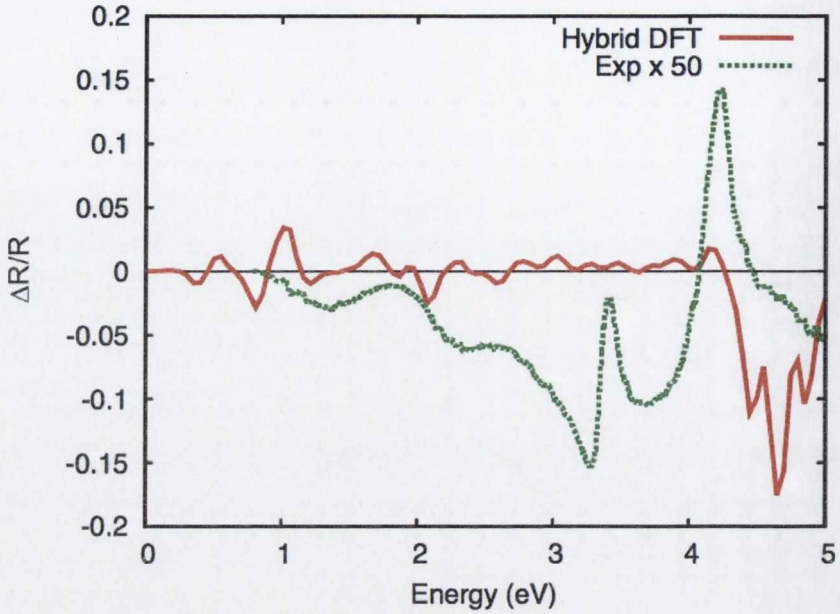


Figure 5.15: Comparison between experimental and calculated RA spectra for Si(110)-(16 × 2) surface. Experimental values were scaled ×50 to compare with calculation.

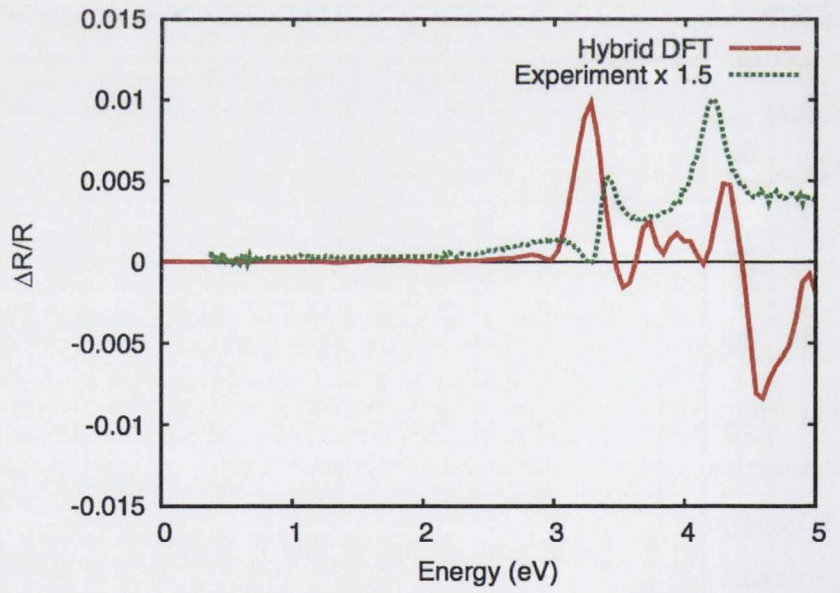


Figure 5.16: Comparison between measured RA spectrum of native oxide layered Si(110) (green dashed line) and calculated RA spectrum for H terminated Si(110)-(1 × 1) slab (red line). The measured values are scaled ×1.5 to compare with calculation.

The size of the unit cell of the Si(110)-(16 × 2) structure is clearly a problem and so the RA spectrum of unreconstructed Si(110)-(1 × 1) was calculated. The

structure was terminated at the top and bottom surfaces of a slab, which consists of 8 bi-layers of Si atoms, with H atoms. After optimising the slab the RA spectrum was calculated (Fig. 5.15). Though the peak positions in experiment and calculation between 3.0 and 3.6 eV are a little different they have same signs. There is a major difference at 4.5 eV (probably due to low k-point density), indicating that an improvement in calculating the bulk response is needed.

5.6 Discussion and conclusion

The clean Si(110) surface remains the only lower index surface of Si whose structure is controversial. The complexity of the (16 × 2) reconstruction appears to exceed even that of the Si(111)-(7 × 7) reconstruction [255]. Single domain surfaces are necessary to explore the full symmetry of the structure, but it is clear that EM associated with DC resistive heating affects the orientation of the single domain with respect to the bulk crystal. Also, under preparation conditions involving shorter heating times, the single domain structure can change to a double domain structure over a period of a few hours at room temperature. Strain driving the migration of Si atoms appears to be a possible explanation.

RA spectra showed surface contributions below 3 eV but, given the richness of the features in the various models of the (16 × 2) structure, the lack of sharp features is disappointing. Azimuthal rotation studies show that the optical axes of these features aligned with the bulk optical axes.

The (16 × 2) structure, with its complex reconstruction, proved to be too challenging for *ab initio* calculations with the computational power available. It is clear that partial optimisation of the structure is not sufficient, and the RA spectrum of H-terminated Si(110)-(1 × 1), which produced much better results overall, indicated that there were still issues with the bulk Si optical response of energies above 4 eV. It appears that the complexity of the (16 × 2) structure is such that the an order-of-magnitude increase in computing power is needed, even with hybrid DFT.

Chapter 6

Ge(001)

6.1 Experiment

Clean, ordered Ge(001) surfaces were prepared by etching and annealing [38, 130, 146] as discussed in Chapter 3. The wafer offcut towards <111> produced a double domain surface whereas; the wafer off cut towards <110> produced a single domain (2 × 1) surface in agreement with previous work [22]. LEED images for both double and single domain surfaces are shown in Figs. 6.1 and 6.2, respectively. In both the cases the splitting of the (0, 0) LEED spot and the half order spots indicated the presence of ordered steps and a preferred dimer orientation parallel to the step edges, for offset samples. The average terrace width for double height steps, is ∼50 Å, which results in a smearing of spots in the sample direction and the spot splitting is happening due to the small domain size across the terrace, and defects such as step edge kinks.

High purity Sb (99.9999 % purity) was deposited onto the clean and ordered substrate using the MBE method discussed in Chapter 3. The substrate was then annealed at 680 K for 15 min to desorb excess Sb [39], producing a reasonably well-ordered (2×1) LEED pattern (Fig 6.3). From the LEED images of clean (Fig. 6.2) and Sb-deposited (Fig. 6.3) Ge(001) it is clear that the dimer orientations are the same for both cases, parallel to the steps and perpendicular to the [110] direction (Fig. 6.4).

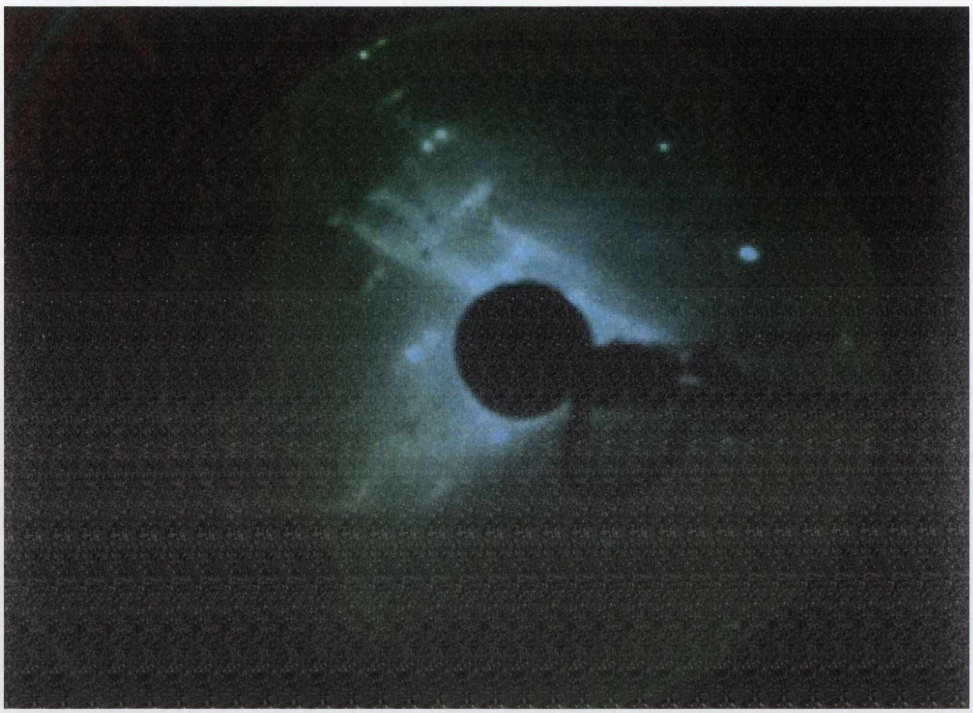


Figure 6.1: Double domain (2 × 1) LEED image of the clean Ge(001) surface with offcut towards <111>, taken at 133.2 eV. The spot splittings are along the direction of the step edges.

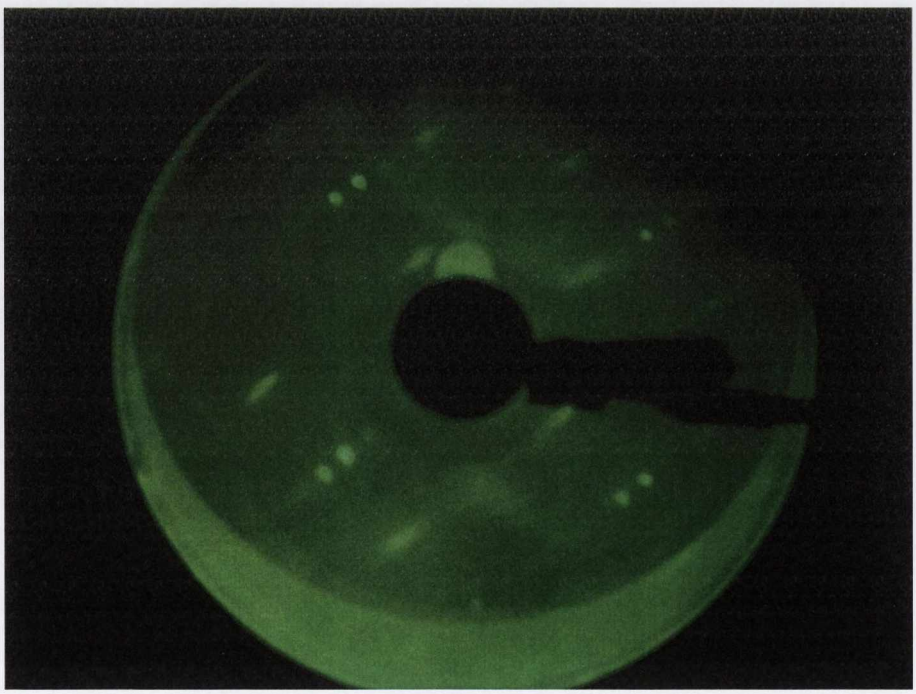


Figure 6.2: Predominantly single domain (2 × 1) LEED image of clean Ge(001) surface, offcut towards <110>, taken at 136.8 eV. The spot splittings are shown along the direction of the step edges.

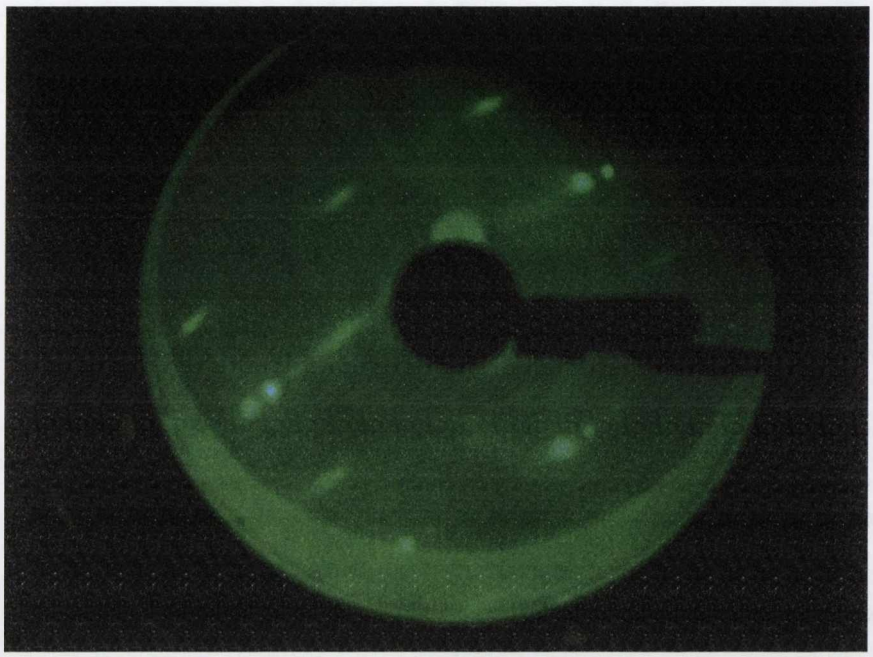


Figure 6.3: Predominantly single domain (2×1) LEED image of Sb deposited on Ge(001) surface, offcut towards <110>, taken at 115.7 eV. The spot splittings are shown along the direction of the step edges.

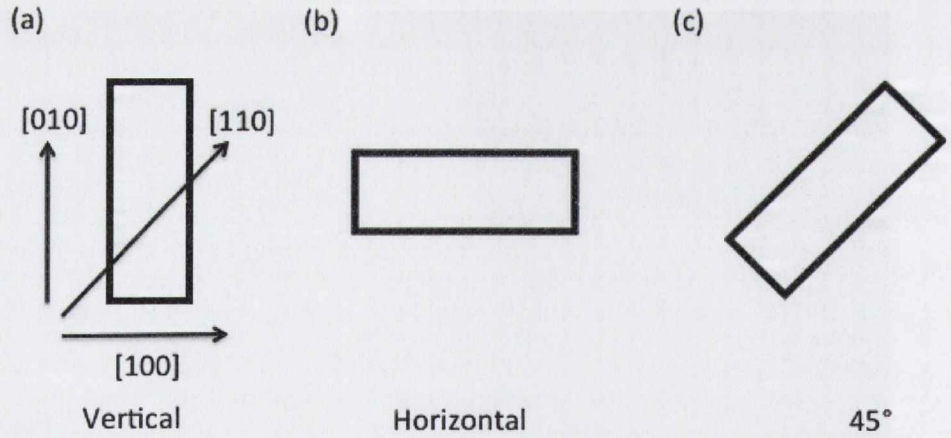


Figure 6.4: Sample positions ((a) vertical, (b) horizontal, and (c) 45^o) with respect to principal axes directions. The substrate is 6^o offcut towards <110>.

After preparation of both clean and Sb deposited Ge(001) surfaces RA responses were measured for each case. The RA responses were measured for the sample at vertical, horizontal and 45^o angles (Fig. 6.4), to determine the window strain as was discussed in chapter 5. Window strain was always subtracted from

the original data.

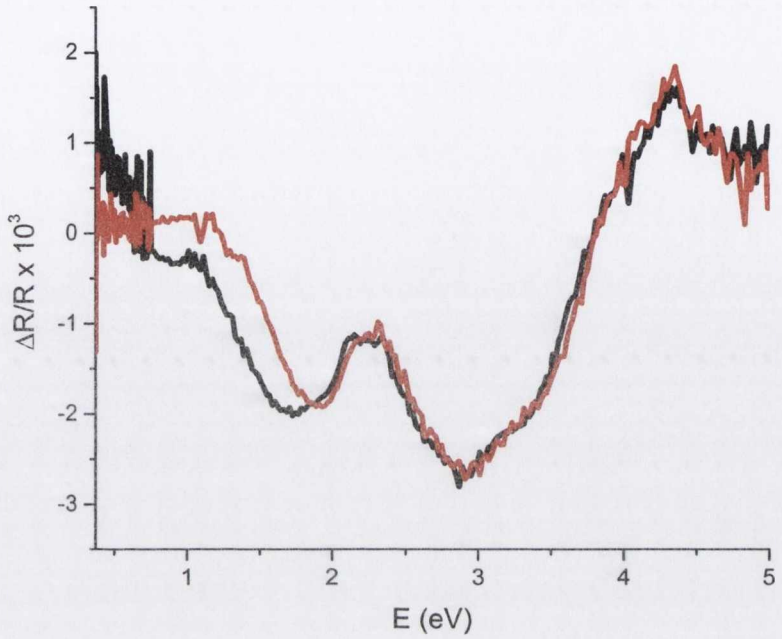


Figure 6.5: Comparison between RA spectra measured from clean Ge(001) samples, offcuts towards <111> (red line) and <110> (black line), which produced double and single domain, respectively. The double domain response was scaled $\times 1.7$ for comparison.

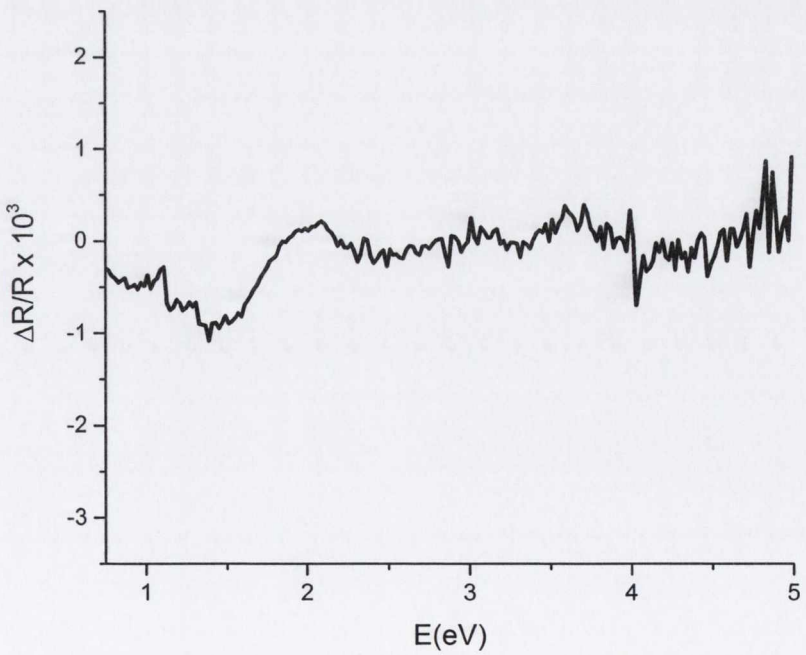


Figure 6.6: Difference between RA spectra of single and double domain clean Ge(001) surfaces.

Figure 6.5 shows a comparison between the RA spectra of clean single and double domain Ge(001)-(2×1) surfaces. The RA response from the double domain surface is scaled ×1.7 to compare with that of single domain surface.It is clear from Figs. 6.5 and 6.6 that the only significant differences occur below 2 eV, the latter one is the difference between RA spectra of single and double domain clean Ge(001) surfaces. The effect of the double domain surface is to eliminate the (2×1) surface contribution from RA spectra [12]. The structure above 2 eV is the signature of 6^o offcut bulk Ge, with no significant surface contribution.

6.2 *Ab initio* calculations

6.2.1 Equilibrium structures of clean Ge(001)

Clean Ge(001) reconstructed surfaces have a small number of atoms in an unit cell and their structures are well accepted, allows new approaches to calculating their electronic and optical properties to be tested. In this work asymmetric dimer structures were assumed for all clean Ge(001) surfaces, as reported previously [38, 132, 136–139]. Figs. 6.7, 6.8 and 6.9 show the superstructures along with the underlying bulk. All the systems contain two reconstructed surfaces (represented by grey atoms) and 7 Ge bilayers (represented by purple atoms) sandwiched between them. The (2×1), p(2×2) and c(4×2) systems contain 32, 48 and 64 atoms, respectively. Those structures were based on Ref. [151] and relaxed using a modified B3LYP hybrid DFT computation technique, discussed in chapter 2.

The figures show that the (2×1) surface has one Ge-Ge dimer, whereas the p(2×2) and c(4×2) surfaces have two Ge-Ge dimers, per unit cell. The Ge-Ge dimers in (2×1) surfaces are in rows, with all the dimers tilted in the same direction. In the p(2×2) and c(4×2) surfaces, dimers are out of phase with consecutive dimers tilted in opposite directions.

Table 6.1 shows the comparison between bond lengths obtained from SXD and

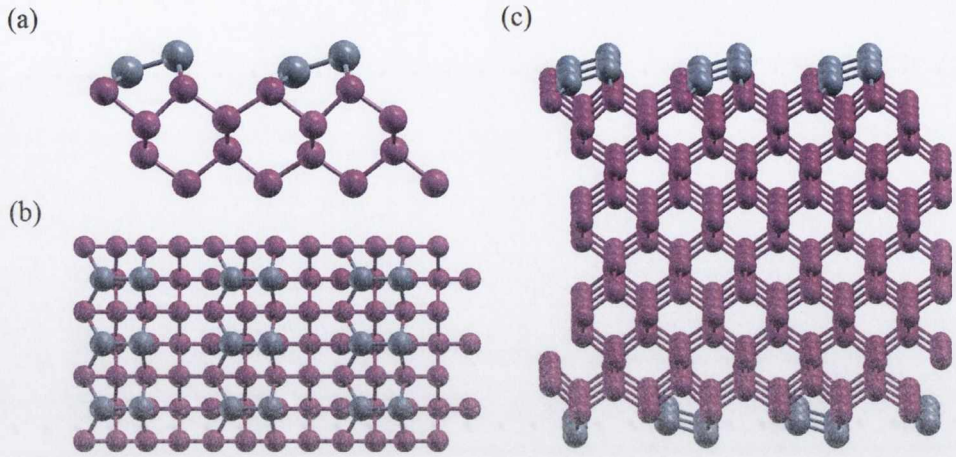


Figure 6.7: Atomic structure of the Ge(001)-(2×1) surface along with its underlying bulk (7 Ge bilayers). (a) and (b) show side and top views, respectively, of Ge dimers with Ge bilayers, (c) shows the full system with optimised geometry. Grey atoms represent surface dimer atoms.

various calculations. The hybrid DFT work here predicts bond lengths of dimers and back bonds almost exactly the same as the SXD experiment [149]. Other DFT studies [154, 155] underestimated dimer distances by up to 5.4%, and back bond distances by up to 0.8%, with respect to SXD.

Table 6.1: Dimer and back bond lengths at the Ge(001)-(2×1) surface in Å.

Method	Dimer distance	Back bond length
SXD[1]	2.55	2.46, 2.57
LDA – DFT[2]	2.48	2.44, 2.53
LDA – DFT[3]	2.41	-
hybridDFT[4]	2.53	2.46,2.57

[1]Ref. [149], [2]Ref. [154], [3]Ref. [155], [4]This work.

Table 6.2: Dimer and back bond lengths at the Ge(001)-c(4×2) surface in Å.

Method	Dimer length	Back bond length
LEED[1]	2.5 ± 0.1	-
LDA – DFT[2]	2.50	2.47, 2.50
hybridDFT[3]	2.59	2.47.2.57

[1]Ref. [150],[2] Ref. [154], [3]This work.

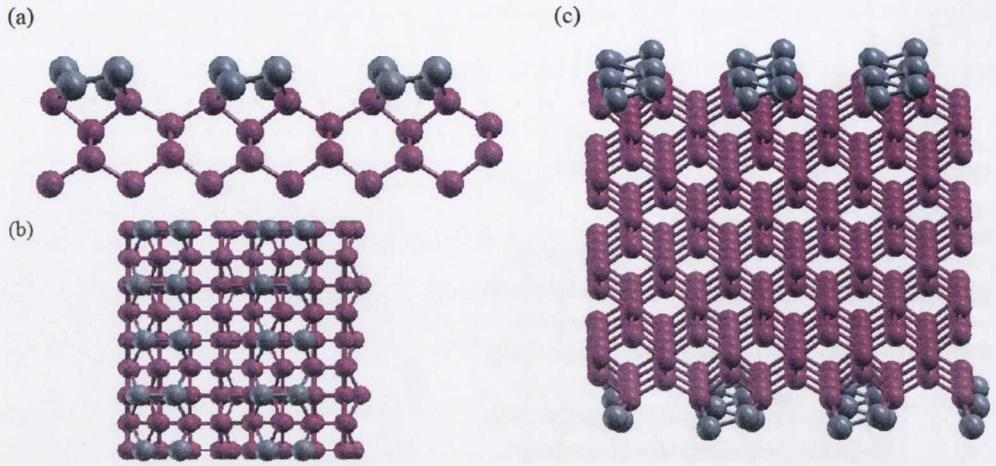


Figure 6.8: Atomic structure of Ge(001)-p(2×2) surface along with its underlying bulk (7 Ge bilayers). (a) and (b) show side and top views, respectively, of Ge dimers with Ge bilayers, (c) shows the full system with its optimised geometry. Grey atoms represent surface atoms.

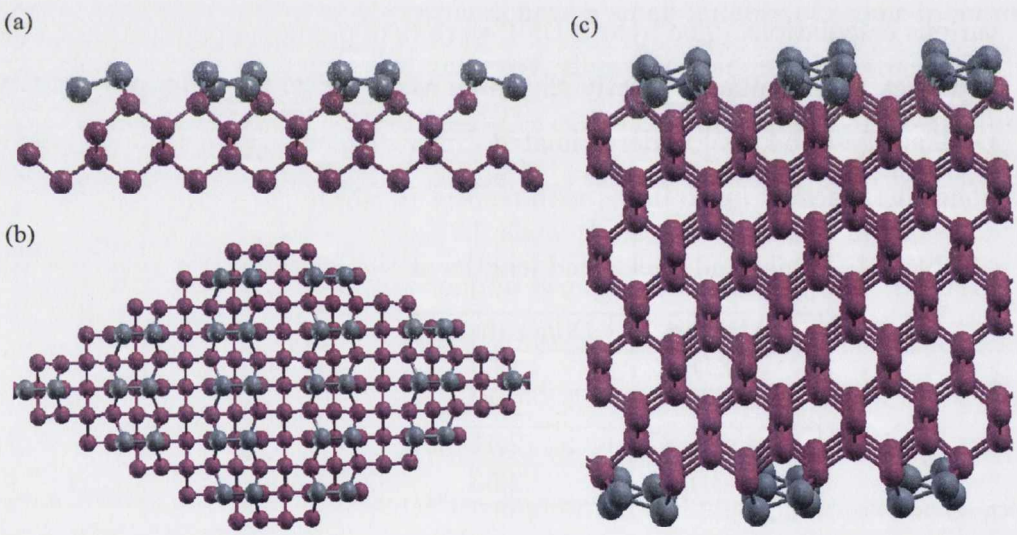


Figure 6.9: Atomic structure of the Ge(001)-c(4 × 2) surface along with its underlying bulk (7 Ge bilayers). (a) and (b) show side and top view, respectively, of Ge dimers with Ge bilayers, (c) shows full system with optimised geometry. Grey atoms represent surface atoms.

For the c(4 × 2) surface a previous DFT calculation [154] is in good agreement with experiment [150] regarding the dimer distance (Table 6.2). The hybrid DFT dimer bond length is 3.6% larger and one of the back bond distances is 2.8%

larger than the previous DFT calculation, but the limited experimental data are such that both calculations are within the experimental error.

6.2.2 Ge(001)-(2 × 1)-Sb

Fig. 6.10 shows the surface structure of Ge(001)-(2 × 1)-Sb along with its bulk. The system also contains 7 Ge bilayers sandwiched between two surface layers of Sb atoms (blue coloured atoms).

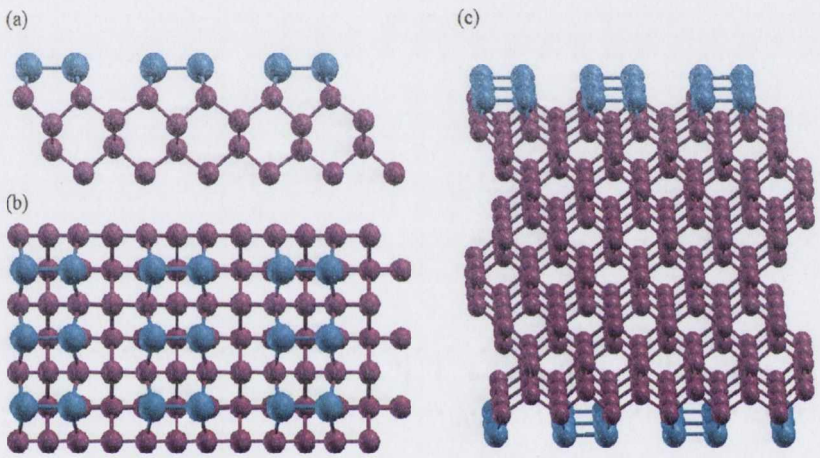


Figure 6.10: Atomic structure of the Ge(001)-(2 × 1)-Sb surface along with its underlying bulk (7 Ge bilayers). (a) and (b) show side and top views, respectively, of Sb dimers with Ge bilayers, (c) shows the full system with optimised geometry. Blue atoms represent surface Sb atoms.

The structure of the Ge(001)-(2 × 1)-Sb surface has been studied by surface X-ray diffraction (SXD) [164] and XSW measurements [39]. In 1992 Lohmeier *et al.*, based on the SXD study, proposed that the Sb dimers formed on Ge(001) are asymmetric with midpoint shifted laterally by 0.16 Å [164]. They also reported the Sb-Sb dimer bond length to be 2.90 Å. Three years later a double domain XSW study [39] reported that Sb atoms form an additional layer on the top of Ge atoms on the Ge(001) surface with Sb-Sb symmetric dimers. According to this study, the Sb-Sb dimers are rotated by 90^o with respect to Ge-Ge dimers, which is consistent with a number of previous studies of Si(001)-(2 × 1)-Sb [256–261].

Here, the LEED images, RA spectra and hybrid DFT calculations of clean and Sb deposited Ge(001) show that the (2 × 1) structures are aligned in the same direction for both the cases, with the dimer bond parallel to the step edges of the vicinal structure.

Table 6.3: Dimer and back bond lengths at the Ge(001)-(2 × 1)-Sb surface in Å.

Method	Dimer distance	Back bond length
SXD[1]	2.90	2.49
XSW[2]	3.06	-
LDA – DFT[3]	2.95	2.62
LDA – DFT[4]	2.94	2.62
hybridDFT[5]	3.00	2.67

[1]Ref. [164], [2]Ref. [39], [3]Ref. [165], [4]Ref. [166], [5]This work.

The hybrid DFT calculations found the Sb dimers to be symmetric, like previous DFT studies [165, 166]. There is general experimental agreement that the Sb dimers are symmetric [256–261]. A SEXAFS study [259] reported the Sb-Sb dimer distance to be 2.88 ± 0.03Å and the Si-Sb back bond distance to be 2.63 ± 0.04 Å on Si(001)-(2 × 1)-Sb surface, while the dimer bond length was reported to be 3.06 Å (Table 6.3) in the XSW study [39]. The bulk bond distances in Si and Ge are 2.35 and 2.45 Å, respectively. Taking the covalent radii from bulk bond distances in Si and Ge and an Sb covalent radius (empirically estimated) of 1.45 Å [262] Sb-Sb dimer, Sb-Si and Sb-Ge back bond distances of 2.90, 2.63 and 2.67 Å are expected at Si and Ge(001)-(2 × 1)-Sb surfaces. The SXD study on Ge(001)-(2 × 1)-Sb surface cited in Table 6.3 predict Sb-Sb dimer distance exactly the same as the sum of the covalent radii of two Sb atoms. However, hybrid DFT and the XSW study predict a value greater than the sum by 0.10 and 0.16 Å, respectively, while two DFT studies [165, 166] reported it less than the sum (Table 6.3). The value of the back bond distance, predicted by previous DFT and SXD studies, is less than the sum of covalent radii of Sb and Ge, while this work reports it exactly the same as the sum. These results are consistent with DFT-LDA generally underestimating bond lengths by ∼1 %

6.3 Band Structure

In this section, electron surface states at clean and Sb-covered Ge(001) surfaces are explored. They have been much less extensively investigated than Si(001) surfaces. Before these calculations the band structure of bulk Ge was calculated and a band gap of 0.64 eV was obtained which is close to experimental value of 0.67 eV [263].

6.3.1 Clean Ge(001)

In 1985 Kevan, with help of high-resolution ARPES and LEED, found a metallic state at the Fermi level [130]. When the sample was cooled below 200 K the metallic state disappeared and LEED images show a transition from a (2×1) to a c(4×2) phase. The metal-semiconductor transition was explained in terms of a metallic state induced by dimer flipping above 200 K. A scanning tunnelling spectroscopy (STS) study reported the co-existence of both (2×1) and c(4×2) domains at room temperature [169]. They also found a metallic state at this temperature and attributed it to dimers flipping. An ARPES study [264] reported that the bottom of conduction (π^*) band is filled above 470 K. Later, Jeon *et al.* [265] concluded that the clean Ge(001) surface is semiconducting at room temperature with a gap of 0.44 eV and the previously reported metallic state, attributed to (2×1) dimers, is weakly visible above room temperature. Further ARPES and LEED studies [266] found that the metallic state has a maximum intensity around 625 K and that it can be explained by thermal occupation of the π^* band derived from (2×1) ordering of asymmetric dimers on the surface.

A combination of DFT and STM was used to claim that the VBM of c(4×2) comes from the back bonds between Ge dimer atoms and the Ge atoms of the next layer [267] with the dimer band being ~0.35 eV lower in energy. Six atomic layers of Ge were used in that work. This claim was contradicted, with the VBM assigned to a bulk state and the back bond state being ~0.4 eV below E_F [268]. The difference arises from the thickness of the slab, which was 10 layers thick for

the later work [268]. It was also found that the dispersion of the top valence band changes quite significantly with the slab thickness [269]. In this work, slabs with 14 atomic layers (7 bilayers) were used, as discussed previously. Fig. 6.11, 6.12 and 6.13 show the real space structures and SBZs of (2×2) and $c(4\times2)$ unit cells, and the electronic structures of asymmetric (2×1), $p(2 \times 2)$ and $c(4 \times 2)$ clean surfaces. Calculations for all phases except the $c(4 \times 2)$ phase were performed using a (2×2) real space unit cell to allow comparison of band dispersions. Each (2×2) or $c(4 \times 2)$ surface unit cell contains two dimers. The clean surfaces therefore have two occupied and two empty surface states.

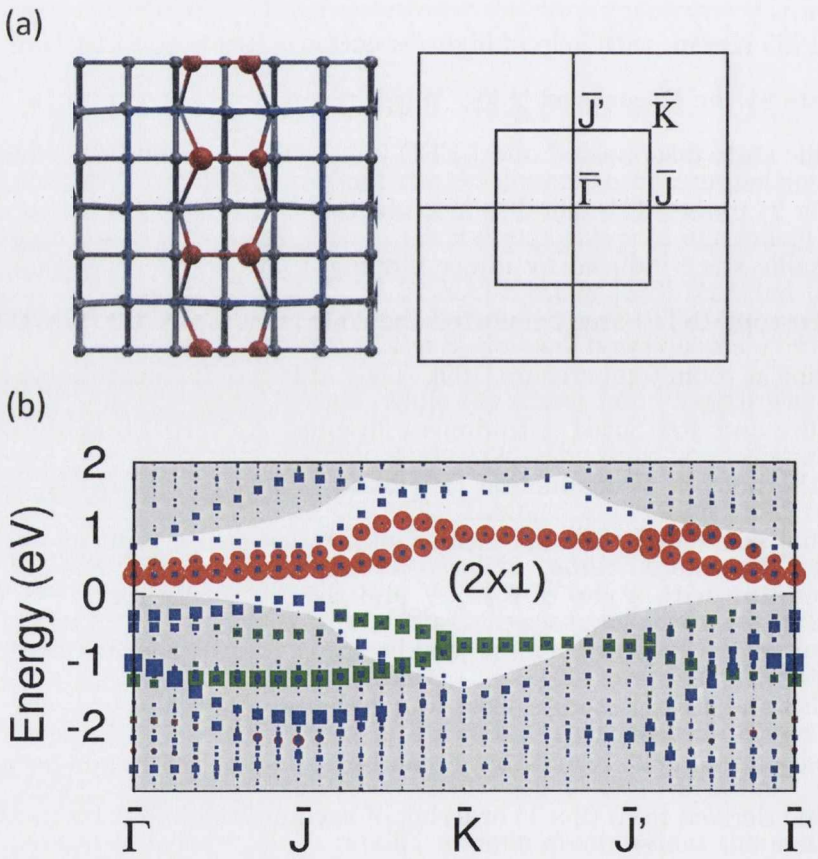


Figure 6.11: (a) Dimer structure of the Ge(001)-$p(2 \times 2)$ clean surface and the (2×2) SBZ, (b) electronic structure of the asymmetric (2×1) clean surface. The surface unit cell of (2×1) structure has been doubled to a (2×2) supercell. Surface band structure is projected onto the Ge dimer atoms and Ge atoms bonded to dimer atoms. The bulk Ge band structure projected onto the SBZ is shown by shading. Band projections onto clean surface dimer up (down) atoms are shown as green squares (red circles), and Ge atoms bonded to dimer atoms are shown as blue squares. In this and subsequent band structures, the size of symbols reflect the degree of localisation on surface atoms.

Table 6.4: Band gaps of clean Ge(001) surfaces from hybrid DFT calculations in eV.

Unit cell	Surface band gap at $\overline{\Gamma}$	Surface band gap at $\overline{K}$ or $\overline{Y}$
(2×1)	0.24	1.68
p(2×2)	0.23	1.59
c(4×2)	0.31	1.55

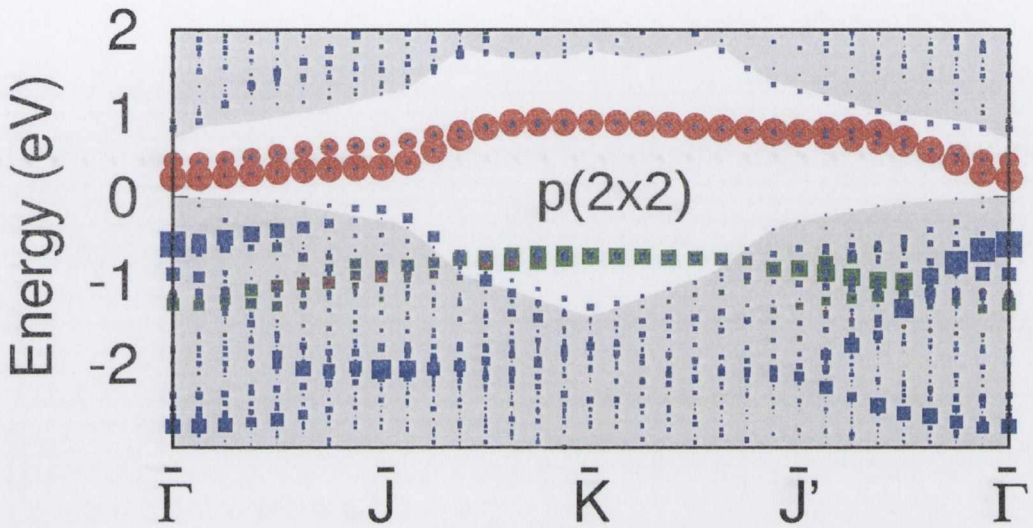


Figure 6.12: Electronic structure of the asymmetric p(2×2) clean surface. Surface band structure is projected onto Ge dimer atoms and Ge atoms bonded to dimer atoms. The bulk Ge band structure projected onto the SBZ is shown by shading. Band projections onto clean surface dimer up (down) atoms are shown as green squares (red circles), Ge atoms bonded to dimer atoms are shown as blue squares.

Figure 6.11 shows the electronic structure of the (2×1) surface. It clearly shows two unoccupied surfaces states (marked by red circles) between $\overline{\Gamma}$ - $\overline{\mathrm{K}}$ and $\overline{\mathrm{J}'}$ - $\overline{\Gamma}$ and they disperse between 0.3-1.1 eV above the VBM, which is a bulk state, in agreement with previous works [268, 270]. The (2×1) phase also has two occupied surface states (marked by green squares) between $\overline{\Gamma}$ - $\overline{\mathrm{K}}$ and $\overline{\mathrm{J}'}$ - $\overline{\Gamma}$, which disperse between 0.2-1.2 eV below the VBM which is very similar to D_{up} state in Ref. [270]. The occupied and unoccupied surface states are coming from the up and down dimer atoms, respectively. Energy states marked as blue squares are associated with the Ge atoms bonded to dimer atoms which are again similar to D_i and D_i^* states described in Ref. [270]. They occur mostly in the bulk band region. The highest occupied surface state disperses in the bulk band region between $\overline{\mathrm{J}'}$-$\overline{\Gamma}$ which is similar to a previous experiment [167] and calculation [271].

Band gaps at two different symmetry points are given in table 6.4. A metallic state, attributed to a flip-flop motion of the dimers [152,169], was not found, but a symmetric p(2 × 2) dimer phase was found to be metallic.

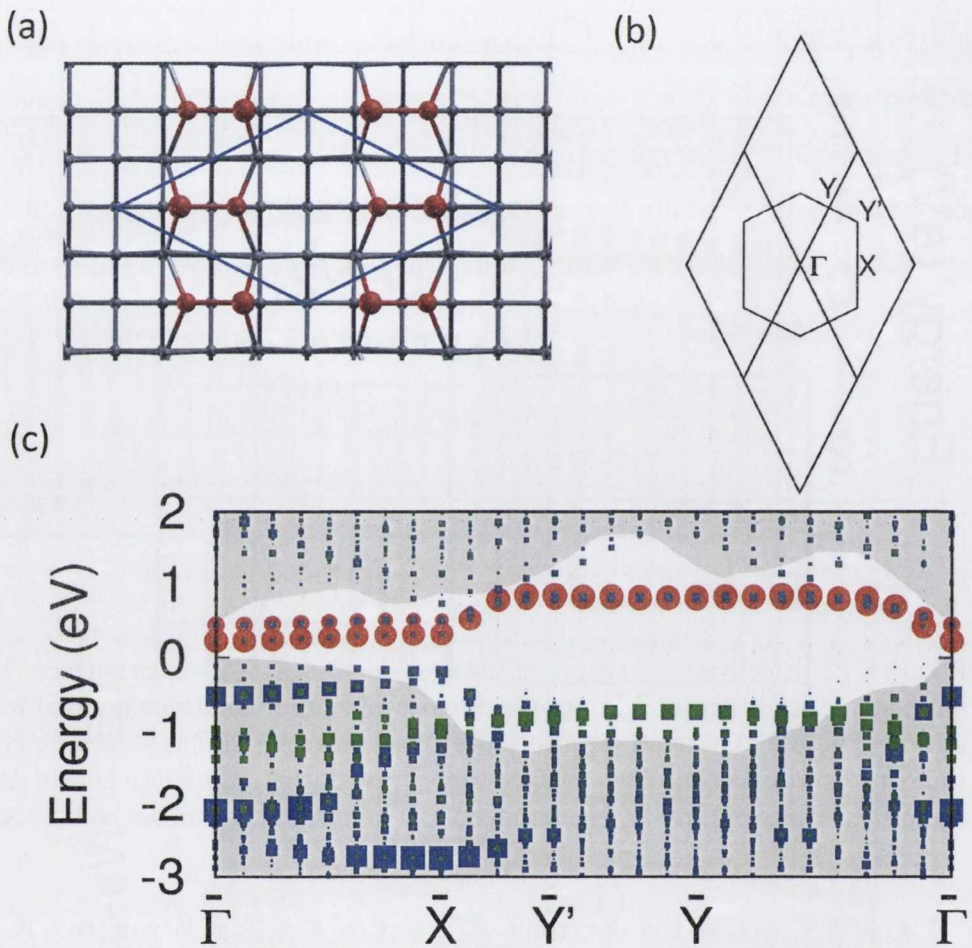


Figure 6.13: (a)Dimer structure, (b) SBZ and (c)electronic structure of the Ge(001)-c(4 × 2) clean surface. Surface band structure is projected onto Ge dimer atoms and Ge atoms bonded to dimer atoms. The bulk Ge band structure projected onto the SBZ is shown by shading. Band projections onto clean surface dimer up (down) atoms are shown as green squares (red circles), Ge atoms bonded to dimer atoms are shown as blue squares.

The electronic structure of p(2 × 2) differs little from that of (2 × 1) (Fig. 6.12). Both occupied and unoccupied states are quite flat and the splitting in these states is not very distinct unlike, (2 × 1) (Fig. 6.11). Also in this case the occupied (red circles) and unoccupied (green squares) states correspond to up and down dimer Ge atoms, respectively and the states marked with blue squares

are coming from the Ge atoms bonded to dimer atoms.

The electronic structure of the clean c(4×2) phase shows very similar dispersion to the p(2 × 2) (Fig. 6.13). The occupied (green squares) and unoccupied (red circles) surface states come from the up and down dimer atoms, respectively, unlike the controversial DFT study discussed previously [267], but in reasonable agreement with Schwingenschlögl *et al.* [170]. The surface band gap at $\overline{\Gamma}$ is 0.31 eV (Table 6.4), which is very close to the surface gap of ~0.44 eV, estimated from ARPES above room temperature, when the lowest empty surface state is populated [265].

Comparing the surface band structures of the Si and Ge clean surfaces, it is found that the band dispersions are similar throughout the SBZ. However, surface band gaps (which occur at $\overline{\Gamma}$) are smaller in the case of Ge (0.2-0.3 eV compared to 0.5-0.6 eV for Si), while energy gaps of occupied and unoccupied dimer states at $\overline{\mathrm{K}}$ (or $\overline{\mathrm{Y}}$ for c(4 × 2)) are larger in the case of Ge (1.5-1.7 eV compared to 1.3-1.5 eV for Si) [272]. Surface state transitions will dominate the RA spectra below the bulk band gap and hence these surface state gaps are expected to be important in the RA spectroscopy of these systems.

6.3.2 Ge(001)-(2 × 1)-Sb

The band structure of Ge(001)-(2 × 1)-Sb is quite different from that of clean Ge surface, with the Sb dimers being symmetric, and the Sb atoms having a dangling lone pair of electrons, which leads to two occupied surface states per Sb atom, and four in total when it forms dimers on the Ge(001) surface.

Figure 6.14 shows the electronic structure of Ge(001)-(2×1)-Sb surface. A pair of nearly degenerate occupied surface states (marked with black solid circles) are localised on the Sb dimer atoms around the $\overline{\mathrm{J}}$ point of the SBZ, nearly 1.5 eV below the VBM. There are two more surface states strongly localised on these atoms around 9 eV below the VBM. There is also a pair of unoccupied surface states on these atoms, just below the conduction band minimum. The states with blue solid squares are localised on the Ge atoms bonded to Sb atoms.

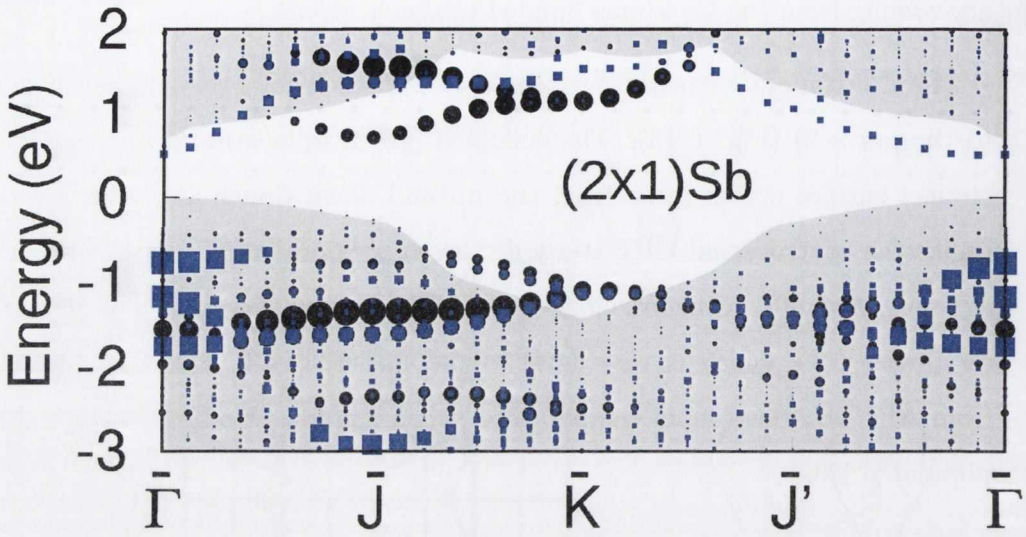


Figure 6.14: Electronic structure of the symmetric (2×1)-Sb surface. The surface unit cell of the (2×1)-Sb structure has been doubled to form a (2×2) supercell. Surface band structure is projected onto Sb dimer atoms and Ge atoms bonded to dimer atoms. The bulk Ge band structure projected onto the SBZ is shown by shading. Sb dimer atoms are shown as black circles and Ge atoms bonded to dimer atoms are shown as blue squares.

6.4 Optical Properties

6.4.1 Bulk Ge

In previous hybrid DFT work on Si(111)-(2×1), a 5% weight for the Fock exchange potential produced very good agreement between the calculated and experimental RA spectra [49]. Here the real and imaginary part of the bulk Ge is calculated using 5% Fock exchange weight. Figure 6.15 shows the real and imaginary part of the bulk dielectric function of Ge. The agreement between theory and experiment [273] is very good. For the imaginary part, the transitions begin at ~0.7 eV which is close to the bulk band gap of 0.74 eV [273]. The use of this weight for the Fock exchange potential again has the effect of correcting the narrow band gaps associated with DFT-LDA.

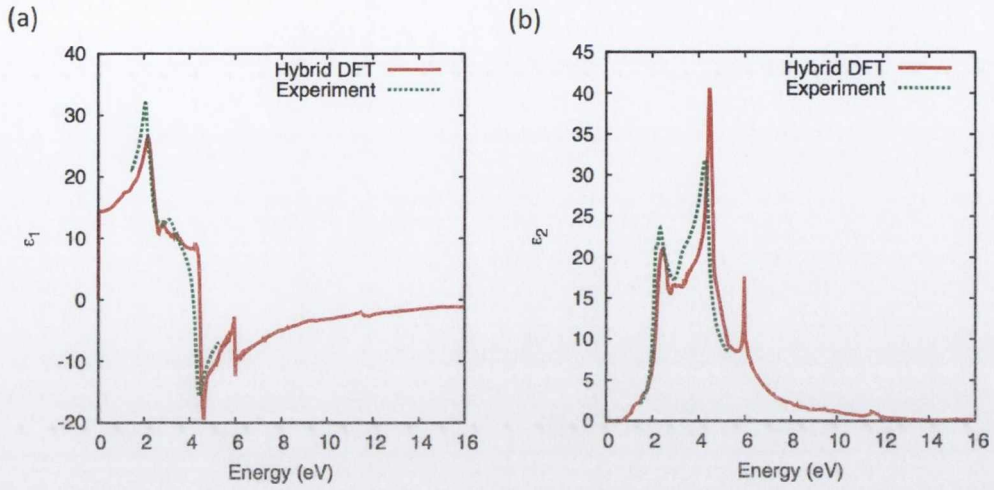


Figure 6.15: (a) Real and (b) imaginary part of the dielectric function of bulk Ge, compared with experimental values. Dashed green and solid red lines represent experiment [273] and theory, respectively.

6.4.2 Clean Ge

The imaginary part of the surface dielectric functions of clean (2×1), p(2×2) and c(4×2) are calculated with electric fields in two perpendicular directions and are compared with the bulk dielectric function of Ge in Figs. 6.16, 6.18, and 6.20. RA spectra of clean Ge(001) surfaces are shown in Figs. 6.17, 6.19 and 6.21. Fig. 6.17 compares calculated RA spectra of clean Ge(001)-(2×1) surface to experimental data for the clean Ge(001) surface from this work and previous works [22,174]. The experimental RA spectrum reported here was obtained from a sample off-cut by 6^o towards [011] direction. The other experimental clean surface spectra were obtained from wafers also offcut 6^o towards [110], but with different preparation processes. They were either prepared by wet etching [274] and annealing, or annealing at 1000 K in an H_2 ambient before a further anneal under N_2 at 573 K to remove the monohydride-H phase from the surface [174]. Previous work cuts off at 1.5 eV, but agreement above this energy is very good for the three independent experiments. The experimental spectra have two minima in the range 1.6-1.8 eV and at 3.0 eV. The maxima occur around 2.2 eV and 4.2 eV, which correspond to E_1 and E_2 critical point transition energies of bulk

Ge. These values are very close to the calculated results of bulk, which produce critical point energies of 2.4 and 4.5 eV (Fig. 6.16).

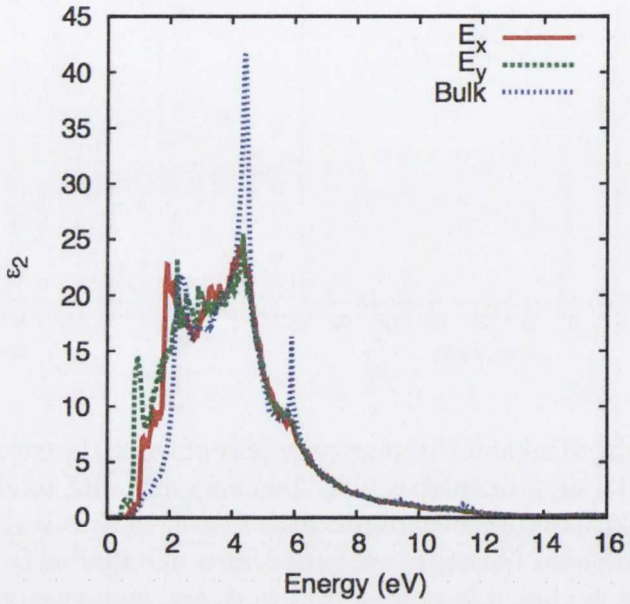


Figure 6.16: Calculated imaginary part of the dielectric function of Ge(001)-(2×1) surface. Red and green dashed lines depict ϵ_2 for the surface with the electric field aligned parallel to the dimer bond (x direction) and dimer row (y direction) directions, respectively. The blue dashed line shows the real part of the calculated bulk dielectric function of Ge.

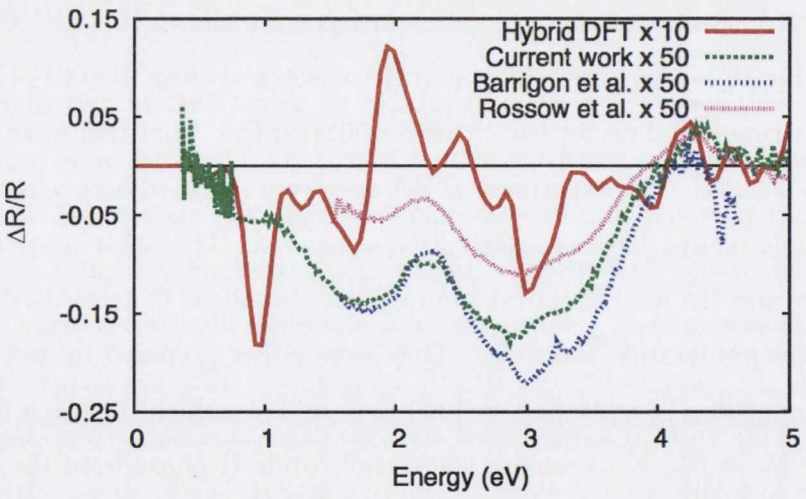


Figure 6.17: RA spectrum of Ge(001)-(2×1). Red and dotted green lines depict the calculation scaled $\times 10$ and experiment scaled by $\times 50$, respectively from this work. Dotted purple and blue lines show the experimental results of Rossow *et al.* [274] and Barrigon *et al.* [174], scaled $\times 50$. Scaling was done for comparison and to make any structure below 1.5 eV larger, in experiment.

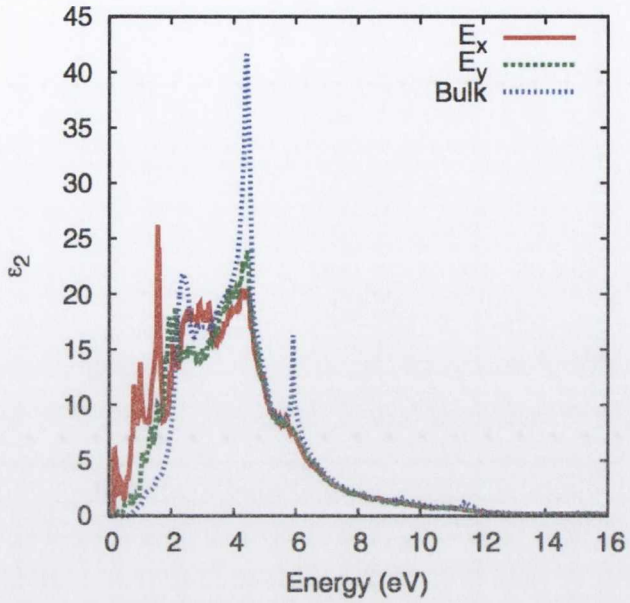


Figure 6.18: Calculated imaginary part of dielectric function of Ge(001)-p(2 × 2) surface. Red and green dashed lines depict ϵ_2 for the surface with electric field aligned in dimer bond (x direction) and dimer row (y direction) directions, respectively. The blue dashed line shows the real part of the calculated bulk dielectric function of Ge.

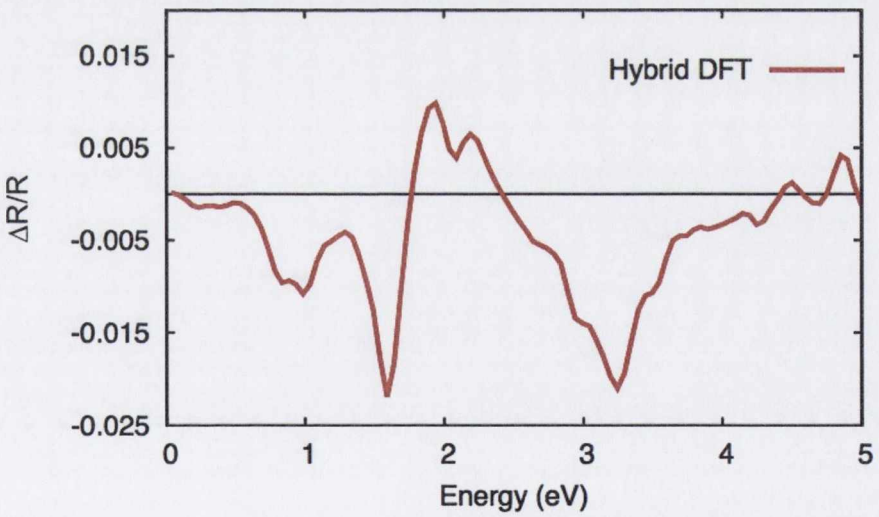


Figure 6.19: Calculated RA spectrum of Ge(001)-p(2 × 2).

The calculated RA spectrum of the clean (2 × 1) surface from hybrid DFT has a large, sharp minimum around 1.0 eV and smaller minimum at 1.6 eV. These energies are above the bulk band gap of ∼0.7 eV, but occur below the calculated

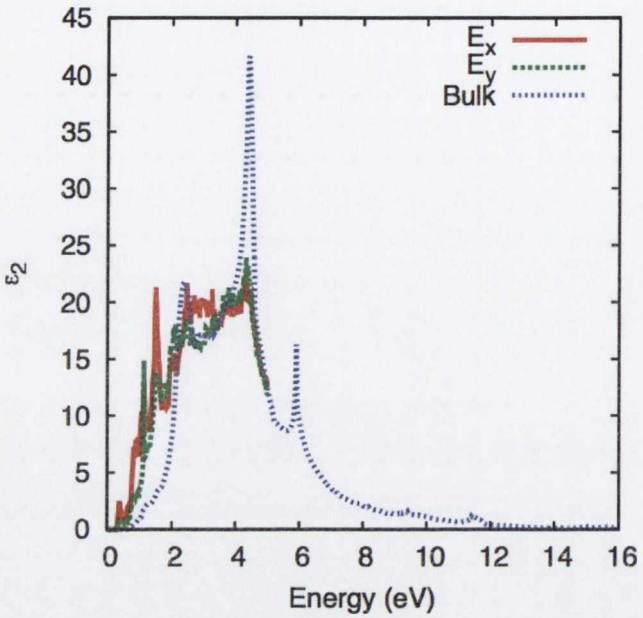


Figure 6.20: Calculated imaginary part of dielectric function of Ge(001)-c(4 × 2) surface. Red and green dashed lines depict ϵ_2 for the surface with electric field aligned in dimer bond (x direction) and dimer row (y direction) directions, respectively. The blue dashed line shows the real part of the calculated bulk dielectric function.

bulk E_1 critical point energy (2.4 eV) in a region where bulk transitions are weak. In this situation, where the real part of the bulk dielectric function is large and slowly varying (Fig. 6.16), maxima and minima in the RA spectrum can be attributed to peaks in the imaginary part of the surface dielectric functions. As surface states mainly localised on Ge back bond atoms lie around 1.0 eV below the unoccupied surface state in the $\overline{\Gamma}$ - $\overline{\mathrm{J}}$ region of the SBZ, the peak at 1.0 eV in RA spectrum can be attributed to transitions between those two energy states. Another minimum at 1.6 eV can be attributed to transitions between occupied-unoccupied dimer atom surface states as the gap between those two states is 1.6 eV. This calculation is quite different from an early *ab initio* MD study [172] ,which has structures with the opposite sign in regions of the spectrum, but very similar with an experimental surface anisotropic dielectric function [270], which has transition peaks at ∼1.2, and 2 eV, coming from Ge dimer transitions and dimer-backbond transitions, respectively. The calculated minimum at 1 eV is absent in measured RA spectra which shows only a little hump at the same

energy. There are few reasons for that; 1) There is a possibility of presence of the other domain rotated by 90^o on the clean surface which is reducing the surface response and 2) possibility of presence of c(4 × 2) unit cell on the clean Ge(001) can not be excluded as well.

The RA spectrum of the p(2 × 2) phase has a very weak minimum at 0.2 eV, while the rest of the RA spectrum looks very similar, except that the intensities of the two minima between 1-1.8 eV are reversed (Fig. 6.19). Figure 6.18 shows bulk and surface dielectric functions for the p(2 × 2) clean surface, where surface state transitions are found at 0.2, 1.0 and 1.6 eV when the electric field is aligned with dimer bonds, while the imaginary part of the dielectric function is relatively featureless when the electric field is aligned with dimer rows. The peaks at 1.0 and 1.6 eV are attributed to the same transitions as (2 × 1). The minimum at 0.2 eV is very weak, due to at least in part to the RA response depending linearly on the spectral energy. The RA spectrum of c(4 × 2) looks quite similar to p(2 × 2) (Fig. 6.21). The peaks below 2.0 eV are attributed to the same transitions as (2 × 1).

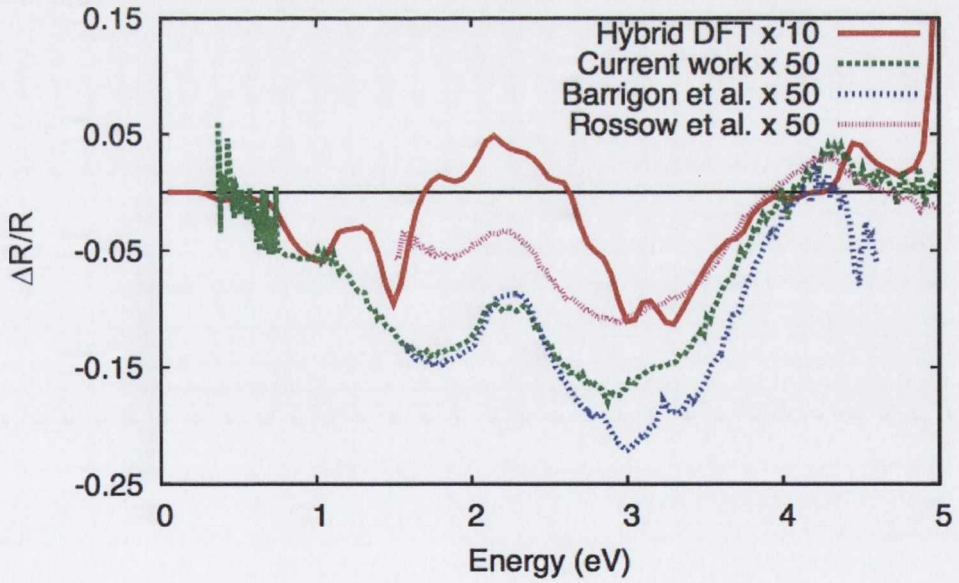


Figure 6.21: RA spectra of Ge(001)-c(4 × 2). Red and dotted green lines depict the calculation scaled ×10 and experiment scaled by ×50, respectively from this work. Dotted purple and blue lines show the experimental results of Rossow *et al.* [274] and Barrigon *et al.* [174], scaled ×50. Scaling was done for comparison and to make any structure below 1.5 eV larger, in experiment.

6.4.3 Ge(001)-(2 × 1)-Sb

The calculated imaginary part of the dielectric function (Fig. 6.22) and the RA spectrum (Fig. 6.23) of the (2 × 1)-Sb surface are very different from the clean surfaces in the region below 2.0 eV and this produces a dramatic change in the RA response, compared to the clean surface, shown in Fig. 6.23. There is a large maximum at ~1.8 eV, which arises from transitions between occupied and unoccupied dimer states. Comparison of Fig. 6.14 with Figs. 6.11-6.13 show that most of the unoccupied dimer states have been moved higher in energy, and some out of the bulk band gap region, resulting in the higher energy optical transitions. A small minimum at ~1.2 eV arises from dimer-backbond transitions. Fig. 6.22 shows that the imaginary part of the dielectric function along the dimer row direction around 1.8 eV is quite featureless, compared to the dimer bond direction.

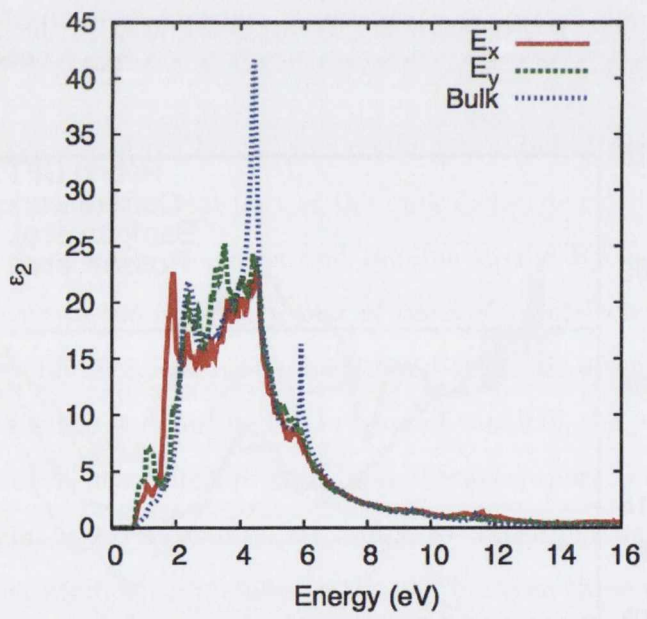


Figure 6.22: Calculated imaginary part of the dielectric function of Ge(001)-(2 × 1)-Sb surface. Red and green dashed lines depict ϵ_2 for the surface with electric field aligned in dimer bond (x direction) and dimer row (y direction) directions, respectively. The blue dashed line shows the real part of the calculated bulk dielectric function.

The RA calculation shows a broad, weak minimum in the spectrum around

1.0 eV, a strong maximum at 1.8 eV, a weaker maximum at 3 eV, and a strong minimum around 3.5 eV. The general share of the (2×1)-Sb spectrum resembles the clean surface spectra above 2.5 eV, for both theory and experiment. Below 2.5 eV, the dramatic change in the RA response on the formation of Sb dimers is well reproduced by the theory, except that the structure is shifted by 0.3-0.4 eV to lower energy, compared to experiment.

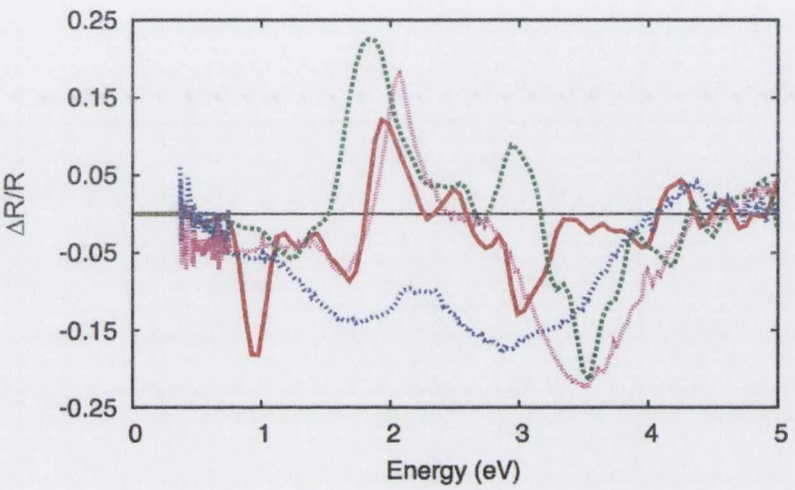


Figure 6.23: RA spectra of Ge(001)-(2×1)-Sb, with clean Ge(001) for comparison. The red line and the dotted blue line show the calculation and experiment, respectively for Ge(001)-(2×1). The green and purple dotted lines show the calculation and experiment for Ge(001)-(2×1)-Sb. The calculated and experimental RA spectra values are scaled $\times 10$ and $\times 50$, respectively. Scaling was done for comparison and to make any structure below 1.5 eV larger, in experiment.

6.5 Comparison with clean Si(001) surfaces

The shapes of RA spectra from clean Si(001) surfaces using hybrid DFT [272] show significant difference from those of clean Ge(001). While symmetric dimers on Ge(001)-(2×1) surface shows metallic behaviour, on Si(001)-(2×1) semiconducting behaviour is found. For symmetric dimers on Si(001)-(2×1) there is a maximum below 1.0 eV (Fig. 6.24). With dimer tilting, this maximum changes to become a minimum and a maximum between 1.0 and 1.5 eV. This is very different from the asymmetric (2×1) phase of clean Ge(001), which has strong minimum around 1.0 and 1.7 eV (Fig. 6.17). Though the shape is very similar

to a previous study [275], experiment shows only a minimum at 1.5 eV, together with a broad minimum around 3.0 eV, neither of which are reproduced by the theory.

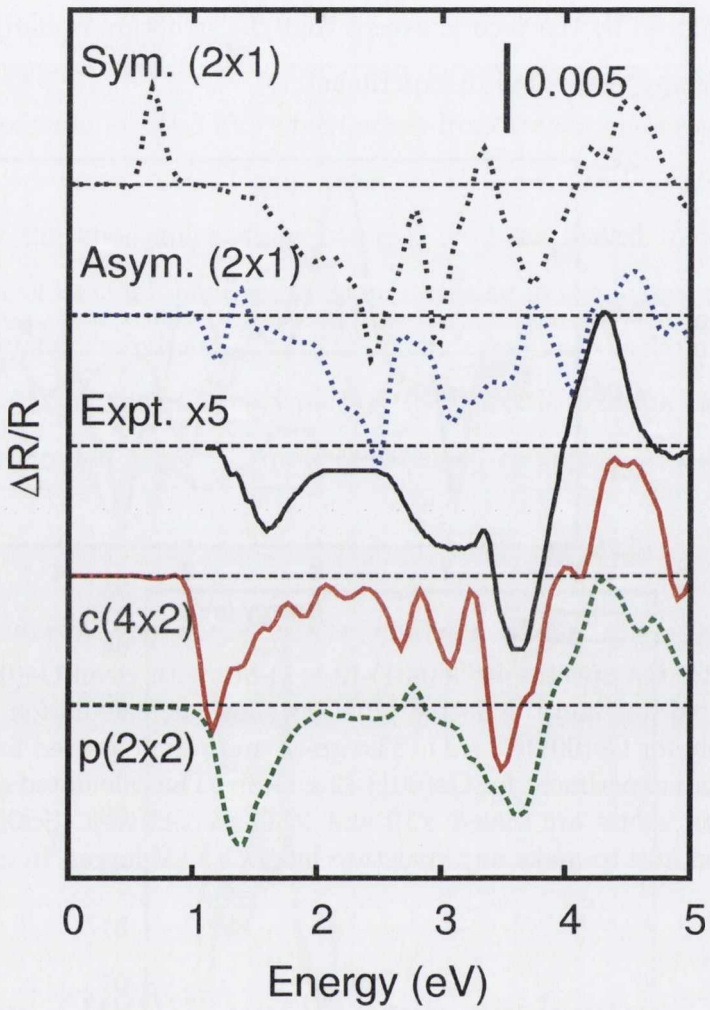


Figure 6.24: RA spectra of clean Si(001) surfaces (after [272]). For comparison experimental values are scaled $\times 5$.

Calculated RA spectra for p(2 × 2) and c(4×2) show better agreement with experiment. Both of them have minima in 1.1-1.3 eV range, which may correspond to 1.5 eV minima in experiment. The experiment is not from vicinal samples—flat sample, single domain prepared by EM. Two minima around 3.0 eV for c(4 × 2), which are absent for p(2 × 2), agree well with the broad minimum around the same energy in experiment. While RA spectra of p(2 × 2) and c(4 × 2) phases

for Si(001) have only one minimum below 2.0 eV, the same surfaces of Ge(001) produce two minima. Those phases have one positive maximum around 2.2 eV for Ge(001), which is absent for Si(001), while Ge(001)-p(2 × 2) and c(4 × 2) surfaces have only one minimum around 3.0 eV. The strong minimum and maximum around 3.5 and 4.5 eV for Si(001)-c(4 × 2) are in very good agreement with experiment.

6.6 Discussion and conclusion

Vicinal (001) wafers, offcut towards <110>, from the double height steps that produce the predominantly single domain surfaces, are necessary to obtain a significant surface RA response. The 6^o offset gives a reasonably well-ordered surface, but the spots broaden and split due to small domain sizes, the high density of steps and defects in the surface structure (fig. 6.1-6.3). It was found that wafers offset towards <111> produce a double domain surface, that for equal population, will have no response from (2 × 1) surface structures. Comparison of the RA response from the single and double domain surfaces shows that, above 2.0 eV, the signal is completely dominated by the response from the vicinal bulk and the steps (Fig. 6.5). Previous RA work, which cut off at 1.5 eV [22, 174], was essentially measuring the bulk step response from the clean surface (Fig. 6.17).

This high density of steps may be responsible for Sb dimers forming parallel to the step edge. On the flat Ge(001) surface the Sb dimer bond forms at 90^o to the original Ge dimer bond [39], but the LEED images, RA spectra and hybrid DFT calculations are all consistent with the Sb dimer bond being formed parallel to both the step edge and the Ge dimer bond direction. This requires a significant displacement of the Ge atoms in the top layer.

Hybrid DFT calculations for Ge surfaces were performed using a Fock exchange potential with 5% weighting. This weighting had been chosen previously for Si(111)-(2 × 1) calculations, as it produced a very good value for the static

dielectric constant of bulk Si, and reproduced the RA spectra well [276]. Using this weighting, bond lengths and band structures were calculated for various clean Ge(001) surface reconstructions, and Ge(001)-(2 $\times$ 1)-Sb, which were in very good agreement with the available experimental data and previous DFT calculations.

Optical calculations of the bulk dielectric function of Ge produced very good agreement with experiment, supporting the conclusions of the previous work on Si that this hybrid DFT approach is very useful in correcting the well known problem, DFT-LDA has with underestimating excited state energies.

The shape of the RA spectra calculated for the various sample structures of both Ge(001) and Si(001) were in good agreement with the experimental results, particularly as differences in the optical signal of less than 1% are being measured. The theoretical RA intensities were up to a factor of 5 larger than the experimental values. This difference is not unexpected, given the defective nature of the vicinal surfaces, the domain structure, and the limited slab thickness, which provides the bulk response. A deposition of Sb to form Ge(001)-(2 $\times$ 1)-Sb produced a dramatic change in the RA response below 2.0 eV, and this was well reproduced by the calculation. Above this energy it is likely that the the steps and the tilting of the bulk will contribute significantly to the response, but this cannot be calculated with the current computing power. In contrast to Si(001), here appears to be no work on using EM to form single domain structures on singular Ge(001). This is a promising area for future work, as it would also largely remove the significant proportion of dimers adjacent to step edges.

Chapter 7

Conclusion and future work

7.1 Conclusion

The main objectives of this thesis were to demonstrate that hybrid DFT offers a computationally efficient approach to calculating the optical response of surfaces and, from the hybrid DFT results, develop an understanding about the relationship between RA spectra and surface structure. RAS measures the reflectance anisotropy in two orthogonal polarisation directions at normal incidence. It achieves surface and interface sensitivity when the bulk material is isotropic and only the surface or interface has an anisotropic signal. The approach involved both calculation and experiment. With this approach some previous, well accepted structures including Si(111)-(2×1), clean Ge(001)-(2×1), p(2×2), c(4×2), Ge(001)-(2 × 1)-Sb were tested and attempts were made to model presently controversial structures like Si(111)-(5 × 2)-Au and Si(110)-(16 × 2).

At the start of this project, the MP chain model of Si(111)-(2 × 1) was used to test the hybrid DFT approach with 5 % Fock exchange weighting, as this weighting reproduced the static dielectric constant of bulk Si accurately. The optimised +MP structure was found to be more stable than the -MP structure by a small energy difference. The bond lengths between different atoms in both MP structures are in good agreement with previous experiments and calculations. Electronic structures of both the surfaces look very similar and revealed that there

are two surface states strongly localised on the inner and outermost atoms in the MP chain. The optical response of either MP structure showed a large peak below 1 eV when the electric field is aligned along the π chain, which is due to the large value of the momentum matrix of transitions between filled and empty states. The calculated RA spectra were in excellent agreement with the previous experiment from which it can be concluded that the hybrid DFT approach was successful for the Si(111)-(2 $\times$ 1) structure.

After the success of the hybrid DFT approach for Si(111)-(2 $\times$ 1), two competitive models (EBH and KK) for the Si(111)-(5 $\times$ 2)-Au surface (with and without Si adatom) were optimised. The main difference between the two models is that they have different Au atom coverages, which is still a controversial issue for the Si(111)-(5 $\times$ 2)-Au surface. EBH and KK models have 0.6 and 0.7 ML Au atom coverages, respectively. The calculated bond lengths at the surfaces of those two models were in good agreement with previous data. Changes in surfaces due to adatom decoration are very similar to those found previously. The existence of well accepted Si HCs and a very important structural unit, named as the $SiAu_4$ butterfly motif, was confirmed. The $SiAu_4$ butterfly motif was not investigated thoroughly in previous works. Electronic structures of both the models revealed that surfaces without adatom show metallic behaviour, with very similar dispersion of the half filled metallic band along the parallel direction of Au chains. The previously predicted gap opening for adatom decorated EBH structure is not found in this work, which is quite disappointing. Among the electronic structures calculated by hybrid DFT, the adatom decorated KK model agrees better with the previous ARPES data, which indicates, like other recent studies, that the KK model with 0.7 ML Au coverage is more likely to be the correct model than EBH structure.

The overall relatively poor agreement between hybrid DFT and experimental RA spectra provides only weak support for the KK model. The recent LDA-DFT RA spectra of EBH model, decorated with 0.5 ML adatom coverage, produced very good agreement with experiment, where it was argued that the RA spectra of adatom decorated Si(111)-(5 $\times$ 2)-Au surface is a collective response from small

domains of clean Si(111)-(5 × 2)-Au and Si(111)-(5 × 4)-Au unit cell with one adatom. The recent evidence for 0.7 ML Au coverage and the KK model means that this structure remains controversial.

Shorter heating process proved to be unreliable in producing the single domain Si(110)-(16 × 2) surface. It is confirmed that the single domain structure obtained by longer heating is very stable. From previous experiments and this work it is clear that the direction of DC current used for heating affects the orientation of the single domain as the 16× row direction is quite different from that of previous experiments with different directions of DC current. A possible explanation appears to be strain driving the Si atoms migration. The experimental RA spectrum was expected to have low energy structures, but lack of distinct structures in the RA spectrum is quite surprising considering that there are so many different structural units in the various models of the surface. The bulk and surface optic axes are found to be oriented in the same direction when the sample was rotated azimuthally. With the current computational resource the (16 × 2) surface proved to be very hard to tackle due to its complex reconstruction and size of the unit cell. Partial optimisation of a thin and H-terminated (16 × 2) slab proved to be insufficient to get agreement between measured and calculated RA spectra. Calculated RA spectra of thick H-terminated Si(110)-(1 × 1) slabs produced much better agreement with the experimental RA spectra from native-oxide-covered Si(110), with some anomaly above 4.0 eV. It seems that to get better agreement for (16 × 2) surface a much thicker optimised slab is needed, and for that, increased computational power is required.

Vicinal Ge(001) wafers, 6^o offcut towards <110> produced predominantly single domain surface with broadened and split spots due to small domain sizes, a high density of steps and defects in the surface structure, whereas wafers 6^o offcut towards <111> produced double domain surface. The surface contribution in the RA response was observed under 2 eV when RA spectra from the double and single domain surfaces were compared, which indicates that the previous experiments, which measured RA spectra over 1.5 eV, obtained the tilted bulk response from the clean surface, with little surface information.

Unlike previous experiments, which found Sb dimers are rotated by 90^o with respect to Ge dimers on the flat surface, this work found that the Sb and Ge dimers form in the same direction. LEED images, RA spectra and hybrid DFT calculations confirmed this fact with Sb dimers aligned along the step edge direction, which indicates significant displacement of Ge atoms in the top layer. It is likely that the narrow terraces and high step density drive this response.

Bond lengths, for different clean Ge(001) and Ge(001)-(2×1)-Sb surfaces, calculated by hybrid DFT with 5 % Fock exchange weighting are in good agreement with available experimental data and previous DFT calculations. The calculated bulk dielectric function of Ge agrees well with experiment, from which it can be said that the band gap problem in LDA-DFT can be tackled well with this hybrid DFT approach for Ge as well as Si.

The shapes of the calculated RA spectra are in good agreement with the measured RA response for clean Ge(001) surfaces. The experimental values are up to 5 times smaller than calculations. This is expected due to the domain structure and defective nature of the vicinal surfaces. Sb deposition produced a well ordered, predominantly single domain Ge(001)-(2×1)-Sb surface. The RA spectrum of that surface, which is well reproduced by calculations, is dramatically different from that of clean Ge(001) surface under 2.0 eV. Over this energy the contributions come mainly from the steps and tilted bulk, which could not be calculated with existing computing power.

So to conclude, it can be said that the approach combining experiment and hybrid DFT was very successful, except for cases where the limitation of computing power arose as a problem. This approach is very promising for understanding other controversial crystal structures and their electronic and optical properties.

7.2 Future work

Theoretical investigation is needed to accurately predict the minimum energy isomer for Si(111)-(2×1) as we found here that the energy difference between + and - MP structures is very small and change of any parameter (as for example k-point density) in the calculation can flip the result. Also, more experimental investigations are needed to understand the quasi 1D behaviour of the MP chain in Si(111)-(2×1).

The coverage of Au atoms in Si(111)-(5×2)-Au is still controversial. The EBH model with 0.6 ML Au atom coverage seems to be an appropriate structure as far as RA spectra is concerned, whereas the KK model with 0.7 ML Au atom coverage, which has been supported recently, appears to be more likely when the electronic structure of that model was compared with ARPES. So this surface needs to be investigated further to get consistency between all the experimental results and calculations and an accurate structure with appropriate Au atom coverage. Once the accurate structure is obtained, the electronic and optical properties need to be understood to get an insight into the behaviour of the quasi-1D Au chain. A theoretical investigation on the effect of variation of adatom coverage on structural, electronic and optical properties of that surface, studied by experiment, is another potential future work.

Only one broad peak is obtained below 2.0 eV in the experimental RA spectrum of the single domain Si(110)-(16×2) surface in spite of a number of predicted features in this surface, which is disappointing. Further investigation of the surface is needed to get an appropriate model of the (16×2) structure. After modelling the structure accurately, the electronic properties need to be studied thoroughly to understand the reasons behind such a large surface reconstruction. Another potential future work is to theoretically determine the orientation of the surface optic axis.

Here, the RA spectra is obtained for clean and Sb covered Ge(001)-(2×1) surfaces at room temperature. Measurement of RA spectra for other clean Ge(001) reconstructed surfaces is a very promising future work.

Appendix A

Detail of Calculations

A modified form of the B3LYP hybrid DFT functional in the CRYSTAL simulation package was used throughout this work. CRYSTAL can also be used for DFT calculations using a number of functionals such as LDA, LDA+U, GGA, GGA+U, Hartree-Fock. A value of 5 % for the Fock exchange weight factor, for both Si and Ge, was used to get good agreement with experimental band gaps and dielectric functions.

Lattice parameters were taken from X-ray diffraction experiments for both bulk Si (5.431 Å) and Ge (5.6575 Å). Then they were relaxed using B3LYP hybrid DFT until the total energy was minimised. The values of relaxed lattice parameters for Si(111)-(2 × 1) are discussed in Chapter 4. For Ge surface reconstructions lattice parameters were kept unchanged from experiments. It can be seen from Chapter 4 that the modified B3LYP hybrid DFT overestimates lattice parameters by about 1 %. Bulk dielectric functions for both Si and Ge were calculated using a 24 × 24 × 24 Monkhorst-Pack grid in the bulk Brillouin zone.

After getting good agreement with experimental dielectric functions for bulk Si and Ge different supercells were made with different k-point densities and thickness, which are discussed later. In case of Si(111)-(2 × 1), 8 Si bilayers (40 atoms) and an 8 × 8 grid were used for the self-consistent field calculations and total energy evaluations. A denser 16 × 32 grid of k-points was used to calculate the optical properties of the system. Si(111)-(5 × 2)-Au and (5 × 4)-Au systems

are made of 4 bilayers of Si atoms with two reconstructed surfaces on both sides with 116 to 238 atoms for different Au deposited Si(111) systems ((5×2) or (5×4) surfaces). A 6 × 6 grid was used while relaxing the structure. An 8 × 20 grid was used to calculate the dielectric function for the system due to our limited computational resource. Due to huge size of Si(110)-(16 × 2) unit cell only a bilayer of Si atoms beneath the surface (382 atoms) was used. The slab was terminated with H atoms on the lower surface. A 4 × 4 Monkhorst-Pack grid was used for energy and geometry optimisation calculation. While calculating the dielectric function of the slab a 2 × 16 grid was used in the SBZ as k-point density to keep the computational expense affordable.

All the Ge(001) supercell slabs contain 7 Ge bilayers sandwiched between two reconstructed surfaces. Different supercell slabs consist of different numbers of Ge atoms; clean (2 × 1), p(2 × 2) and c(4 × 2) slabs contain 32, 48 and 64 Ge atoms, respectively. Ge(001)-(2 × 1)-Sb system consists of 32 atoms. For self-consistent energy minimisation a 6 × 6 grid was used for every Ge(001) systems. But to calculate dielectric functions different optimised meshes of k-points were used for different slabs. A 16 × 32 mesh was used for clean and Sb deposited (2 × 1) superstructures. For both p(2 × 2) and c(4 × 2) phase a 20 × 20 grid was used.

Tolerances for lattice sum convergence within the CRYSTAL program were chosen to be 8, 8, 8 and 12 for Si-Au systems. For all other systems they were chosen as 7, 7, 7 and 14. Convergence of each force calculation was observed, based on minimisation of total energy. A total energy minimisation tolerance of 10^{-7} Hartree (10^{-6} eV) was used throughout. Lattice parameters for different slabs are shown below in table A.1.

Table A.1: Lattice parameters for different slabs.

Systems	a(Å)	b(Å)	$\alpha(^o)$
Si(110)-(16 × 2)	49.910	13.222	87.470
Si(111)-(2 × 1)	7.719	3.878	90.000
Si(111)-(5 × 2)	16.843	7.728	83.413
Ge(001)-(2 × 1) and (2 × 1)-Sb	8.000	4.000	90.000
Ge(001)-c(4 × 2)	9.008	9.008	53.130

Appendix B

Basis Sets

The Gaussian orbital basis sets are used in the CRYSTAL codes (Versions CRYSTAL06 and CRYSTAL09 are used). These basis sets describe the orbitals that generate the wave-function and the density function to start the DFT SCF calculations and are tested for convergence and slightly modified in cases where slow convergence is found.

Initially all-electron basis sets for Si and Ge were used for both Si and Ge surfaces. This approach worked quite well for small systems such as Si(111)-(2×1) and Ge(001) surfaces. The desired values for energy minimisations were achieved quickly. But for large systems such as Si(111)-(5×2)-Au and Si(110)-(16×2) the all electron basis sets did not meet the requirement in term of time. Pseudopotential basis sets were used in these cases. A huge reduction in computer time was seen and the criteria for convergence was fulfilled for Si(111)-(5×2)-Au and Si(110)-(16×2) optimisation calculation ran much quicker than before. The pseudo-potential basis set for Au was used throughout this project.

The data provided here are the prefactors (a_i) and exponents (C_i) of Gaussian functions and the form is given by,

$$\Psi(\mathbf{r}) = \sum_i C_i e^{a_i(\mathbf{r}-\mathbf{r_A})^2}, \tag{B.0.1}$$

where $\mathbf{r}_A$ is the atomic position.

Silicon(Si)

All-electron basis set:

This basis set was generated by Pascale *et al.* and Noel *et al.* [277,278].

```
14  6
0   0       8          2.          1.0
    87645.8 0.000237
    12851.8 0.00192
    2786.28 0.0109
    728.043 0.0496
    219.516 0.1668
    75.9006 0.363
    29.4602 0.4051
    11.9891 0.1504
0   1       6          8.          1.0
    165.958 -0.00884   0.00909
    39.3727 -0.0859    0.0601
    12.7112 -0.0712    0.1952
    4.7177  0.4147     0.3384
    1.8482  0.6168     0.3006
    0.7365  0.1154     0.0648
0   1       3          2           1.
    4.1752  -0.0199    -0.0087
    1.4472  -0.1864    -0.00438
    0.5023  0.0967     0.2207
0   1       1          0.          1.
    0.322   1.         1.
0   1       1          0.          1.
    0.13    1.         1.
0   3       1          0.          1.
    0.6     1.
```

Pseudopotential basis set:

```
214       4
INPUT
4.        0          1            1          1   0   0
          2.71362197 26.62331865  0
          1.96687987 10.92995391  0
          2.71001600 -4.66941200  0
0         1          3            4.0        1.
          4.1752     -0.0199      -0.0087
          1.4472     -0.1864      -0.00438
          0.5023     0.0967       0.2207
```

0	1	1	0.	1.
	0.322	1.	1.	
0	1	1	0.	1.
	0.13	1.	1.	
0	3	1	0.	1.
	0.6	1.		

Germanium(Ge)

All-electron basis set:

32	8			
0	0	9	2.0	0.9352
	2233310.0	0.0000395		
	313044.0	0.000348		
	64056.8	0.00219		
	15552.0	0.0114		
	4344.31	0.0483		
	1368.86	0.159		
	484.106	0.3535		
	187.139	0.4229		
	74.8445	0.1494		
0	1	7	8.0	0.9278
	5165.19	-0.000434	0.00103	
	1175.7	-0.00789	0.00978	
	351.419	-0.0664	0.0583	
	121.338	-0.1465	0.2199	
	46.9314	0.2643	0.4445	
	19.7761	0.737	0.394	
	8.3635	0.2365	0.093	
0	1	6	8.0	0.9189
	97.5662	0.00473	-0.017	
	34.994	-0.0706	-0.0736	
	15.0609	-0.3186	0.1458	
	6.3274	0.2932	0.9938	
	2.6735	0.9281	1.2549	
	1.1047	0.2879	0.4207	
0	3	6	10.0	1.0
	195.459	0.00478		
	57.3182	0.0379		
	20.7748	0.1536		
	8.1369	0.3857		
	2.9767	0.5762		
	0.9404	0.34236		

```
0  3          1          0.0          1.0
   0.5582     1.0
0  1          3          4.0          1.0
   2.95668    -0.04577   -0.161747
   1.08723    -0.322189  1.89298
   0.611098   0.298642   -5.99368
0  1          1          0.0          1.0
   0.3500     1.0        1.0
0  1          1          0.0          1.0
   0.1486     1.0        1.0
```

Gold(Au)

Pseudopotential basis set:

This basis set was generated by Weihrich *et al* [279]. Effective core pseudopotentials (ECP) modified from Hay and Wadt [280]

```
279        7
INPUT
19.        5          6          4   5   0   0
           622.6287956  -60.0000000  -1
           136.2843607  -555.5292312  0
           33.1549781   -168.0019785  0
           9.9894895    -63.0399875   0
           3.0481312    -4.2516681    0
           194.7374304  3.0000000     -2
           351.5327447  38.6020880    -1
           122.3270402  864.8370727   0
           32.0914617   374.9935520   0
           5.2451812    289.7910100   0
           4.4916223    -152.4532773  0
           420.6158801  2.0000000     -2
           109.4417815  73.8885625    -1
           34.1714280   326.6729872   0
           5.9879750    126.5814591   0
           219.2666158  3.0000000     -2
           122.7297786  55.6793149    -1
           63.1063369   449.1987335   0
           18.3684520   215.0269091   0
           4.4972844    64.0840995    0
0          0          4          2.  1.
           2.8090     -1.203037
           1.5950     1.675385
```

```
    0.5327    0.352918
    0.2826    -0.001158
0   2         3          6.   1.
    3.6840    -0.278885
    1.6660    0.777981
    0.5989    0.478106
0   0         4          2.   1.
    2.8090    0.473068
    1.5950    -0.759732
    0.5327    -0.422037
    0.2826    0.53240
0   0         1          0.   1
    0.14      1.0
0   2         1          0.   1
    0.22      1.0
0   3         2          9.   1.
    1.2870    0.535907
    0.4335    0.485830
0   3         1          0.   1.
    0.25 1.
```

Antimony(Sb)

All electron basis set:

This basis set was generated by Causa *et al* [281] with ECP modified (DURAND) by Durand *et al.* [282]

```
251         3
DURAND
0           1          2          3.0        0.0
            0.652716   -0.818377  -0.199304
            0.334043   1.044557   0.544199
0           1          1          0.0        0.0
            0.10       1.0        1.0
0           3          1          0.0        0.0
            0.25       1.0
```

Appendix C

Jones Matrices

The Jones matrix method is one of the most popular ways to describe linearly polarised light. It was first described by R.C. Jones [283, 284] in 1941. Polarised light is represented by Jones vector and linear optical components are represented by Jones matrices. When light crosses an optical element the resulting polarisation of the emerging light is found by taking the product of the Jones matrix of the optical element and the Jones vector of the incident light. Note that Jones calculus is only applicable to light that is already fully polarised. Light which is randomly polarised, partially polarised, or incoherent must be treated using Mueller matrix method. The Jones vector is described as

$$\begin{pmatrix} E_x e^{i\phi} \\ E_y e^{i\phi} \end{pmatrix} \tag{C.0.1}$$

Where E_i is the electric field intensity and ϕ is the phase. It is normal to normalise the magnitude of this vector. The following are the most common input vectors that can be used.

Linear (x-direction) $\begin{pmatrix} 1 \\ 0 \end{pmatrix}$

Linear (y-direction) $\begin{pmatrix} 0 \\ 1 \end{pmatrix}$

Linear (45° from axis) $\frac{1}{\sqrt{2}}\begin{pmatrix} 1 \\ 1 \end{pmatrix}$

Right Circular $\frac{1}{\sqrt{2}}\begin{pmatrix} 1 \\ -i \end{pmatrix}$

Left Circular $\frac{1}{\sqrt{2}}\begin{pmatrix} 1 \\ i \end{pmatrix}$

Common components are:

Linear polariser (x-direction) $\begin{pmatrix} 1 & 0 \\ 0 & 0 \end{pmatrix}$

Linear polariser (y-direction) $\begin{pmatrix} 0 & 0 \\ 0 & 1 \end{pmatrix}$

Linear polariser (45° from axis) $\frac{1}{2}\begin{pmatrix} 1 & 1 \\ 1 & 1 \end{pmatrix}$

Half Wave Plate $\begin{pmatrix} Cos2\theta & Sin2\theta \\ Sin2\theta & -Cos2\theta \end{pmatrix}$

Quarter wave plate $\begin{pmatrix} Cos^2\theta + iSin^2\theta & (1-i)Sin\theta Cos\theta \\ (1-i)Sin\theta Cos\theta & Sin^2\theta + iCos^2\theta \end{pmatrix}$

Here θ is the angle between the fast axis and the x axis.

Appendix D

FlexRAS Labview Program

A LabView program was used to record RA spectra. This program was designed to be flexible in allowing the user to exchange many of the components to suit the samples being tested. Its basic logic was quite simple, it proceeded as follows.

1. Initialise Components
   1. Set PEM voltage for required start energy
   2. Set to detector for required start energy
   3. Set time constant
   4. Set filter to dark
   5. Read dark DC
   6. Set filter for required energy
   7. Set monochromator for required energy
   8. Read AC voltage and optimise sensitivity
2. Measuring
   1. Set PEM voltage for required energy
   2. Set monochromator for required energy
   3. Set filter for required energy
   4. Check detector (If needs to be changed go to 4.1)
   5. Read AC
   6. Check sensitivity
      (optimise if needed and read AC again)
   7. Read DC

3. Calculating RAS
   1. Take AC value and scale by any damping factor
   2. Take DC value and subtract dark DC
   3. Divide corrected AC by corrected DC
   4. Save energy, RAS, AC and DC
   5. Step energy and return to point 2.1, until finish energy is reached

4 Changing detector
   1. Change to detector needed
   2. Set filter to Dark
   3. Record Dark DC
   4. Set filter to required for energy
   5. Return to point 2.4

Included here are some screen shots of the various modes of operation of the RAS LabView program.

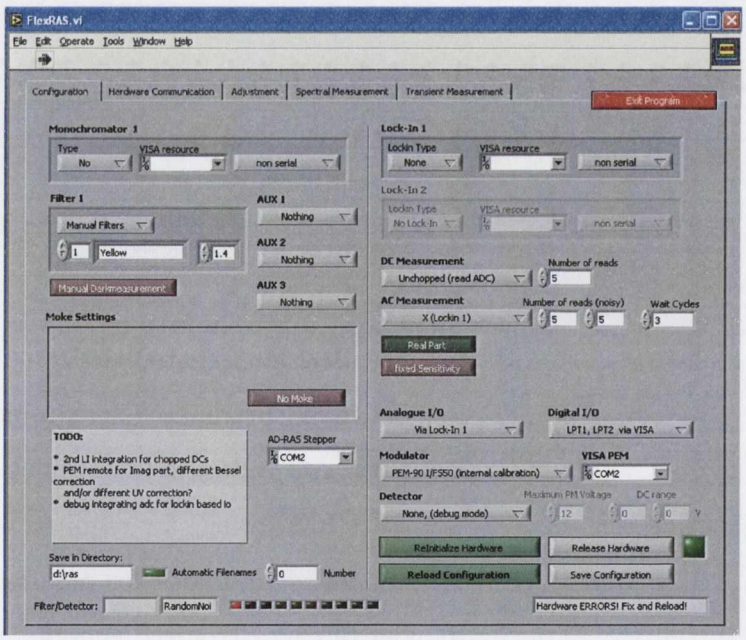


Figure D.1: The front panel of the RAS LabView program, options are selected to do with the different components being used and various measurement. Options such as wait times between readings and number of times to record each point can also be adjusted.

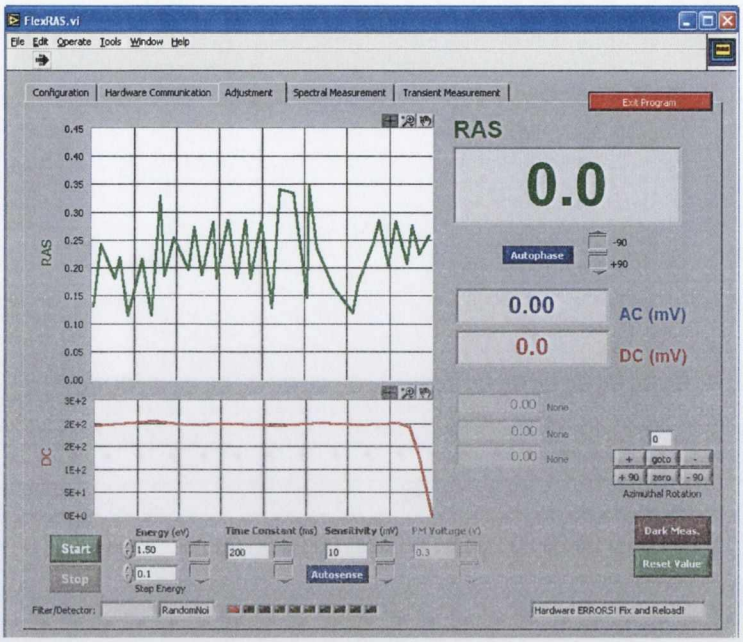


Figure D.2: The Adjustment mode, this mode is used for alignment

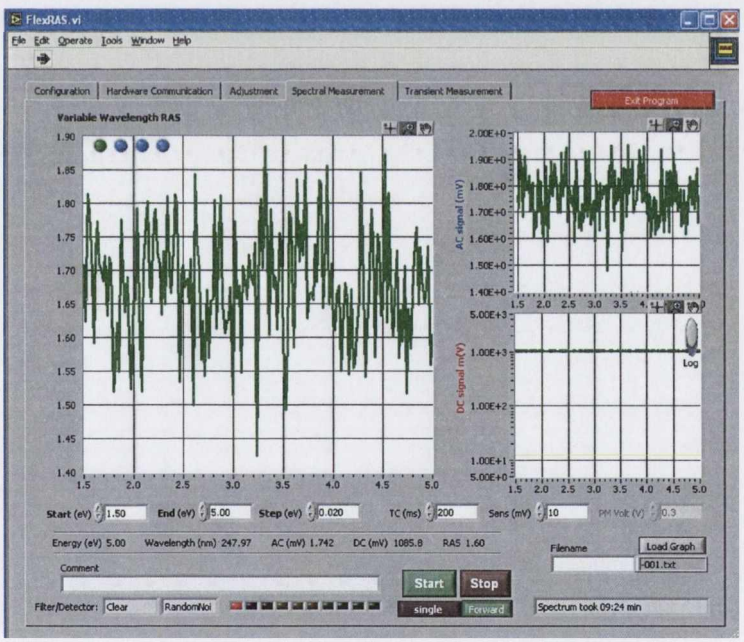


Figure D.3: Main Spectral mode, the energy is stepped and points are recorded. Changes can be made to energy step size, time constant, start and finish energy. Spectra can be recorded both forwards (IR-UV) and backwards (UV-IR). Multiple spectra can also be recorded. The sensitivity is optimised automatically as the spectra is recorded.

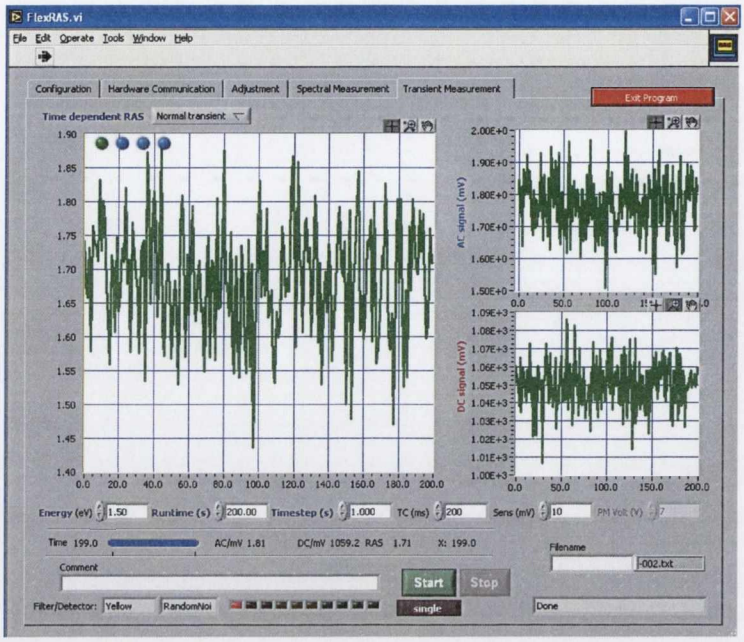


Figure D.4: Transient mode allows changes at a particular energy to be monitored over time. Any energy can be chosen and the length of time to record for can be changed.

References

[1] J.F. McGilp. Optical second-harmonic generation for studying surfaces and interfaces. *J. Phys.: Condens. Mat.*, 1:85, 1989.

[2] J. F. McGilp. Probing surface and interface structure using optics. *Journal of Physics: Condensed Matter*, 22(8):084018, 2010.

[3] D.E. Aspnes. Above-bandgap optical anisotropies in cubic semiconductors: a visible-near ultraviolet probe of surfaces. *J. Vac. Sci. Technol. B*, 3(5):1498 – 506, Sept.-Oct. 1985.

[4] D. Aspnes and A. Studna. Anisotropies in the Above-Band-Gap optical spectra of cubic semiconductors. *Phys. Rev. Lett.*, 54:1956–1959, Apr 1985.

[5] D. E. Aspnes, J. P. Harbison, A. A. Studna, and L. T. Florez. Optical reflectance and electron diffraction studies of molecular-beam-epitaxy growth transients on GaAs(001). *Phys. Rev. Lett.*, 59:1687, Oct 1987.

[6] D.E. Aspnes and A.A. Studna. Reflectance-difference spectroscopy of (110) GaAs and InP. *J. Vac. Sci. Technol. A*, 5(4):546, 1987/07/.

[7] D.E. Aspnes, J.P. Harbison, A.A. Studna, and L.T. Florez. Reflectance-difference spectroscopy system for real-time measurement of crystal growth. *Appl. Phys. Lett.*, 52(12):957 – 9, 1988/03/21.

[8] D.E. Aspnes, J.P. Harbison, A.A. Studna, and L.T. Florez. Application of reflectance difference spectroscopy to molecular-beam epitaxy growth of GaAs and AlAs. *J. Vac. Sci. Technol. A*, 6(3):1327 – 32, 1988/05/.

[9] J.P. Harbison, D.E. Aspnes, A.A. Studna, and L.T. Florez. Optical reflectance measurements of transients during molecular-beam epitaxial growth on (001)GaAs. *J. Vac. Sci. Technol. B*, 6(2):740 – 2, 1988/03/.

[10] J.P. Harbison, D.E. Aspnes, A.A. Studna, L.T. Florez, and M.K. Kelly. Oscillations in the optical response of (001)GaAs and AlGaAs surfaces during crystal growth by molecular beam epitaxy. *Appl. Phys. Lett.*, 52(24):2046 – 9, 1988/06/13.

[11] V.L. Berkovits, I.V. Makarenko, T.A. Minashvili, and V.I. Safarov. Optical transitions on GaAs[110] surface. *Sol. St. Comm.*, 56(5):449 – 450, 1985.

[12] Wolfgang Richter and J. F. McGilp. Optical in situ surface control during MOVPE and MBE growth [and discussion]. *Phil. Trans. R. Soc. A*, 344(1673):453–467, 1993.

[13] P. Weightman, D. S. Martin, R. J. Cole, and T. Farrell. Reflection anisotropy spectroscopy. *Reports on Progress in Physics*, 68(6):1251, 2005.

[14] D. S. Martin, R. J. Cole, and P. Weightman. Effects of ion bombardment on the optical and electronic properties of Cu(110). *Phys. Rev. B*, 72:035408, Jul 2005.

[15] D. S. Martin, A. Maunder, and P. Weightman. Thermal of the Cu(110) surface studied by reflection anisotropy spectroscopy and scanning tunnelling microscopy. *Phys. Rev. B*, 63:155403, Mar 2001.

[16] D.S. Martin, N.P. Blanchard, and P. Weightman. The effect of surface morphology upon the optical response of Au(110). *Surface Science*, 532535(0):1 – 7, 2003. Proceedings of the 7th International Conference on Nanometer-Scale Science and Technology and the 21st European Conference on Surface Science.

[17] L. D. Sun, M. Hohage, P. Zeppenfeld, R. E. Balderas-Navarro, and K. Hingerl. Enhanced optical sensitivity to adsorption due to depolarization of anisotropic surface states. *Phys. Rev. Lett.*, 90:106104, Mar 2003.

[18] J. Bremer, J.-K. Hansen, K. Stahrenberg, and T. Worren. The influence of surface steps on the optical and electronic anisotropy of Ag(110). *Surface Science*, 459:39 – 48, 2000.

[19] Z Sobiesierski, D I Westwood, and C C Matthai. Aspects of reflectance anisotropy spectroscopy from semiconductor surfaces. *Journal of Physics: Condensed Matter*, 10(1):1, 1998.

[20] Roman Forker and Torsten Fritz. Optical differential reflectance spectroscopy of ultrathin epitaxial organic films. *Phys. Chem. Chem. Phys.*, 11:2142–2155, 2009.

[21] Regina Passmann, Priscila Favero, Wolf Gero Schmidt, Ronei Miotto, Walter Braun, Wolfgang Richter, Michael Kneissl, Norbert Esser, and Patrick Vogt. Adsorption structure of cyclopentene on InP(001)(2×4). *Phys. Rev. B*, 80:125303, Sep 2009.

[22] T. Yasuda, L. Mantese, U. Rossow, and D. E. Aspnes. Surface-induced optical anisotropies of single-domain (2×1) reconstructed (001) Si and Ge surfaces. *Phys. Rev. Lett.*, 74:3431–3434, Apr 1995.

[23] G. Bussetti, C. Goletti, P. Chiaradia, and G. Chiarotti. Infrared reflectance anisotropy spectroscopy of Si(111) $- 2 \times 1$: Surface excitons and polarons. *Phys. Rev. B*, 72:153316, Oct 2005.

[24] G. Bussetti, C. Goletti, P. Chiaradia, and T. Derry. Optical gap between dangling-bond states of a single-domain diamond C(111) $- 2 \times 1$ by reflectance anisotropy spectroscopy. *EPL (Europhysics Letters)*, 79(5):57002, 2007.

[25] S Chandola, J Jacob, K Fleischer, P Vogt, W Richter, and J F McGilp. Optical and electronic properties of Ag nanodots on Si(111). *Journal of Physics: Condensed Matter*, 18(30):6979, 2006.

[26] N McAlinden and J F McGilp. Using surface and interface optics to probe the capping, with amorphous Si, of Au atom chains grown on vicinal Si(111). *Journal of Physics: Condensed Matter*, 21(47):474208, 2009.

[27] K. Fleischer, J. Jacob, S. Chandola, N. Esser, and J. F. McGilp. Using reflectance anisotropy spectroscopy to characterize capped silver nanostructures grown on silicon. *physica status solidi (c)*, 5(8):2556–2560, 2008.

[28] J. R. Power, P. Weightman, and J. D. O'Mahony. Strong optical anisotropy of the single-domain 5×2-Au reconstruction on vicinal Si(111). *Phys. Rev. B*, 56:3587–3590, Aug 1997.

[29] F. Pedreschi, J.D. Omahony, P. Weightman, and J.R. Power. Evidence of electron confinement in the single-domain (4×1)-in superstructure on vicinal Si(111). *Appl. Phys. Lett.*, 73(15):2152 – 4, 1998/10/12.

[30] J. Jacob, N. McAlinden, K. Fleischer, S. Chandola, and J. F. McGilp. Reflectance anisotropy studies of 5×2-Au structures grown on Si(111) surfaces with different step formations. *physica status solidi (c)*, 5(8):2569–2572, 2008.

[31] L. F. Lastras-Martiinez, M. Chavira-Rodriguez, R. E. Balderas-Navarro, J. M. Flores-Camacho, and A. Lastras-Martinez. Reflectance difference spectroscopy of GaAs(001) under a [110] uniaxial stress. *Phys. Rev. B*, 70:035306, Jul 2004.

[32] D. Papadimitriou and W. Richter. Highly sensitive strain detection in silicon by reflectance anisotropy spectroscopy. *Phys. Rev. B*, 72:075212, Aug 2005.

[33] E. Liarokapis, D. Papadimitriou, J. Rumberg, and W. Richter. Raman and RAS measurements on uniaxially strained thin semiconductor layers. *physica status solidi (b)*, 211(1):309–316, 1999.

[34] C. G. Tang, Y. H. Chen, X. L. Ye, Z. G. Wang, and W. F. Zhang. Strain-induced in-plane optical anisotropy in (001) GaAs and AlGaAs superlattice studied by reflectance difference spectroscopy. *Journal of Applied Physics*, 100(11):113122, 2006.

[35] Steven C. Erwin, Ingo Barke, and F. J. Himpsel. Structure and energetics of Si(111)-(5×2)-Au. *Phys. Rev. B*, 80:155409, Oct 2009.

[36] N. D. Kim, Y. K. Kim, C.-Y. Park, H. W. Yeom, H. Koh, E. Rotenberg, and J. R. Ahn. High-resolution photoemission spectroscopy study of the single-domain Si(110)-16 × 2 surface. *Phys. Rev. B*, 75:125309, Mar 2007.

[37] K. C. Pandey. Reconstruction of Semiconductor Surfaces: Buckling, Ionicity, and π-Bonded Chains. *Phys. Rev. Lett.*, 49:223–226, Jul 1982.

[38] J. A. Kubby, J. E. Griffith, R. S. Becker, and J. S. Vickers. Tunneling microscopy of Ge(001). *Phys. Rev. B*, 36:6079, Oct 1987.

[39] A Lessmann, W Drube, and G Materlik. Backreflection XSW and ARUPS studies of Sb/Ge(001) – 2 × 1. *Surface Science*, 323(12):109 – 117, 1995.

[40] Z. Q. Chen, S. J. Wang, M. Maekawa, A. Kawasuso, H. Naramoto, X. L. Yuan, and T. Sekiguchi. Thermal evolution of defects in as-grown and electron-irradiated zno studied by positron annihilation. *Phys. Rev. B*, 75:245206, Jun 2007.

[41] Zhian He, M. Stevens, David J. Smith, and P. A. Bennett. Dysprosium silicide nanowires on Si(110). *Applied Physics Letters*, 83(25):5292, 2003.

[42] S. Liang, R. Islam, David J. Smith, P. A. Bennett, J. R. OBrien, and B. Taylor. Magnetic iron silicide nanowires on Si(110). *Applied Physics Letters*, 88(11):113111, 2006.

[43] Erwin Rosenberg. Germanium: environmental occurrence, importance and speciation. *Reviews in Environmental Science and Bio/Technology*, 8(1):29, 2009.

[44] D. Haneman. Surface Structures and Properties of Diamond-Structure Semiconductors. *Phys. Rev.*, 121:1093–1100, Feb 1961.

[45] F. J. Himpsel, P. Heimann, and D. E. Eastman. Surface states on Si(111) – (2 × 1). *Phys. Rev. B*, 24:2003–2008, Aug 1981.

[46] H. Sakama, A. Kawazu, and K. Ueda. Structural studies of Si(111)2 × 1 surfaces using low-energy electron diffraction. *Phys. Rev. B*, 34:1367–1370, Jul 1986.

[47] F. Ancilotto, W. Andreoni, A. Selloni, R. Car, and M. Parrinello. Structural, electronic, and vibrational properties of Si(111) $-$ 2 $\times$ 1 from ab initio molecular dynamics. *Phys. Rev. Lett.*, 65:3148–3151, Dec 1990.

[48] Geng Xu, Bingcheng Deng, Zhaoxian Yu, S. Y. Tong, M. A. Van Hove, F. Jona, and I. Zasada. Atomic structure of the cleaved Si(111) $-$ (2 $\times$ 1) surface refined by dynamical leed. *Phys. Rev. B*, 70:045307, Jul 2004.

[49] Charles H. Patterson, Soumya Banerjee, and John F. McGilp. Optical and phonon excitations of modified pandey chains at the Si(111) $-$ 2 $\times$ 1 surface. *Phys. Rev. B*, 84:155314, Oct 2011.

[50] K. C. Pandey and J. C. Phillips. Energy Bands of Reconstructed Surface States of Cleaved Si. *Phys. Rev. Lett.*, 34:1450–1453, Jun 1975.

[51] D. J. Chadi. Energy-Minimization Approach to the Atomic Geometry of Semiconductor Surfaces. *Phys. Rev. Lett.*, 41:1062–1065, Oct 1978.

[52] M. Zitzlsperger, R. Honke, P. Pavone, and U. Schrder. Ab initio calculation of the structure, the electronic states and the phonon dispersion of the Si(111) $-$ (2 $\times$ 1) surface. *Surface Science*, 377379(0):108 – 111, 1997. European Conference on Surface Science.

[53] F. J. Himpsel, P. M. Marcus, R. Tromp, Inder P. Batra, M. R. Cook, F. Jona, and H. Liu. Structure analysis of Si(111)2 $\times$ 1 with low-energy electron diffraction. *Phys. Rev. B*, 30:2257–2259, Aug 1984.

[54] John E. Northrup, Mark S. Hybertsen, and Steven G. Louie. Many-body calculation of the surface-state energies for Si(111)2 $\times$ 1. *Phys. Rev. Lett.*, 66:500–503, Jan 1991.

[55] B.I. Craig and P.V. Smith. Slab-mindo calculations on the Si(111)2 $\times$ 1 surface. *Surface Science*, 225(3):225 – 232, 1990.

[56] A. A. Stekolnikov, J. Furthmüller, and F. Bechstedt. Absolute surface energies of group-IV semiconductors: Dependence on orientation and reconstruction. *Phys. Rev. B*, 65:115318, Feb 2002.

[57] J. K. Garleff, M. Wenderoth, K. Sauthoff, R. G. Ulbrich, and M. Rohlfing. 2×1 reconstructed Si(111) surface: STM experiments versus ab initio calculations. *Phys. Rev. B*, 70:245424, Dec 2004.

[58] G. Bussetti, B. Bonanni, S. Cirilli, A. Violante, M. Russo, C. Goletti, P. Chiaradia, O. Pulci, M. Palummo, R. Del Sole, P. Gargiani, M. G. Betti, C. Mariani, R. M. Feenstra, G. Meyer, and K. H. Rieder. Coexistence of Negatively and Positively Buckled Isomers on n^+-doped Si(111) $- 2 \times 1$. *Phys. Rev. Lett.*, 106:067601, Feb 2011.

[59] F. G. Allen and G. W. Gobeli. Work function, photoelectric threshold, and surface states of atomically clean Silicon. *Phys. Rev.*, 127:150–158, Jul 1962.

[60] D. E. Eastman and W. D. Grobman. Photoemission densities of intrinsic surface states for Si, Ge, and GaAs. *Phys. Rev. Lett.*, 28:1378–1381, May 1972.

[61] John E. Northrup and Marvin L. Cohen. Reconstruction mechanism and surface-state dispersion for Si(111)$-(2\times1)$. *Phys. Rev. Lett.*, 49:1349–1352, Nov 1982.

[62] R. I. G. Uhrberg, G. V. Hansson, J. M. Nicholls, and S. A. Flodström. Experimental Evidence for One Highly Dispersive Dangling-Bond Band on Si(111)2×1. *Phys. Rev. Lett.*, 48:1032–1035, Apr 1982.

[63] P. Perfetti, J. M. Nicholls, and B. Reihl. Unoccupied surface-state band on Si(111)2×1. *Phys. Rev. B*, 36:6160–6163, Oct 1987.

[64] P. Chiaradia, A. Cricenti, S. Selci, and G. Chiarotti. Differential reflectivity of Si(111)2×1 surface with polarized light: A test for surface structure. *Phys. Rev. Lett.*, 52:1145–1147, Mar 1984.

[65] Per Mrtensson, Antonio Cricenti, and Göran V. Hansson. Photoemission study of the antibonding surface-state band on Si(111)2×1. *Phys. Rev. B*, 32:6959–6961, Nov 1985.

[66] F. Ciccacci, S. Selci, G. Chiarotti, and P. Chiaradia. Electron-phonon interaction in optical absorption at the Si(111)2 × 1 surface. *Phys. Rev. Lett.*, 56:2411–2414, Jun 1986.

[67] G. Chiarotti, S. Nannarone, R. Pastore, and P. Chiaradia. Optical absorption of surface states in ultrahigh vacuum cleaved (111) surfaces of Ge and Si. *Phys. Rev. B*, 4:3398–3402, Nov 1971.

[68] S. Nannarone, P. Chiaradia, F. Ciccacci, R. Memeo, P. Sassaroli, S. Selci, and G. Chiarotti. Surface states in Si(111)2 × 1 and Ge(111)2 × 1 by optical reflectivity. *Solid State Communications*, 33(6):593 – 595, 1980.

[69] R. Del Sole and E. Tosatti. Surface state excitons in semiconductors. *Solid State Communications*, 22(5):307 – 310, 1977.

[70] Michael Rohlfing and Steven G. Louie. Excitons and optical spectrum of the Si(111) – (2 × 1) surface. *Phys. Rev. Lett.*, 83:856–859, Jul 1999.

[71] R. Del Sole and Annabella Selloni. Chain model of Si(111)2 × 1 surface: Optical properties and surface-state excitons. *Phys. Rev. B*, 30:883–893, Jul 1984.

[72] Lucia Reining and R. Del Sole. Quasi-one-dimensional excitons and the optical properties of Si(111)2 × 1. *Phys. Rev. Lett.*, 67:3816–3819, Dec 1991.

[73] R. Feenstra, W. Thompson, and A. Fein. Real-space observation of π-bonded chains and surface disorder on Si(111)2×1. *Phys. Rev. Lett.*, 56:608–611, Feb 1986.

[74] C. Goletti, G. Bussetti, F. Arciprete, P. Chiaradia, and G. Chiarotti. Infrared surface absorption in Si(111)2 × 1 observed with reflectance anisotropy spectroscopy. *Phys. Rev. B*, 66:153307, Oct 2002.

[75] C Goletti, G Bussetti, P Chiaradia, and G Chiarotti. Optical transitions and sum rules at clean semiconductor surfaces. *Journal of Physics: Condensed Matter*, 16(39):S4289, 2004.

[76] C. Kittel. *Introduction to Solid State Physics.* Wiley, 8th edition edition.

[77] J. Lefebvre, J.M. Fraser, Y. Homma, and P. Finnie. Photoluminescence from single-walled carbon nanotubes: a comparison between suspended and micelle-encapsulated nanotubes. *Applied Physics A*, 78(8):1107, 2004.

[78] R. E. Peierls. *Quantum Theory of Solids.* Clarendon: Oxford, 8th edition.

[79] H. W. Yeom, S. Takeda, E. Rotenberg, I. Matsuda, K. Horikoshi, J. Schaefer, C. M. Lee, S. D. Kevan, T. Ohta, T. Nagao, and S. Hasegawa. Instability and charge density wave of metallic quantum chains on a Silicon surface. *Phys. Rev. Lett.*, 82:4898–4901, Jun 1999.

[80] C. González, Jiandong Guo, J. Ortega, F. Flores, and H. H. Weitering. Mechanism of the band gap opening across the order-disorder transition of Si(111)-(4×1)-In. *Phys. Rev. Lett.*, 102:115501, Mar 2009.

[81] M. Hashimoto, Y. Fukaya, A. Kawasuso, and A. Ichimiya. Phase transition of In/Si(111) surface studied by reflection high-energy positron diffraction. *e-Journal of Surface Science and Nanotechnology*, 7:436, 2009.

[82] H.E. Bishop and J.C. Riviere. Segregation of gold to the silicon (111) surface observed by auger emission spectroscopy and by leed. *J. Phys. D: J. Appl. Phys.*, 2(12):1635, 1969.

[83] I.R. Collins, J.T. Moran, P.T. Andrews, R. Cosso, J.D. O'Mahony, J.F. McGilp, and G. Margaritondo. Angle-resolved photoemission from an unusual quasi-one-dimensional metallic system: a single domain Au-induced 5×2 reconstruction of Si(111). *Surf. Sci.*, 325(1-2):45 – 49, 1995.

[84] R. Losio, K. N. Altmann, and F. J. Himpsel. Continuous transition from two- to one-dimensional states in Si(111)-(5×2)-Au. *Phys. Rev. Lett.*, 85:808–811, Jul 2000.

[85] J. L. McChesney, J. N. Crain, V. Pérez-Dieste, Fan Zheng, M. C. Gallagher, M. Bissen, C. Gundelach, and F. J. Himpsel. Electronic stabilization of a 5×4 dopant superlattice on Si(111)5×2-Au. *Phys. Rev. B*, 70:195430, Nov 2004.

[86] Won Hoon Choi, Pil Gyu Kang, Kyung Deuk Ryang, and Han Woong Yeom. Band-Structure Engineering of Gold Atomic Wires on Silicon by Controlled Doping. *Phys. Rev. Lett.*, 100:126801, Mar 2008.

[87] H. S. Yoon, S. J. Park, J. E. Lee, C. N. Whang, and I.-W. Lyo. Novel Electronic Structure of Inhomogeneous Quantum Wires on a Si Surface. *Phys. Rev. Lett.*, 92:096801, Mar 2004.

[88] Pil-Gyu Kang, Hojin Jeong, and Han Woong Yeom. Hopping Domain Wall Induced by Paired Adatoms on an Atomic Wire: Si(111)-(5 × 2)-Au. *Phys. Rev. Lett.*, 100:146103, Apr 2008.

[89] I. Barke, S. Polei, V. v. Oeynhausen, and K-H. Meiwes-Broer. Confined Doping on a Metallic Atomic Chain Structure. *Phys. Rev. Lett.*, 109:066801, Aug 2012.

[90] Tadashi Abukawa and Yoshiki Nishigaya. Structure of the Si(111)-(5 × 2)-Au surface. *Phys. Rev. Lett.*, 110:036102, Jan 2013.

[91] E. Bauer. The Si-(111)(5 × 1) Au structure. *Surface Science*, 250(13):L379 – L382, 1991.

[92] I. Barke, F. Zheng, S. Bockenhauer, K. Sell, V. v. Oeynhausen, K. H. Meiwes-Broer, S. C. Erwin, and F. J. Himpsel. Coverage-dependent faceting of Au chains on Si(557). *Phys. Rev. B*, 79:155301, Apr 2009.

[93] I. Matsuda and S. Hasegawa. Fermiology and transport in metallic monatomic layers on semiconductor surfaces. *J. Phys.: Condens. Matter.*, 19(35):355007, 5 Sept. 2007.

[94] Steven C. Erwin. Self-Doping of Gold Chains on Silicon: A New Structural Model for Si(111)-(5 × 2)-Au. *Phys. Rev. Lett.*, 91:206101, Nov 2003.

[95] P. Perfetti, S. Nannarone, F. Patella, C. Quaresima, A. Savoia, F. Cerrina, and M. Capozi. Energy loss spectroscopy (ELS) on the Si-Au system. *Solid State Communications*, 35(2):151 – 153, 1980.

[96] Lonny E. Berman, Boris W. Batterman, and Jack M. Blakely. Structure of submonolayer gold on silicon (111) from x-ray standing-wave triangulation. *Phys. Rev. B*, 38:5397, Sep 1988.

[97] H. Minoda, Y. Tanishiro, N. Yamamoto, and K. Yagi. Growth of Si on Au deposited Si(111) surfaces studied by uhv-rem. *Appl. Surf. Sci.*, 60-61:107, 1992.

[98] L. D. Marks and R. Plass. Atomic structure of Si(111)- (5×2)-Au from high resolution electron microscopy and heavy-atom holography. *Phys. Rev. Lett.*, 75:2172–2175, Sep 1995.

[99] Se Gab Kwon and Myung Ho Kang. Identification of the Au coverage and structure of the Au/Si(111) $-$ (5×2) surface. *Phys. Rev. Lett.*, 113:086101, Aug 2014.

[100] Kazuyuki Sakamoto and R. I. G. Uhrberg. Atomic and electronic structures of metal induced Si(111)-(3×1) reconstructed surfaces. *e-Journal of Surface Science and Nanotechnology*, 2:210–221, 2004.

[101] Steven C. Erwin and Hanno H. Weitering. Theory of the "honeycomb chain-channel" reconstruction of Si(111)-(3×1). *Phys. Rev. Lett.*, 81:2296–2299, Sep 1998.

[102] J. K. Kim, K. S. Kim, J. L. McChesney, E. Rotenberg, H. N. Hwang, C. C. Hwang, and H. W. Yeom. Two-dimensional electron gas formed on the indium-adsorbed Si(111)$\sqrt{3} \times \sqrt{3}$-Au surface. *Phys. Rev. B*, 80:075312, Aug 2009.

[103] R Bennewitz, J N Crain, A Kirakosian, J-L Lin, J L McChesney, D Y Petrovykh, and F J Himpsel. Atomic scale memory at a silicon surface. *Nanotechnology*, 13(4):499, 2002.

[104] Feng-Chuan Chuang, Chia-Hsiu Hsu, Cai-Zhuang Wang, and Kai-Ming Ho. Honeycomb chain structure of the Au/Si(111)-(5×2) surface reconstruction: A first-principles study. *Phys. Rev. B*, 77:153409, Apr 2008.

[105] Sampsa Riikonen and Daniel Sánchez-Portal. First-principles study of the atomic and electronic structure of the Si(111)-(5×2)-Au surface reconstruction. *Phys. Rev. B*, 71:235423, Jun 2005.

[106] N McAlinden and J F McGilp. Using surface and interface optics to probe the capping, with amorphous Si, of Au atom chains grown on vicinal Si(111). *Journal of Physics: Condensed Matter*, 21(47):474208, 2009.

[107] R. Losio, K. N. Altmann, and F. J. Himpsel. Continuous transition from two- to one-dimensional states in Si(111)-(5 × 2)-Au. *Phys. Rev. Lett.*, 85:808, Jul 2000.

[108] K. N. Altmann, J. N. Crain, A. Kirakosian, J.-L. Lin, D. Y. Petrovykh, F. J. Himpsel, and R. Losio. Electronic structure of atomic chains on vicinal Si(111)-Au. *Phys. Rev. B*, 64:035406, Jun 2001.

[109] Myung Ho Kang and Ji Young Lee. Theoretical investigation of the Au/Si(111)-(5 × 2) surface structure. *Surf. Sci.*, 531(1):1 – 7, 2003/05/10.

[110] Iwao Matsuda, Matthias Hengsberger, Felix Baumberger, Thomas Greber, Han Woong Yeom, and Jürg Osterwalder. Reinvestigation of the band structure of the Si(111)5 × 2-Au surface. *Phys. Rev. B*, 68:195319, Nov 2003.

[111] N. McAlinden and J. F. McGilp. New evidence for the influence of step morphology on the formation of Au atomic chains on vicinal Si(111) surfaces. *EPL (Europhysics Letters)*, 92(6):67008, 2010.

[112] Dr. Nial McAlinden. PhD thesis.

[113] Kenta Arima, Jun Katoh, Shinya Horie, Katsuyoshi Endo, Tomoya Ono, Shigetoshi Sugawa, Hiroshi Akahori, Akinobu Teramoto, and Tadahiro Ohmi. Hydrogen termination of Si(110) surfaces upon wet cleaning revealed by highly resolved scanning tunneling microscopy. *Journal of Applied Physics*, 98(10):103525, 2005.

[114] Kazuyuki Sakamoto, Martin Setvin, Kenji Mawatari, P. E. J. Eriksson, Kazushi Miki, and R. I. G. Uhrberg. Electronic structure of the Si(110)-

(16 × 2) surface: High-resolution ARPES and STM investigation. *Phys. Rev. B*, 79:045304, Jan 2009.

[115] Yoichi Yamada, Antoine Girard, Hidehito Asaoka, Hiroyuki Yamamoto, and Shin-ichi Shamoto. Single-domain Si(110)-(16 × 2) surface fabricated by electromigration. *Phys. Rev. B*, 76:153309, Oct 2007.

[116] Yoichi Yamada, Antoine Girard, Hidehito Asaoka, Hiroyuki Yamamoto, and Shin-ichi Shamoto. Controlling the surface chirality of Si(110). *Phys. Rev. B*, 77:153305, Apr 2008.

[117] Youiti Yamamoto. Atomic arrangements of 16 × 2 and (17,15,1) 2 × 1 structures on a Si(110) surface. *Phys. Rev. B*, 50:8534, Sep 1994.

[118] H. Ampo, S. Miura, K. Kato, Y. Ohkawa, and A. Tamura. Atomic configuration of hydrogenated and clean Si(110) surfaces. *Phys. Rev. B*, 34:2329, Aug 1986.

[119] Toshu An, Masamichi Yoshimura, Izumi Ono, and Kazuyuki Ueda. Elemental structure in Si(110)-"16×2" revealed by scanning tunneling microscopy. *Phys. Rev. B*, 61:3006, Jan 2000.

[120] William E. Packard and John D. Dow. Si(110)-16 × 2 and Si(110)-5 × 1 surface reconstructions: Stretched-hexagon face-centered adatom model. *Phys. Rev. B*, 55:15643, Jun 1997.

[121] A. Crincenti, B. Nesterenko, P. Perfetti, G. LeLay, and C. Sebenne. Electronic states of a clean Si(110) 16 × 2 surface studied by angle resolved photoemission and surface differential reflectivity. *Journal of Vacuum Science & Technology A*, 14(4):2448, 1996.

[122] Enrico G. Keim, Herbert Wormeester, and Arend van Silfhout. Chemical titration of clean silicon surfaces with N_2O and O_2: Atomic nature of 5 × 1 reconstructed Si(110). *Journal of Vacuum Science & Technology A*, 8(3):2747, 1990.

[123] T Ichikawa, T Sueyosi, T Sato, M Iwatsuki, F Udagawa, and I Sumita. Ge(110) surface reconstruction observed with scanning tuneling microscopy. *Solid State Communications*, 93(6):541 – 545, 1995.

[124] R. Butz and H. Lth. The structure of clean and SiGe-covered Si(110) surfaces. *Surface Science*, 365(3):807 – 816, 1996.

[125] Martin Setvín, Veronika Brázdová, David R. Bowler, Kota Tomatsu, Kan Nakatsuji, Fumio Komori, and Kazushi Miki. Electronic structure of Si(110)-(16 × 2) studied by scanning tunneling spectroscopy and density functional theory. *Phys. Rev. B*, 84:115317, Sep 2011.

[126] L. Grill, A. Santoni, S. Prato, L. Petaccia, and S. Modesti. Temperature dependence of the photoemission spectra of Si(110) between 300 and 1630 k. *Surface Science*, 474(13):55 – 63, 2001.

[127] Elena Ferraro, Conor Hogan, Maurizia Palummo, and Rodolfo Del Sole. Optical properties of the long-range Si(110)-(16 × 2) reconstruction from first principles. *physica status solidi (b)*, 249(6):1148, 2012.

[128] A. Cricenti, P. Perfetti, B. Nesterenko, G. LeLay, and C. Sebenne. Electronic states on clean Si(110)16 × 2 and Si(110)2 × 3-Sb surfaces by photoeemission and optical spectroscopy. *Journal of Electron Spectroscopy and Related Phenomena*, 76:481 – 486, 1995. Proceedings of the Sixth International Conference on Electron Spectroscopy.

[129] R. J. Hamers, R. M. Tromp, and J. E. Demuth. Scanning tunneling microscopy of Si(001). *Phys. Rev. B*, 34:5343–5357, Oct 1986.

[130] S. D. Kevan. Surface states and reconstruction on Ge(001). *Phys. Rev. B*, 32:2344, Aug 1985.

[131] E. Landemark, R.I.G. Uhrberg, P. Kruger, and J. Pollmann. Surface electronic structure of Ge(001)2 × 1: experiment and theory. *Surf. Sci.*, 236(3):359 – 64, 1990/10/.

[132] M. Mitome and K. Takayanagi. The direct observation of the Ge(001) dimer structure by high resolution UHV transmission electron microscopy. volume 242, pages 69 – 72, Netherlands, 1991/02/.

[133] V.E. Zubkus, P.J. Kundrotas, S.N. Molotkov, V.V. Tatarskij, and E.E. Tornau. Monte carlo study of surface reconstruction in Ge(001). *Surf. Sci.*, 243(1-3):295 – 302, 1991/02/.

[134] R. E. Schlier and H. E. Farnsworth. Proceedings of second conference on semiconductor surfaces. *Physics and Chemistry of Solids*, 14:299, 1960.

[135] D. J. Chadi. Atomic and Electronic Structures of Reconstructed Si(100) Surfaces. *Phys. Rev. Lett.*, 43:43–47, Jul 1979.

[136] G. Le Lay, J. Kanski, P. O. Nilsson, U. O. Karlsson, and K. Hricovini. Surface core-level shifts on Ge(100):$c(4 \times 2)$ to 2×1 and 1×1 phase transitions. *Phys. Rev. B*, 45:6692, Mar 1992.

[137] P. Krüger, A. Mazur, J. Pollmann, and G. Wolfgarten. First-Principles Electronic Structure Theory for Semi-infinite Semiconductors with Applications. *Phys. Rev. Lett.*, 57:1468, Sep 1986.

[138] M. Needels, M. C. Payne, and J. D. Joannopoulos. *Ab initio* molecular dynamics on the Ge(100) surface. *Phys. Rev. Lett.*, 58:1765, Apr 1987.

[139] M. Needels, M. C. Payne, and J. D. Joannopoulos. High-order reconstructions of the Ge(100) surface. *Phys. Rev. B*, 38:5543, Sep 1988.

[140] B.A.G. Kersten, H.J.W. Zandvliet, D.H.A. Blank, and A. van Silfhout. Step structure of vicinal Ge(001) surfaces. *Surf. Sci.*, 322(1-3):1 – 7, 1995/01/01.

[141] T. Sato, T. Sueyoshi, T. Amakusa, M. Iwatsuki, and H. Tochihara. Comment on 'Step structure of vicinal Ge(001) surfaces' by B.A.G. Kersten, H.J.W. Zandvliet, D.H.A. Blank and A. van Silfhout. *Surf. Sci.*, 340(3):328 – 32, 1995.

[142] T. Sato, M. Iwatsuki, and H. Tochihara. Detection of the flip-flop motion of buckled dimers on a Ge(001) surface by STM. *J. Electron. Microsc.*,

48(1):1 – 7, 1999.

[143] J. Ihm, D. H. Lee, J. D. Joannopoulos, and J. J. Xiong. Structural phase diagrams for the surface of a solid: A total-energy, renormalization-group approach. *Phys. Rev. Lett.*, 51:1872–1875, Nov 1983.

[144] Harold J.W. Zandvliet. The ge(0 0 1) surface. *Physics Reports*, 388(1):1 – 40, 2003.

[145] Takeshi Tabata, Tetsuya Aruga, and Yoshitada Murata. Order-disorder transition on Si(001): c(4×2) to (2×1). *Surface Science Letters*, 179(1):L63 – L70, 1987.

[146] A. D. Johnson, C. Norris, J. W. M. Frenken, H. S. Derbyshire, J. E. MacDonald, R. G. Van Silfhout, and J. F. Van Der Veen. Combined $(1 \times 2) \rightarrow (1 \times 1)$ transition and atomic roughening of Ge(001) studied with surface x-ray diffraction. *Phys. Rev. B*, 44:1134, Jul 1991.

[147] R.J. Culbertson, Y. Kuk, and L.C. Feldman. Subsurface strain in the Ge(001) and Ge(111) surfaces and comparison to silicon. *Sur. Sci.*, 167(1):127–140, 1986.

[148] Toshihiro Ichikawa and Shozo Ino. Double diffraction spots in RHEED patterns from clean Ge(111) and Si(001) surfaces. *Surface Science*, 85(2):221 – 243, 1979.

[149] X. Torrelles, H.A. van der Vegt, V.H. Etgens, P. Fajardo, J. Alvarez, and S. Ferrer. The structure of the $\mathrm{Ge}(001) - (2 \times 1)$ reconstruction investigated with x-ray diffraction. *Surface Science*, 364(3):242 – 252, 1996.

[150] Tetsuroh Shirasawa, Seigi Mizuno, and Hiroshi Tochihara. Structural analysis of the c(4 × 2) reconstruction in Si(001) and Ge(001) surfaces by low-energy electron diffraction. *Surface Science*, 600(4):815, 2006.

[151] Yoshihide Yoshimoto, Yoshimichi Nakamura, Hiroshi Kawai, Masaru Tsukada, and Masatoshi Nakayama. Ge(001) surface reconstruction studied using a first-principles calculation and a monte carlo simulation. *Phys. Rev. B*, 61:1965, Jan 2000.

[152] S. D. Kevan and N. G. Stoffel. Metal-insulator transition on the Ge(001) surface. *Phys. Rev. Lett.*, 53:702, Aug 1984.

[153] R.J. Culbertson, Y. Kuk, and L.C. Feldman. Subsurface strain in the Ge(001) and Ge(111) surfaces and comparison to silicon. *Surf. Sci.*, 167(1):127 – 40, 1986//.

[154] L. Spiess, A. J. Freeman, and P. Soukiassian. Ge(100)2 × 1 and $c(4 \times 2)$ surface reconstructions studied by *ab initio* total-energy molecular-force calculations. *Phys. Rev. B*, 50:2249–2258, Jul 1994.

[155] P. Krger and J. Pollmann. Theoryofadsorption : Ordered monolayers from Na to Cl on Si(001) and Ge(001). *Applied Physics A Solids and Surfaces*, 59(5):487, 1994.

[156] N. Jedrecy, M. Sauvage-Simkin, R. Pinchaux, J. Massies, N. Greiser, and V.H. Etgens. Asymmetric versus symmetric dimerization on the Si(001) and As/Si(001)2×1 reconstructed surfaces as observed by grazing incidence x-ray diffraction. *Surface Science*, 230(13):197 – 204, 1990.

[157] R. D. Bringans, R. I. G. Uhrberg, M. A. Olmstead, and R. Z. Bachrach. Surface bands for single-domain 2×1 reconstructed Si(100) and Si(100):As. Photoemission results for off-axis crystals. *Phys. Rev. B*, 34:7447–7450, Nov 1986.

[158] R. I. G. Uhrberg, R. D. Bringans, R. Z. Bachrach, and John E. Northrup. Symmetric arsenic dimers on the Si(100) surface. *Phys. Rev. Lett.*, 56:520–523, Feb 1986.

[159] R. S. Becker, T. Klitsner, and J. S. Vickers. Arsenic-terminated silicon and germanium surfaces studied by scanning tunnelling microscopy. *Journal of Microscopy*, 152(1):157, 1988.

[160] J.F. Morar, U.O. Karlsson, R.I.G. Uhrberg, J. Kanski, P.O. Nilsson, and H. Qu. Angle-resolved photoemission study of the As/Ge(100) interface. *Applied Surface Science*, 4142(0):312 – 316, 1990.

[161] D. H. Rich, F. M. Leibsle, A. Samsavar, E. S. Hirschorn, T. Miller, and T.-C. Chiang. Adsorption and interaction of Sb on Si(001) studied by scanning tunneling microscopy and core-level photoemission. *Phys. Rev. B*, 39:12758–12763, Jun 1989.

[162] D. H. Rich, T. Miller, and T.-C. Chiang. Electronic and chemical properties of In and Sb adsorbed on Ge(100) studied by synchrotron photoemission. *Phys. Rev. B*, 41:3004–3016, Feb 1990.

[163] J. P. Pique, Y. Chen, R. W. Field, and J. L. Kinsey. Chaos and dynamics on 0.5-300 ps time scales in vibrationally excited acetylene: Fourier transform of stimulated-emission pumping spectrum. *Phys. Rev. Lett.*, 58:475–478, Feb 1987.

[164] Martin Lohmeier, H.A. van der Vegt, R.G. van Silfhout, E. Vlieg, J.M.C. Thornton, J.E. Macdonald, and P.M.L.O. Scholte. Asymmetrical dimers on the Ge(001) $-$ 2 $\times$ 1 $-$ Sb surface observed using x-ray diffraction. *Surface Science*, 275(3):190 – 200, 1992.

[165] Noboru Takeuchi. Symmetric dimers on the Ge(100) $-$ 2 $\times$ 1 $-$ Sb surface. *Phys. Rev. B*, 55:2417–2419, Jan 1997.

[166] R. Shaltaf, M. akmak, E. Mete, G.P. Srivastava, and . Ellialtolu. Ab initio study of the one-monolayer Sb/Ge(001) interface. *Surface Science*, 566568, Part 2(0):956 – 960, 2004. Proceedings of the 22nd European Conference on Surface Science.

[167] L. Kipp, R. Manzke, and M. Skibowski. An intrinsic metallic surface state on Ge(001)2 $\times$ 1. *Solid State Commun.*, 93(7):603, 1995/02/.

[168] L. Kipp, R. Manzke, and M. Skibowski. The surface band gaps of Ge(001)(2 $\times$ 1). volume 269-270, pages 854 – 9, Netherlands, 1992.

[169] Oguzhan Gurlu, Harold J. W. Zandvliet, and Bene Poelsema. Electronic properties of (2 $\times$ 1) and c(4 $\times$ 2) domains on Ge(001) studied by scanning tunneling spectroscopy. *Phys. Rev. Lett.*, 93:066101, Aug 2004.

[170] U. Schwingenschlögl and C. Schuster. Electronic structure of the c(4 × 2) reconstructed Ge(001) surface. *Chem. Phys. Lett.*, 449(1-3):126 – 9, 2007.

[171] D.J. Wentink, H. Wormeester, P. de Boeij, C. Wijers, and A. van Silfhout. Optical anisotropy of Ge(001)2 × 1. *Surf. Sci. (Netherlands)*, 274(2):270, 1992.

[172] A.I. Shkrebtii and R. Del Sole. Microscopic calculation of structure and optical properties of Ge(001)$c(4 \times 2)$. *Surf. Sci.*, 331-333(pt B):1288, 1995.

[173] Sebastian Brckner, Enrique Barrigón, Oliver Supplie, Peter Kleinschmidt, Anja Dobrich, Claas Lbbel, Ignacio Rey-Stolle, Henning Dscher, and Thomas Hannappel. Ge(100) surfaces prepared in vapor phase epitaxy process ambient. *physica status solidi (RRL) Rapid Research Letters*, 6(4):178–180, 2012.

[174] Enrique Barrigón, Sebastian Brückner, Oliver Supplie, Peter Kleinschmidt, Ignacio Rey-Stolle, and Thomas Hannappel. Optical in situ monitoring of hydrogen desorption from Ge(100) surfaces. *Applied Physics Letters*, 102(11):111608, 2013.

[175] L. H. Thomas. The calculation of atomic fields. *Mathematical Proceedings of the Cambridge Philosophical Society*, 23:542–548, 1927.

[176] E. Fermi. Un metodo statistico per la determinazione di alcune priopriet dell'atomo. *Rend. Accad. Naz. Lincei*, 6, 1927.

[177] P. Hohenberg and W. Kohn. Inhomogeneous electron gas. *Phys. Rev.*, 136:B864–B871, Nov 1964.

[178] M. P. Allen and D. J. Tildesley. *Computer Simulation of Liquids*. Oxford University Press, 1987.

[179] B. T. Thole, P. Carra, F. Sette, and G. van der Laan. X-ray circular dichroism as a probe of orbital magnetization. *Phys. Rev. Lett.*, 68:1943–1946, Mar 1992.

[180] G. Ortiz. Gradient-corrected pseudopotential calculations in semiconductors. *Phys. Rev. B*, 45:11328–11331, May 1992.

[181] Andrea Dal Corso, Stefano Baroni, and Raffaele Resta. Density-functional theory of the dielectric constant: Gradient-corrected calculation for silicon. *Phys. Rev. B*, 49:5323–5328, Feb 1994.

[182] W. Kohn and L. J. Sham. Self-consistent equations including exchange and correlation effects. *Phys. Rev.*, 140:A1133–A1138, Nov 1965.

[183] Stefano Baroni and Raffaele Resta. *Ab initio* calculation of the macroscopic dielectric constant in silicon. *Phys. Rev. B*, 33:7017–7021, May 1986.

[184] R. O. Jones and O. Gunnarsson. The density functional formalism, its applications and prospects. *Rev. Mod. Phys.*, 61:689–746, Jul 1989.

[185] W. Kohn and L. J. Sham. Self-consistent equations including exchange and correlation effects. *Phys. Rev.*, 140:A1133–A1138, Nov 1965.

[186] Frank Herman, John P. Van Dyke, and Irene B. Ortenburger. Improved statistical exchange approximation for inhomogeneous many-electron systems. *Phys. Rev. Lett.*, 22:807–811, Apr 1969.

[187] Andrew E. DePristo and Joel D. Kress. Rational function representation for accurate exchange energy functionals. *The Journal of Chemical Physics*, 86(3), 1987.

[188] J. P. Perdew, D. C. Langreth, and V. Sahni. Corrections to the local density approximation: Gradient expansion versus wave-vector analysis for the metallic surface problem. *Phys. Rev. Lett.*, 38:1030–1033, May 1977.

[189] David C. Langreth and M. J. Mehl. Beyond the local-density approximation in calculations of ground-state electronic properties. *Phys. Rev. B*, 28:1809–1834, Aug 1983.

[190] John P. Perdew. Accurate density functional for the energy: Real-space cutoff of the gradient expansion for the exchange hole. *Phys. Rev. Lett.*, 55:1665–1668, Oct 1985.

[191] A. D. Becke. Density-functional exchange-energy approximation with correct asymptotic behavior. *Phys. Rev. A*, 38:3098–3100, Sep 1988.

[192] John P. Perdew. Density-functional approximation for the correlation energy of the inhomogeneous electron gas. *Phys. Rev. B*, 33:8822–8824, Jun 1986.

[193] John P. Perdew and Wang Yue. Accurate and simple density functional for the electronic exchange energy: Generalized gradient approximation. *Phys. Rev. B*, 33:8800–8802, Jun 1986.

[194] John P. Perdew. Erratum: Density-functional approximation for the correlation energy of the inhomogeneous electron gas. *Phys. Rev. B*, 34:7406–7406, Nov 1986.

[195] John P. Perdew and Yue Wang. Accurate and simple analytic representation of the electron-gas correlation energy. *Phys. Rev. B*, 45:13244–13249, Jun 1992.

[196] Leslie C. Wilson and Mel Levy. Nonlocal wigner-like correlation-energy density functional through coordinate scaling. *Phys. Rev. B*, 41:12930–12932, Jun 1990.

[197] Chengteh Lee, Weitao Yang, and Robert G. Parr. Development of the colle-salvetti correlation-energy formula into a functional of the electron density. *Phys. Rev. B*, 37:785–789, Jan 1988.

[198] E. Engel, J.A. Chevary, L.D. Macdonald, and S.H. Vosko. Asymptotic properties of the exchange energy density and the exchange potential of finite systems: relevance for generalized gradient approximations. *Zeitschrift fr Physik D Atoms, Molecules and Clusters*, 23(1):7–14, 1992.

[199] John P. Perdew, J. A. Chevary, S. H. Vosko, Koblar A. Jackson, Mark R. Pederson, D. J. Singh, and Carlos Fiolhais. Atoms, molecules, solids, and surfaces: Applications of the generalized gradient approximation for exchange and correlation. *Phys. Rev. B*, 46:6671–6687, Sep 1992.

[200] G. Ortiz and P. Ballone. Pseudopotentials for non-local-density functionals. *Phys. Rev. B*, 43:6376–6387, Mar 1991.

[201] Axel D. Becke. Density functional thermochemistry. I. The effect of the exchange-only gradient correction. *The Journal of Chemical Physics*, 96(3), 1992.

[202] P. Ballone and R. O. Jones. Density functional study of phosphorus and arsenic clusters using local and nonlocal energy functionals. *The Journal of Chemical Physics*, 100(7), 1994.

[203] P. Bagno, O. Jepsen, and O. Gunnarsson. Ground-state properties of third-row elements with nonlocal density functionals. *Phys. Rev. B*, 40:1997–2000, Jul 1989.

[204] K. Laasonen, F. Csajka, and M. Parrinello. Water dimer properties in the gradient-corrected density functional theory. *Chemical Physics Letters*, 194(3):172 – 174, 1992.

[205] Changyol Lee, David Vanderbilt, Kari Laasonen, R. Car, and M. Parrinello. *Ab initio* studies on the structural and dynamical properties of ice. *Phys. Rev. B*, 47:4863–4872, Mar 1993.

[206] Lars Stixrude, R. E. Cohen, and D. J. Singh. Iron at high pressure: Linearized-augmented-plane-wave computations in the generalized-gradient approximation. *Phys. Rev. B*, 50:6442–6445, Sep 1994.

[207] T. C. Leung, C. T. Chan, and B. N. Harmon. Ground-state properties of Fe, Co, Ni, and their monoxides: Results of the generalized gradient approximation. *Phys. Rev. B*, 44:2923–2927, Aug 1991.

[208] D. J. Singh and J. Ashkenazi. Magnetism with generalized-gradient-approximation density functionals. *Phys. Rev. B*, 46:11570–11577, Nov 1992.

[209] Alberto García, Christian Elsässer, Jing Zhu, Steven G. Louie, and Marvin L. Cohen. Use of gradient-corrected functionals in total-energy calculations for solids. *Phys. Rev. B*, 46:9829–9832, Oct 1992.

[210] M. Körling and J. Häglund. Cohesive and electronic properties of transition metals: The generalized gradient approximation. *Phys. Rev. B*, 45:13293–13297, Jun 1992.

[211] V. Ozoliņš and M. Körling. Full-potential calculations using the generalized gradient approximation: Structural properties of transition metals. *Phys. Rev. B*, 48:18304–18307, Dec 1993.

[212] N. A. W. Holzwarth and Y. Zeng. Core-cancellation functions for evaluating exchange-correlation functionals in first-principles pseudopotential calculations. *Phys. Rev. B*, 49:2351–2361, Jan 1994.

[213] X. J. Kong, C. T. Chan, K. M. Ho, and Y. Y. Ye. Cohesive properties of crystalline solids by the generalized gradient approximation. *Phys. Rev. B*, 42:9357–9364, Nov 1990.

[214] Yu-Min Juan and Efthimios Kaxiras. Application of gradient corrections to density-functional theory for atoms and solids. *Phys. Rev. B*, 48:14944–14952, Nov 1993.

[215] Axel D. Becke. A new mixing of Hartree-Fock and local density functional theories. *The Journal of Chemical Physics*, 98(2), 1993.

[216] A.D. Becke. Density-functional thermochemistry. III. the role of exact exchange. *J. Chem. Phys.*, 98(7):5648, 1993.

[217] Chengteh Lee, Weitao Yang, and Robert G. Parr. Development of the colle-salvetti correlation-energy formula into a functional of the electron density. *Phys. Rev. B*, 37:785, Jan 1988.

[218] Perdew J. P. *Electronic Structure of Solids '91.*

[219] Xiaobing Feng. Electronic structures and ferromagnetism of Cu- and Mn-doped ZnO. *J. Phys., Condens. Matter.*, 16(24):4251, 2004.

[220] S.H. Vosko, L. Wilk, and M. Nusair. Accurate spin-dependent electron liquid correlation energies for local spin density calculations: a critical analysis. *Can. J. Phys.*, 58(8):1200 – 11, 1980.

[221] R. Dovesi, V. R. Saunders, C. Roetti, R. Orlando, C. M. Zicovich-Wilson, F. Ascale, B. Civalleri, K. Doll, N. M. Harrison, I. Bush, P. D'Acro, and M. Llunell. CRYSTAL.

[222] Hendrik J. Monkhorst and James D. Pack. Special points for Brillouin-zone integrations. *Phys. Rev. B*, 13:5188–5192, Jun 1976.

[223] Anton Kokalj. Computer graphics and graphical user interfaces as tools in simulations of matter at the atomic scale. *Computational Materials Science*, 28(2):155 – 168, 2003. Proceedings of the Symposium on Software Development for Process and Materials Design.

[224] G. Kresse and J. Furthmüller. Efficient iterative schemes for *ab initio* total-energy calculations using a plane-wave basis set. *Phys. Rev. B*, 54:11169–11186, Oct 1996.

[225] Paolo Giannozzi, Stefano Baroni, Nicola Bonini, Matteo Calandra, Roberto Car, Carlo Cavazzoni, Davide Ceresoli, Guido L Chiarotti, Matteo Cococcioni, Ismaila Dabo, Andrea Dal Corso, Stefano de Gironcoli, Stefano Fabris, Guido Fratesi, Ralph Gebauer, Uwe Gerstmann, Christos Gougoussis, Anton Kokalj, Michele Lazzeri, Layla Martin-Samos, Nicola Marzari, Francesco Mauri, Riccardo Mazzarello, Stefano Paolini, Alfredo Pasquarello, Lorenzo Paulatto, Carlo Sbraccia, Sandro Scandolo, Gabriele Sclauzero, Ari P Seitsonen, Alexander Smogunov, Paolo Umari, and Renata M Wentzcovitch. Quantum espresso: a modular and open-source software project for quantum simulations of materials. *Journal of Physics: Condensed Matter*, 21(39):395502, 2009.

[226] Laszlo Turi and J. J. Dannenberg. Correcting for basis set superposition error in aggregates containing more than two molecules: ambiguities in the calculation of the counterpoise correction. *The Journal of Physical Chemistry*, 97(11):2488–2490, 1993.

[227] F. Wooten. *Optical properties of solids.* New York ; London : Academic Press, 1972.

[228] A. Rowan S. Galamić-Mulaomerović and C. H. Patterson. EXCITON.

[229] J.D.E. McIntyre and D.E. Aspnes. Differential reflection spectroscopy of very thin surface films. *Surf. Sci.*, 24(2):417 – 34, 1971.

[230] S. Selci, F. Ciccacci, G. Chiarotti, P. Chiaradia, and A. Cricenti. Surface differential reflectivity spectroscopy of semiconductor surfaces. *J. Vac. Sci. Technol. A*, 5(3):327, 1987.

[231] R.J. Cole, B.G. Frederick, and P. Weightman. Substrate dependence of adlayer optical response in reflectance anisotropy spectroscopy. *J. Vac. Sci. Technol. A*, 16(5):3088 – 95, 1998.

[232] Tsutomu Sat. Spectral emissivity of silicon. *Japanese Journal of Applied Physics*, 6(3):339, 1967.

[233] G. Le Lay, J. Kanski, P. O. Nilsson, U. O. Karlsson, and K. Hricovini. Surface core-level shifts on Ge(100): $c(4 \times 2)$ to 2×1 and 1×1 phase transitions. *Phys. Rev. B*, 45:6692–6699, Mar 1992.

[234] Dr. Eberl. MBE Componeten.

[235] L. J. Clarke. *Surface Crystallography: An Introduction to Low Energy Electron Diffraction.* Chichester: Wiley, 1984.

[236] J. C. Rivire. Auger electron spectroscopy. *Contemporary Physics*, 14(6):513, 1973.

[237] G. Chiarotti, G. Del Signore, and S. Nannarone. Optical detection of surface states on cleaved (111) surfaces of Ge. *Phys. Rev. Lett.*, 21:1170, 1968.

[238] John F. McGilp. Optical characterisation of semiconductor surfaces and interfaces. *Prog. Surf. Sci.*, 49(1):1 – 106, 1995.

[239] K. N. Altmann, J. N. Crain, A. Kirakosian, J.-L. Lin, D. Y. Petrovykh, F. J. Himpsel, and R. Losio. Electronic structure of atomic chains on vicinal Si(111)-Au. *Phys. Rev. B*, 64:035406, Jun 2001.

[240] S. Chandola, K. Hinrichs, M. Gensch, N. Esser, S. Wippermann, W. G. Schmidt, F. Bechstedt, K. Fleischer, and J. F. McGilp. Structure of Si(111)-

in nanowires determined from the midinfrared optical response. *Phys. Rev. Lett.*, 102:226805, Jun 2009.

[241] C. Violante, A. Mosca Conte, F. Bechstedt, and O. Pulci. Geometric, electronic, and optical properties of the Si(111)2 × 1 surface: Positive and negative buckling. *Phys. Rev. B*, 86:245313, Dec 2012.

[242] B.G. Streetman and S. Banerjee. *Solid State Electronic Devices.* Pearson Education, 2015.

[243] D. Straub, L. Ley, and F. Himpsel. Conduction-band and surface-state critical points in Si: An inverse-photoemission study. *Phys. Rev. Lett.*, 54:142–145, Jan 1985.

[244] Maurizia Palummo, Nadine Witkowski, Olivier Pluchery, Rodolfo Del Sole, and Yves Borensztein. Reflectance-anisotropy spectroscopy and surface differential reflectance spectra at the Si(100) surface: Combined experimental and theoretical study. *Phys. Rev. B*, 79:035327, Jan 2009.

[245] Charles H. Patterson. Exciton: a code for excitations in materials. *Molecular Physics*, 108:3181, 2010.

[246] J. Rath and A. Freeman. Generalized magnetic susceptibilities in metals: Application of the analytic tetrahedron linear energy method to Sc. *Phys. Rev. B*, 11:2109–2117, Mar 1975.

[247] D Grozea, E Landree, L.D Marks, R Feidenhans'l, M Nielsen, and R.L Johnson. Direct methods determination of the Si(111)-(6 × 6)Au surface structure. *Surface Science*, 418(1):32 – 45, 1998.

[248] J.D. O'Mahony, C.H. Patterson, J.F. McGilp, F.M. Leibsle, P. Weightman, and C.F.J. Flipse. The Au-induced 5 × 2 reconstruction on Si(111). *Surface Science*, 277(1-2):L57 – L62, 1992.

[249] H. S. Yoon, J. E. Lee, S. J. Park, I. W. Lyo, and M. H. Kang. Electronic and geometric structure of Si(111)-5 × 2. *Phys. Rev. B*, 72:155443, Oct 2005.

[250] K. Seino and F. Bechstedt. First-principles calculations of energetics and electronic structure for reconstructed Si(111) – $(5 \times n)$ – Au surfaces. *Phys. Rev. B*, 90:165407, Oct 2014.

[251] Tetsuroh Shirasawa, Wolfgang Voegeli, Takehiro Nojima, Yusaku Iwasawa, Yudai Yamaguchi, and Toshio Takahashi. Identification of the structure model of the Si(111)-(5×2)-Au surface. *Phys. Rev. Lett.*, 113:165501, Oct 2014.

[252] Optical Fingerprints of Si Honeycomb Chains and Atomic Gold Wires.

[253] Fabian Hötzeltzel, Kaori Seino, Christian Huck, Olaf Skibbe, Friedhelm Bechstedt, and Annemarie Pucci. Metallic properties of the Si(111) – $5 \times 2 - au$ surface from infrared plasmon polaritons and ab initio theory. *Nano Letters*, 15(6):4155, 2015. PMID: 25978621.

[254] Yuta Yokoyama, Tatsuya Yamazaki, and Hidehito Asaoka. Change of Si(110) reconstructed structure by Ge nanocluster formation. *Journal of Crystal Growth*, 378:230 – 232, 2013. The 17th International Conference on Molecular Beam Epitaxy.

[255] A. A. Stekolnikov, J. Furthmüller, and F. Bechstedt. Long-range surface reconstruction: Si(110)-(16×2). *Phys. Rev. Lett.*, 93:136104, Sep 2004.

[256] S. Y. Tong, H. Huang, C. M. Wei, W. E. Packard, F. K. Men, G. Glander, and M. B. Webb. Low-energy electron diffraction analysis of the Si(111)7×7 structure. *Journal of Vacuum Science Technology A*, 6(3), 1988.

[257] D. H. Rich, A. Samsavar, T. Miller, F. M. Leibsle, and T.-C. Chiang. Degenerate doping and conduction-band properties of si studied by synchrotron photoemission of Sb/Si(001). *Phys. Rev. B*, 40:3469–3472, Aug 1989.

[258] D. H. Rich, G. E. Franklin, F. M. Leibsle, T. Miller, and T.-C. Chiang. Synchrotron photoemission studies of the Sb-passivated Si surfaces: Degenerate doping and bulk band dispersions. *Phys. Rev. B*, 40:11804–11816, Dec 1989.

[259] A. Cricenti, S. Selci, A. C. Felici, L. Ferrari, G. Contini, and G. Chiarotti. Si(100)1 × 1-Sb and Si(100)2 × 1-Sb surfaces studied with angle-resolved photoemission and surface differential reflectivity. *Phys. Rev. B*, 47:15745–15749, Jun 1993.

[260] M. Richter, J. C. Woicik, J. Nogami, P. Pianetta, K. E. Miyano, A. A. Baski, T. Kendelewicz, C. E. Bouldin, W. E. Spicer, C. F. Quate, and I. Lindau. Surface extended-x-ray-absorption fine structure and scanning tunneling microscopy of Si(001)2 × 1 − Sb. *Phys. Rev. Lett.*, 65:3417–3420, Dec 1990.

[261] W.F.J. Slijkerman, P.M. Zagwijn, J.F. van der Veen, D.J. Gravesteijn, and G.F.A. van de Walle. The interaction of Sb overlayers with Si(001). *Surface Science*, 262(12):25 – 32, 1992.

[262] J. Nogami, A. A. Baski, and C. F. Quate. Structure of the Sb terminated Si(100) surface. *Applied Physics Letters*, 58(5), 1991.

[263] J. C. Slater. Atomic radii in crystals. *The Journal of Chemical Physics*, 41(10), 1964.

[264] Kan Nakatsuji, Yasumasa Takagi, Fumio Komori, Hideaki Kusuhara, and Akira Ishii. Electronic states of the clean Ge(001) surface near fermi energy. *Phys. Rev. B*, 72:241308, Dec 2005.

[265] C. Jeon, C. C. Hwang, T. H. Kang, K. J. Kim, B. Kim, Y. Chung, and C. Y. Park. Evidence from ARPES that the Ge(001) surface is semiconducting at room temperature. *Phys. Rev. B*, 74:125407, Sep 2006.

[266] P. E. J. Eriksson, M. Adell, Kazuyuki Sakamoto, and R. I. G. Uhrberg. Origin of a surface state above the fermi level on Ge(001) and Si(001) studied by temperature-dependent ARPES and LEED. *Phys. Rev. B*, 77:085406, Feb 2008.

[267] M. W. Radny, G. A. Shah, S. R. Schofield, P. V. Smith, and N. J. Curson. Valence surface electronic states on Ge(001). *Phys. Rev. Lett.*, 100:246807, Jun 2008.

[268] Binghai Yan, Chiyung Yam, Andreia Luisa da Rosa, and Thomas Frauenheim. Comment on "valence surface electronic states on Ge(001)". *Phys. Rev. Lett.*, 103:189701, Oct 2009.

[269] M. W. Radny, G. A. Shah, S. R. Schofield, P. V. Smith, and N. J. Curson. Radny *et al.* reply:. *Phys. Rev. Lett.*, 103:189702, Oct 2009.

[270] Herbert Wormeester, Derk Jan Wentink, Paul L. de Boeij, Chris M. J. Wijers, and Arend van Silfhout. Surface states of the clean and oxidized Ge(001) surface studied with normal-incidence ellipsometry. *Phys. Rev. B*, 47:12663–12671, May 1993.

[271] H. M. Tütüncü, S. J. Jenkins, and G. P. Srivastava. Atomic geometry, electronic structure, and vibrational properties of the Ge(001)(2×1) surface. *Phys. Rev. B*, 57:4649, Feb 1998.

[272] S. Banerjee, J. F. McGilp, and C. H. Patterson. Reflectance anisotropy spectroscopy of clean and Sb covered Ge(001) surfaces and comparison with clean Si(001) surfaces. *physica status solidi (b)*, 252(1):78–86, 2015.

[273] E. D. Palik (ed.). *Handbook of Optical constants of Solids.* Academic Press, New York, 1997.

[274] U. Rossow, L. Mantese, and D.E. Aspnes. Surface-induced optical anisotropy of Si and Ge. *J. Vac. Sci. Technol. B*, 18(4):2229, 2000/07/.

[275] Maurizia Palummo, Giovanni Onida, Rodolfo Del Sole, and Bernardo S. Mendoza. *Ab initio* optical properties of Si(100). *Phys. Rev. B*, 60:2522–2527, Jul 1999.

[276] A. Ciucivara, B. R. Sahu, S. Joshi, S. K. Banerjee, and L. Kleinman. Density functional study of Si(001)-Si(110) and Si(100)-Si(110) interfaces. *Phys. Rev. B*, 75:113309, Mar 2007.

[277] Fabien Pascale, Claudio M. Zicovich-Wilson, Roberto Orlando, Carla Roetti, Piero Ugliengo, and Roberto Dovesi. Vibration frequencies of $Mg_3Al_2Si_3O_{12}$ Pyrope. An ab initio study with the CRYSTAL code.

The Journal of Physical Chemistry B, 109(13):6146–6152, 2005. PMID: 16851679.

[278] Y. Noel, M. Catti, Ph. DArco, and R. Dovesi. The vibrational frequencies of forsterite Mg_2SiO_4: an all-electron ab initio study with the CRYSTAL code. *Physics and Chemistry of Minerals*, 33(6):383–393, 2006.

[279] Richard Weihrich and Irina Anusca. Halbantiperowskite II: zur kristallstruktur des $Pd_3Bi_2S_2$. *Zeitschrift fr anorganische und allgemeine Chemie*, 632(2):335–342, 2006.

[280] P. Jeffrey Hay and Willard R. Wadt. Ab initio effective core potentials for molecular calculations. Potentials for K to Au including the outermost core orbitals. *The Journal of Chemical Physics*, 82(1), 1985.

[281] M. Causà, R. Dovesi, and C. Roetti. Pseudopotential Hartree-fock study of seventeen III-V and IV-IV semiconductors. *Phys. Rev. B*, 43:11937–11943, May 1991.

[282] Philippe Durand and Jean-Claude Barthelat. A theoretical method to determine atomic pseudopotentials for electronic structure calculations of molecules and solids. *Theoretica chimica acta*, 38(4):283–302, 1975.

[283] R. Clark Jones. A new calculus for the treatment of optical systems. *J. Opt. Soc. Am.*, 31(7):488, Jul 1941.

[284] Henry Hurwitz Jr. and R. Clark Jones. A new calculus for the treatment of optical systems. *J. Opt. Soc. Am.*, 31(7):493–495, Jul 1941.